UNIVERSITY OF SOUTHAMPTON
FACULTY OF PHYSICAL AND APPLIED SCIENCES
SCHOOL OF ELECTRONICS AND COMPUTER SCIENCE

Radio Over Fiber Systems

by

Salman Ghafoor
B.Sc, M.Sc

A doctoral thesis submitted in partial fulfilment of the requirements for the award of Doctor of Philosophy at the University of Southampton

June 2012

SUPERVISOR:
Prof. Lajos Hanzo
M.Sc, Ph.D, FREng, FIEEE, FIEE, DSc,
Chair of Telecommunications
School of Electronics and Computer Science

University of Southampton
Southampton SO17 1BJ
United Kingdom

𝔇edicated to my family

UNIVERSITY OF SOUTHAMPTON

ABSTRACT

Faculty of Engineering, Science and Mathematics
School of Electronics and Computer Science

Thesis submitted in partial fulfilment of the requirements for the award of Doctor of Philosophy

Radio Over Fiber Systems

by Salman Ghafoor

The three main types of Radio Over Fiber (ROF) communication systems, namely analogue ROF, baseband ROF and digitized ROF are investigated. Optical fibers are increasingly replacing copper wires. In long-haul, high-bit-rate communication systems optical fiber has already become the dominant mode of transmission due to its enormous bandwidth and low loss. ROF facilitate the seamless integration of optical and wireless communication systems. Since the RF spectrum is limited, wireless systems rely on re-using the frequencies at different geographic locations, but the ever-increasing tele-traffic demands require ever-reduced cell-sizes. This enables wireless systems to provide high data rates for a reduced number of users by assigning each of them a larger fraction of the total bandwidth. Furthermore, higher frequencies, expanding to the microwave and mm-wavelength bands are capable of supporting increased data rates. Since high-frequency signals travel shorter distances due to their higher path-loss, the cell sizes have to be further reduced. This reduction in cell size implies that more Radio Access Units (RAUs) are required for the increased number of cells, which are located close to each other. Conceiving these RAUs relying on complex signal processing is costly. Therefore, it is desirable to have simple RAUs that are connected to a central unit where all the signal processing tasks are carried out. In this scenario, ROF plays an important role in connecting these RAUs to the central unit. The major factors that makes ROF suitable is its transparency to the type of RF signal being transported, the large available bandwidth of fiber and its low attenuation.

The first type of ROF communication investigated is baseband ROF (BROF), where electronic baseband data is directly transmitted over the fiber after Electronic-to-Optical (EO) conversion. Baseband optical communications generally transmit optical pulses that have a Gaussian time-domain profile associated with the most compact spectrum for transmitting baseband digital data. Optical pulsed laser sources are capable of generating narrow Gaussian pulses that may be used for high-rate systems relying on ON-OFF keying. All-optical regeneration of signals is investigated, where the signals transmitted over large distances may be regenerated at regular intervals. The second type of ROF communication is analogue ROF (AROF), where the analogue RF signal is transmitted over the fiber using an optical carrier. Finally, digitized ROF (DROF) communication is discussed, which digitizes the RF signal at the transmitter and after transmitting it over the fiber, it converts the digital signal back to analogue at the receiver. The thesis is concluded with the comparative study of the pros and cons of BROF, AROF and DROF techniques.

Acknowledgements

I would like to express my sincere gratitude to my supervisor Prof. Lajos Hanzo for his continous support and guidance during my studies. Prof. Hanzo is a source of great help and motivation and I have benefited a lot from his knowledge and vast experience.

I am extremely thankful to my family for their support and motivation during my studies. I would specially like to thank my mother for her support and prayers that have enabled me to achieve difficult milestones in my life. I have always received great motivation from my family in times when I am facing difficulties.

Declaration of Authorship

I, Salman Ghafoor, declare that the thesis entitled

Radio Over Fiber Systems

and the work presented in this thesis are both my own, and have been generated by me as the results of my own original research. I confirm that:

- this work was done wholly or mainly while in candidature for a research degree at this University;
- where any part of this thesis has previously been submitted for a degree or any other qualification at this University or any other institution, this has been clearly stated;
- where I have consulted the published work of others, this is always clearly stated;
- where I have quoted from the work of others, the source is always given. With the exception of such quotations, this thesis is entirely my own work;
- I have acknowledged all main sources of help;
- where the thesis is based on work done by myself jointly with others, I have made clear exactly what was done by others and what I have contributed myself;
- parts of this work have been published, as seen in List of Publications.

Signed:.....

Dated:.....

Publications

Conference Papers

1. **S. Ghafoor** and L. Hanzo, Reduced Dispersion Duplex DQPSK Radio-Over-Fiber Communications Using Single-Laser-Based Multiple Side-Bands, in IEEE International Conference on Communications (ICC), Kyoto, Japan, June 2011, pp. 15.

2. **S. Ghafoor** and P. Petropoulos, Effect of Dispersion Slope of Highly Nonlinear Fibre on the Performance of Self Phase Modulation Based 2R-Optical Regenerator, in IEEE International Conference on Computer Technology and Development (ICCTD), Cairo, Egypt, November 2010, pp. 144 - 148.

Journal Papers

1. **S. Ghafoor** and L. Hanzo, ”Sub-Carrier-Multiplexed Duplex 64-QAM Radio-over-Fiber Transmission for Distributed Antennas”, IEEE Communications Letters, vol. 15, No. 12, pp. 1368-1371, 2011.

2. X. Xu, R. Zhang, **S. Ghafoor** and L. Hanzo, ”Imperfect Digital Fibre Optic Link Based Cooperative Distributed Antennas with Fractional Frequency Reuse in Multicell Multiuser Networks”, IEEE Vehicular Technology Journal, vol. 60, No. 9, pp. 4439-4449, 2011.

3. **S. Ghafoor**, V. A. Thomas and L. Hanzo, ”Duplex Digitized Transmission of 64-QAM Signals Over a Single Fiber Using a Single Pulsed Laser Source”, IEEE Communications Letters, vol. PP, No. 99, pp. 1-4, 2012.

4. V. A. Thomas, **S. Ghafoor** and L. Hanzo, ”A Full-Duplex Diversity-Assisted Hybrid Analogue/Digitized Radio Over Fibre for Optical/Wireless Integration”, Accepted in IEEE Communications Letters.

5. **S. Ghafoor** and L. Hanzo, ”Baseband Fiber Aided 60 GHz Star-Like Distributed Antenna System Architecture”, Submitted to IEEE Communications Letters.

List of Symbols

A_{eff}: Effective Area of Fiber Core

α: Fiber Attenuation

D: Fiber Dispersion Parameter

β: Fiber Mode Propagation Constant.

ε: Extinction ratio of MZM.

γ: Fiber Nonlinear Parameter

f: Frequency of the Optical Signal

I_{bias}: Bias Current of the Laser

i_{PD}: Photodetector Current

I_{sat}: Saturation Current of the Laser

I_{th}: Threshold Current of the Laser

L_D: Dispersion Length of the Fiber

L_{eff}: Effective Length of the Fiber

L_{NL}: Nonlinear Length of the Fiber

N: Soliton Order

n: Refractive Index

n_2: Nonlinear Index Coefficient

P_e: Probability of Error

q: Electron Charge

η: Efficiency

η_L: Quantum Efficiency of the Laser

R: Responsivity of the Photodetector

R_{spon}: Rate of Spontaneous Emission

R_{stim}: Rate of Stimulated Emission

ρ: EAM Chirp Factor

T: Temperature

T_o: Optical pulse width at $1/e$ of peak power.

V_π: Voltage Required to Induce a Phase-Shift of π for each of the MZM arms

λ: Wavelength of the Optical Signal

Glossary

ADC: Analogue-to-Digital Converter

AMPS: Analogue Mobile Phone System

APON: Asynchronous Transfer Mode Passive Optical Network

AROF: Analogue Radio Over Fiber

ASE: Amplified Spontaneous Noise

ATM: Asynchronous Transfer Mode

AWG: Arrayed Waveguide Grating

BERT: Bit Error Rate Tester

BPON: Broadband Passive optical Network

BROF: Baseband Radio Over Fiber

BS: Base Station

CAPEX: Capital Expenses

CDMA: Code Division Multiple Access

CIR: Carrier-to-Interference Ratio

CNR: Carrier-to-Noise Ratio

CU: Central Unit

CW: Continous Wave

DAC: Digital-to-Analogue Converter

DAS: Distributed Antenna System

DCF: Dispersion Compensating Fiber

DD-MZM: Dual-Drive Mach-Zehnder Modulator

DFB: Distributed Feedback

DL: Downlink

DROF: Digitized Radio Over Fiber

DSB: Double Sideband

DSB-SC: Double Sideband Suppressed Carrier

DSL: Digital Subscriber Line

EAM: Electroabsorption Modulator

EDFA: Erbium Doped Fiber Amplifier

EO: Electrical-to-Optical

EPON: Ethernet Passive Optical Network

EVM: Error Vector Magnitude

FDCHTF: Frequency Domain Channel Transfer Function

FDMA: Frequency Division Multiple Access

FP: Fabry-Perot

FWHM: Full-Width at Half Maximum

GFM: Generic Framing Method

GPON: Gigabit Passive Optical Network

GSM: Global System for Mobile Communications

GVD: Group Velocity Dispersion

HDTV: High-Definition Television

HNLF: Highly Nonlinear Fiber

HSPA: High-Speed Packet Access

IMD: Intermodulation Distortion

IMDD: Intensity Modulation Direct Detection

ISM: Industrial Scientific and Medical

ITU: International Telecommunications Union

LD: Laser Diode

LOS: Line of Sight

MAN: Metropolitan Area Network

MDS: Minimum Discrenable Signal

MIMO: Multiple Input Multiple Output

MMF: Multi Mode Fiber

mm-wave: Millimeter Wave

MS: Mobile Station

MSC: Mobile Switching Center

MZI: Mach-Zehnder Interferometer

MZM: Mach-Zehnder Modulator

NF: Noise Figure

OADM: Optical Add-Drop Multiplexer

OCS: Optical Carrier Suppression

ODSB: Optical Double Sideband

OE: Optical-to-Electrical

OFDM: Orthogonal Frequency Division Multiplexing

OLT: Optical Line Terminal

ONU: Optical Network Unit

OPEX: Operating Expenses

OSNR: Optical Signal-to-Noise Ratio

OSO: Optical Sampling Oscilloscope

OSSB+C: Optical Single Sideband plus Carrier

OTDM: optical Time Division Multiplexing

PD: Photodetector

PON: Passive Optical Network

PSTN: Public Switched Telephone Network

QAM: Quadrature Amplitude Modulation

RAU: Radio Access Unit

RHD: Remote Heterodyne Detection

RIN: Relative Intensity Noise

ROF: Radio Over Fiber

SCM: Sub-Carrier Multiplexed

SFDR: Spurous Free Dynamic Range

SMF: Single Mode Fiber

SMS: Short Message Service

SNR: Signal-to-Noise Ratio

SPM: Self Phase Modulation

SSB: Single Sideband

SSFM: Split-Step Fourier Method

TDM: Time Division Multiplexing

TDMA: Time Division Multiple Access

TIR: Total Internal Reflection

UL: Uplink

VOIP: Voice Over Internet Protocol

WDM: Wavelength Division Multiplexing

WiFi: Wireless Fidelity

WiMax: Worldwide Interoperability for Microwave Access

XOR: Exclusive OR

XPM: Cross Phase Modulation

Contents

Abstract **iii**

Acknowledgements **iv**

declaration **v**

Publications **vi**

List of Symbols **vii**

1 Introduction **1**

1.1 The Growth of Wireless Communication 1

1.1.1 Wireless Access Technologies 2

1.2 Cellular Architecture 3

1.2.1 Traffic Cells 4

1.2.2 Macrocellular Network 4

1.2.3 Microcellular Network 4

1.2.4 Picocells 4

1.3 Challenges in Wireless Communications 5

1.3.1 Bandwidth Bottleneck in the Access Network 6

1.3.2 Spectral Congestion 6

1.3.3 Large Number of Base Stations and Cost Efficiency 7

1.3.4 Frequent Handovers and Variable Traffic Profile 7

1.3.5 Integration of Multiple Services and Future Compatibility 7

1.4 Radio Over Fiber for Wireless Communications . . . 7
1.4.1 Advantages of Optical Fibers . . . 8
1.5 Optical Access Networks . . . 9
1.5.1 Time Division Multiplexed PONs . . . 10
1.6 Solutions for Future High-Bandwidth Access Networks . . . 11
1.6.1 Bandwidth-Efficient Modulation Schemes . . . 11
1.6.2 Transmission Band Expansion . . . 11
1.6.3 Multicore Fibers . . . 12
1.6.4 Network Coding for Next-Generation PONs . . . 12
1.6.5 Dynamic Optical Networks . . . 12
1.7 Objectives and Structure of the Thesis . . . 13
1.8 Novel Contributions . . . 14
1.9 Conclusions . . . 16

2 Components of Optical Communication Systems 17

2.1 Optical Transmitter . . . 19
2.1.1 Continous Wave Semiconductor Laser . . . 19
2.1.1.1 Distributed Feedback Semiconductor Lasers . . . 21
2.1.2 Directly Modulating Semiconductor Lasers . . . 22
2.1.3 Pulsed Semiconductor Lasers . . . 23
2.1.4 External Modulation . . . 23
2.1.4.1 Mach-Zehnder Modulator . . . 24
2.1.4.2 Dual-Drive Mach-Zehnder Modulator . . . 25
2.1.4.3 Electroabsorption Modulators . . . 26
2.2 Optical Fiber . . . 27
2.2.1 Attenuation of the Fiber . . . 28
2.2.2 Fiber Dispersion . . . 29
2.2.3 Fiber Nonlinearity . . . 31
2.3 Optical Receiver . . . 33
2.3.1 Principle of Photo-detection . . . 33
2.3.2 Photodetector Parameters . . . 33

2.3.3 PIN Photodiode . . . 35
2.4 Optical Amplifiers . . . 35
2.5 Optical Filters . . . 38
2.5.1 Grating Filters . . . 38
2.5.2 Arrayed Waveguide Grating Filter . . . 39
2.5.3 Fabry-Perot Filters . . . 40
2.6 Passive Optical Components . . . 40
2.6.1 Optical Couplers/Splitters and Multiplexers/Demultiplexers . . . 41
2.6.2 Optical Isolator and Circulator . . . 42
2.7 Conclusions . . . 43

3 Radio Over Fiber Communication 45
3.1 Methods of Transporting RF Signals Over Fiber . . . 45
3.1.1 Intensity Modulation Relying on Direct Detection . . . 46
3.1.2 Remote Heterodyne Detection Technique . . . 47
3.2 Multiplexing Techniques in ROF Systems . . . 49
3.2.1 Sub-Carrier Multiplexing . . . 49
3.2.2 Wavelength Division Multiplexing . . . 49
3.3 Analogue ROF System Architecture . . . 50
3.3.1 Impairments in Analogue ROF Systems . . . 51
3.3.1.1 Modulator-Induced Impairments . . . 52
3.3.1.2 Laser Noise . . . 53
3.3.1.3 Fiber-Induced Impairments . . . 53
3.3.1.4 Nonlinear Photo-detection . . . 54
3.3.1.5 Optical Amplification and Filtering . . . 54
3.3.2 Analogue ROF Link Analysis . . . 54
3.3.3 Optical Linearization Techniques for Analogue ROF . . . 56
3.4 Digitized ROF . . . 57
3.5 Baseband ROF . . . 58
3.6 Impairments in Pulsed Optical Communication . . . 59
3.6.1 Optical Pulsed Signal Regeneration . . . 61

3.7 Conclusions . . . 62

4 Baseband ROF and Optical Pulse Regeneration 64

4.1 Baseband ROF Architecture . . . 64

4.1.1 Time and Wavelength Division Multiplexed Optical Pulsed System Architecture . . . 65

4.2 Pulsed Signal Regeneration . . . 66

4.2.1 Self Phase Modulation Based Regenerator . . . 67

4.2.2 Self-Phase Modulation Based Regenerator Operating Principle . . . 68

4.2.3 Self Phase Modulation Based Regenerator Transfer Functions . . . 71

4.3 Characterization of the SPM Based Regenerator . . . 72

4.3.1 Spectral and Temporal Effects of Dispersion Slope . . . 73

4.3.2 Effect of Dispersion Slope on the Transfer Functions . . . 75

4.3.3 Effect on Power Gain of the Regenerator . . . 77

4.3.4 Reduction in Pulse-to-Pulse Overlapping . . . 78

4.4 Baseband ROF Aided 60 GHz Wireless Systems . . . 79

4.4.1 The Proposed Baseband Distributed Antenna System Architecture . . . 81

4.4.2 Physical Layer Design of the Baseband DAS Architecture . . . 82

4.4.2.1 Demultiplexing and Multiple 60 GHz Signal Generation . . . 85

4.4.3 Performance Results . . . 86

4.4.4 Effect of Time Delay Mismatch . . . 89

4.5 Conclusions . . . 90

5 Analogue ROF Communication 91

5.1 Analogue ROF Architecture . . . 91

5.2 Background - Centralized Distributed Antenna Systems . . . 92

5.3 Single Laser Based DAS Ring Architecture . . . 93

5.4 Generating Multiple Side-bands Using OCS . . . 95

5.5 The Proposed Bi-directional Ring Architechture . . . 97

5.6 Performance of the AROF Ring Network . . . 101

5.6.1 EVM to BER Performance Relationship . . . 102

5.7 Effect of Parameter Variations on the Proposed Ring Architecture . . . 106

5.7.1 Effect of DC Bias Variations . . . 106
5.7.2 Effect of DD-MZM RF Drive Signal Frequency Variations . . . 107
5.7.3 Effect of DD-MZM RF Drive Signal Amplitude Variations . . . 109
5.8 Millimeter-Wave DAS Architecture . . . 111
5.8.1 Generation of Millimeter-Waves by Low-Frequency Local Oscillators . . . 112
5.9 The Proposed Millimeter-Wave Architecture . . . 113
5.10 Performance of the Proposed Virtual MIMO Architecture . . . 117
5.11 Effect of Parameter Variations on the Proposed Virtual MIMO Architecture . . . 119
5.11.1 Effect of DC Bias Variations . . . 119
5.11.2 Effect of DD-MZM RF Signal Frequency Variations . . . 120
5.11.3 Effect of DD-MZM RF Signal Amplitude Variations . . . 122
5.12 Conclusions . . . 123

6 Digitized ROF Communication 127

6.1 Digitized ROF Architecture . . . 127
6.2 Background - Digitized ROF . . . 127
6.3 Bandpass Sampling Technique . . . 129
6.3.1 Sampling Frequencies Required for Bandpass Sampling . . . 130
6.3.2 Effect of Guard Bands on Bandpass Sampling . . . 132
6.3.3 Effect of Spectral Replica on the Sampling Rate . . . 134
6.3.4 Nyquist Sampling . . . 135
6.3.5 Retrieving the Analogue Signal from the Bandpass Sampled Signal . . . 135
6.4 Digitized Transmission of 64-QAM RF Signal . . . 136
6.4.1 Simulation Model of the Digitized ROF Transmission . . . 136
6.4.2 Design of the Proposed Digitized Link . . . 137
6.4.3 Design of the Wavelength Converter . . . 141
6.4.4 Performance Results of the Digitized ROF Link . . . 141
6.5 Effect of ADC/DAC Parameters on the Performance . . . 143
6.5.1 Noise in Bandpass Sampled Signal . . . 145
6.5.1.1 Effect of Varying the Out-of-Band Noise . . . 146
6.5.2 Effect of ADC Sampling Clock Jitter . . . 146

6.6 Digitized Transmission of Multiple 64-QAM RF Signals . . . 149
6.6.1 Transmitter Setup for Downlink Signals . . . 149
6.6.2 Receiver Setup for Downlink Signals . . . 150
6.6.3 Transmitter/Receiver for the Uplink Signals . . . 151
6.6.4 Performance Results of the Two-Channel Transmission Link . . . 151
6.7 Conclusions . . . 152

7 Conclusions and Future Work **155**
7.1 Chapter Summaries . . . 155
7.1.1 Chapter 1 - Introduction . . . 155
7.1.2 Chapter 2 - Components of Optical Communication Systems . . . 156
7.1.3 Chapter 3 - Radio Over Fiber Communication . . . 157
7.1.4 Chapter 4 - Baseband ROF and Optical Pulse Regeneration . . . 157
7.1.5 Chapter 5 - Analogue ROF Communication . . . 158
7.1.6 Chapter 6 - Digitized ROF Communication . . . 159
7.2 Design Guidelines . . . 159
7.3 Future Work . . . 162
7.3.1 Radio Over Plastic Optical Fiber . . . 162
7.3.2 Radio Over Wireless Optical Links . . . 162

Appendices **i**

8 Appendix **i**
8.1 Pulse Propagation Equation - Split Step Fourier Method . . . i
8.2 Analogue-to-Digital and Digital-to-Analogue Conversions . . . iii

Chapter 1

Introduction

1.1 The Growth of Wireless Communication

The previous decade has seen a huge increase in the number of wireless communication subscribers. One of the major catalyst for this tremendous growth is the migration of Internet users from fixed to mobile networks [1]. Additionally, the development of high-bandwidth services such as High Definition TV (HDTV), video on demand, video conferencing, interactive gaming and Voice Over IP (VOIP) have also contributed to the bandwidth requirements. Most of the above mentioned services can be accessed from portable devices, such as smart phones and tablets, which are becoming affordable due to the competition among different manufacturers. Smart phones are increasingly used for accessing high-bandwidth applications and services, which are supported by the development of high-performance digital electronics. Service providers are offering new services such as cloud computing, which provides data access, data storage and computing for users on the move without the physical presence of the system on the user's device. These services are provided over the Internet and are based on Internet protocols.

The growth of wireless communication can be quantified in terms of the number of mobile cellular and mobile broadband subscribers. Figure 1.1 shows the yearly rise in subscriptions of different communication systems, which was compiled by the International Telecommunication Union (ITU) [2]. The subscriptions are per 100 inhabitants from the year 2000 to 2010. Around the year 2000 the number of fixed telephone line and broadband subscribers was higher than that of their mobile counterparts. However, by the year 2001, the number of mobile telephone subscriptions exceeded the fixed line telephone subscriptions. On the other hand, the subscriptions for mobile broadband services exceeded the fixed broadband subscriptions by mid 2007, mostly due to the development of smart phones and tablets. By the year 2010, the mobile telephone subscriber penetration have increased to 76.2 $\%$, while the mobile broadband subscriber penetration increased to 13.6 $\%$, as shown in Figure 1. Figure 1.1 also shows that the number of Internet users has increased steadily over the decade, reaching 30.1 $\%$ in 2010.

The increase of mobile data traffic is shared among various devices. Table 1.1 presents the av-

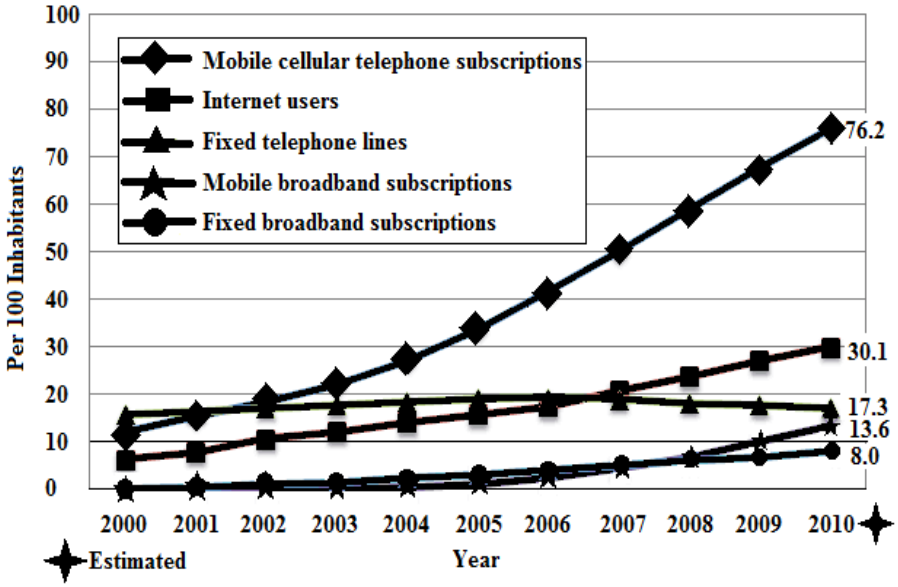

Figure 1.1: Global Telecommunication subscriptions per 100 inhabitants (Source: ITU [2]).

erage mobile data traffic for the most popular devices that were used by customers during the year 2009, 2010 and the forecast until the year 2015. The data was obtained from Cisco's global mobile data traffic forecast [3]. The average traffic per device shown in Table 1.1 is in MB per month. It can be observed from Table 1.1 that along with laptops and netbooks, the smart phones and tablets are one of the major contributors to the increase in average traffic. Furthermore, according to [3], mobile video is the major contributor to the mobile data traffic. Mobile video accounted for 49.8 % of mobile data traffic in 2010.

Table 1.1: Average mobile data traffic (MB per month) for various devices (Source: Cisco [3].

Device Type	**2009**	**2010**	**2015**
Non-Smart Phones	1.5	3.3	54
Smart Phones	35	79	1272
Portable Gaming Console	Not available	250	879
Tablet	28	405	2311
Laptop and Netbook	1145	1708	6522
Machine-to-machine	3	35	166

1.1.1 Wireless Access Technologies

There are three dominant techniques in wireless communication networks [4], namely the classic cellular technology, Wireless Fidelity (WiFi) and Worldwide Interoperability for Microwave Ac-

cess (WiMax). Cellular technology mainly transmits voice signals between mobile phones. One of the first commercial 1G cellular service was the Analogue Mobile Phone Service (AMPS), which used Frequency Division Multiple Access (FDMA), where a bandwidth of 30 kHz per user was assigned. With the increase in the number of mobile phone users, the digital 2G systems were developed. The predominant 2G system is the Global System of Mobile Communication (GSM), which uses Time Division Multiple Access (TDMA) to transmit eight digital channels per carrier in a bandwidth of 200 kHz and to transmit data at a rate of 9.6 $kbps$ per user. The 2G system also supports Short Messaging Service (SMS). In the 3G systems an increased data rate is provided along with voice traffic using Code Division Multiple Access (CDMA). The most advanced version of 3G systems use the so-called High-Speed Packet Access (HSPA) mode [5] for delievering data of speeds up to 14 $Mbps$ [4]. Higher data rates may be transmitted by an enhanced version referred to as HSPA+, where a data rate of 40 $Mbps$ is achieved in the downlink direction. The cellular technology typically uses the 1 and 2 GHz licensed frequency bands for communication over long distances.

The WiFi technology obeys the IEEE 802.11a/b/g standard for wireless communication in local-area networks and uses the unlicensed Industrial, Scientific and Medical (ISM) band, which makes it one of the most popular wireless technology. The maximum data rate for WiFi communication is 54 $Mbps$ and the maximum range is about 100 m [6]. WiFi can operate in a centralized scenario, where a Central Unit (CU) directs and controls the transfer of data to multiple wireless users. WiFi is also suitable for Ad Hoc networks, where data transmission is managed and controlled by the user nodes. The chipsets used for enabling WiFi communication in laptops and smart phones are inexpensive, therefore making it the most widely deployed wireless Internet network [1].

WiMax technology relies on the IEEE 802.16 standard for wireless communication, which uses both the licensed and the ISM frequency bands. The maximum data rate transmitted by WiMax may reach 75 $Mbps$ in the coverage range of 3-5 km [4]. For longer distances, such as 15 km, the data rate is reduced to nearly 28 $Mbps$ [4], [6]. Since WiMax operates over larger distances, it is more suitable for single-hop point-to-multi-point communication. In multi-hop communication scenarios, WiMax suffers from a reduced through-put and latency. The distances over which a WiMax signal can be transmitted makes it a suitable option for Metropolitan Area Networks (MAN).

1.2 Cellular Architecture

Before discussing the implementational challenges and solutions proposed for broadband wireless systems, this section provides a brief introduction to the cellular architecture that is commonly used in wireless communications. The cellular architecture is developed in order to efficiently transmit radio signals to the users. The architecture takes into account issues such as frequency reuse, coverage and cost efficiency. The different parts of the cellular architecture are discussed as

follows.

1.2.1 Traffic Cells

Radio coverage is divided into geographic regions referred to as a cell, which is the basic coverage unit in a cellular system. Cells are generally represented as hexagons, as shown in Figure 1.2. Naturally, the actual shape of a cell is not hexagonal due to both man-made structures and natural obstructions. Cells are generally sectorized in order to increase the capacity in a densely populated area. The sectorization makes use of directional antennas as opposed to omni-directional antennas. Figure 1.2 shows three sectored cells that make use of three directional antennas to cover the entire cell. Cell sectorization also has the advantage of reducing interference among the co-channel cells. Based on the radius of the cell, a cellular network can be divided into the following types [7].

1.2.2 Macrocellular Network

Macrocellular networks use cells of large radii for example in the range of 16 km to 48 km [7]. Such cells are generally used in areas of low user density. The cells may rely on sectorization, depending upon the number of users. Such cells use low frequency RF signals, which have the capability of travelling longer distances compared to high frequency signals. The cells can be reduced in size and increased in number, if there is a need to support an increased number of users.

1.2.3 Microcellular Network

Microcellular radio networks have lower cell radii that are in the range of 200 m to 1 km [7]. These networks are generally used in high-traffic density areas, like city centers or dense residential areas. Again, the cells in a microcellular networks often use cell sectorization in order to increase capacity. The network shown in Figure 1.2 represents the generalized structure of a microcellular network. A group of BSs are connected to a single Central Base Station (CBS), as shown in Figure 1.2. A group of CBSs are connected to a Mobile Switching Center (MSC) which connects the microcellular network to the Public Switched Telephone Network (PSTN).

1.2.4 Picocells

Picocells are generally used inside office buildings, airports and shopping malls. They have cells radii in the range of 10 m to 200 m [7]. Picocells may use high frequency RF signals, for example in the range of 60 GHz. These high frequency signals provide a large bandwidth potential over a shorter distance. At the time of writing, a lot of research is dedicated to picocells for providing future high bandwidth multimedia services to subscribers [8], [9]. Due to the small cell size and

short range of the high frequency signals, a high number of individual cells are required to cover a certain area [10].

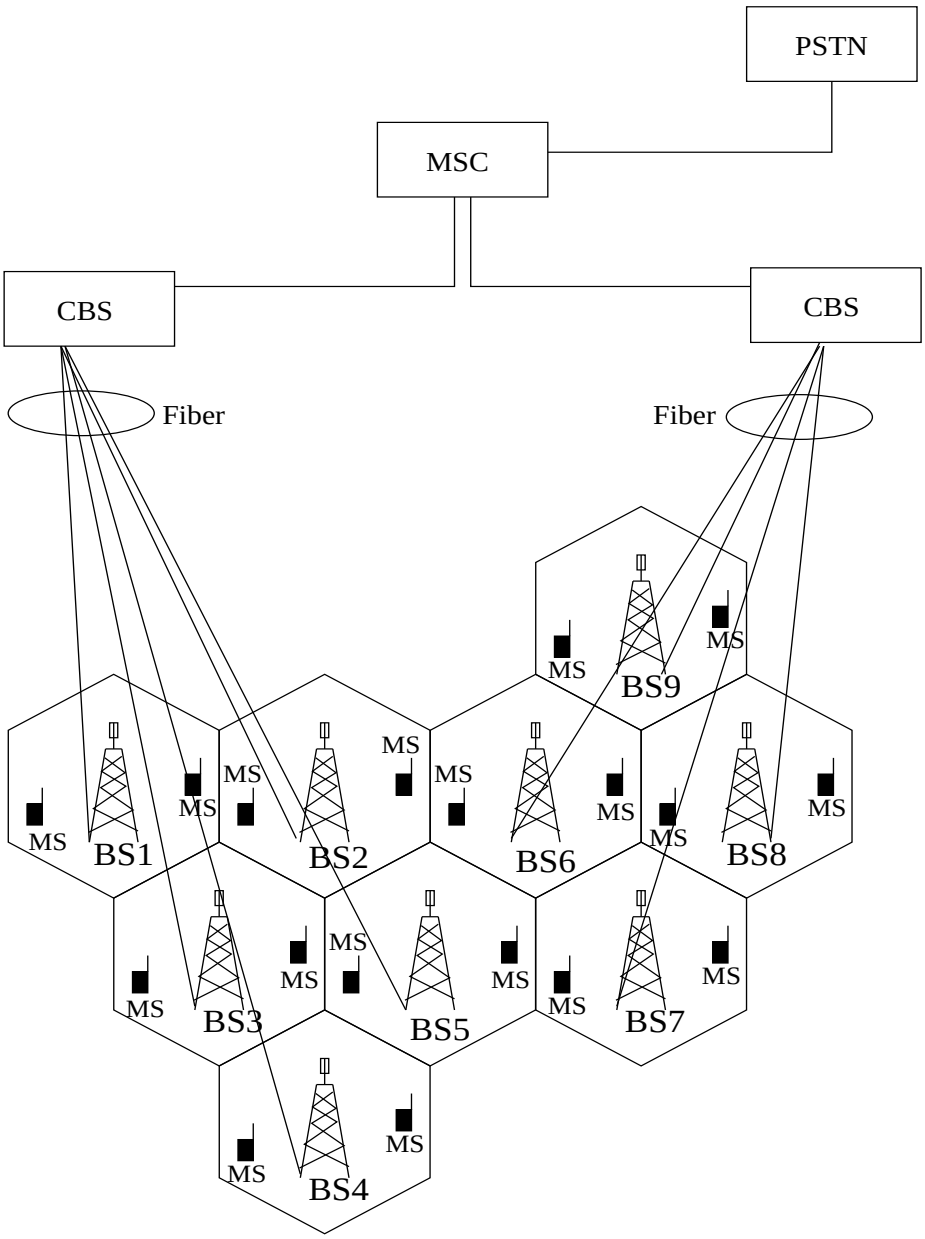

Figure 1.2: A microcellular network using optical fibers to connect different CBSs to the MSC.

1.3 Challenges in Wireless Communications

This section discusses some of the major challenges faced in implementing broadband wireless communications.

1.3.1 Bandwidth Bottleneck in the Access Network

The bandwidth of the core transport networks, which generally use fiber optic communications has reached high values, such as 1 THz supporting rates up to 1 $Tbps$, [6], [11], while experimental demonstrations of data rates higher than 10 $Tbps$ have been reported over fiber lengths longer than 500 km [12]. However, the major bandwidth bottleneck is in the last-mile wireless access networks, which use technologies that are limited in bandwidth and propagation distances. Current broadband services are provided using access technologies that include Digital Subscriber Loop (DSL) (ITU-T, G.922), coaxial cable (ITU-T J.112/122) and wireless technologies like WiFi and WiMax. The data rates per user and maximum coverage distance of these technologies are summarized in Table 1.2 [6]. It can be observed from Table 1.2 that the maximum data rates and transmission distances are limited for DSL and coaxial links. WiFi provides a maximum data rate of 54 $Mbps$ over a short distance of say, 100 m. On the other hand, WiMax has a longer maximum coverage distance of 15 km, but at a lower data rate of 28 $Mbps$. Hence a major challenge for broadband service providers is the design of high-bandwidth access networks, which are capable of supporting communications over longer distances. This will reduce the cost of installation by using a single central station for a larger number of users.

Table 1.2: Data rates and maximum reach for various access networks [6].

Service	Data Rate per User	Maximum Reach
ADSL	2 $Mbps$ (typical)	5.5 km
VDSL	20 $Mbps$ (typical)	1 km
Coaxial	2 $Mbps$ (typical)	0.5 km
WiFi	54 $Mbps$ (max)	0.5 km
WiMax	28 $Mbps$ (max)	15 km

1.3.2 Spectral Congestion

Due to the increase of various high-bandwidth applications, the most benign, low frequency radio spectrum is becoming overcrowded. A natural option is the use of higher carrier frequencies for example millimeter-waves (mm-waves) at say 60 GHz. High frequency carriers have a potentially high instantaneous bandwidth. However, the radio channel's noise is directly proportional to the bandwidth [13]. Therefore, in order to maintain the required Carrier-to-Noise Ratio (CNR), the radio channel power has to be proportionately increased. Furthermore, high frequency radio signals are attenuated substantially due to the intrinsic absorption by the atmosphere. The high attenuation and noise imposed upon the high frequency carriers reduces the range of the wireless link.

1.3.3 Large Number of Base Stations and Cost Efficiency

High-bandwidth systems using high frequency carriers require a large number of BSs, since the wireless signal range for high frequency carriers is low. In order to cope with the increasing bandwidth demand per user, network operators have to split the existing cells and hence use smaller cells. However, increasing the number of cells and therefore the number of BSs is not always a feasible option due to the higher infrastructure costs involved. A major challenge faced by network operators is that of increasing the network capacity, while keeping the capital expenses (CAPEX) and operating expenses (OPEX) to a minimum [1]. Although the data traffic per user is increasing, the average revenue per user does not tend to increase in proportion, which causes a relative increase in the CAPEX and OPEX.

1.3.4 Frequent Handovers and Variable Traffic Profile

As mentioned in the previous section, small cell sizes are required to fulfill the high-bandwidth demand of users. Due to the small cell size, the number of handovers for a user's mobile receiver will increase. This may result in the loss of packets during the process of handovers [14]. Similarly, due to user mobility, the traffic profile of a certain cell may change rapidly. Therefore, service providers need to design the access networks by ensuring that the resources are allocated dynamically [15]. The sharing of network resources among several cells make the access network both flexible and cost-effective.

1.3.5 Integration of Multiple Services and Future Compatibility

The bandwidth requirements and characteristics of the signals used for broadband wireless communications are different from those of the operational optical fiber links. In order to cope with the increasing bandwidth demand in a cost-effective manner, service providers are actively considering solutions that make use of the already deployed fixed lines. The network designed for broadband wireless access should have the ability to be readily integrated with the fixed line based services. Finally, the solution should be 'future proof', so that future systems or standards should be able to use the same network.

1.4 Radio Over Fiber for Wireless Communications

One of the major access network solutions for future high-bandwidth wireless communication systems is based on optical fibers for the transmission of radio signals between the BSs and MSC, for example [7], [8], [16] [17]. Such a communication system is generally referred to as a Radio Over Fiber (ROF) solution. In ROF, the radio signal is used for intensity modulating an optical carrier. Figure 1.3 shows the simplified diagram of a ROF link, where the radio signal is converted

into an optical signal in an electronic-to-optical (EO) converter at the CU. The optical signal is transmitted through the fiber and detected at the BS, where an optical-to-electronic (OE) converter recovers the original RF signal, which is amplified and transmitted from the BS antenna to the MS, as shown in Figure 1.3. This technique of transmitting the RF signals using an optical carrier over the fiber has numerous advantages over the conventional copper wire solutions. In the following sections, we will discuss some of the major advantages that make the ROF system a suitable choice for the transmission of mobile communication signals.

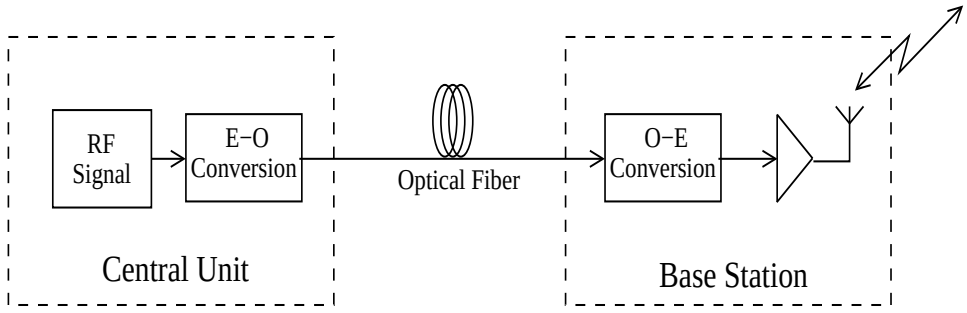

Figure 1.3: Simple ROF link.

1.4.1 Advantages of Optical Fibers

Optical fibers used for optical communications have a low loss compared to their electronic counterparts. The typical power-loss for a commercially available Single Mode Fiber (SMF) is about 0.2 dB/km, which allows us to cover large distances without amplification [18]. In the scenario where an ROF signal is transmitted from a BS to multiple Radio Access Units (RAUs) such as for example Distributed Antennas (DAs), typically no amplification is required. This makes the link inexpensive and free from the additional noise of amplifiers.

The substantial bandwidth of the optical fiber used in ROF communication is a major advantage. The Third Telecommunications Window (TTW) spanning from 1530 nm to 1560 nm, which is also called the Erbium band, has a bandwidth of nearly 3.8 THz. Different methods of exploiting most of this bandwidth are under investigation in both baseband as well as in ROF communications [19], [20], [21]. In baseband communications, higher order modulation schemes modulating the phase of the carrier are being used [19]. The Wavelength Division Multiplexing (WDM) technique [21], [22] is also used in ROF communication in order transmit high-rate, high-bandwidth RF signals over a single fiber. Along with WDM, the Sub-Carrier Multiplexing (SCM) technique [23], [24] that transmits multiple RF channels over a single wavelength has also found wide-ranging applications [25], [18]. Optical communication in the Erbium band relies on the ability of Erbium Doped Fiber Amplifiers (EDFAs) to amplify wavelengths spanning from 1530 nm to 1560 nm simultaneously using a single EDFA [26], [27]. The high-bandwidth of EDFAs makes optical communications more cost-efficient than electronic communication, where separate amplifiers are needed to amplify RF signals of different frequencies.

In a ROF-aided multicell network, a large number of DAs are distributed spatially to provide near-uniform coverage [16], [28]. Since each DA covers a small area, the RF power required by each DA is low. Due to the low loss of optical fibers, this low RF power can be delievered without the employment of amplifiers, hence the power efficiency of the ROF network increases. The employment of a low power at the DA, has the further advantage of reduced inter-cell interference. If a higher power is used at the transmitter of a DA, there is a higher probability that the signal from this DA will interfere with the signal of an adjacent DA. By using small cells, the so-called area spectral efficiency of the wireless network expressed in $Bit/sec/Hz/km$ is also increased since the frequency bands can be re-used in multiple cells [28], [29]. Again, having a dense set of DAs enables the wireless system to provide near-uniform coverage. The low complexity and low cost DAs makes it possible for them to be used in large numbers by the service providers. Hence they can be used to ubiquitously on lamp-posts, etc to provide coverage in areas that are generally not well covered by the over-sailing macrocells. These areas include the back side of buldings, tunnels or street corners. Furthermore, the centralized structure of the ROF network facilitates dynamic resource and capacity allocation, depending upon the roaming patterns of users [16], [20]. As a further benefit of using a large number of DAs employed in a Distributed Antenna System (DAS), Line of Sight (LOS) operation can be achieved. This mitigates the deliterous propagation effects at the MSs hence providing an improved quality of service for the users. Optical signals are inherently immune to electromagnetic interference from the surroundings.

In a ROF communication system, the RAUs used are of compact size and simple in functionality. Most of the RAUs are simply composed of a photodetector (PD), an electronic bandpass filter, an amplifier and an antenna. In the scenario where the RF signal is transmitted over a copper wire, an upconverter is required at the RAU, making it more complex and hence more costly. The use of such RAUs on a large scale will make the overall wireless network design more costly. Transmitting the RF signal over the fiber does not require up-conversion at the RAU, therefore making the RAU cost-effective. Optical fibers are made of silicon, which is not a reactive material. This makes the fiber less prone to enviromental effects, such as corrosion. Therefore the maintanance cost of the optical fiber network is low. Since an optical carrier is modulated by the electronic amplitude variations of the RF signal, the ROF link is transparent to the type of RF signal transmitted. Therefore, optical fibers can transmit RF signals having any modulation format at a high symbol rate. This enables the fiber to be used for arbitrary services that might become available in the future for the customers. Therefore upgrading the wireless services will not affect the fiber network.

1.5 Optical Access Networks

A simple approach to provide broadband access to users is based on point-to-point Ethernet connections for every user. Due to the popularity and economy of scale for Ethernet technology, the components are inexpensive. However, the Ethernet deployment requires active components that

consume power. Installing and maintaining powered equipment cabinets is expensive, specially when the network is rolled out in a densely populated area.

Passive Optical Networks (PONs) provide a feasible solution to this problem [6]. The previous decade has seen a considerable decrease in the cost of optical components and network deployment. PONs take advantage of the low power loss of optical fibers to avoid the employment of active components like amplifiers, which dissipate power. To provide coverage in a densely populated area, PONs typically use a tree topology, as shown in Figure 1.4, where an Optical Line Terminal (OLT) is located at the root and Optical Network Units (ONUs) are at the leaves. The hardware and bandwidth of the tree topology is shared among the users. As shown in Figure 1.4, a PON supports full-duplex transmission where the downstream and upstream traffic is transmitted over different wavelengths. An optical splitter divides the power among the ONUs, which then transmits the relevant data to the users.

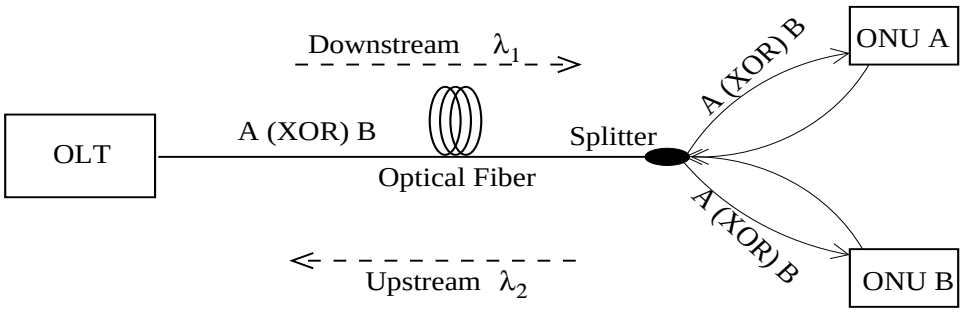

Figure 1.4: PON architecture

1.5.1 Time Division Multiplexed PONs

Since a PON uses a point-to-multipoint architecture, a multiple access technique is required for multiplexing the signals of different users. At the time of writing typically Time Division Multiplexing (TDM) is used as the multiple-access technique in the so-called TDM-PONs [6], [30], which allows the users to share the fiber in the time domain on a time-slot by time-slot basis as well as the hardware used in the CU. TDM-PONs have been standardized for broadband access as Asynchronous Transfer Mode (ATM) PON (APON), Broadband (BPON) and Gigabit PON (GPON) by the ITU (ITU G983) as well as Ethernet PON (EPON) by the IEEE 802.3a-h. Table 1.3 compares the characteristics of three main TDM-PON standards [6]. It can be observed from Table 1.3 that the maximum average bandwidth per user is provided by EPON, but the number of users for a single EPON is limited to 16. GPON has the maximum bitrate of 2.488 $Gbps$ and supports up to 64 users. The framing technology used for BPON is ATM, while GPON uses both ATM and the Generic Framing Method (GFM) [6]. The IEEE EPON uses the Ethernet framing technique for conveying TDM data.

Table 1.3: TDM-PON comparison [6]

Type	EPON	BPON	GPON
Standard	IEEE 802.3a-h	ITU G.983	ITU G.984
Framing	Ethernet	ATM	GFM/ATM
Maximum Bitrate	1 $Gbps$	622 $Mbps$	2.488 $Gbps$
Users per PON	16	32	64
Average Bitrate per User	60 $Mbps$	32 $Mbps$	40 $Mbps$
Cost	Lowest	Low	Medium

1.6 Solutions for Future High-Bandwidth Access Networks

Although ROF provides a suitable solution as an access network for high-bandwidth wireless communication, the continuous increase in the bandwidth demand requires the network operators to enhance the performance of the ROF links. This section discusses some of the solutions proposed for future optical networks.

1.6.1 Bandwidth-Efficient Modulation Schemes

State-of-the-art optical communication is capable of supporting 80 wavelengths carrying a bitrate of 40 $Gbps$ per wavelength in the C-band, which spans between 1530 nm to 1560 nm, corresponding to a bandwidth of 3.8 THz [31]. In the past, the transmission systems coped with the increasing bandwidth demand by increasing the number of wavelengths transmitted through a single fiber. In the mid to late 1990s, the optical systems used 16 wavelengths, each having a data rate of 2.5 $Gbps$, hence having a bandwidth efficiency of 0.01 $b/s/Hz$ [31]. Again, state-of-the-art systems use 80 wavelengths, each having a data rate of 40 $Gbps$, resulting in a bandwidth efficiency of 0.8 $b/s/Hz$. The increase in the bandwidth efficiency has been achieved by using advanced modulation schemes. In [32], it has been shown that theoretically the bandwidth efficiency can reach up to 7 $bits/sec/Hz$ for a transmission system having a distance of 2000 km. This implies that a practical system should be able to reach a bandwidth efficiency of at least 3 or 4 $bits/sec/Hz$. Hence the research community is working for conceiving more sophisticated optical modulation schemes for increasing the attainable bit-rate. A further increase in the bandwidth efficiency can be achieved by exploiting both the in-phase and quadrature-phase polarization of the optical carrier, giving rise to polarization multiplexing.

1.6.2 Transmission Band Expansion

As mentioned in Section 1.6.1, the operational optical systems mainly use the C-band for the transmission of optical signals. Expansion of the transmission window to higher wavelengths

such as for example to the L-band, which spans from 1565 nm to 1625 nm can significantly increase the transmission capacity of the already operational fibers [26]. The L-band has a lower kilometric loss than the C-band and hence provides a suitable option for expansion. State-of-the-art optical amplifier technology enables the amplification of multiple wavelengths of the C-band using a single optical amplifier [32], [26]. If the L-band is used for data transmission, it is important to design wide-band amplifiers having a high gain across the L-band.

1.6.3 Multicore Fibers

Since the capacity of a single fiber having a single-core is becoming limited, a conceptually straight-forward solution is to use multiple parallel fibers. However, an increase in the number of parallel fibers is coupled with an increase in the number of optical amplifiers, switches, multiplexers and other passive components used in the optical network. Therefore, increasing the number of fibers is not a cost-effective solution. Hence, multicore fibers have been developed that are capable of carrying signals in parallel cores within a single fiber [33], albeit this technology is still in its infancy.

1.6.4 Network Coding for Next-Generation PONs

A major goal of the next-generation ROF systems is to increase the achievable throughput by selecting the most suitable technologies from both the optical and wireless communication solutions. A particularly beneficial technique is network coding, conceived for PONs to form the so-called next-generation PONs (NG-PONs) [30]. Consider the PON architecture shown in Figure 1.4. In the absence of network coding, the OLT transmits the data for ONU A and ONU B in separate time slots. By using network coding, the OLT computes A(XOR)B and sends the resulting coded data to both ONU A and ONU B in the same time slot. At each ONU, the data is decoded by comparing the ONU's information with the received coded data. Therefore, the throughput of the systems is increased by transmitting the data of each ONU in a single time slot. It has been shown in [34] and [35] that network coding increases the throughput of the system, makes routing simple and less prone to transmission errors.

1.6.5 Dynamic Optical Networks

The solutions discussed until now throughout Section 1.6 require technological changes in the existing systems. In this section, we briefly discuss dynamic optical networks, which concerns the architecture of the system. Optical access networks provide the most suitable solution for broadband wireless systems [21], [22]. Due to the mobile nature of the wireless users, the teletraffic profile of wireless networks is different from that of fixed networks. In this scenario, the wavelength assigned to a particular RAU may not be in use at certain times of the day, while another RAU may be conveying a heavy traffic load. Therefore, to cope with such situations, future

optical access networks should be able to dynamically allocate optical channels [15], [21], [20]. This dynamic channel allocation philosophy implies that the optical networks should be able to perform dynamic wavelength allocation according to the wireless tele-traffic profile. The data-to-wavelength mapping should be controlled by the CU, where all the signal processing tasks are performed. The CU would detect the changes in the wireless network traffic by observing the data transmission demands imposed on different RAUs and then allocate idle wavelength to the RAU under higher traffic load.

1.7 Objectives and Structure of the Thesis

The thesis discusses the three major types of ROF communications solutions, namely Baseband ROF (BROF), Analogue ROF (AROF) and DROF (DROF) [36], [37], [38]. The BROF system transmits the radio data in the baseband format using an optical carrier. The baseband data is up-converted at the RAU to the RF carrier of say 2 GHz for transmission to the MSs. The AROF system directly modulates the optical carrier with the analogue RF signal. In DROF transmission, the analogue RF signal is digitized at the CU using analogue-to-digital converters and the resultant digitized signal is transmitted over the fiber using an optical carrier. The operating principle as well as the advantages and disadvantages of these systems are investigated in the thesis.

Chapter 2 describes the operating principle of the components used in optical fiber communication systems, including the transmitter/receiver pair, the fiber-based trasmission medium, optical amplifiers, optical filters and the required passive optical components. Familiarity with these components will be assumed in Chapters 4, 5 and 6 of the thesis.

Chapter 3 provides a detailed introduction to ROF communication systems. The three major types of ROF communication systems that are BROF, AROF and DROF are detailed. The advantages and disadvantages as well as the impairments imposed by each type of ROF communication system are highlighted in Chapter 3, along with the characteristics of pulse propagation in optical fibers and its modelling techniques.

Chapter 4 describes *baseband* optical communications with special emphasis on ROF signal transmission, including a simple amplitude regenerator proposed for optical pulsed transmission. We study the effect of fiber parameters on the performance of the regenerator. The chapter is concluded with a performance evaluation of a physical layer design conceived for BROF based cooperative DASs.

Chapter 5 considers an AROF system in detail, proposing an AROF ring architecture relying on a single laser source for feeding three different RAUs using 64-level Quadrature Amplitude Modulation (64-QAM) in a virtual Multiple Input Multiple Output (MIMO) type architecture. The advantages of these architectures conceived for future ROF networks are discussed and performance results are presented to demonstrate the feasibility of the proposed architectures.

In contrast to the baseband solution of Chapter 4 and the AROF technique of Chapter 5, Chapter

6 aims for designing DROF systems. A physical layer design is presented that uses optical signal processing for the transmission of digitized 64-QAM signals. The process digitizing the analogue RF signal is detailed and the performance of the proposed architecture is characterized.

Finally, Chapter 7 concludes the thesis highlighting a range of ideas for future work. The organization of the thesis is visualized at a glimpse in the block diagram of Figure 1.5.

1.8 Novel Contributions

1. Chapter 4 describes a simple amplitude regenerator where the major contributions for its characterization are summarized in Table 4.3. As discussed in Table 4.3, much of the research on the physical structure of the regenerator has been focussed on the properties of the fiber for the sake of optimizing the regenerator's performance. However, all theoretical and numerical studies in the open literature have considered so far a negligible dispersion slope for the fiber used in the regenerator. Against this background, we have characterized the effects of the fiber's dispersion slope used in a baseband regenerator setup on its performance [39]. We demonstrated that fibers exhibiting similar optical properties at the wavelength of operation, but having different dispersion slopes result in markedly different regeneration performance. Therefore, this property can be exploited for fine-tuning the performance characteristics of the regenerator for the sake of achieving the target performance. Some of the advantages of employing fibers having a high dispersion slope in the regenerator include achieving a high power gain and a high resilience against pulse-to-pulse overlapping at high bit rates.

2. Table 4.4 summarizes the major contributions towards AROF, which shows that these studies use continuous wave optical transmission of the AROF data. However, using continuous wave carrier is not feasible for performing cost-effective all-optical signal processing. keeping this in view, a physical layer design conceived for *baseband* transmission in a star-like architecture is presented in Chapter 4 [40]. The baseband RF data is transmitted using optical pulsed techniques over a long fiber. The star-like architecture considered may be employed in a DAS composed of 6 RAUs at spatially distinct locations. The baseband data is transmitted to each RAU as an amplitude modulated 60 GHz signal.

3. In Chapter 5, we propose a scheme for transmitting duplex 16-QAM AROF signals using four SCM channels in a ring architecture by generating multiple optical side-bands from a single low-cost off-the-shelf laser source at the MSC [41]. The feasibility of transmitting the ROF signals over each optical side-band is assessed on the basis of the signal's Error Vector Magnitude (EVM) performance. As a further benefit, duplex transmissions to three different RAUs are supported simultaneously without requiring a separate laser source at each RAU, where the conventional solution of using three separate laser sources would require their phase-coherent synchronization. Hence all the complex signal processing tasks are performed at the MSC, which facilitates a low-complexity, low-cost RAU or DAS design.

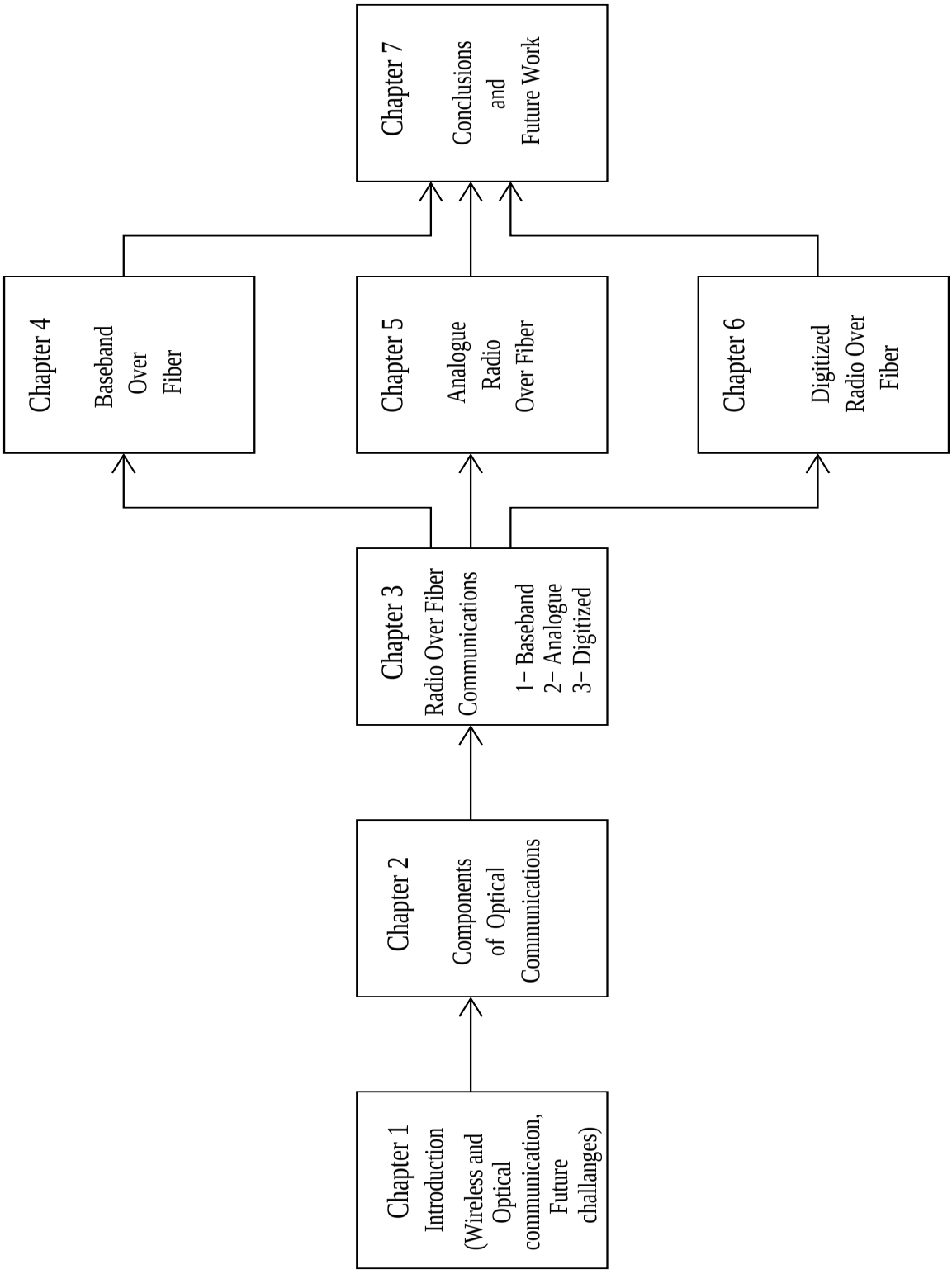

Figure 1.5: Organization of the thesis

We also characterize the performance of our proposed scheme in the presence of realistic parameter variations and show that the quality of the ROF signals conveyed to the different RAUs may be dynamically controlled by appropriately varying the device parameters used at the MSC.

4. Again in Chapter 5, we demonstrate the feasibility of transmitting SCM 64-QAM AROF signals in a DAS architecture by incorporating coherent optical carriers [42]. Our scheme simultaneously transmits four AROF signals to two different RAUs in a duplex architecture using only a single laser source at the CU. The AROF signals may be transmitted at two different frequencies of 50 GHz and 25 GHz, which may be chosen by adjusting the optical connectors used at the RAUs.

5. Finally in Chapter 6 of the thesis, we propose a novel scheme for the transmission of *digitized* RF signals using pulsed optical communication [43]. Table 6.1 mentions the major studies performed on the digitized transmission of RF signals. However, all the studies mentioned in Table 6.1 concentrate on the feasibility of transmitting multiple RF signals of the same or different technologies. On the contrary, we propose a cost-efcient UL/DL physical layer design for the DROF link. More explicitly, we conceive the digitized transmission of 64-QAM signals over a 25 km of SMF between a MSC and a BS.

1.9 Conclusions

The conclusions of the chapter are summarized below:

- With the proliferation of high-bandwidth wireless services, the network providers are facing high bandwidth demands.
- These challenges can only be met by using an increased number of BSs to provide a high capacity and seamless coverage.
- The application is spreading in the form of TDM PONS due to the development of inexpensive and power-efficient optical components.
- ROF aided DASs contribute one of the most suitable choices for network providers in order to cope with the increasing bandwidth demand.

Chapter 2

Components of Optical Communication Systems

This chapter highlights the operating principle of the main optical components that are generally used in an optical communication system. Our contributions in the thesis are focussed on the design and performance of the optical system architectures. It is therefore important to understand both the operating principle as well as the specific location of the optical components in the system architecture. The basic architecture is similar for different types of communication systems, such as for example fixed or wireless systems. Figure 2.1 shows the simplified block diagram of an optical communication system, as well as its optical components. It should be noted that there are many types of optical components commercially available for performing the same task, but we have limited our scope to the components that will be used in our work. The selection of these components is based on their popularity and cost-efficiency. As shown in Figure 2.1, the transmitter of an optical communication system consists either of a Continuous Wave (CW) or of a pulsed laser source. The CW laser is used for both analogue as well as for baseband communications, while the pulsed laser is generally used for baseband signal transmission. We will consider semiconductor based lasers, since they are widely used and are comparatively inexpensive. The laser sources may be either directly or externally modulated by the data signal. A directly modulated laser is followed by the transmission medium, as shown in Figure 2.1. By contrast, for the case of external modulation, the laser source is passed through an external modulator before being transmitted over the medium, as shown in Figure 2.1. There are three main types of external modulators that will be discussed in this chapter. The transmission medium used in optical communications is predominantly silicon fiber, but plastic fibers are also emerging at the time of writing. We will discuss the most commonly used transmission fiber known as the Single Mode Fiber (SMF). Optical signals transmitted over long fibers require amplification at regular intervals. The amplification is performed in the active component block of Figure 2.1. The most widely used optical amplifier is the EDFA [26], [27], which will be discussed in Section 2.4. Figure 2.1 also shows the associate network components, such as optical filters and other passive devices that will be discussed Section 2.5 and 2.6, respectively. Finally, the operating principle of the optical receiver which is

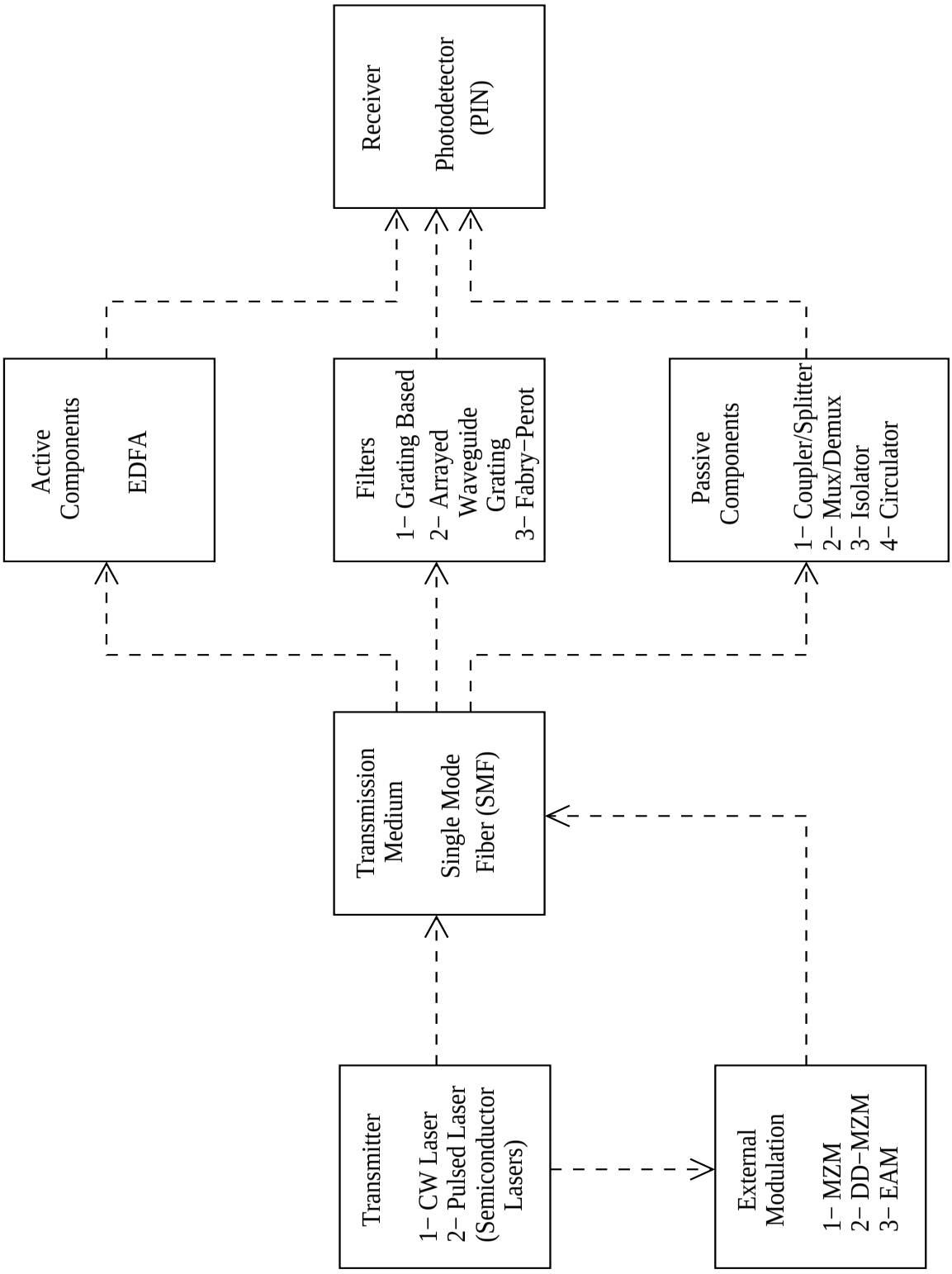

Figure 2.1: Block diagram of an optical communication system.

essentially a PD, is described in Section 2.3. The type of receiver discussed is a PIN photodiode, which is the most common type of semiconductor PD used in optical communications [44].

2.1 Optical Transmitter

The basic function of an optical transmitter is to convert an electronic signal into an optical signal, hence performing the EO conversion. The main component of an optical transmitter is the light source called laser. Semiconductor lasers are commonly used as optical sources for the EO conversion. They have many advantages which include low cost, small size, reliability and suitability for high frequency electrical signals (up to 25 GHz) when modulated directly [44]. Let us now discuss the types and operating principle of semiconductor lasers in Section 2.1.1.

2.1.1 Continous Wave Semiconductor Laser

A laser is a device that emits or amplifies coherent radiations in the infrared [26], visible or ultraviolet region of the spectrum [45]. A laser source exploits the principle of stimulated emission, where excited electrons in a higher energy state are stimulated by an impinging photon. Due to this stimulation, the electron falls to a lower energy state and at the same time it releases another photon of exactly the same characteristics as the one that was stimulated. A laser source is composed of three essential elements, namely the so-called gain medium, pumping mechanism and the optical feedback mechanism, as shown in Figure 2.2 [45]. In order to excite electrons, the gain medium which consists of a suitable amount of atoms, molecules or ions is continuously pumped by external energy. The external pumping stimulates the electrons of the atoms to jump to higher energy levels, a condition which is generally known as population inversion. After stimulated emission, the photons oscillate in the laser cavity, as shown in Figure 2.2. The laser cavity provides a feedback mechanism by reflecting most of the photons back into the cavity, but some of the photons escape through the appropriately designed cavity walls having a reduced reflectivity. These escaped photons give rise to coherent light at a specific wavelength that is dependent upon the particular material used in the gain medium. The electrons in the excited state can also emit photons spontaneously, i.e without any stimulation. This spontaneous emission of photons is a source of noise in lasers. For a laser source to emit light continuously, the rate of stimulated emission denoted by R_{stim} should always be higher than the rate of spontaneous emission denoted as R_{spon}. Mathematically the following relation should be satisfied [44]:

$$R_{stim}/R_{spon} = \{exp(hf/k_BT) - 1\}^{-1} \gg 1, \tag{2.1}$$

where h is Plank's constant, f is the frequency of the light emitted, k_B is the Boltzmann constant and T is the absolute temperature. The above equation can be satisfied if the number of electrons in the excited state is higher than the number of electrons in the ground state.

In case of semiconductor lasers, intrinsic semiconductor materials constitute the gain medium

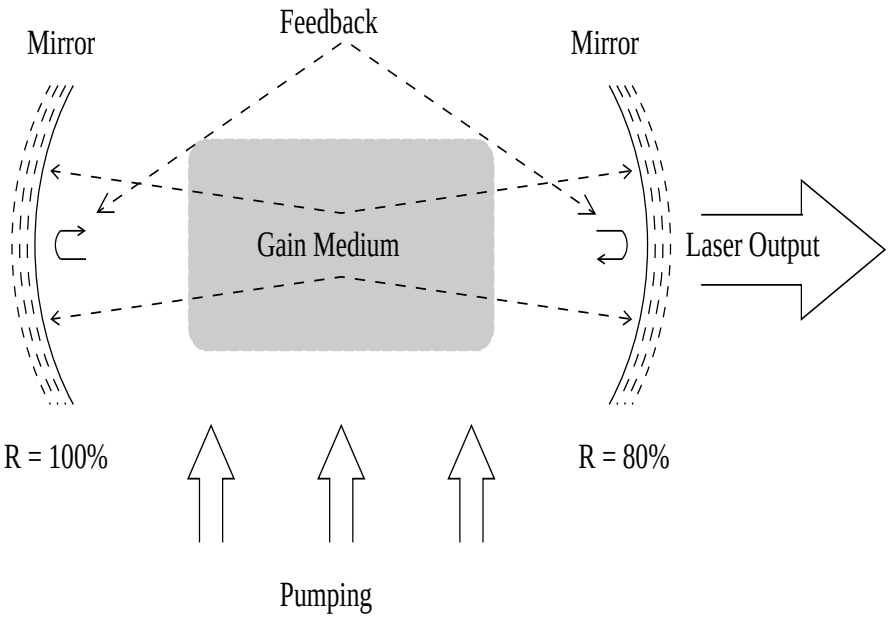

Figure 2.2: Operating principle of a laser.

of Figure 2.2 [45]. Since intrinsic semiconductor materials have a low concentration of free electrons and holes, they are doped with impurities to form n-type and p-type materials, which have a high concentration of electrons and holes, respectively. When the n-type and p-type materials are brought in contact with each other, a p-n junction is formed, as shown in Figure 2.3 [44]. The electrons and holes are diffused across the junction until an equilibrium state is reached, at which point no further diffusion takes place. At this equilibrium state, there exists a strong electric field across the junction due to the presence of oppositely charged electrons and holes on the two sides of the junction. When applying an electric voltage to the p-n semiconductor shown in Figure 2.3, the electric field across the p-n junction is reduced. This results in the diffusion of electrons and holes across the junction. Every time an electron crosses the junction and diffuses into a hole, it releases energy in the form of light. The wavelength of the emitted light is dependent upon the electric field strength across the junction, which in turn can be controlled by the level of doping used in the n-type and p-type materials. In case of semiconductor lasers, light reflection required for optical feedback shown in Figure 2.2 is achieved through the cleaved ends of the semiconductor block, as shown in Figure 2.3. It is the change of refractive index between the laser end and the outside material, that typically reflects 30 $\%$ of light back to the gain medium.

Like all other semiconductor components, lasers also generate noise, which is commonly referred to as Relative Intensity Noise (RIN). The RIN terminology collectively represents the noise due to variations in the intensity, phase and frequency of the laser light. There are two main reasons for these variations, namely spontaneous emission and electron-hole combination. Again, spontaneous emission is a phenomenon, where the excited electron in a higher energy state jumps to a lower energy state without stimulation, hence releasing a photon of random phase and frequency. The electron-hole combination, which is also termed as Shot Noise occurs due to the filling of holes with the free electrons in the semiconductor material.

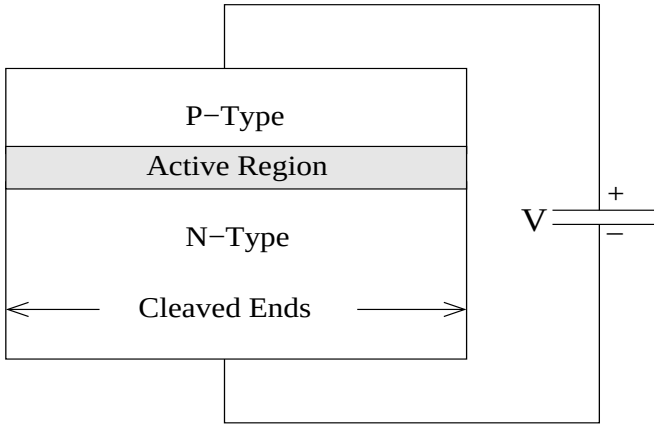

Figure 2.3: Structure of a simple semiconductor laser.

2.1.1.1 Distributed Feedback Semiconductor Lasers

The most common type of semiconductor lasers used in optical communications is constituted by the Distributed Feedback (DFB) Laser [46]. As the terminology implies, the feedback in case of DFB lasers is achieved not only by the end facets, but it is distributed along the entire length of the active region, as shown in Figure 2.4. The reflection of light is achieved through appropriate grating, which is composed of portions of alternate low and high refractive indices repeated periodically along the length of the semiconductor. Some portion of light is reflected at each change of the refractive index regardless of how gradual or abrupt the refractive index change is. Depending upon the specific periodicity of the high/low-index grating, seen in Figure 2.4, the reflected light of a certain wavelength may add constructively due to interfering phase-coherently and hence the laser emitted predominantly consists of light of this particular wavelength. Lasers of different wavelengths can be manufactured by appropriately adjusting the above-mentioned periodicity of the grating seen in Figure 2.4 inside the active region.

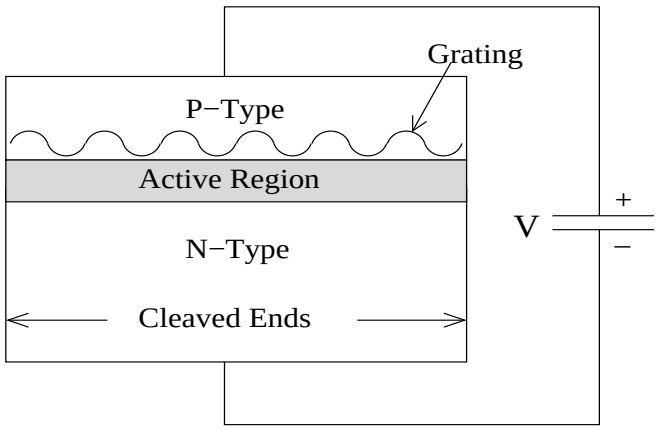

Figure 2.4: Structure of a DFB semiconductor laser

2.1.2 Directly Modulating Semiconductor Lasers

The simplest and cheapest method of EO conversion is that of directly modulating a CW laser [47]. As mentioned in Section 2.1.1, the semiconductor lasers of Figure 2.3 are biased appropriately in order for them to emit light. If the RF electronic signal to be transmitted over the fiber is applied to an appropriately biased laser, the output optical power of the laser varies almost linearly with the RF signal applied to it. However, there is a limited linear region in the laser's response to an RF voltage applied to it. The output optical power versus input current of a typical semiconductor laser along with the characteristic parameters is shown in Figure 2.5 [7]. It can be seen that a certain minimum value of input current referred to as the threshold current I_{th} is required, before the laser starts emitting a considerable amount of light. There is also a certain value of input current, beyond which the output optical power of the laser saturates. This value of current is so-called the saturation current I_{sat}. Between the currents I_{th} and I_{sat} there exists a linear region, where a change in the input current produces a proportional change in the output power of the laser. In order to accomodate the entire peak-to-peak variations in the input RF signal, the laser has to be biased to the operating point of I_{bias} using a DC source. The RF signal is then superimposed on the DC source.

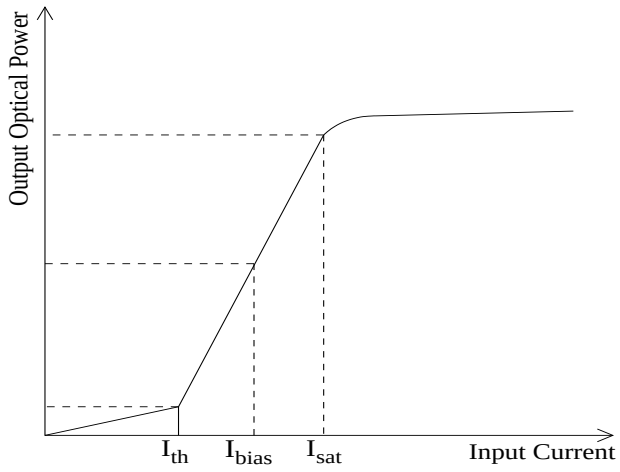

Figure 2.5: Ouput optical power of semiconductor laser versus input current

Mathematically the output optical power is related to the input current by the following relation [7]:

$$P_{op} = \frac{hf}{q}\eta_L(I - I_{th}), \tag{2.2}$$

where η_L denotes the laser's quantum efficiency[1], h denotes Plank's constant, f is the frequency of the emitted photon and q is an electron's charge.

[1]The laser's quantum efficiency is defined as the average number of photons generated per electron.

2.1.3 Pulsed Semiconductor Lasers

In baseband optical communication systems relying on TDM for transmitting multiple channels typically pulsed semiconductor lasers are used. The optical pulses are generated by gain switching applied to the DFB laser diode (LD) [48], [49], [50], as shown in the schematic of Figure 2.6 [51]. Gain switching uses a periodic high-frequency sinusoidal signal to generate optical pulses of the same repetition rate as the applied sinusoidal signal, shown by the stylised plot of Figure 2.6. The optical pulses generated can have a pulse duration which is much shorter than the time period of the sinusoidal signal used to drive the CW laser. The DFB LD is biased to an operating point that is just below its threshold level, where only spontaneous emission is released by the laser. When for example a sinusoidal RF signal is superimposed on the DC bias, seen as I_{bias} in Figure 2.5, the positive voltage cycle of the sinusoidal signal adds to the DC bias and increases the current beyond the threshold level. Hence the DFB LD's stimulated emission is triggered, which we might refer to as lasing. During this period, a large number of photons are generated which results in a fall of the carrier density below the threshold level. Therefore, the DFB LD stimulated emission is curtailed before the positive cycle of the RF signal is completed. Then again, the positive cycle of the RF signal is followed by a negative cycle, during which the injection current is reduced to a low level. Hence, the carrier density is increased during the period, when the DFB LD is not lasing. On the next positive cycle, another laser pulse is emitted and this process continues until the electronic signals applied to the laser are switched off. Therefore, the process of gain-switching can be used for the efficient generation of short duration optical pulses at the repetition rate of the applied sinusoidal RF signal, as shown by the stylized plot of figure 2.6.

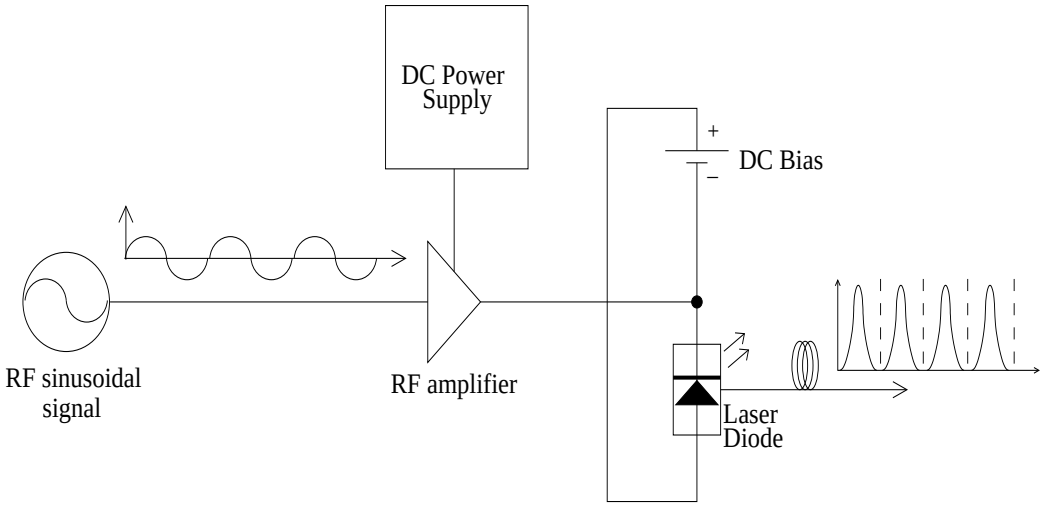

Figure 2.6: Schematic of a Gain Switched Laser.

2.1.4 External Modulation

Although the direct modulation of semiconductor lasers is a low-complexity and cost-effective method of generating intensity modulated optical signals, it is limited to low-frequency electronic

signals. Directly modulating a laser at high frequencies that are close to the laser's relaxation resonance frequency, increases the generation of laser RIN [52], which then gives rise to variations in the phase of the optical signal, an effect termed as phase noise [47]. The group delay of the signal is defined as the first derivative of the optical phase with respect to optical frequency and the dispersion parameter is a measure of the second derivative of the optical phase with respect to optical frequency. Therefore, the phase noise of the optical signal will result in different group velocities while travelling through a dispersive fiber. Consequently, the variations in the group velocities will result in intensity modulation of the optical signal, as described in [53]. In case of digital optical communications transmitting optical pulses over long fibers, the laser's phase noise tends to become the factor limiting the maximum distance before regeneration is required. In order to avoid the impairments imposed by direct modulation of the laser using high-bandwidth signals, typically external modulators are used [52]. In Sections 2.1.4.1, 2.1.4.2 and 2.1.4.3, three main types of external modulators relying on different physical effects are discussed.

2.1.4.1 Mach-Zehnder Modulator

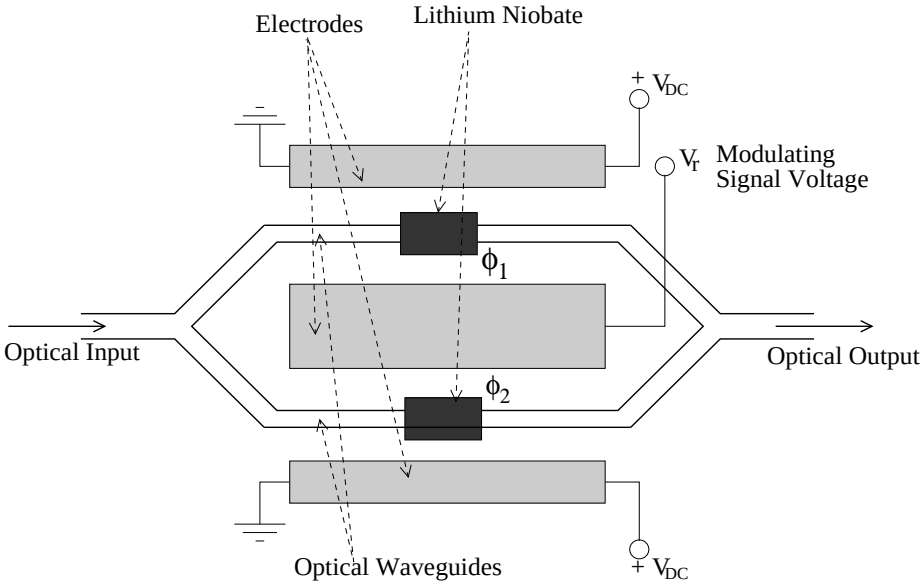

Figure 2.7: MZM using a Lithium Niobate phase modulator in the upper and lower arm of a MZI [54].

The most popular commercially used type of optical modulator is the Mach-Zehnder Modulator (MZM) [44]. The schematic of a typical single-drive MZM is shown in Figure 2.7, which is reminiscent of the Mach-Zehnder Interferometer (MZI). As shown in Figure 2.7, the optical input of the MZM is split in path 1 and path 2 with the aid of the optical waveguides seen in Figure 2.7. Initially, the optical signals in each path have the same phase ϕ_1 and ϕ_2, therefore, $\phi_1 - \phi_2 = 0$. It can be observed from Figure 2.7 that each optical waveguide is surrounded by electrodes which are connected to the DC bias voltage and the modulating signal voltage. These voltages are used to vary the phase of the optical signal in in path 1 and path 2 with the aid of the so-called linear electro-

optic effect [52]. This electro-optic phenomenon typically occurs in nonlinear optical mediums such as optical crystals, where the application of an external electric field changes the refractive index of the crystal. When light is passed through such a crystal, its phase is modulated due to variation in the refractive index caused by the amplitude variations of the applied modulating voltage. In the absence of the modulating voltage shown in Figure 2.7, the DC bias voltages keep the refractive index of the crystals at values such that no phase variation is imposed on the signals in path1 and path2. With the application of the modulating voltage, the phase of the optical signals in path 1 and path 2 changes in proportion to the amplitude of the applied modulating voltage. When the phase-modulated optical signals in path1 and path2 are superimposed at the right of Figure 2.7, they result in an optical signal whose amplitude depends upon the phase difference between signals of path 1 and path 2. Hence the amplitude variation of the modulating signal voltage is used to impose phase variations ϕ_1 and ϕ_2 on the optical signals in path 1 and path 2, respectively. The difference in the phase ϕ_1 and ϕ_2 results in amplitude variations of the optical signal at the output of the MZM. This type of MZM is called a single-drive MZM, since the same modulating voltage is applied to both the arms of the MZM, as shown in figure 2.7. The most widely used nonlinear optical crystal in the design of MZMs is the lithium niobate crystal [55]. The reason for the popularity of lithium niobate is its ability to operate at a high frequency, its efficient coupling with optical fibers and low chirp-induced contamination of the optical signals [55]. Chirp is defined as the linear variation in the instantaneous frequency of the optical pulse with time [56]. The optical power at the output of the MZM in terms of the input optical power may be written as [54]:

$$P_o(t) = P_i(t) \cdot cos_2 \left[\Delta\phi(t)\right], \tag{2.3}$$

where $P_i(t)$, $P_o(t)$ and $\phi(t)$ are the input optical power, the output optical power and the total phase difference between the optical signals in the two arms of the MZM seen in Figure 2.7. The phase difference in the two arms can be written as:

$$\Delta\phi(t) = \frac{\phi_1(t) - \phi_2(t)}{2}, \tag{2.4}$$

where $\phi_1(t)$ and $\phi_2(t)$ are the phase differences in path 1 and path 2 of the MZM due to the modulating voltage, as shown in Figure 2.7.

2.1.4.2 Dual-Drive Mach-Zehnder Modulator

In contrast to the single-drive MZM of Figure 2.7, the Dual-Drive MZM (DD-MZM) allows the application of different voltages namely V_{r1} and V_{r2} to the upper and lower arms of the MZI, as seen in Figure 2.8 [54]. It can be observed from the schematic that a DD-MZM has separate electrodes for the DC bias voltage and the RF signals. This allows for the application of independent phase shifts to the two optical signals in the arms of the MZM. As a benefit, the DD-MZM can be used to generate various types of modulated signals, such as for example Single-Side-Band (SSB) Modulation [57]. The SSB modulation is achieved by applying a suitable DC voltage to one of the DC electrodes, while grounding the other DC electrode. At the same time, both the RF signal

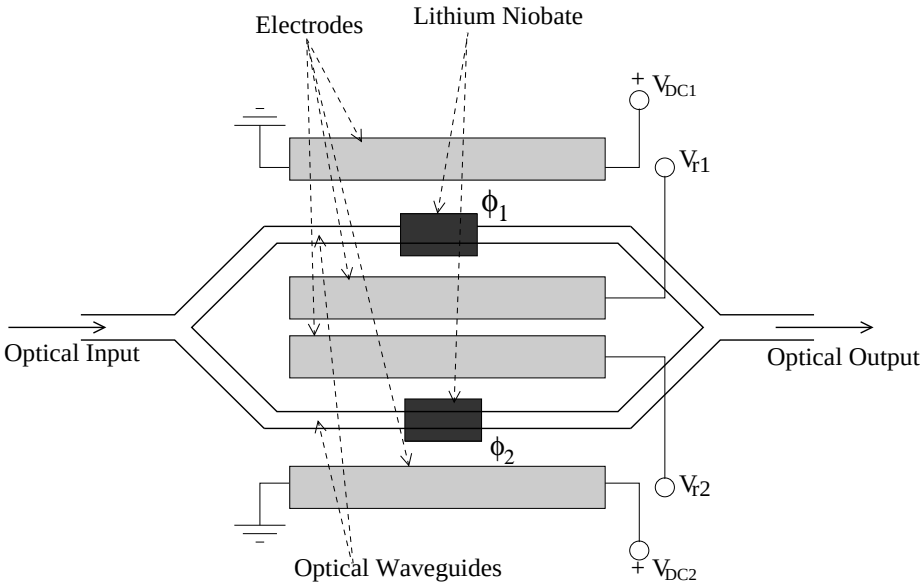

Figure 2.8: Schematic of a DD-MZM [54]. In contrast to the single-drive MZM of Figure 2.7, different modulating signals - namely V_{r1} and V_{r2} may be applied to the upper and lower arms.

electrodes are driven by splitting the same RF signal and shifting the phase of one of the splitted signals by π, as described in [57].

2.1.4.3 Electroabsorption Modulators

The third major type of optical intensity modulators is constituted by the Electro-absorption Modulator (EAM), where the absorption coefficient of a material is modulated in response to the external voltage [52]. The light-absorption of the material directly modulates the intensity of the optical signal passing through it. EAMs are primarily manufactured using semiconductor materials, such as for example Indium Gallium Arsenide (InGaAs) and Indium Aluminium Arsenide (InAlAs) [52]. The same materials are used for manufacturing semiconductor lasers and PDs. Hence EAMs manufactured from these semiconductor materials are eminently suitable for integration with the semiconductor lasers and PDs used in the optical link.

The mathematical relationship of the output optical field of an EAM versus the input optical field can be written as [54]:

$$E_o(t) = E_i(t) \cdot TF_{EAM} \cdot exp\left(\frac{j\rho}{2} \cdot lnTF_{EAM}\right) \tag{2.5}$$

where $E_o(t)$ and $E_i(t)$ represent the input and output optical fields respectively, TF_{EAM} represents the power transfer function of the modulator, while ρ is the chirp factor [58]. The power transfer function of the EAM can be written as:

$$TF_{EAM} = (1 - m) + m \cdot D(t), \tag{2.6}$$

where m is the modulation index of the modulator and $D(t)$ is the instantaneous value of the data signal applied to it.

2.2 Optical Fiber

Optical fibers are used as the most popular transmission medium in optical communication systems. Optical fibers exploit the principle of Total Internal Reflection (TIR), where light entering the fiber at a certain angle remains confined to the core due to reflections from the boundary of the core. The reason for the reflection of light at the boundary of the core is the significant change in the refractive index at the core boundary. As shown in Figure 2.9, an optical fiber is made of silicon and it is cylindrical in shape, consisting of two sections, the inner core and the outer cladding. The refractive index of the cladding is made significantly lower than that of the core. Since a change in refractive index results in the reflection of light, the light entered at a certain angle into the fiber remains confined to the core [59].

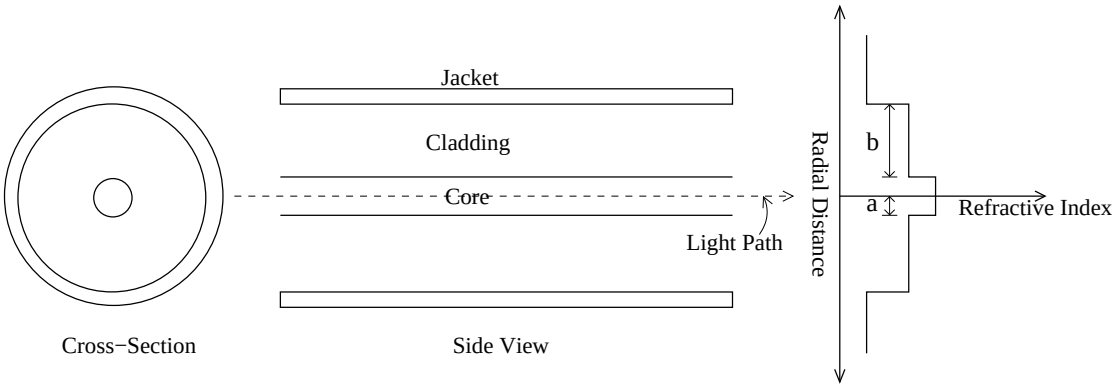

Figure 2.9: Structure of a SMF showing its cross-section and refractive index profile.

We will discuss the most common type of fiber used in optical communications, namely the SMF [44], as shown in Figure 2.9. It is referred to as being single mode, since it allows only one mode of light to pass through it, due to its small core radius. If the core radius is on the order of the wavelength of light used, then only a single mode of light travels through it following an almost a straight path without reflections [59]. The refractive index profile shown in Figure 2.9 generally obeys a step-index profile, since the refractive index of the core is a step higher than that of the cladding, i.e. there is no gradual transition between them, as seen in Figure 2.9. The core diameter of a typical SMF is 8 - 10 μm and its cladding diameter is 125 μm. Since the core radius of SMF is comparable to the wavelength of light used in optical communications, the TIR is no longer responsible for the confinement of light to the SMF. Instead, it is the step-change in the refractive index of the SMF that helps in confining the light to the fiber [59]. In a transmission medium having a homogeneous refractive index, light spreads due the phenomenon of diffraction. Therefore the width of a beam of light traveling through a homogeneous medium will increase, but fortunately the beam-width may be controlled by carefully designing the refractive index profile of the medium. If the refractive index of the medium near the center of the beam is kept high compared to the periphery, then the light at the center travels slower than at the periphery. The reduced speed of light at the center compared to that at the periphery enables the medium to keep the light focused, by preventing it from spreading out. The refractive index profile of the SMF

shown in Figure 2.9 was designed to keep the light focused, so that it travels along the core for long distances.

Like any other transmission medium, optical fiber also imposes impairments on the signal that is transmitted through it, which include attenuation, dispersion and nonlinearity. In the following sections, we discuss each of them in detail.

2.2.1 Attenuation of the Fiber

The fiber attenuates any signal that passes through it. There are two main reasons for fiber attenuation, namely material absorption and Rayleigh scattering [44]. Material absorption can be further divided into two categories, intrinsic absorption and extrinsic absorption. Intrinsic absorption is due to the silica itself, which is used to make the fiber, while extrinsic absorption is due to impurities in silica. Material absorption exists due to the electronic or vibrational resonances within the fiber material. The attenuation due to intrinsic absorption in silica occurs due to electronic resonance occuring for wavelengths in the ultrviolet region, while due to vibrational resonance for wavelengths in the infrared region. The major impurity causing extrinsic absorption is the presence of water vapours in silica. These vapours cause attenuation peaks near the 2.73 μm wavelength region due to vibrational resonance of Oxygen and hydrogen (OH) ions [44]. The dependence of material absorption on the wavelength of light can be observed from Figure 2.10 [44], which shows the amount of attenuation in dB/km versus the wavelength for different sources of material absorption. It can be observed from Figure 2.10 that the intrinsic absorption occurs only in the ultraviolet as well as infrared region and it remains small in magnitude.

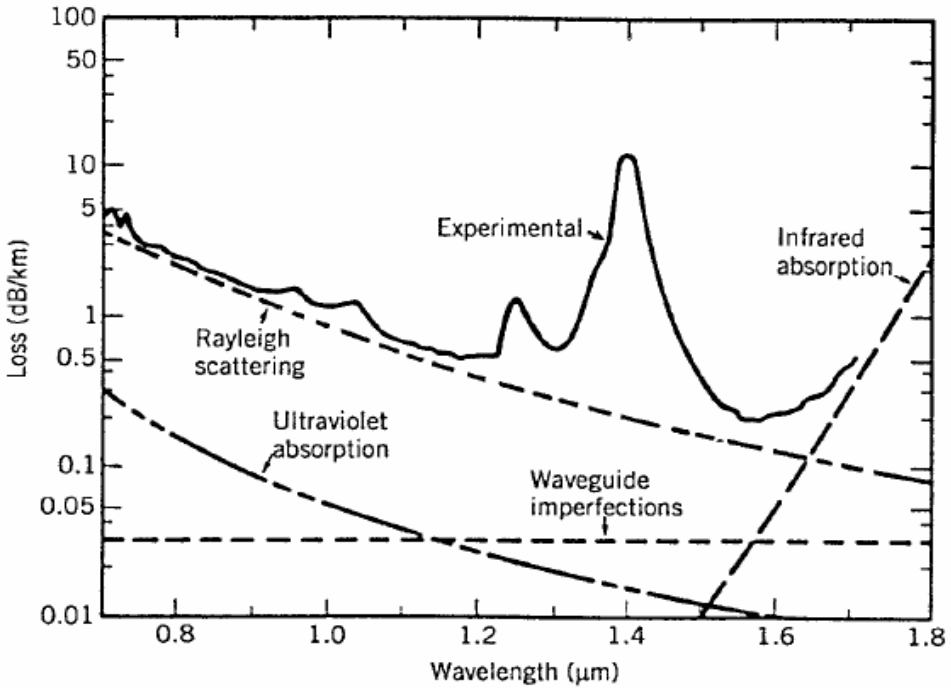

Figure 2.10: Losses in SMF versus wavelength [After [44]].

The second major source of attenuation in optical fibers is Rayleigh scattering, which is caused due to minor refractive index variations within the fiber core. These refractive index inhomogeneities are due to variations in the silica density within the core, which are caused by imperfect manufacturing of the fiber. A small part of the light traveling through the fiber is reflected every time a change in refractive index is encountered. Since the reflected light is not received at the other end, Rayleigh scattering is a major cause of optical signal attenuation. It can be observed from Figure 2.10 that the attenuation caused by Rayleigh scattering is considerably higher than that of material absorption. As mentioned in [44], the Rayleigh scattering induced attenuation increases inverse proportionately with the fourth power of the wavelength. Therefore, as observed from Figure 2.10, the attenuation due to Rayleigh scattering is lower at higher wavelengths.

Figure 2.10 also shows the total attenuation due to the combined effect of all the sources of absorptions. The overall attenuation α of the fiber may be written mathematically as:

$$\alpha = \frac{10}{L} log_{10}(\frac{P_{out}}{P_{in}}), \tag{2.7}$$

where P_{in} and P_{out} are the input and output optical powers of a fiber of length L. Again, the peaks observed in the experimental plots are due to the extrinsic absorption caused by water vapours in silica. In order to keep the signal attenuation to a low value, the wavelengths of light chosen in optical communications are in the 1.3 μm and 1.5 μm bands. As observed in Figure 2.10, the overall attenaution of the fiber is as low as 0.2 dB/km in these regions.

2.2.2 Fiber Dispersion

Fiber dispersion is a phenomenon where light of different wavelengths travels at different speeds within the fiber. The reason for dispersion is the wavelength-dependence of the refractive index of silica used for manufacturing the optical fiber. An optical signal, be it CW or pulsed, is always composed of a finite range of wavelengths. Hence due to refractive index variations, each wavelength travels at a different speed along the length of fiber. Therefore, the optical pulses received at the output of the fiber are typically broadened owing to dispersion. Figure 2.11 shows the variation of dispersion with wavelength of the optical signal [56]. It can be observed from the figure that dispersion is negative for wavelengths below 1310 nm and becomes positive for wavelengths higher than 1310 nm. However, the slope of the dispersion versus wavelength plot, which is also called the dispersion slope, remains positive over the complete range of wavelengths. The wavelength of 1310 nm, where the dispersion changes sign is generally termed as the zero-dispersion wavelength [56]. Since dispersion is the derivative of group refractive index of silica with respect to wavelength, the sign change indicates that the group index decreases with an increase in wavelength until 1310 nm, and increases for wavelengths beyond 1310 nm [56]. Therefore, the group velocity of the optical signal, which is inversely proportional to the group refractive index, increases with an increase in wavelength until 1310 nm, and decreases for an increase in the wavelength beyond 1310 nm.

The effect of dispersion is different for analogue and digital communication systems. Since

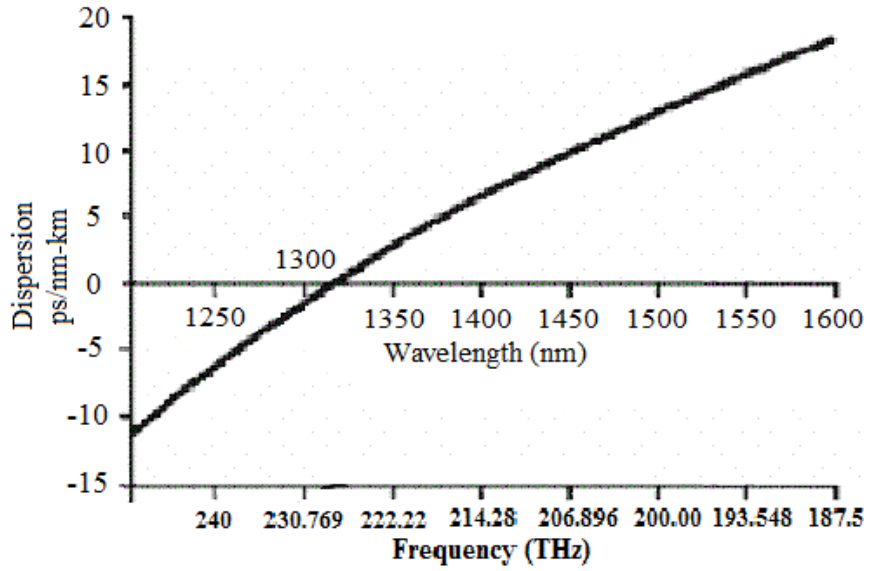

Figure 2.11: Fiber dispersion versus wavelength/frequency [After [56]]

analogue systems use CW lasers, they do not experience noticeable broadening of the signal in time domain while travelling through a dispersive fiber. The CW signals have a narrow bandwidth, therefore the wavelengths at the edges of the spectral width have a small difference between them. Due to this small difference in the wavelengths, their speed in the optical fiber is almost similar, hence avoiding the broadening of the signal in the time domain. Instead, dispersion effects analogue systems in a different manner. When a CW signal is intensity modulated with an electronic signal, sidebands are formed on both sides of the CW carrier frequency. The sidebands are located at a frequency shift which is equal to the frequency of the electronic signal. Due to difference in frequencies of the sidebands, fiber dispersion induces variable phase changes on these sidebands while the analogue signal travels through the fiber. At the receiver, heterodyne reception takes place as part of the process of photodetection [60]. Therefore, the output of the PD is the sum of the two received sideband's intensity. For the scenario, where the phase of the pair of received sidebands is opposite due to undergoing different amounts of dipersion, the output signal of the PD becomes almost zero due to the destructive superposition of the sideband signals. By contrast, when the phase shifts of the two sidebands are the same, the output of the PD becomes maximum due to the constructive superposition of the sideband signals. Therefore, the output of the PD varies as a function of the phase difference between the two sidebands [57]. The relationship between the power P_{rf} detected at the output of the PD for a fibre having a length L and a dispersion parameter D is given by [60]:

$$P_{rf} \quad \propto \quad cos[\pi LcD(\frac{f_{rf}}{f})^2], \tag{2.8}$$

where c is the speed of light, f_{rf} is the frequency of the RF signal and f is the central frequency of the optical carrier. Observe from Equation 2.8 that the quality of the received RF signals will be affected, depending upon both their central frequencies and upon the kilometric dispersion of the fiber.

Let us now consider the effect of dispersion in case of baseband communication systems using optical pulses to transmit the digital data. Optical pulses have a narrow but finite pulse width which results in a broad spectrum. The effect of a fixed kilometric fiber dispersion is more pronounced on narrower pulses having a wide spectrum. Due to the presence of a wide range of frequencies, the frequency component at one end of a broad spectrum travels at a different speed compared to the frequency component at the upper end. This broadens the pulses in the time domain, which might hence overlap with the adjacent pulses. Figure 2.12 shows the overlap of adjacent pulses in the time domain due to dispersion, where the optical pulses at the transmitter are within the time allotted to each bit. However, after the signal was transmitted over a dispersive fiber, each pulse broadens in the time domain and the tails of two adjacent pulses might overlap, thus potentially imposing detection errors. Since high-bit rate Optical TDM systems require short pulse-widths, they suffer from the effects of dispersion. Increasing the fiber length further degrades the dispersion.

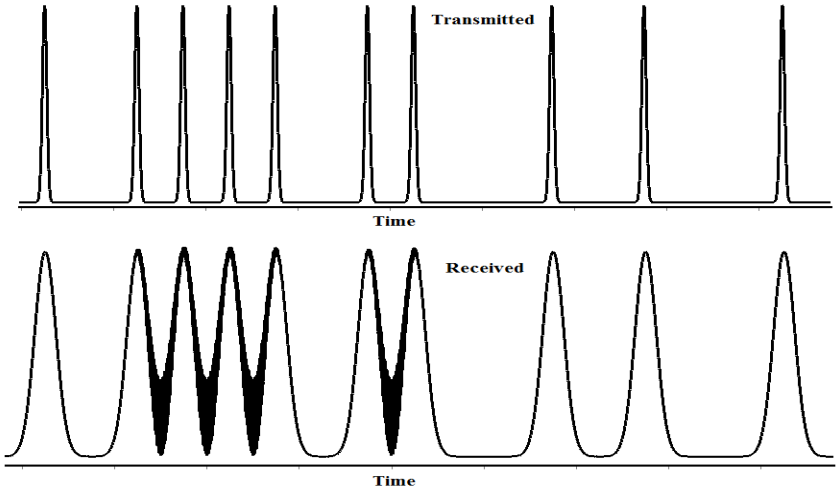

Figure 2.12: Optical pulses before and after transmission through an optical fiber link.

2.2.3 Fiber Nonlinearity

Like any other di-electric medium, the response of the optical fiber becomes nonlinear upon increasing the intensity of light traveling through it. The nonlinearity of a fiber is quantized in terms of its nonlinearity parameter γ defined as [56]:

$$\gamma = \frac{n_2 \omega_\circ}{c A_{eff}}, \tag{2.9}$$

where n_2 is the nonlinearity index of the fiber, A_{eff} is the effective area of the fiber core, $\omega_\circ$ is the frequency of light and c is the speed of light in vacuum. Observe from Equation 2.9 that the nonlinearity parameter may be varied by adjusting either the nonlinearity index or the effective area of the fiber core. The nonlinearity index n_2 depends upon the material of the fiber and can be controlled by adding impurities to silica [56]. The nonlinearity of the fiber typically results in harmonics of the signal and hence broadens the spectrum of the optical signal. When an optical signal

having a finite spectral bandwidth travels through a fiber, the phase of each spectral component is also affected by the nonlinearity of the fiber. This phase-change of the spectral components results in further new frequencies and hence gives rise to broadening of the spectrum [56]. The spectral broadening imposed by nonlinearity is aggravated by increasing the power of the optical signal. The spectral broadening phenomenon is shown in the stylized illustration of Figure 2.13, where the spectrum of an optical pulse is shown at different distances along the fiber, demonstrating that upon increasing fiber-length, the spectrum of the signal broadens.

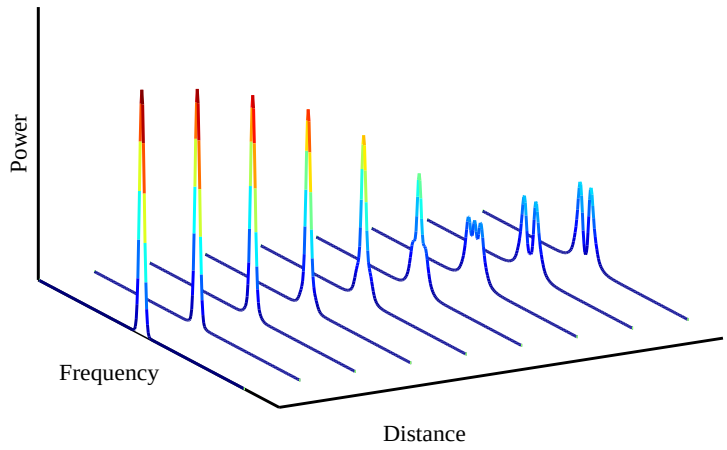

Figure 2.13: Spectral evolution of an optical pulse along the length of fiber.

Since the spectral broadening occurs due to change in the spectral phase of the signal along the length of the fiber, it is termed as phase modulation. When the phase modulation is imposed by the signal's own excessive intensity, it is referred to as Self Phase Modulation (SPM) [56]. When two optical signals are travelling side-by-side in time, as in TDM systems, the intensity of one signal has an effect on the phase of the other. This type of phase modulation is termed as Cross Phase Modulation (XPM). Naturally, fibers having a high nonlinearity parameter will cause more substantial spectral broadening of the optical signal, which is highly undesirable in optical communication systems [44]. Therefore fibers designed for optical communication tend to have a comparitively large effective core area so as to make the nonlinear parameter as low as possible, as shown by Equation 2.9. Recall from Section 2.2 that the limit imposed on the effective area is determined by the maximum tolerable width still facilitating the transmission of a single mode of the optical signal propagating through the fiber. The nonlinearity of the fiber mainly affects the family of digital communication systems using optical pulses. Optical pulses having a sharp rise and decay in time domain have a broad spectrum and hence undergo higher SPM. The relation between the optical pulse's power profile and the phase-distortion-induced frequency shift $\delta\omega_{SPM}$ imposed by SPM may be written as [56]:

$$\delta\omega_{SPM} = \gamma L_{eff} \frac{dP(t)}{dt}, \tag{2.10}$$

where L_{eff} is the effective fiber length and $\frac{dP(t)}{dt}$ is the optical pulse power profile's rate of change. It can be observed from Equation 2.10 that the frequency shift induced by SPM is high for narrow optical pulses exhibiting a high derivative. Equation 2.10 also shows that the effect of fiber nonlinearity is negligible for analogue optical systems using CW signals, since the value of $\frac{dP(t)}{dt}$ for a relatively narrow-band CW signal is typically low.

2.3 Optical Receiver

The task of an optical receiver is to perform the OE conversion of its input signal. In this section, we will discuss the process of photodetection, the parameters of a PD and the design of a commonly used PD termed as the PIN photodiode.

2.3.1 Principle of Photo-detection

Photodetectors are made of semiconductor materials. When light falls on a semiconductor material, photons are absorbed by the electrons in the valence band of the semiconductor [59]. These electrons in the valence band gain energy from the absorbed photon and thus move to the conduction band of the semiconductor material. Therefore an electron-hole pair is formed, which on the application of an external potential, gives rise to the flow of electric current, referred to as photocurrent [59]. The process of photo-detection is shown in the stylized illustration of Figure 2.14, where an electron absorbs a single photon to move into the conduction band. In order for the electron transition to occur, the energy of the incident photon should be equal to the energy difference between the valence and conduction band, as indicated by the vertical line in Figure 2.14. The simplest form of a PD is based on a combination of p-type and n-type materials forming a p-n junction. When light falls on this type of a reverse-biased p-n junction, electron-hole pairs are generated that flow in the opposite direction due to the voltage applied. The width of the p-n junction determines the amount of current flow.

2.3.2 Photodetector Parameters

Let us now discuss some of the PD parameters, namely its responsivity, quantum efficiency and bandwidth. The responsivity R of a PD is defined as the ratio of the photocurrent I_p generated, to the optical power P_{in} incident on the PD, which is formulated as:

$$R = \frac{I_p}{P_{in}}. \tag{2.11}$$

The quantum efficiency η of a PD is a measure of how efficiently the PD converts the incident light into electric current, namely as the ratio of the rate of electron generation to the rate of photon incidence on the PD [44]. The rate of electron generation is given by the ratio of the current flow

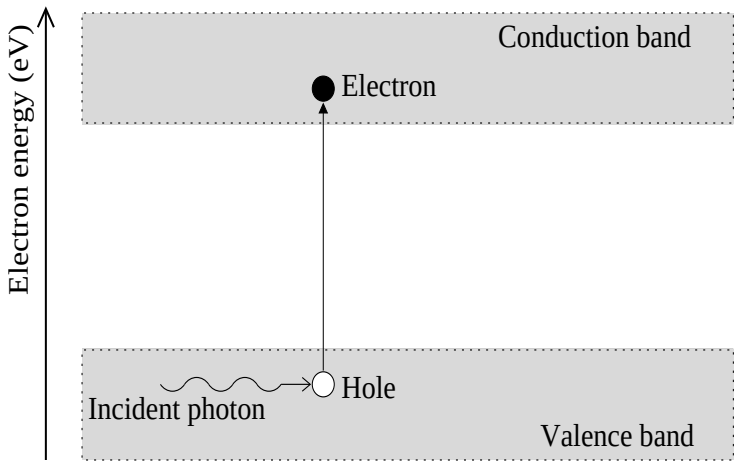

Figure 2.14: The principle of photodetection.

to the charge of an electron, while the rate of photon incidence is given by the ratio of the total incident power to the energy absorbed, when an electron jumps from a lower energy level to a higher level. Hence the quantum efficiency can be expressed as:

$$\eta = \frac{I_p/q}{P_{in}/hf} = \frac{hf}{q}R, \tag{2.12}$$

where q is the electron charge, h is Plank's constant and f is the frequency of the incident photon. The bandwidth of a PD predetermines, how promptly it responds to changes in the incident light. The bandwidth in turn depends upon the rise time T_r, which is defined as the time it takes for the current to rise from 10 $\%$ to 90 $\%$ of its final value for a step change in the power of the incident light [44]. Considering the p-n junction based PD of Figure 2.15, the rise time is dependent both upon the RC time constant and on the transit time of the PD. The capacitance C of a p-n junction based PD is determined by the length L_d of the depletion region which separates oppositely charged electrons and holes. The transit time is the time required for an electron to travel from one end of the PD to the other. The rise time T_r of a PD can be written as [44]:

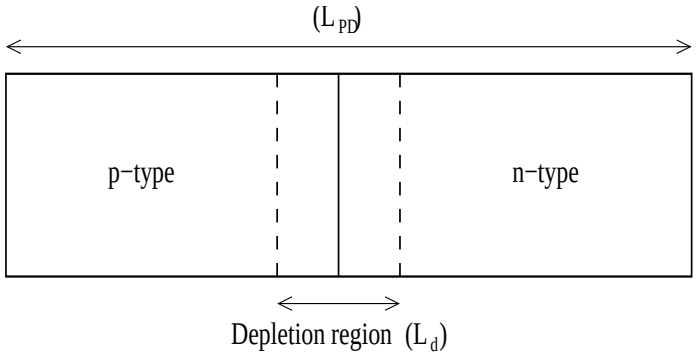

Figure 2.15: Structure of a P-N junction photodiode.

$$T_r = (ln9)(\tau_{tr} + \tau_{RC}), \tag{2.13}$$

where τ_{tr} and τ_{RC} denote the transit time and RC time constant of the PD. The values of τ_{tr} and τ_{RC} are dependent upon the design of the PD. Due to the analogy between the PD and RC circuit, the bandwidth of the PD can be expressed in a way similar to that of the RC circuit as:

$$\Delta F = 1/[2\pi(\tau_{tr} + \tau_{RC})]. \tag{2.14}$$

Equation 2.14 implies that the bandwidth of a PD can be increased both by reducing the RC time constant and by the transit time of the PD. The reduction in transit time can be achieved by reducing the length L_{PD} of the PD, since the transit time is related to L_{PD} by:

$$t_{tr} = L_{PD}/\upsilon_d, \tag{2.15}$$

where υ_d is the velocity of the electrons drifting across the length L_d of the depletion region. A reduction in the length of the PD would reduce the surface area on which the light falls. Therefore the rate of electron generation will decrease, which in turn will reduce the responsivity and efficiency of the PD. This implies that there is a trade-off between the bandwidth and responsivity of a PD.

2.3.3 PIN Photodiode

Apart from the drift of electrons across the depletion region, the photocurrent can also be generated through diffusion of electrons and holes. As mentioned earlier, the drift current is generated due to light falling on the depletion region of the PD. Similarly, the diffusion current is generated by the light falling on the n-type and p-type materials in the PD. The electrons and holes generated in p-type and n-type materials respectively, have to diffuse towards the depletion region boundary, before they can drift to the opposite sides. This diffusion of electrons and holes is a slow process and hence delays the response of the PD to a sudden change in the intensity of the incident light. In order to reduce the diffusion current, the length of the p-type and n-type materials can be decreased, hence making the drift current dominant over the diffusion current. This can be achieved by inserting an intrinsic semiconductor material between the n-type and p-type materials, hence increasing the length of the depletion region, while decreasing the length of n-type and p-type regions [61], as shown in Figure 2.16 [44]. Due to the particular structure of the PD, it is generally called PIN photodiode, where P, I and N stands for the p-type, intrinsic and n-type materials, respectively.

2.4 Optical Amplifiers

Naturally, the optical fiber attenuates light, as discussed in Section 2.2.1. Furthermore, in an optical network, there are multiple passive components, such as add-drop multiplexers, filters, splitters and couplers, whose insertion losses reduce the signal power. Therefore optical amplifiers are required at regular intervals in order to maintain a suitable signal power along the transmission link. The

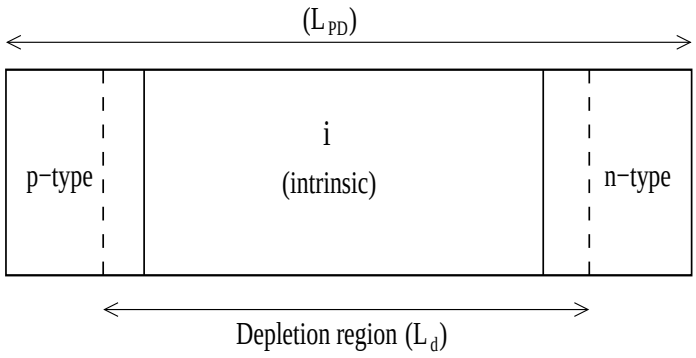

Figure 2.16: Structure of a PIN photodiode.

most common optical amplifier used in optical communication systems is the EDFA [26]. EDFAs work in a manner similar to lasers namely by pumping a gain medium, which is made of an Erbium doped fiber. Recall from Figure 2.2 that as a result of pumping, the electrons in the gain medium jump to higher-energy states. These electrons are stimulated by photons of an incoming optical signal to jump to a lower-energy state, while releasing a photon of the same characteristics as that of the incoming signal. Therefore, the newly generated photon will have the same phase, polarization and direction of motion as the incident photon. This process was referred to as stimulated emission in Section 2.1.1 and results in increasing in the optical input signal's power. The wavelength of the light emitted when an electron jumps from a higher energy state to the lower one is dependent upon the material used to dope the fiber. For Erbium doping, this wavelength lies in the region spanning from 1525 nm to 1570 nm [26], which coincides with the wavelength region where the fiber attenuation was shown to be the lowest in Figure 2.10. Therefore, Erbium is a suitable dopant for amplifiers used in optical communications. In Erbium, the electrons can be excited to reach many different energy levels, but we will consider only two levels namely E_2 and E_3 that are at a higher energy than the ground level E_1, as shown in Figure 2.17 [59]. The upward pointing arrows in Figure 2.17 indicate pumping of the Erbium ions with the aid of a laser having a wavelength of 980 nm, since pumping at 980 nm consumes a low power. When the electron is raised to level E_3, it spontaneously jumps down to level E_2 and then to level E_1. The transition time from E_3 to E_2 is much shorter than that of the transition from E_2 to E_1. Therefore, most of the electrons stay at level E_2 for a longer time and hence increasing the amplification probability of an input signal in the wavelength range of 1525 nm to 1570 nm.

Figure 2.18 shows the structure of a typical EDFA [26]. The gain medium is divided into two parts by using two segments of Erbium doped fiber. Each of the gain media is pumped using 980 nm pump laser diodes that are coupled to the Erbium doped fiber. There is an isolator and an optical filter between the two segments of an Erbium doped fiber. The purpose of the isolator is to prevent the light from travelling in the backward direction towards the signal source, for example due to reflections in the optical network. The filter is used to reject out-of-band noise from the signal. After passing through both Erbium doped fiber segments, the amplified optical signal is filtered again to reject any out-of-band noise introduced by the amplification process. The passive components in the schematic including the optical filters, the coupler and the isolator are

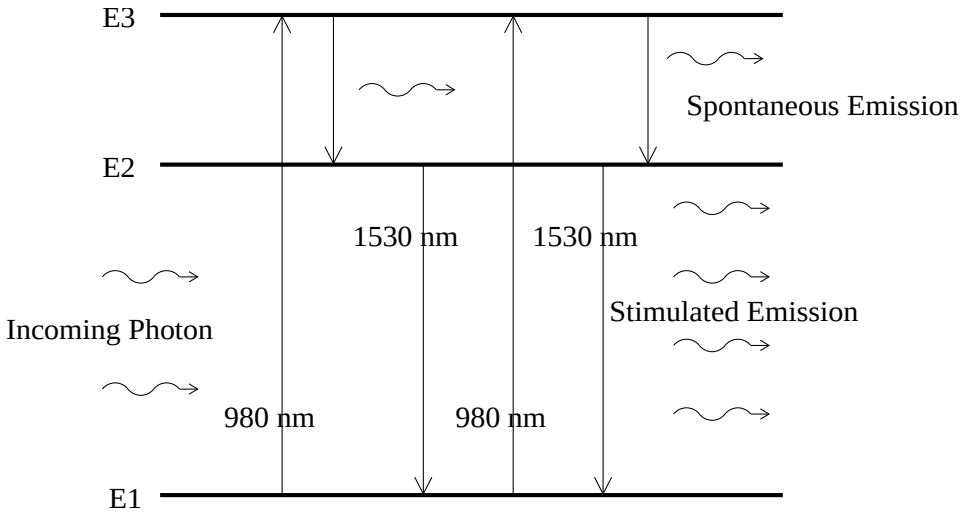

Figure 2.17: Basic principle of doped fiber amplification.

introduced in the Sections 2.5 and 2.6.

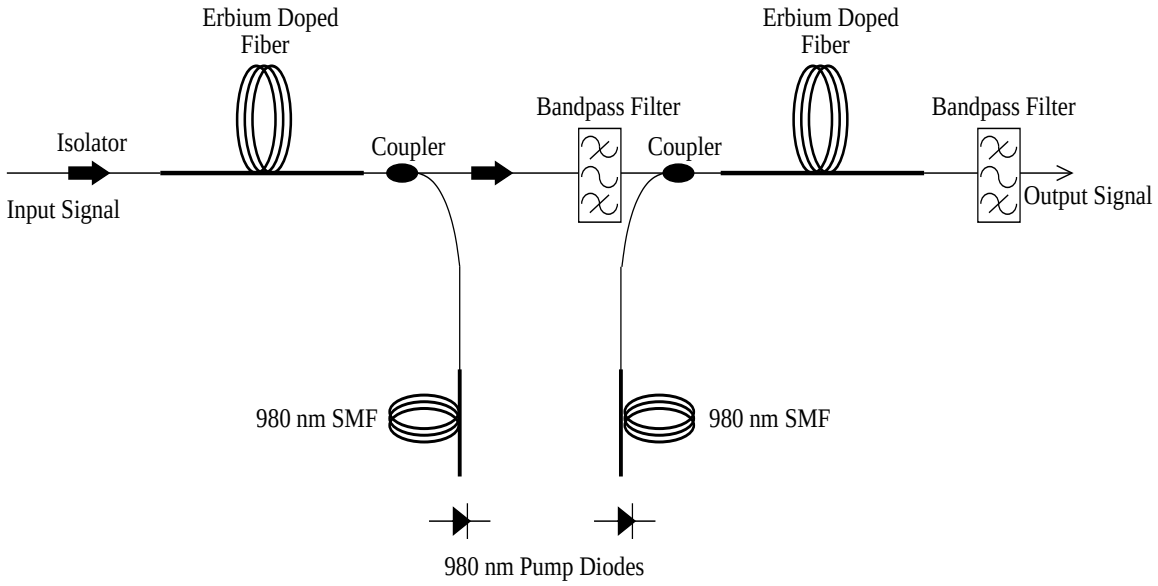

Figure 2.18: Structure of a typical EDFA.

Similar to lasers, the optical amplifiers also generate some noise, which reduces the signal to noise ratio of the output signal. The main source of noise is the so-called Amplified Spontaneous Emissions (ASE) Noise. The reason for this noise is the spontaneous jump of electrons from higher energy state to the lower energy state, releasing a photon of random phase and random direction, as indicated at the top right corner of Figure 2.17. The EDFAs used for ROF and baseband optical pulsed communication have generally similar characteristics, albeit it is desirable to have an EDFA for pulsed communication which is less nonlinear, hence resulting in reduced spectral broadening of the signal being amplified. This can be achieved by increasing the effective core area of the Erbium doped fiber used in the EDFA as a gain medium.

2.5 Optical Filters

Optical filters, which may be used for example to separate a single of mutiple optical signals from a WDM signal. Optical filters are also widely used to reject out-of-band ASE noise imposed on the desired signals. Some of the desirable features of an optical filter are a high out-of-band signal rejection, temperature independent operation, low insertion loss, compact size and low cost. In this section, we will discuss the four most common optical filters used in communications.

2.5.1 Grating Filters

Grating filters exploit the phenomenon of light-diffraction to different wavelengths of an input optical signal. The grating filter of Figure 2.19 uses a diffraction grating, which is esentially a glass having a rectangular cross-section and multiple slits or groves. When light composed of different wavelengths impinges on such a grating, it passes through the narrow slits and spreads out at the output due to diffraction. Hence each slit effectively acts like a separate source of light. An important quality of diffraction grating is that for a unique set of discrete angles, the light diffracted from the multiple slits facing in different directions are in phase [62]. This coherent phase relationship results in constructive interference among various diffracted wavefronts at spatially separate points at the opposite side of the diffraction grating. The condition for constructive intereference to occur for a grating having a uniform slit spacing of d between two consecutive slits and an incident light of wavelength λ is given by [62]:

$$d \cdot sin\theta = m \cdot \lambda, \tag{2.16}$$

where m is the diffraction order and θ is the diffraction angle.

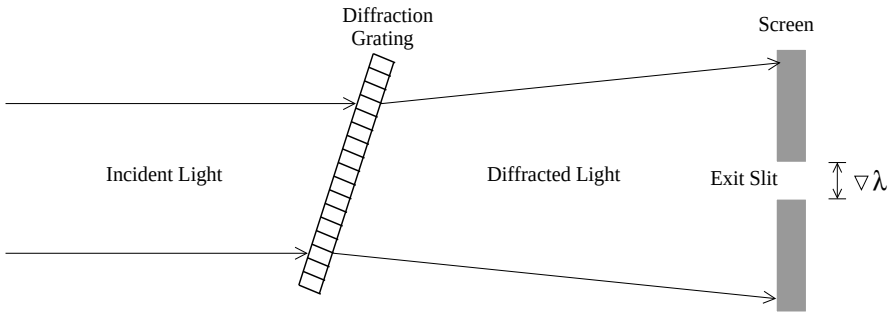

Figure 2.19: Operating principle of a Tunable Grating Filter [62].

Again, the operating principle of a grating filter based on a diffraction grating can be understood from the simplified diagram shown in Figure 2.19 [62]. The optical signal to be filtered impinges on a diffraction grating, which results in a diffraction pattern at the opposite side. The diffraction pattern is composed of multiple bright spots of light at different wavelengths separated spatially. The spatial distance among the different bright spots depends both upon the slit spacing of the grating and on the distance of the screen used for observing the pattern. A narrow bandwidth of

light can be filtered out by using an exit slit located at some distance from the diffraction grating. The bandwidth retained depends upon the size of the exit slit. In order to construct a tunable grating filter, the diffraction grating is mounted on a mechanical structure that can be rotated externally. When the diffraction grating rotates, the diffraction pattern on the screen also shifts, resulting in different retained wavelengths exiting the exit slit.

2.5.2 Arrayed Waveguide Grating Filter

The grating filter described in the previous section uses a diffraction grating for achieving spatial dispersion of the input optical signal. In this section, we discuss the Arrayed Waveguide Grating (AWG) filter, which uses optical waveguides for achieving a spatial separation similar to the grating filter. AWG filters rely on the principle of optical interferometers [63]. The simplest interferometer is the MZI, which is composed of two optical couplers connected by two separate waveguides in order to filter a single wavelength, in a fashion that is reminiscent of the MZM of Figure 2.7. Similarly, the AWG is composed of two optical couplers that are connected by more than two waveguides in order to filter multiple wavelengths [63] using the principle shown in Figure 2.20 [64].

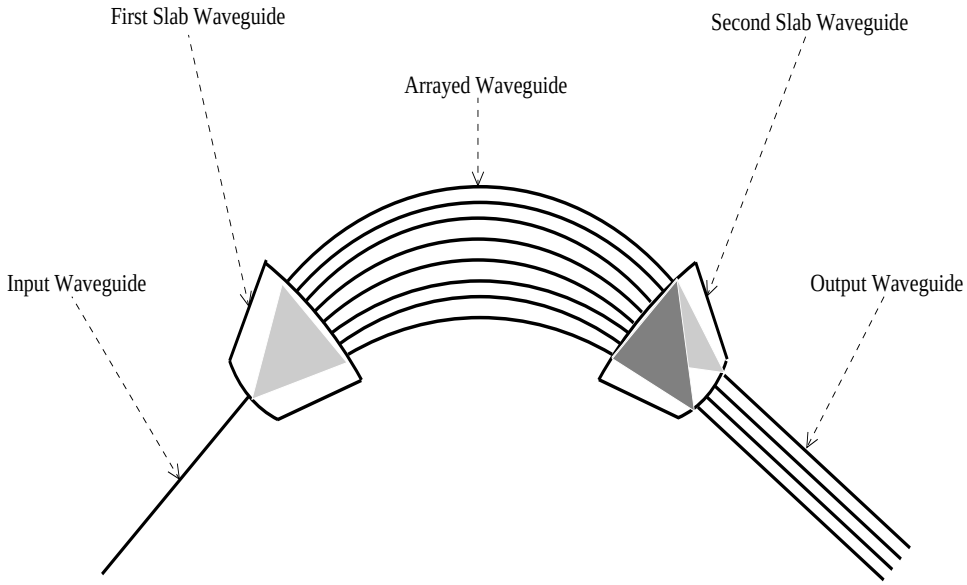

Figure 2.20: Structure of a typical AWG. The free space propagation region of Figure 2.19 is replaced with the combination of arrayed and slab waveguides.

Observe from Figure 2.20 that the AWG consists of input and output waveguides, two slab waveguides and a set of arrayed waveguides, which are made up of silica. When the optical signal passing through the input waveguide enters the first slab waveguide, it diverges in the free propagation region of the slab waveguide, as shown in Figure 2.20. The signal that spreads in the first slab waveguide is captured by the set of arrayed waveguides which function as dispersive elements and are arranged to have a constant length-difference between the adjacent waveguides. The length of each waveguide is chosen by ensuring that a particular wavelength undergoes the

same dispersion in each waveguide. Therefore, after travelling through the free propagation region of the second slab waveguide, all the optical signals having a particular wavelength contructively focus their output on a single output waveguide, as shown in Figure 2.20. The length-difference $\triangle L$ of the adjacent arrayed waveguides required for acheiving the contructive focussing of all the optical signals having a particular wavelength can be written as [65]:

$$\triangle L = m \cdot \frac{\lambda_c}{n_g}, \tag{2.17}$$

where m is the order and n_g is the effective refractive index of the arrayed waveguide. The central wavelength of the incident optical signal is represented by λ_c in Equation 2.18.

2.5.3 Fabry-Perot Filters

A Fabry-Perot (FP) filter exploits the interference of light in a resonating cavity. The resonating cavity of the FP filter consists of two highly reflective mirrors that are placed parallel to each other at a distance L, as shown in Figure 2.21 [59]. The input light enters into the cavity through the left mirror and after traveling a distance of L it falls on the reflective side of the right mirror. A part of the light exits through the right mirror, while a part of it is reflected back into the cavity. The percentage of light refracted or reflected depends upon the reflectivity of the mirrors. The resonating cavity structure of the FP filter can be used to filter out a particular wavelength by choosing the length of the cavity to be an integer multiple of half the wavelength, that is $L = m\lambda/2$, where m is an integer and λ is the wavelength to be retained [59]. Light having a particular wavelength λ interferes constructively after going through a round-trip inside the cavity and the resultant high intensity light exits through the right facet. The power transfer function P_{TF} of the filter in terms of wavelength is given by [59]:

$$P_{TF} = \frac{\left(1 - \frac{A}{1-R}\right)^2}{\left(1 + \left(\frac{2\sqrt{R}}{1-R} sin(2\pi nL/\lambda)\right)^2\right)}, \tag{2.18}$$

where A and R are the absorption loss and reflectivity of the each mirror's respectively and n is the refractive index of the cavity.

2.6 Passive Optical Components

Passive optical components play a vital role in an optical network. Some of the major tasks performed by passive components are coupling or splitting of signals, wavelength multiplexing/demultiplexing and isolation of backward reflections. In the following sections, we introduce the most commonly used passive optical components in communication systems.

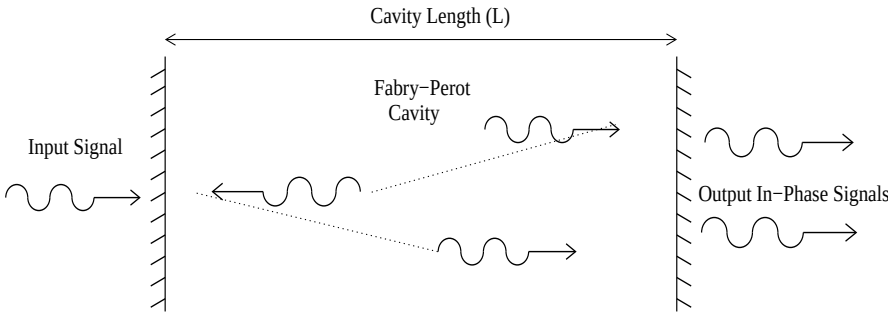

Figure 2.21: Operating principle of a FP filter.

2.6.1 Optical Couplers/Splitters and Multiplexers/Demultiplexers

Couplers are used for either combining or splitting optical signals, as seen for example in Figure 2.18. The most common type of couplers is the fused fiber coupler shown in Figure 2.22 [59] which is fabricated by simply fusing two optical fibers together. When two fibers are brought close to each other and aligned appropriately in parallel, light is coupled from one to the other, where the amount of coupling depends on how close the parallel fibers are to each other. A pair of the free ends is used as the input port, while the other free pair is used as the output port, as shown in Figure 2.22. The amount of light output from the two output ports may be controlled by adjusting the distance between the two fused fibers, as well as by varying the parallel coupling lengths of the fibers.

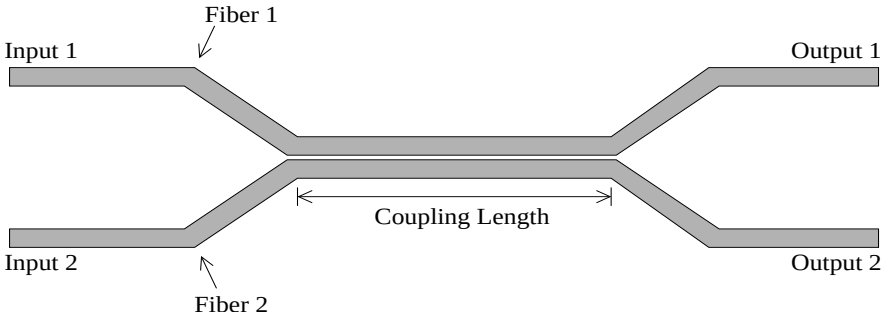

Figure 2.22: A fused fiber coupler.

The principle of a multiplexer is quite similar to that of a coupler. A multiplexer has multiple inputs and a single output. A demultiplexer uses a combination of optical splitters and filters. The splitter is used for dividing the input signal into multiple paths, while the filters separate particular frequencies. The AWG filter of Figure 2.20 can be used to multiplex or demultiplex optical signals. Furthermore, the FP filter of Figure 2.21 can be designed to have multiple passbands, periodically repeated at different frequencies. The design can be carried out by selecting suitable lengths and a refractive index for the cavity shown in Figure 2.21.

2.6.2 Optical Isolator and Circulator

The operating principle of optical isolators and circulators is similar. An isolator allows light to pass through it in one direction, while attenuates the light passing in the opposite direction. Isolators are mainly used at the input of optical amplifiers and lasers so as to protect them from any light reflecting backwards, as seen for example in Figure 2.18. In an optical network, light travelling in a particular direction can get reflected at the interface of different components in the link. These reflections are mainly due to a change of refractive index of the particular component.

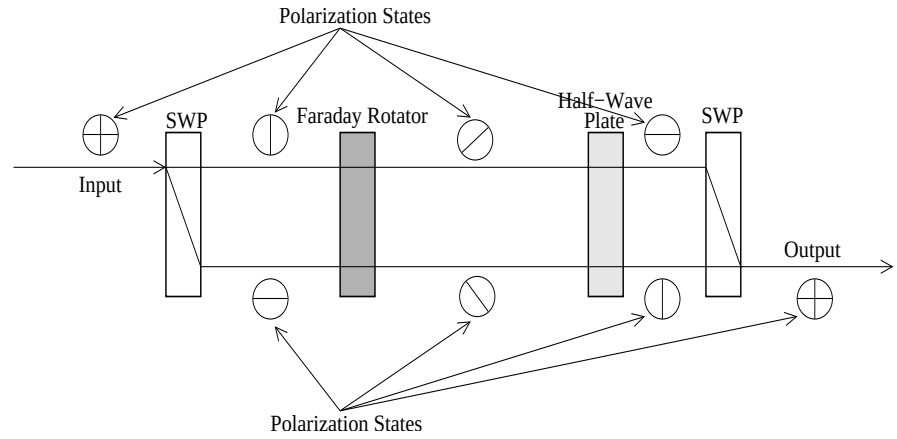

(a) Light propagating from left to right.

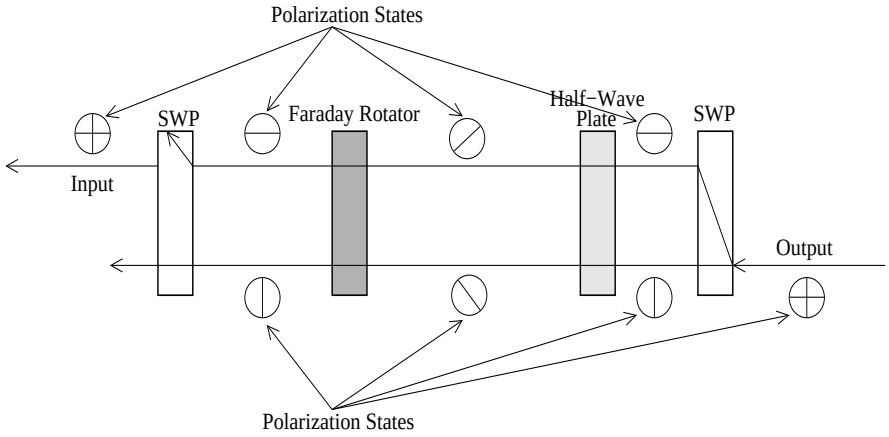

(b) Light propagating from right to left.

Figure 2.23: Operating principle of an isolator [59].

The operating principle of a polarization-independent isolator can be understood from Figure 2.23. The light signal which is composed of two orthogonal polarization states is passed through a spatial walk-off polarizer (SWP), which has different refractive indices for different polarizations. This variation in the refractive index results in spatial separation of the two orthogonally polarized lights, while travelling through the SWP. The polarization states of the light signal are shown by the circles in Figure 2.23. At the output of the SWP, two light signals having orthogonal polarization states are generated. These two signals are passed through a Faraday rotator [59], which rotates the polarization state of each by 45°, as shown in Figure 2.23a. The Faraday rotator is a non-reciprocal device, hence it always rotates the polarization state by 45°,

regardless which side the light enters into the rotator from. After the Faraday rotator, the light is passed through a half-wave plate, which is a reciprocal device, hence light entering from the left is rotated by 45° in the clockwise direction, while light entering from the right is rotated by 45° in the anti-clockwise direction. As observed from Figure 2.23a, the combination of the Faraday rotator and the half-wave plate changes the polarization axis by 90°. At the output, another SWP is used that operates in an inverse fashion w.r.t the SWP used at the input. Therefore, the two light signals with different polarization axes are combined to form a single signal. By contrast, for light entering in the opposite direction, that is from right to left, the combination of the half-wave plate and the Faraday rotator cancel the effect of each other. Therefore, the states of polarization remain unchanged, which results in scattering the two light signals at the output of the final SWP, as shown in Figure 2.23b.

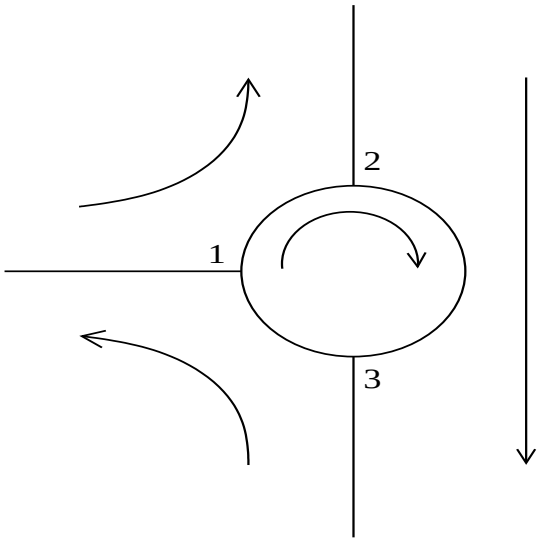

Figure 2.24: Operating principle of a circulator. The operating principle of the isolator of Figure 2.23 is used to achieve isolation among different ports.

The operating principle of a circulator is similar to that of the isolator seen in Figure 2.23. The only difference is in the number of ports, with the isolator being a two-port device, while the circulator can have 3 or 4 ports, depending upon its specific application. Figure 2.24 shows the operating principle of a three-port circulator. It can be observed from Figure 2.23 that light entering from port 1, 2 and 3 exits through port 2, 3 and 1, respectively.

2.7 Conclusions

We have discussed the different components used in optical fiber communications systems, like the one seen in Figure 2.1 which is composed of a transmitter, receiver, optical fiber, optical amplifiers and passive components, such as filters, couplers and isolators. The components used in baseband as well as analogue and digital optical systems are similar. The conclusions of the chapter are summarized as follows.

- Optical transmitters are composed of CW or pulsed laser sources which may be directly or externally modulated with the electronic data signal.
- The optical signal is transmitted over the optical fiber which is generally manufactured from silica. Like any other transmission channel, the optical fiber induces impairments over the signal due to its attenuation, dispersion and nonlinearity.
- The optical receiver is generally a photo-diode, which generates electronic carriers upon detecting light. These carriers constitute the output current of the optical receiver which is proportional to the amount of light received.
- In order to compensate for the attenuation of the optical fiber, optical amplifiers are used in the network at regular intervals. The most commonly used optical amplifier is the EDFA, as discussed is Section 2.4.
- The operating principle of the optical filters is generally based on the interference of light. The commonly used optical filters are Grating filters, Arrayed Waveguide filters and Fabry-Perot filters.
- Optical couplers and multiplexers or splitters and demultiplexers are required in order to combine or separate multiple optical signals, respectively. The flow of the optical signal is controlled using optical isolators and circulators.

Chapter 3

Radio Over Fiber Communication

This chapter provides an introduction to the three main types of ROF communication systems considered in the thesis, namely to AROF, BROF and DROF communication systems [37], [36] seen in the classification tree of Figure 3.1. This classification is based on the format of the RF signal transmitted over the fiber. The methods of transporting and multiplexing the RF signal in each type of communication system is described in detail. The chapter also discusses the main impairments imposed on the RF signal by each type of communication link. Different methods of reducing the effects of impairments on the ROF signals are discussed in this thesis. Finally, the suitability of each particular type of ROF links is evaluated in different scenarios.

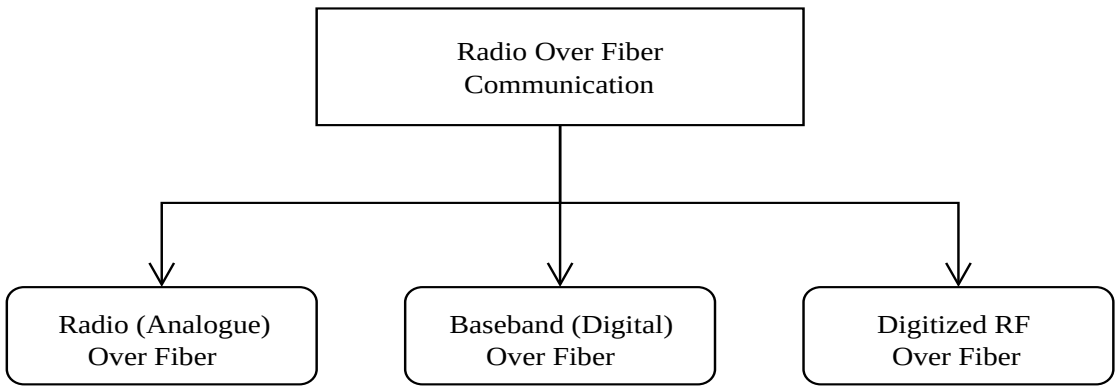

Figure 3.1: AROF, BROF and DROF communication systems.

3.1 Methods of Transporting RF Signals Over Fiber

Before we discuss each type of the ROF communication system in detail, the two main methods of transmitting and receiving RF signals over optical fiber are discussed in this section [66], whereas, the multiplexing techniques used in the ROF systems are discussed in Section 3.2.

3.1.1 Intensity Modulation Relying on Direct Detection

Intensity modulation combined with direct detection (IMDD) is the simplest of all the methods conceived for transporting RF signals over fiber [67], [10], where the intensity of the optical carrier is varied proportionately to the intensity of the RF signal transmitted. Intensity modulation can be implemented using either direct modulation or external modulation. Direct intensity modulation of an optical source involves the application of the RF signal to the drive voltage of a LD, as seen in Figure 3.2. The RF signal is superimposed on a DC bias signal so that the intensity of the optical output of the laser varies in a direct relationship with the variations of the RF signal. This method is the simplest and most cost-effective method, since it uses the minimal number of components. However, direct modulation of the optical lasers is not suitable for high-frequency RF communication systems, because we argued in Section 2.1.4 that for high-frequency ($\geq$ 10 GHz) communication the external modulation regime of Figure 2.7 is used.

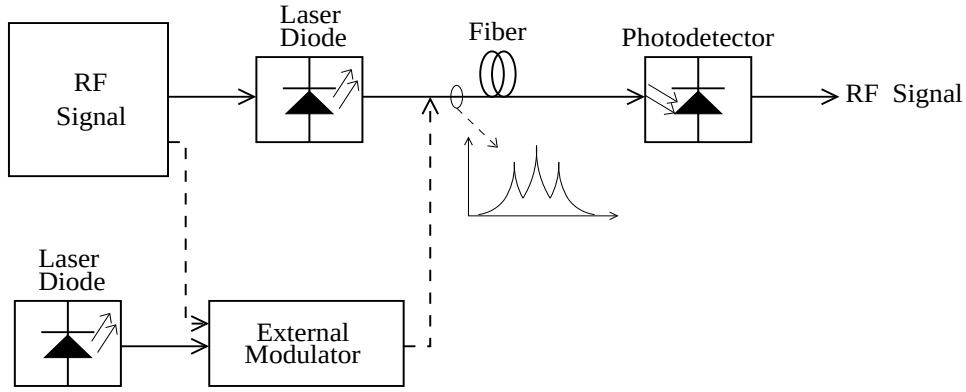

Figure 3.2: Operating principle of intensity modulation aided (upper branch) or external modulation based ROF transmitter (lower branch) and its PD-based direct detection. The external modulator may be for example the MZM of Figure 2.7.

In external modulation the modulator is used for modulating the intensity of an optical carrier. The external modulator generally used in optical communications is the MZM [55] of Figure 2.7, as described in Section 2.1.4.1. External modulation may provide further advantages compared to direct modulation. For example, the effect of fiber-dispersion imposed on externally modulated laser light may be reduced by using SSB modulation of the optical carrier [57]. One of the major disadvantages of external modulation is the cost of using the modulator to perform intensity modulation. The IMDD technique can be used for transmitting both single- and multi-level modulated RF signals, where the RF signal is simply retrieved by detecting the optical signal using a PD. The spectral plot of a DSB intensity modulated optical signal is shown by the stylized plot of Figure 3.2.

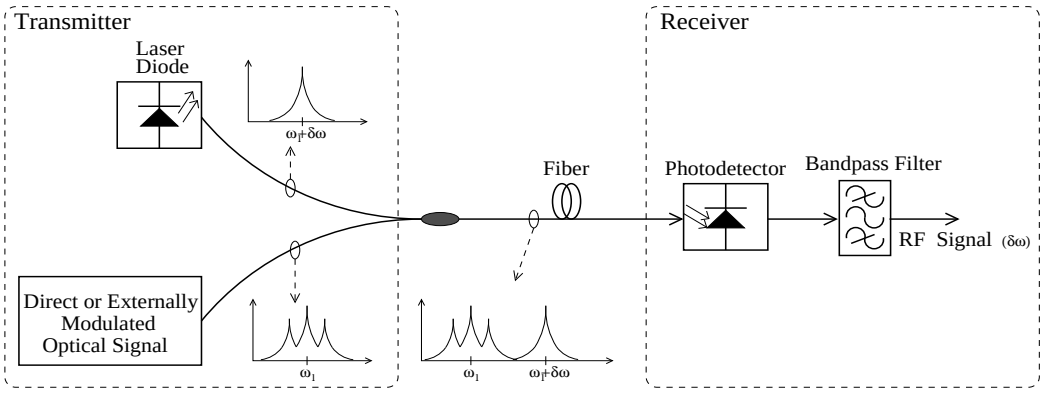

Figure 3.3: Remote heterodyne detection applied to direct or externally modulated received signals. This transmission scheme generates mm-wavelength RF signals at the output of the PD, as opposed to the transmission scheme of Figure 3.2.

3.1.2 Remote Heterodyne Detection Technique

The Remote Heterodyne (RHD) technique has been used for a long time in optical communications [66]. It relies on the coherent mixing of two optical carriers in a PD, which results in a high-frequency current at the output of the PD. Figure 3.3 shows the operating principle of the RHD technique with the help of stylized plots for the spectra of the two optical carriers. It can be observed from Figure 3.3 that the modulated optical signal at a frequency of ω_1 is mixed with the unmodulated optical carrier generated at a shifted wavelength of $(\omega_1 + \delta\omega)$. The unmodulated carrier is required to perform heterodyne detection at the photo-detector. The addition of the unmodulated carrier increases the power consumption and reduces the available optical bandwidth, but as a benefit, the use of high frequency local oscillators for up-converting RF signal to mm-wavelength at the receiver may be eliminated [66]. Furthermore, the up-converted RF signal is of good quality due to lesser noise [66]. The combined optical signal is passed through the fiber and detected by the PD, where coherent mixing of the two carriers generates the RF signal both at the difference and the sum of their frequencies as well as at multiple harmonics. An electronic bandpass filter is used to extract the RF signal at the desired frequency, as shown in Figure 3.3. More explicitly, the frequency of the data modulated output signal is given by the frequency difference of the two input optical carriers. For example, when the pair of optical fields $E_1 =\mid E_1 \mid \cdot cos(\omega_1 t)$ and $E_2 =\mid E_2 \mid \cdot cos(\omega_2 t)$ having frequencies of ω_1 and ω_2 impinge upon a PD, the resultant output current i_{PD} becomes proportional to the square of the sum of the two fields [68], which may be written as:

$$i_{PD} \propto [\mid E_1 \mid cos(\omega_1 t) + \mid E_2 \mid cos(\omega_2 t)]^2. \tag{3.1}$$

Taking the square of the terms in the bracket, we have:

$$i_{PD} \propto \mid E_1 \mid^2 cos^2(\omega_1 t) + \mid E_2 \mid^2 cos^2(\omega_2 t) + 2 \mid E_1 \mid\mid E_2 \mid \cdot cos(\omega_1 t) cos(\omega_2 t). \tag{3.2}$$

Using the trigonometric expansion, we arrive at:

$$\begin{aligned} i_{PD} &\propto \mid E_1 \mid^2 cos^2(\omega_1 t) + \mid E_2 \mid^2 cos^2(\omega_2 t) \\ &+ \mid E_1 \mid\mid E_2 \mid \cdot cos(\omega_1 + \omega_2)t + \mid E_1 \mid\mid E_2 \mid \cdot cos(\omega_1 - \omega_2)t. \end{aligned} \tag{3.3}$$

At the output of the PD, a bandpass filter is used for retaining the desired term containing $(w_1 - w_2) = \delta\omega$, as shown in Figure 3.3. The limit of the maximum frequency bandwidth is typically imposed by the PD's bandwidth. Some of the methods used for generating the optical frequencies of ω_1 and ω_2 for mixing in the PD are the following:

- The two different frequencies mentioned in the above example and required for heterodyning may be generated using a dual mode DFB laser similar to Figure 2.4 that has two different oscillation modes [69]. A disadvantage of this method is the requirement of a high-power electronic drive signal to achieve phase-locking between the two laser modes. Furthermore, the mm-wavelength signal generated is very sensitive to variations in the power of the electronic drive signal [69].

- Splitting a single-frequency laser output into two paths and shifting the frequency of one of the laser paths [70]. This method requires a complex splitter and frequency-shifter, hence it is unsuitable for low-cost ROF links.

- SSB modulation of an optical signal as discussed in Section 2.1.4.2 [71]. The technique described in [71] requires a fairly complex integrated modulator for generating the SSB signal.

- Carrier suppression applied to an optical signal generated by Double Side-Band (DSB) modulation [72]. The main advantage of this technique is its low-complexity implementation along relying on a single laser source.

The technique of carrier-suppression combined with the generation of higher-order sidebands (DSB-SC) has been widely researched as a benefit of its simplicity and good performance [73], [74], [75]. This method is hence also often referred to as the Optical Carrier Suppression (OCS) technique, which will be discussed in detail in Chapter 5. During the decade spanning from 2000 to 2010 there has been renewed interest in 60 GHz communications, since it is eminently applicable to high-rate, short-range indoor communications in the unlicensed band. There are many advantages of using the RHD technique for the generation of mm-wavelength frequencies in the vicinity of 60 GHz, for example. RHD method is capable of generating a wide range of frequencies at the output of the PD. Since two optical signals are involved in generating the required mm-wavelength carriers, therefore the resultant RF signal may have a high CNR, provided that the optical carriers used have a high OSNR. Furthermore, since the RF data signal may be transmitted at a low frequency, such as $\leq 1\, GHz$, the chromatic dispersion has a negligible effect on the data [57]. One of the major disadvantages of this technique however is its sensitivity to the LD's phase noise and frequency drift [75]. Even high-quality lasers may have some phase noise and frequency drift due to

temperature changes and spontaneous emissions, which is directly imposed on the mm-wavelength carriers generated.

3.2 Multiplexing Techniques in ROF Systems

In order to transmit multiple channels over fiber typically, two different multiplexing techniques are used, which are discussed below.

3.2.1 Sub-Carrier Multiplexing

The Sub-Carrier Multiplexing (SCM) technique [29], [76] multiplexes the RF channels in the electronic domain. The signals of multiple channels having different center frequencies are simply superimposed electronically and the resultant electronic signal is used for intensity modulating an optical carrier. Figure 3.4 shows the operating principle of the SCM technique, where three RF signals are superimposed and the resultant composite signal is used for intensity modulating the LD. The spectrum of the output optical signal is shown by the stylized plot of Figure 3.4, where it can be observed that the optical carrier is accompanied by three sidebands representing the three RF modulating signals. The SCM channels can have different types of signal modulations and the optical carrier can be modulated either using the direct modulation or the external modulation schemes [29] of Figure 3.2 discussed in Section 3.1.1. SCM has the advantage that it requires only a single optical source. A major disadvantage of SCM however, which will be discussed in Section 3.3.1, is its sensitivity to nonlinear effects imposed by the ROF system.

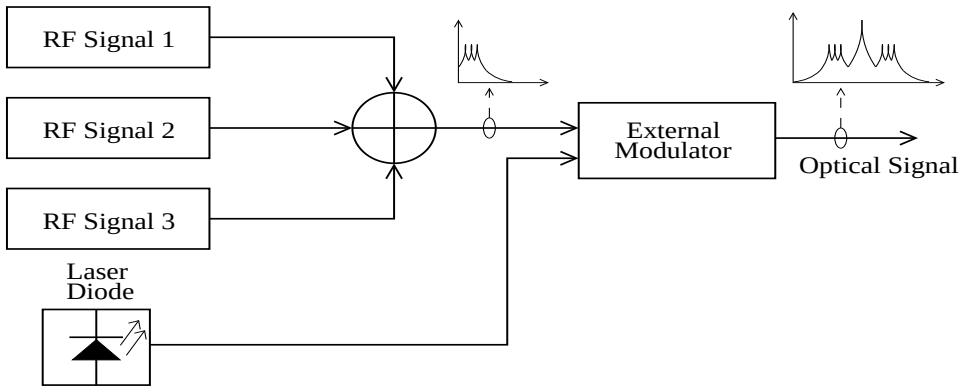

Figure 3.4: Operating principle of the SCM technique.

3.2.2 Wavelength Division Multiplexing

As an alternative to the SCM of Section 3.2.1, ROF communication may also use the WDM technique for better exploiting the large bandwidth of optical fibers [77], [78], [79]. Multiple channels

are transmitted upon modulating different optical carriers by the RF channels and then multiplexing them optically, as shown in Figure 3.5. Figure 3.5 also shows the stylized plots of the spectra at different stages of the WDM signal generation. Since a single RF channel is transported over a single optical carrier, the effect of laser nonlinearity imposed on the RF channels remains moderate. One of the major disadvantages of the WDM technique is the cost involved in using different laser sources for each RF channel. Furthermore, while travelling across the fiber, the optical signal at a certain wavelength is affected by the adjacent channels. The intensity modulated signal of adjacent channels may impose phase variations on the optical signal through XPM, as discussed in Section 2.2.3, which in turn distorts the RF signal transported by the optical carrier [18], [80]. In order to exploit the advantages of both the SCM discussed in Section 3.2.1 and of WDM, studies have been performed that rely on a combination of these two techniques [76], [25]. In Chapter 5 of the thesis, we will conceive a novel technique that relies on a single-laser source, rather than on multiple sources for generating multiple sidebands, each of which is intensity modulated and multiplexed before being transmitted to the BSs.

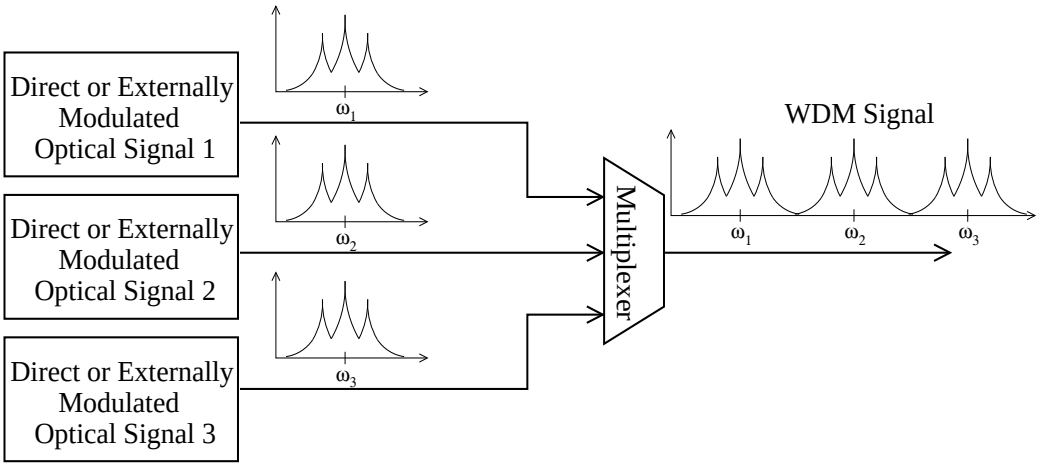

Figure 3.5: Operating principle of the WDM technique. The modulation techniques were portrayed in Figure 3.2, where the external modulator may be the MZM of Figure 2.7

3.3 Analogue ROF System Architecture

In AROF communication systems, the RF carrier modulated by the baseband data is transmitted over the fiber using an optical carrier, where frequency up-conversion and carrier modulation are peformed at the CU. The RF signal simply modulates an optical carrier with the aid of an EO up-converter at the transmitter, while at the reciever the RF signal is recovered using an OE down-converter. This configuration makes the RF signal transmission simple by performing most of the signal processing tasks at the CU.

Figure 3.6 shows the typical architecture of a duplex AROF communication link. An electronic RF carrier that is modulated by the baseband data further modulates an optical carrier in the EO

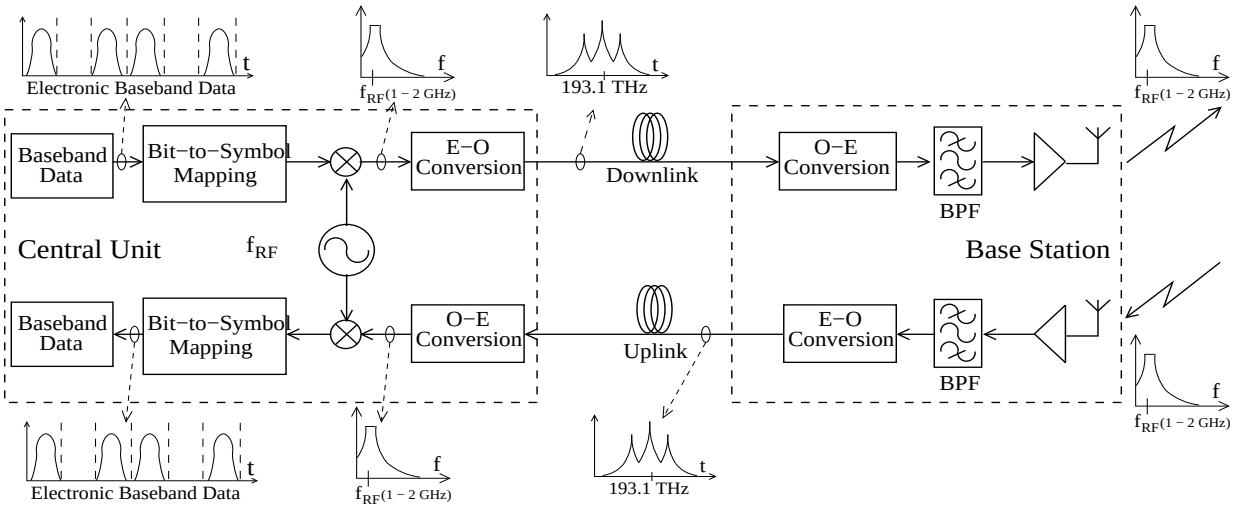

Figure 3.6: System architecture of an AROF communication system.

block. The EO conversion can be achieved either by direct modulation according to Figure 3.2 or by externally modulating a LD using a MZM modulator of Figure 2.7. The type of optical modulation used depends upon the frequency of the RF signal to be transmitted. For low-frequency RF signals (less than 10 GHz carrier) typically the direct modulation of Figure 3.2 is used, while for high-frequency ($\geq 10GHz$ carrier) RF signals the MZM external modulator of Figure 2.7 may be used. The modulated optical carrier whose stylized spectrum is shown in Figure 3.6, is then passed to the BS through an optical fiber. For long-distance communication systems typically the SMF described in Section 2.2 is used. The optical signal received at the BS is converted back to an electronic signal in the OE block of Figure 3.6. The OE block consists of a PD that converts light into an electronic signal. The output of the OE block is an RF signal, which is bandpass filtered to remove the harmonic frequencies generated due to the nonlinear nature of the process of photodetection. The resultant RF signal is amplified and transmitted through the antenna to the MSs, as shown in Figure 3.6. The same antenna can be used for receiving the incoming signals of the BS by using the duplexer, which separates the incoming RF signal from the outgoing signal. The RF signal received at the BS is amplified and converted to an optical signal in the EO block. The optical signal, which is shown by the stylized spectrum seen in Figure 3.6, is transmitted to the CU using either the same or a different optical fiber. At the CU, OE conversion is used for retrieving the RF signal originally transmitted from the BS. For long-distance ROF transmission, the EDFA's of Section 2.4 may be used for amplifying the optical signal. Since optical fibers have a low attenuation (0.2 dB/km), ROF transmission over short distances, for example within buildings, does not require optical amplifiers.

3.3.1 Impairments in Analogue ROF Systems

Naturally, the devices used in ROF systems impose impairments on the optical signal, which in turn distorts the RF signal received at the receiver. The major source of impairments is the nonlinearity of optical devices such as lasers, modulators and PDs [24]. These impairments are discussed

separately in the following sections.

3.3.1.1 Modulator-Induced Impairments

SCM ROF systems typically use the external modulation scheme of Figure 3.2, as a benefit of the reduced noise and chirp of the laser diode as well as the high bandwidth provided, as discussed in Section 3.1.1. When multiple RF signals are applied to an external modulator, as in the case of SCM, spurious out-of-band spectral components are generated due to the modulator's non-linearity. These spectral components give rise to Inter-Modulation Distortion (IMD) components at the receiver. These IMD components severely degrade the performance of the system, because their power may even become higher than the system's noise power [81]. Figure 3.7 shows the stylized spectrum of an Optical Double Side-Band (ODSB) signal, which may be generated by intensity modulating an optical signal with the aid of two SCM RF signals having frequencies of f_1 and f_2. It can be observed from Figure 3.7 that apart from the original spectral components of f_1 and f_2, numerous spurious components also appear in the spectrum. It may be observed from Figure 3.7 that some of the IMD components are located at a considerable distance from the signal components on the frequency grid, hence the corresponding IMD products may be readily filtered out. By contrast, some of the IMD products such as $(2f_1 - f_2)$ and $(2f_2 - f_1)$ are located close to the desired signal frequencies of f_1 and f_2, hence they cannot be readily filtered out. Therefore, it is these IMD products that substantially reduce the Carrier-to-Interference Ratio (CIR) [82]. In Section 3.3.3, we will discuss some of the methods capable of reducing the effects of IMD on the CIR.

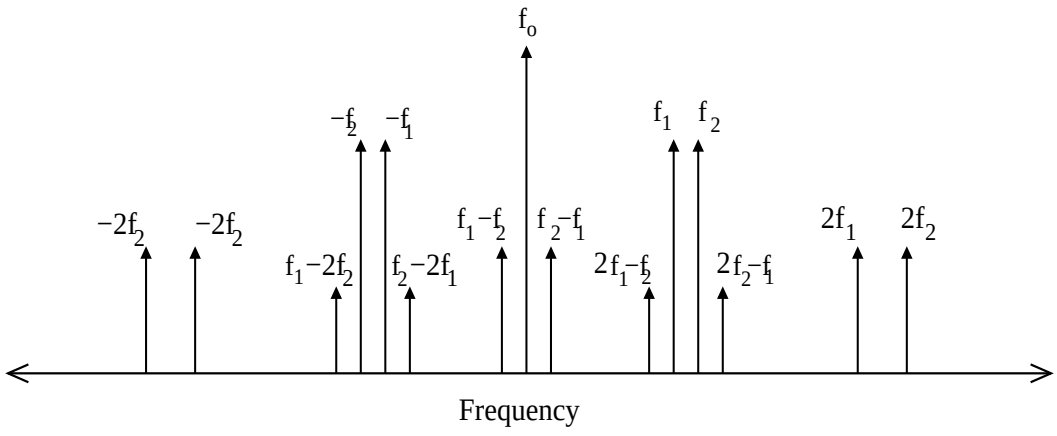

Figure 3.7: Spectrum of an example optical DSB signal.

The external modulators of Section 2.1.4 also impose some residual chirp on the modulated signal. As discussed in Section 2.1.4.1, chirp is the linear variation in the instantaneous frequency of the optical pulse with time [56]. This chirp becomes a source of distortion, when the signal travels through the optical fiber, because the phase modulation is converted to amplitude variation by the linear dispersion of the fiber, as mentioned in [83], [84]. Furthermore, the modulation efficiency of the two branches of the MZM of Figure 2.7 may be different, which results in some

residual phase modulation or deleterious intensity modulation of the optical output signal [85], where the modulation efficiency is defined as the ratio of modulated light to the total light [55]. The residual phase modulation is converted into intensity modulation by the effects of fiber dispersion, as discussed in [53]. Additionally, the DC bias voltage of the lithium niobate crystal used in each branch of the MZM of Figure 2.7 may drift slightly due to temperature variations, which results in intensity variations in the modulated output signal [85].

3.3.1.2 Laser Noise

There are two main types of noise in lasers, namely the phase noise and the RIN [86], as discussed in Section 2.1.1. Both of the noise sources are due to the spontaneous emissions of photons in lasers. Recall from Section 2.1.1 that apart from the stimulated emission, the lasers also produce spontaneous emissions in the cavity, which results in the generation of photons having a random phase, polarization and direction. Again the random generation of photons is responsible for intensity variations known as RIN, while the random phase of the photons results in phase fluctuations known as phase noise [86], as discussed in Section 2.1.1. Directly modulating a laser may also cause distortion of the RF signals, if the drive current values involved in the schematic of Figure 3.2 become high, for example in the case of the high Peak-to-Average-Power Ratios (PAPR) of OFDM signals [13]. These distortions are due to the nonlinear relation of the laser's output power versus the drive current, which becomes nonlinear for high input drive currents, as seen in Figure 2.5.

3.3.1.3 Fiber-Induced Impairments

The interplay between the fiber-induced linear dispersion and the chirp imposed by both the modulators as well as the lasers results in intermodulation distortions owing to the mixing of various sidebands of the modulated optical carrier [83]. The generation of intermodulation distortions is more pronounced in SCM signals due to the presence of multiple RF carriers in the modulating signal [84], [24]. The linear dispersion of the optical fiber also results in variable power attenuation at the output of the PD for intensity modulated optical signals [60], [57], [87]. Recall from Figure 3.2, that an optical signal, whose intensity is modulated by a RF signal has two sidebands, one on each side of the optical carrier frequency. When the intensity-modulated signal travels through the fiber, the linear dispersion of the fiber changes the phases of these two sidebands. Since the two sidebands are at different frequencies, they undergo different phase changes. At the PD, the heterodyne detection process of Figure 3.3 in Section 3.1.2 takes place and depending upon the specific phase shifts of the two sidebands, the output signal of the PD may be attenuated in power. This effect is generally referred to as power attenuation [57]. The power attenuation effect imposed by dispersion is more pronounced in case of high frequencies, since the sidebands are located far apart and hence the phase shift imposed on each of them may be quite different.

3.3.1.4 Nonlinear Photo-detection

At high received optical powers, the PD becomes saturated due to the emission of a large number of photons [67], as described in Section 2.3. This results in clipping of the output current and therefore, the RF signal becomes distorted. Furthermore, the optical signal received by the PD may have multiple optical sidebands, which results in the generation of harmonics at the output of the PD due to the process of heterodyning [66]. These harmonics interfere with the desired RF signal and hence they impose impairments. The PD also generates thermal noise due to the internal resistance of the PD and shot noise owing to the statistical nature of the process of photodetection [59].

3.3.1.5 Optical Amplification and Filtering

As mentioned in Section 2.4, EDFAs are the most commonly used optical amplifiers in fiber optic communication systems. EDFAs generate ASE noise, which reduces the signal to noise ratio of optical signals. The photons in an EDFA are generated by the process of both stimulated as well as spontaneous emissions, as described in Section 2.4. The photons generated through stimulated emission are the ones that contribute towards the amplification of the input optical signal. By contrast, the photons generated through spontaneous emission exhibit a random phase, polarization and direction of motion, hence they contribute towards the ASE noise described in Section 2.4. As the terminology suggests, these randomly generated photons are amplified further, while travelling through the Erbium doped fiber. A ROF signal has sidebands at multiples of the modulating electronic signal frequency. Any change imposed on the sidebands will cause distortion in the RF signal at the receiver. For example, an optical filter used in a fiber optic communication network for adding or dropping wavelengths will attenuate the harmonics present in the optical spectrum. Due to this attenuation of harmonics, the characteristics of the RF signal retrieved at the PD will be different from those of the transmitted RF signal.

3.3.2 Analogue ROF Link Analysis

In this section we will discuss the overall performance erosion imposed on the ROF link by the different sources of impairments mentioned in Section 3.3.1. The impairments inflicted upon the ROF link affect both the DL and UL transmission of the RF signals. In the DL direction, the impairments contribute to the wideband noise and hence impose increased interference between the mobiles. By contrast, in the UL direction, the impairments degrade the sensitivity of the CU receiver. A general criterion for the evaluation of an ROF link is its so-called Spur-Free Dynamic Range (SFDR) [88] which takes into account both the noise and the distortion of the link. The SFDR can be interpreted with the aid of Figure 3.8, where the RF input power to the link is plotted against its output RF power [88]. Figure 3.8 also shows the power variation of IMD products with respect to the input signal power. It can be observed from Figure 3.8 that for a certain range of input RF power, the output RF power varies linearly, while beyond this range this range, the output power starts saturating. The extent of saturation is defined by using a parameter referred to as the 1

dB compression point, which represents the input power that causes a drop of 1 dB in comparison to the linear gain of the link. The horizontal line seen in Figure 3.8 shows the output noise level of the link. The specific input power for which the output signal power crosses this horizontal line is termed as the Minimum Discernable Signal (MDS) power [88]. From Figure 3.8, SFDR is defined as the power difference between the MDS and the point, where the distortion power equals the noise power of the link. Therefore, SFDR is a measure of linearity for the link and should be as high as possible for the high-integrity operation of the ROF system. Figure 3.8 also shows a point, where the projected linear plots of the output signal power and the distortion power intersect each other. At this point, the output signal power is equal to the distortion power and is generally referred to as the Third Order Intercept, denoted as IP3.

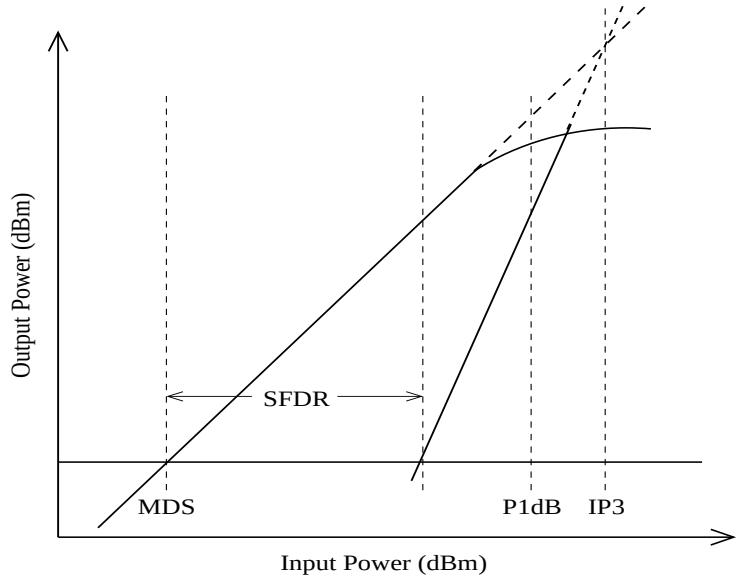

Figure 3.8: Input versus output RF power of an AROF link.

In order to evaluate the performance of a ROF link, two further parameters are generally considered, namely the link-gain and the Noise Figure (NF). The link-gain is defined as the product of the square of slope efficiency of the modulation device and the square of the responsivity of the detection device [89]. The slope efficiency S_{mzm} of a MZM used as an external modulator may be written as [89]:

$$S_{mzm} = \frac{\pi P_{in} T_{ff} R_s}{2V_\pi}, \tag{3.4}$$

where P_{in} is the input optical power to the MZM, T_{ff} is the fiber-to-fiber transmission of the modulator, R_s is the source impedence and V_π is the On-Off switching voltage of the MZM. It can be observed from Equation 3.5 that in order to increase the gain of a ROF link, the input power of the link should be increased. Furthermore, the MZM should be designed to have a low value of V_π. The NF is defined as the difference in output and input noise power of the link, where the output and input noise powers have units of dB. A link's input noise power is due to the thermal noise generated at T_o = 290 K, while the output noise power is due to the amplification of this input thermal noise. Hence NF can be mathematically written as [89]:

$$NF = 10 \cdot log \left[\frac{N_{out}}{kT_o B_{link} \cdot G_i} \right], \tag{3.5}$$

where N_{out} is the output noise power, B_{link} is the link bandwidth, G_i is the link gain and k is the Boltzmann's constant. It can be observed from Equation 3.5 that in order to have a low NF, the noise added by different components in the ROF link should be kept low.

3.3.3 Optical Linearization Techniques for Analogue ROF

As discussed in Section 3.3.1, the IMD components generated by the external modulator such as the MZM of Figure 2.7 in Section 2.1.4 constitute a major source of distortion in ROF communication systems. Optical linearization techniques have been proposed in order to reduce the effect of nonlinearities in the ROF link. This section summarizes some of the most wide-spread linearization techniques that have been proposed in the literature.

The second order IMD components may be eliminated by biasing a symmetric MZM at 50 $\%$ of its maximum dynamic range [90]. At this bias voltage, the even-order IMD products are almost cancelled, while the odd-order IMD products are minimized, as argued in [90]. As mentioned in Section 2.1.4, the optical signals passing through the two arms of the MZM are phase modulated by electro-optic effect. For a DC bias at 50 $\%$ of the maximum dynamic range, the phase shift in each of the arms for even-order components are opposite. Since the output of the MZM is the sum of the optical signals in the two arms, the even-order sidebands are suppressed for a symmetric MZM. The DC bias point of the MZM may of course change with temperature, hence in order to minimize the second order terms, the bias point should be kept constant. Therefore, in order to control the bias voltage of the MZM, the authors of [90] proposed a dual-output MZM, where the two output optical signals have a complementary phase change imposed on them by the modulator. One of the outputs of the MZM is used as the ROF signal, while the second output is used in a feedback loop in order to control the DC bias point of the MZM.

In [82], a linearization technique conceived for Optical Single Sideband plus Carrier (OSSB+C) modulated signals is proposed. The OSSB+C modulated signals are particularly suitable for transmission over dipsersive fibers, since they do not give rise to power attenuation of the PD's output due to fiber dispersion [57], as discussed in Section 3.3.1.3. The technique proposed in [82] uses optical filtering for removing the optical components that contribute most substantially to the IMD products, such as for example the frequencies $(2f_1 - f_2)$ and $(2f_2 - f_1)$, as mentioned in Section 3.3.1.1. Since the rest of the IMD products generally appear at frequencies far away from the desired signal's frequency band, the IMD products $(2f_1 - f_2)$ and $(2f_2 - f_1)$ shown in Figure 3.7 constitute the major source of distortion in the ROF link. In [82], the optical carrier was divided into two branches, one of which is modulated, while the other one is attenuated to achieve a suitable power in order to reduce nonlinear effects in the fiber. Since the IMD products $(2f_1 - f_2)$ and $(2f_2 - f_1)$ are located relatively near the modulated optical carrier, as seen in Figure 3.7, the

modulated signal sidebands are retained by an optical filter, while these IMD products are attenuated along with the carrier. The filtered output is then coupled with the unmodulated carrier for the sake of generating the resultant OSSB+C signal. Using this technique, an overall improvement of 9 dB is achieved in the Carrier-to-IMD power ratio of the signal [82].

A similar technique is proposed in [91], where two MZMs are connected in parallel as described in Section 2.1.4.1. One of the MZMs is used for generating an optical suppressed-carrier signal, where the optical carrier and the even-indexed sidebands are suppressed. Hence the IMD products $(2f_1 - f_2)$ and $(2f_2 - f_1)$, which are in the vicinity of the optical carrier may be eliminated. The second modulator is used for attenuating the carrier to a suitable level, which is then later coupled to the optical suppressed-carrier signal. It has been shown in [91] that the above technique gives a 10 dB improvement in the CIR of the ROF signal.

3.4 Digitized ROF

DROF involves the digitization of the analogue RF signal before tramsission over the fiber. The analogue RF signal is converted to a series of binary electronic pulses in an Analogue-to-Digital Converter (ADC) and after EO conversion, the resultant optical signal is transmitted over the fiber [37], [92], [93]. The architecture of a typical DROF system is shown in Figure 3.9. Again, the analogue RF baseband data is first converted to another multi-level analogue signal having a relatively low carrier frequency, such as 0.5 to 0.8 GHz in the multi-level modulation block, which is then frequency translated to a higher frequency (f_{RF} = 1-2 GHz). The resultant high frequency analogue signal is digitized in the ADC block and after EO conversion, the signal is transmitted over the fiber. The spectrum of the optical signal at the output of the EO conversion block is shown by the stylized plot of Figure 3.9, which is composed of discrete frequency components that are located at a frequency spacing equal to the data rate of the digitized signal.

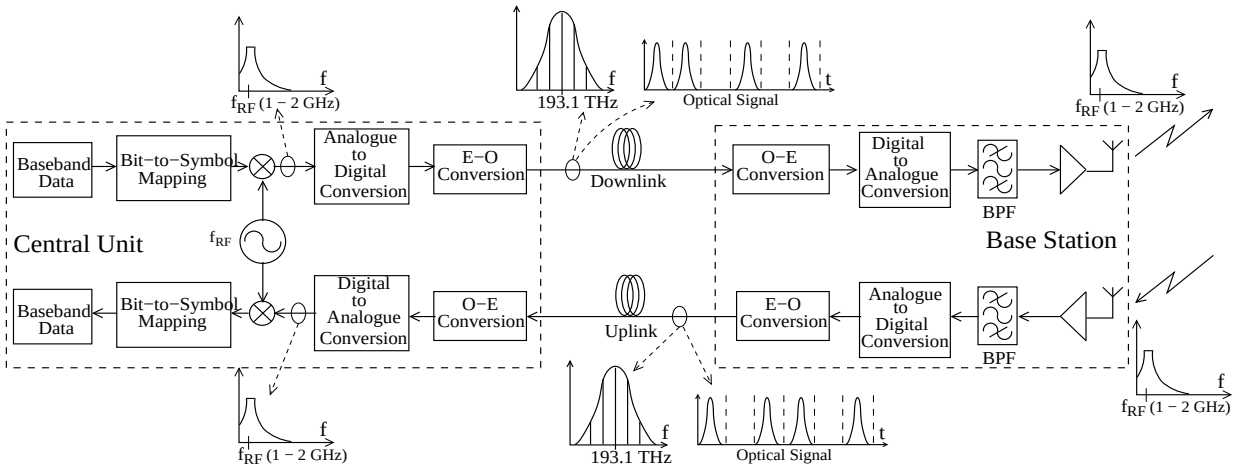

Figure 3.9: DROF system. The main difference with respect to the AROF system of Figure 3.6 is the inclusion of the ADC/DAC pair.

At the receiver, the optical pulses are converted to electronic pulses in the OE block and digital-to-analogue conversion (DAC) is performed to retreive the high frequency analogue signal. The bandpass sampling technique, which will be discussed is Section 6.3 is a widely used solution conceived for generating the discrete-time samples, before performing ADC and DAC [92], [94], [95]. The resultant RF signal is bandpass filtered, amplified and transmitted by the antenna. The same process is repeated for the uplink transmission of the RF signal, as shown in Figure 3.9.

The DROF signal can be transported by a CW or by a pulsed carrier, relying on baseband optical communication, which is discussed in Section 3.5. In comparison to the AROF scheme of Figure 3.6, the DROF scheme limits the length of the ROF link to a lesser extent due to the reduction of its dynamic range [93], as long as the received optical signal's power remains within the sensitivity limits of the optical receiver. Therefore, the major source of impairment in the DROF link is the ADC/DAC quantization and jitter noise [37].

3.5 Baseband ROF

In BROF communication, the baseband data is directly transmitted over the fiber without up-conversion to a RF carrier [36]. At the transmitter, the baseband electronic signal is converted to optical signal using the EO converter of Figure 3.10. The spectrum of the signal at the output of the EO converter is shown by the stylized plot of Figure 3.10. It can be observed from the stylized plot that the spectrum of the BROF signal is composed of discrete frequency components, similar to the DROF spectrum. The discrete frequencies are located at a frequency spacing equal to the data rate of the BROF signal. After transmission through the fiber, the optical signal is photo-detected to retrive the baseband electronic data, as shown in Figure 3.10. After OE conversion, the detected baseband data is processed and frequency translated to a high frequency RF carrier. Similarly, the RF signal received through the antenna is downconverted to the baseband and after EO conversion, it is transmitted over the fiber back to the BS.

BROF has many advantages that make it a feasible choice for the transmission of RF signals. Optical baseband signals are fairly immune to optical noise due to their digital nature and hence this enables the signal to be transmitted over longer distances. Cost effective Off-the-shelf optical components are used in the BROF communication links. Baseband optical communication also provides the option of all-optical signal processing that includes signal regeneration at regular distances [96], [97], [98], [99], multiplexing of signals [100], [101] and various logical operations, such as AND, OR and XOR [102], [103], [104].

In the forthcoming sections, the pulse propagation model used in optical pulsed communication is described in detail.

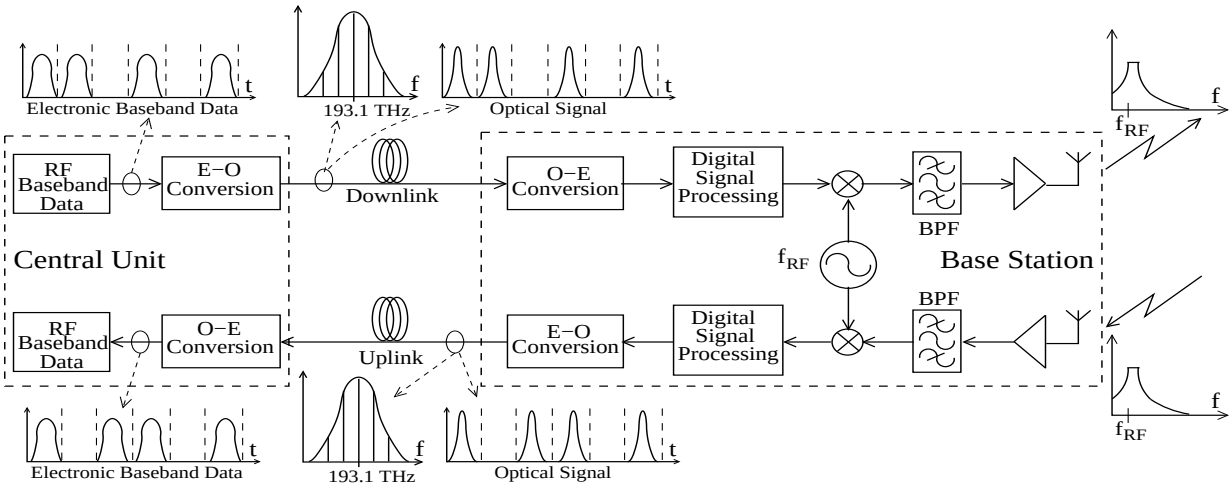

Figure 3.10: BROF system. The main difference with respect to the AROF scheme of Figure 3.6 and the DROF arrangement of Figure 3.9 is the absence of the RF up-converter and that of the ADC/DAC schemes, respectively.

3.6 Impairments in Pulsed Optical Communication

Pulsed optical communication is referred to the systems that use optical pulses for transmitting data. As mentioned in Section 2.2, the optical fiber imposes *attenuation, dispersion and nonlinear distortions*, as the signal travels through it. In order to elaborate on all these effects, the temporal and spectral evolution of a single optical pulse along the fiber are shown in Figure 3.11a and 3.11b, respectively. The results shown in Figure 3.11 are obtained by using the Split-Step Fourier Method (SSFM) [56] detailed in the Appendix. The optical pulse considered has a Gaussian-shaped time-domain profile with a pulse width of 20 ps, center wavelength/frequency of 1550 nm/193.54 THz and peak power of 100 mW. A 32 km long single mode fiber is used having a dispersion parameter of D = 17 $ps \cdot nm^{-1} \cdot km^{-1}$ and nonlinearity parameter of γ = 1 $W^{-1} \cdot km^{-1}$. Recall briefly that the attenuation of the optical fiber causes a reduction in the power of the optical signal travelling through it and this attenuation can be simply compensated by optical amplifiers, such as the EDFAs [26] discussed in Section 2.4. The effect of attenuation may be observed in Figure 3.11, where the peak power of the optical pulse reduces, while travelling through the fiber.

The second main type of impairment imposed by the optical fiber is *dispersion*, which is due to the refractive index variation of the fiber versus the frequency [56]. This frequency-dependent refractive index forces the frequency components of the optical signal to travel at different speeds through the fiber, which results in a frequency-dependent group-delay. Due to this propagation speed difference, the optical pulse broadens in the time domain, as routinely encountered due to the linear dispersion and observed from the temporal plot shown in Figure 3.11a. The pulse broadening becomes a severe problem in case of high bit-rate communication systems, where the adjacent pulses might become smeared into each other [44].

The third main type of impairment imposed by the optical fiber is due to the *nonlinear reponse*

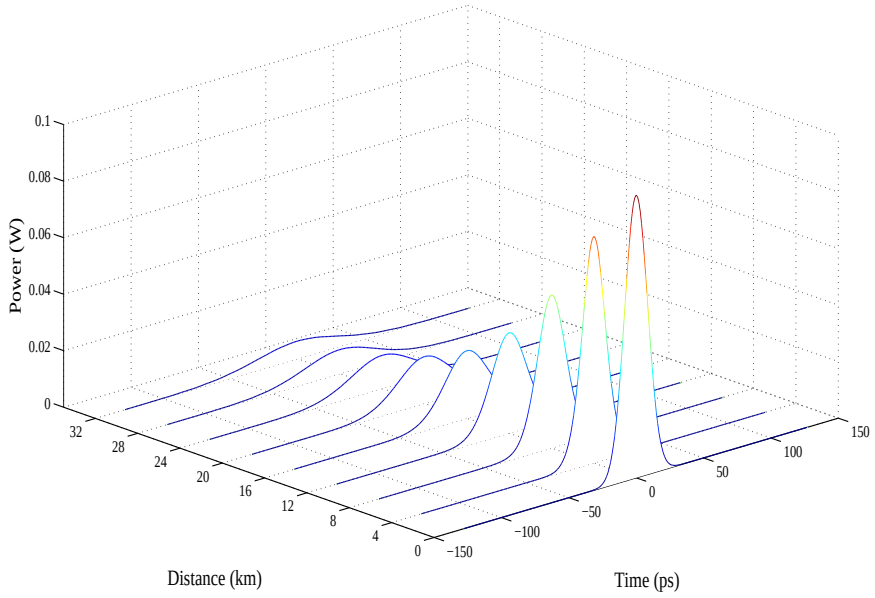

(a) Temporal plot

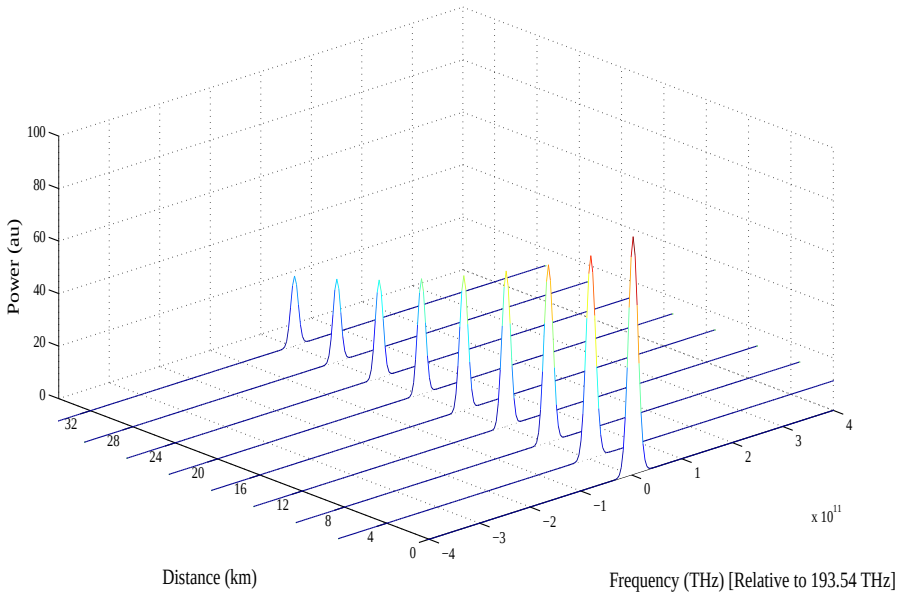

(b) Spectral plot

Figure 3.11: Evolution of an optical pulse in an optical fiber.

of silicon fiber to high-power optical signals [56], as described in Section 2.2.3. When a high-power optical pulse travels through the optical fiber, its spectrum is broadened due to the mixing of adjacent frequency components of the pulse. Naturally, the frequency components that synthesize the finite-bandwidth optical pulse have commensurately higher powers in case of a high-power optical signal. Therefore, the adjacent high-power frequency components result in the proliferation of out-of-band frequencies, owing to their inter-modulation products, while the signal is travelling through the fiber [56]. The nonlinearity of the fiber is generally a problem in case of high-power signal transmission, but naturally, may be avoided by using low-power signals. Indeed, it may be observed from the spectrum shown in Figure 3.11b that the effect of nonlinearity is not overwhelming for systems using SMFs. However, in scenarios, where the optical signal is transmitted over long stretches of fiber, both the linear and nonlinear distortion affects the signal to such an extent that it may not be recoverable at the receiver. Hence long-haul links require the employment of regenerators at regular intervals in order to compensate for the deleterious effects of the fiber. Therefore in Section 3.6.1, we discuss the operating principles optical signal regeneration.

3.6.1 Optical Pulsed Signal Regeneration

Optical signal regeneration is essential for baseband optical communications, since long distances up to hundreds of kilometers are involved in the transmission of baseband optical signals [96]. As the signal propagates through a network, it suffers from different types of impairments. There are two main reasons for these impairments, firstly the physical characteristics of the fiber, which includes attenuation, chromatic dispersion and non-linearity, while the second is the components used in the transmission network, such as for example add-drop filters, multiplexers and amplifiers. The goal of a regenerator is to restore the original signal generated at the transmitter and then to re-transmit it to the receiver. At the time of writing, typically electronic regeneration techniques are used, which require OE and EO conversion [96]. However, in order to achieve high bit rates, this method of regeneration is not suitable due to the electronic bandwidth limitations of the devices used. For this reason all-optical techniques are being investigated, which use the ultra-fast optical devices for regenerating the signal.

There are three main functions of a regenerator, which are as follows [96]:

- Re-amplification: Re-amplification is required in order to compensate for the attenuation of the fiber over the length of the transmission line.
- Re-shaping: Re-shaping is required to refresh the signal by restoring its original shape, which is distorted due to the impairments inflicted by the optical link.
- Re-timing: Re-timing is required for reducing the timing jitter.

The above-mentioned regenerator schemes are referred to as 1R, 2R and 3R, depending on whether they provide re-amplification, re-shaping and re-timing, respectively. The basic regen-

eration scheme already in operation is the re-amplification, which uses Rare-Earth doped optical amplifiers or Lumped Raman amplifiers [26], as discussed in Section 2.4.

Figure 3.12 shows the block diagram of the different fucntions that are performed by a 3R optical regenerator [96], which is composed of three main blocks. The first block is an adaptation interface, whose function is to condition (for example in terms of power level, initial shape, out-of-band ASE filtering) the input signals so that they become suitable for the following blocks of the regenerator. The adaptation interface block of Figure 3.12 has two outputs, one of which is forwarded to the nonlinear gate, while the other to a decision control block. The nonlinear gate is responsible for blocking the input signals below a certain threshold as well as limiting the signal levels that are above this threshold. Ideally, the nonlinear gate should have a step response with a zero-valued dead-zone in the middle. In the decision control block, the clock signal is recovered from the data and after conditioning, it is forwarded to the nonlinear gate. This clock signal is referred to as a control signal in the block diagram of Figure 3.12, because its function is to control the clock timing of the nonlinear gate. In the absence of this control signal the regenerator performs reshaping and re-amplification only.

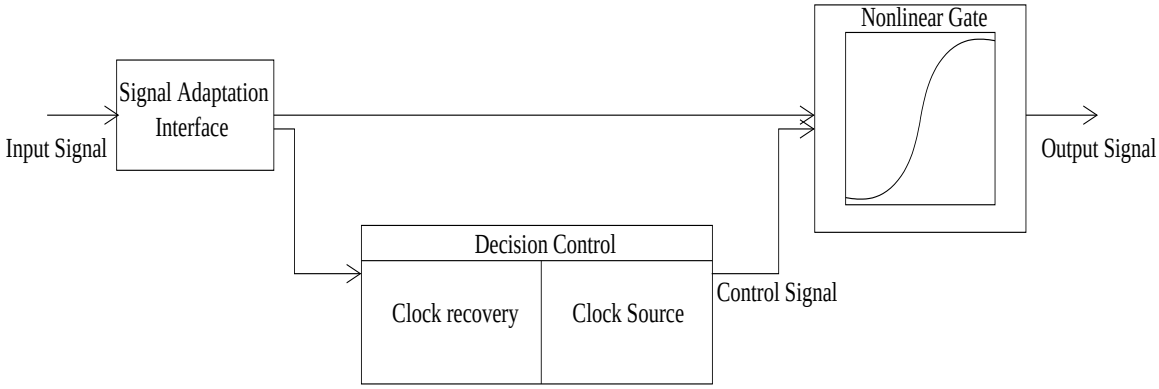

Figure 3.12: Block diagram of an optical 3R regenerator.

Chapter 4 will return to the topic of regeneration by discussing a particular type of all-optical regenerators that performs re-amplification and re-shaping with the aid of nonlinear optical signal processing.

3.7 Conclusions

In this chapter we have introduced different types of ROF communication systems, which are classified on the basis of the RF signal format transmitted. The conclusions of the chapter are summarized below.

- The RF signals are generally transmitted using intensity modulation and are detected by direct detection or remote heterodyne detection techniques.

- Typically SCM is used for multiplexing the RF signals in the electronic domain, while WDM is employed for multiplexing the ROF signals in the optical domain.
- The ROF link inflicts impairments upon the RF signals transmitted over it due to inter-modulation, nonlinear photo-detection, laser noise, fiber induced impairments and optical amplification.
- The DROF uses an ADC and DAC for transmitting the RF signal using a CW or pulsed optical carrier over the optical fiber.
- The pulse propagation in optical fiber may be modelled using the Split-Step Fourier Method of Section 3.6.

Chapter 4

Baseband ROF and Optical Pulse Regeneration

This chapter discusses the family of BROF communications using pulsed optical systems, which facilitate the employment of both Optical Time Division Multiplexing (OTDM) as well as WDM techniques over long optical fibers. As mentioned in Section 3.6.1, optical signal regeneration is used in order to compensate for the impairments induced by the optical fiber link. In Section 4.2 of this chapter, we will discuss the operating principle of a simple pulse regenerator used for amplifying and re-shaping the optical signal and characterize its performance in Section 4.3. The physical layer design of the pulsed optical system is presented in Section 4.4 in the context of a cooperative distributed antenna aided scenario. The attainable performance is characterized using both the optimum parameters as well as in the presence of realistic parameter variations.

4.1 Baseband ROF Architecture

Figure 4.1 shows the typical architecture used in a BROF communication system. It can be observed from Figure 4.1 that the electronic baseband signal is directly converted to optical signal in the E-O conversion block, which is then conveyed over the transmission medium. At the receiver, photodetection is performed in the O-E conversion block for retrieving the electronic baseband signal. The baseband data is up-converted to obtain a RF signal in the up-conversion block, as shown in Figure 4.1. The up-converted signal is transmitted through the antenna after filtering and amplification, as shown in Figure 4.1. It will be demonstrated in Section 5.1 that in contrast to the BROF architecture of Figure 4.1, the AROF system of Figure 5.1 performs up-conversion at the transmitter. Furthermore, the DROF system architecture of Figure 6.1 to be discussed in Section 6.1 performs further processing of the analogue signal by converting it into a digital signal before its transmission over the optical channel. The digital signal is converted back to analogue signal at the receiver.

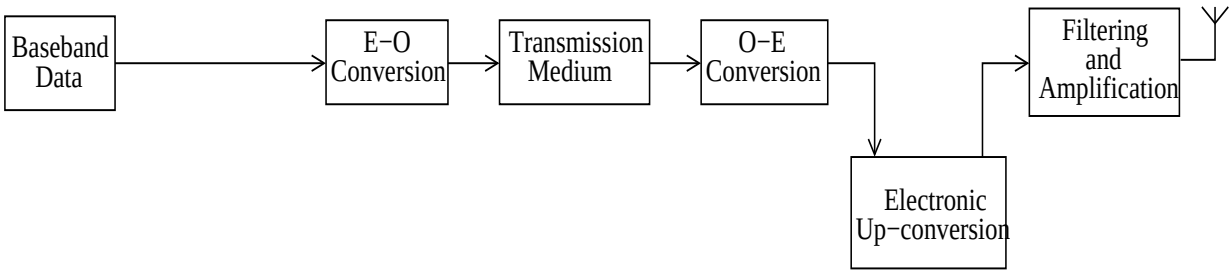

Figure 4.1: General architecture of a BROF system.

4.1.1 Time and Wavelength Division Multiplexed Optical Pulsed System Architecture

Optical baseband communications typically relies on a combination of WDM and TDM in order to increase the attainable throughput of the system, since WDM transmits for example four parallel streams at different frequencies/wavelengths at quadrupled rate. Alternatively, TDM might be used for multiplexing several streams but it may also be combined with WDM. Figure 4.2 shows the simplified block diagram of an optical pulsed communication system. A single pulsed laser source having a wavelength of λ_1, as shown by the stylized plot in Figure 4.2, is then split into four paths using an optical splitter in preparation for the ensuing time-division multiplexing of four streams. The signal in each path is modulated by a 10 $Gbit/s$ baseband data stream using MZMs. The optical pulses used have a typical pulse width ranging from 6 ps to 8 ps in order to generate a 40 $Gbit/s$ TDM signal with a duty cycle of 25 $\%$ to 33 $\%$. The four 10 $GBit/s$ modulated optical signals are then time division multiplexed by using three delay lines for delaying three of the streams by one, two and three bit-periods, respectively. This stage is then followed by a quad-input multiplexer whose output is shown by the stylized plot in Figure 4.2. Again, the delay lines are based on fibers whose lengths are chosen to ensure that the pulses in each of the four paths remain within a single bit interval of width 25 ps. It can be observed from the stylized plot in Figure 4.2 that the multiplexed signal has four times the data rate of each of the input signal to the multiplexer. After being time division multiplexed, the signal is wavelength division multiplexed with four similar TDM streams having different central wavelengths. In this way a total bit rate of 4x40 $Gbit/s$ is achieved. The number of wavelengths used in the architecture of Figure 4.2 was set to four as an illustrative example. In practice the number of wavelengths can be even further increased depending upon the specific requirements of the link considered. The TDM/WDM signal is then transmitted over multiple sections of a SMF and dispersion compensating fiber (DCF)[1], as seen in Figure 4.2. The data of each channel at the receiver is recovered by demultiplexing the combined wavelength-multiplexed and time-multiplexed signal.

In general, optical amplification is needed after every 50km to 60km span of fiber [96]. However, in scenarios, where the optical signal is degraded beyond a certain limit, optical regenerators

[1]The DCF is arranged to have a Frequency-Domain Channel Transfer Function (FDCHTF), which results in a frequency-independent constant after concatenation with the SMF itself

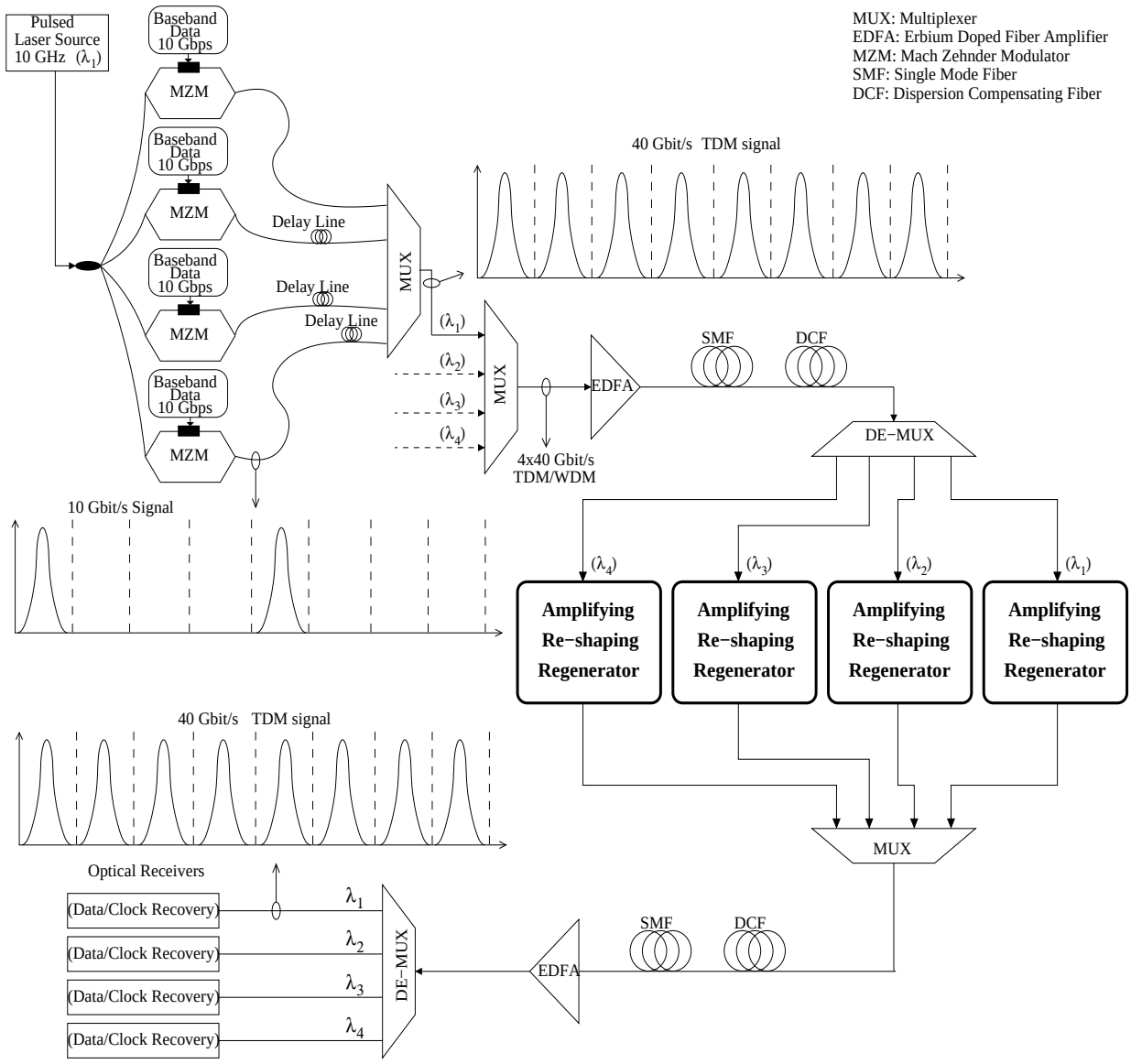

Figure 4.2: System architecture of a typical baseband optical communication system.

are used for amplifying and re-shaping the signal [96], as shown in Figure 4.2. Section 4.2 of this chapter discusses optical signal regeneration in detail, with special emphasis on an SPM based regenerator.

4.2 Pulsed Signal Regeneration

As mentioned in Section 4.1.1, optical pulsed signals transmitted over long optical fibers require regeneration at regular intervals. In a long optical link, the effect of linear dispersion, nonlinear distortion and signal reflections due to network components may escalate to an extent that signal amplification becomes insufficient for regenerating the signal into a reliably detectable shape [96]. Therefore, regenerators are used at regular intervals in order to avoid that the optical signal becomes undetectable. At the time of writing, most of the research is dedicated to the development

of all-optical regenerators, since they do not require any signal format conversion from optical-to-electrical and back to optical [96], [105]. In the following sections, we will discuss a low-complexity all-optical regenerator design that may be used for regenerating the optical pulses, as shown in Figure 4.2.

4.2.1 Self Phase Modulation Based Regenerator

In this section we study the optical regenerator block of Figure 4.2 that performs amplification and re-shaping of the optical input signal. Among the various fiber-based regenerators that have been proposed for all-optical signal regeneration, the one proposed by Mamyshev [106] is the most popular one owing to its implementational simplicity and efficiency. The Mamyshev regenerator as shown in Figure 4.3, uses SPM, as described in Section 2.2.3, to impose spectral broadening on the incoming signal and the resultant broadened spectrum is then filtered at an offset wavelength to obtain a reshaped and re-amplified signal. The SPM is achieved in a Highly Nonlinear Fiber (HNLF) by amplifying the input signal of the regenerator. A HNLF is a specifically designed fiber section, which imposes specifically designed nonlinear distortion by reducing the effective core area A_{eff} of the fiber, as discussed in Section 2.2.3.

The SPM based regenerator has attracted much research attention since it was first proposed by Mamyshev [106]. Some of the major studies that have been performed on the SPM based regenerators are summarized in Table 4.1.

Table 4.1: Summary of major contributions on SPM based regenerators.

Author(s)	Contribution
[99] B-E Olsson *et al.* 2002	The effects of the regenerator on input signals having varying pulse widths and suffering from Polarization Mode Dispersion (PMD) are investigated. It has been observed that the regenerator performs best for a HNLF having a negative dispersion coefficient. with reference to a wavelength of 1310 nm. This is due to lower amplitude fluctuations caused by beating between the signal pulse and optical noise, while travelling through the HNLF having a negative dispersion coefficient.
[107] C. Finot *et al.* 2004	The choice of optimal input power to acieve maximum BER and extinction ratio improvement is discussed. The impact of fluctuations in the input signal's temporal width as well as amplitude on the output signal of the regenerator is demonstrated. It has been shown that the fluctuations in the input signal's temporal width and amplitude cause some timing jitter in the output signal.
[108] N. Yoshikane *et al.* 2004	Experimental investigations of SPM based regenerators are presented in the context of optical bandlimited TDM signals at a data rate of 42.7 $Gbps$, transmitted over a fiber length of

Continued on Next Page...

Table 4.1 – Continued

Author(s)	Contribution
	2500 km. It was demonstrated that by placing the SPM based regenerator ahead of the optical receiver, a Q-factor improvement of about 1.5 dB is achieved.
[109] T. N. Nguyen *et al.* 2006	Considers the effects of input and output filters on the achievable performance of the regenerator in the presence of non-coherent noise. It has been shown that the input filter is essential for rejecting the out-of-band optical noise in the input signal, while the output filter is essential for preserving the modulation format of the optical signal.
[110] M. Aoudeh *et al.* 2006	The Q-factor performance of the regenerator is optimized for signals affected by residual dispersion and/or ASE noise. The optimization is carried out by varying the bandwidth and center frequency of the output optical filter. It was concluded from the numerical simulations that for selecting the filter bandwidth and center frequency, a trade-off has to be struck between the improvement in Q-factor and extinction ratio of the output signal.
[111] M. Rochette *et al.* 2006	Advantages of the SPM based regenerator over conventional regenerators are discussed. It has been shown that the SPM based regenerator is capable of selectively attenuating ASE noise, which results in a direct improvement of the BER. Since noise results in random pulse widths, the selective attenuation of noise is achieved by using the pulse-width discrimination property of the SPM-based regenerator.
[112] L. Provost *et al.* 2007	The SPM based regenerator is numerically characterized in detail. A design map is derived which relates both the physical parameters parameters of the regenerator and the input optical signal to the regenerator performance. The design map may be used to identify the optimum parameters for generating a certain output from the regenerator.

4.2.2 Self-Phase Modulation Based Regenerator Operating Principle

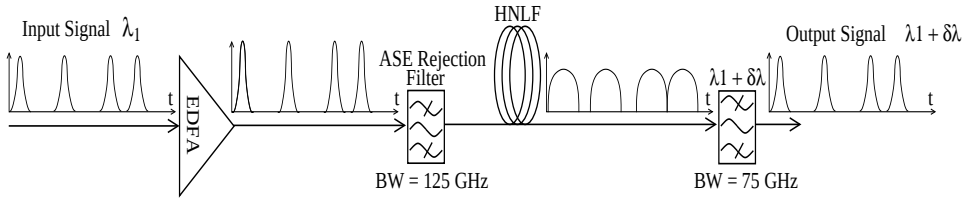

Figure 4.3: Schematic of typical Mamyshev regenerator, which is a beneficial instantiation of the regenerator blocks seen in Figure 4.2

The operating principle of the regenerator can be understood from Figure 4.3, which shows

the schematic of a typical Mamyshev regenerator [106]. The regenerator of Figure 4.3 represents a single regenerator block operating at a single optical frequency, as shown in Figure 4.2. For illustration, we opted for the input optical frequency of λ_1, as shown in Figure 4.2 and Figure 4.3. The optical input signal having a center frequency of 194 THz/1545 nm consists of Gaussian-shaped time-domain pulses having a bandwidth-time (BT) product of about 0.45 repeated at time-intervals of 25 ps, i.e. at a frequency of 40GHz and having a Full Width Half Maximum (FWHM)[2] pulse duration of τ = 6ps. The FWHM pulse width of τ = 6 ps corresponds to a bandwidth of about 0.45/6x10^{-12} = 75 GHz. Therefore, the input optical Gaussian pulses have a repetition rate of 40 GHz and a bandwidth of 75 GHz. The input signal is first amplified by the EDFA of Figure 4.3 and passed through an ASE rejection filter having a bandwidth of 125 GHz, as shown by the stylized plots in Figure 4.3. The bandwidth of 125 GHz is chosen in order to accommodate the input signal bandwidth of 75 GHz as well as 25 GHz guard bands on each side of the spectrum. The task of the ASE rejection filter is to remove any optical noise outside the bandwidth of the input signal. The filtered signal is then spectrally broadened by the action of the SPM in the HNLF, which exhibits a dispersion of -1.7 $ps \cdot nm^{-1} \cdot km^{-1}$ at the signal frequency of 194THz. The attenuation of the HNLF is 2.1dB/km and its nonlinearity coefficient is 18 $W^{-1} \cdot km^{-1}$. Initially we have assumed a dispersion slope value of 0.023 $ps \cdot nm^{-2} \cdot km^{-1}$, which is considered typical for commercial Germanium-doped HNLFs. Recall from Section 2.2.2 that the dispersion slope of the fiber is the rate of change of its dispersion with respect to the frequency of the optical signal. Signal regeneration is achieved by the action of the optical band-pass filter of Figure 4.3, which is placed immediately after the HNLF and carves into the broadened spectrum at an offset frequency/wavelength relative to that of the input signal. (In our case the filter position is at a shorter wavelength relative to the central wavelength of the input signal and 3nm away from it.) The filter has a Gaussian frequency-domain response and a 3-dB bandwidth of 75GHz, which ensures that the pulses at the output have a similar width to those at the input. The parameters of the regenerator are summarized in Table 4.2.

Table 4.2: Parameters of the Self Phase Modulation based regenerator.

Parameter	**Value**
Center Frequency/Wavelength of Input Optical Signal	194 THz/1545 nm
Repetition Rate of Input Optical Signal	40GHz
Pulse Width of Input Optical Signal	6ps
Bandwidth of Input Optical Signal	75 GHz
Average Power of Input Optical Signal	0.18 W
Bandwidth of ASE Rejection Filter	125 GHz
Dispersion Parameter of the HNLF	-1.7 $ps.nm^{-1}.km^{-1}$
Attenuation of the HNLF	2.1dB/km

Continued on Next Page...

[2]The FWHM is the pulse width at a point where the power is half of the peak power of the pulse

Table 4.2 – Continued

Parameter	**Value**
Nonlinearity Coefficient of the HNLF	18 $W^{-1}.km^{-1}$
Dispersion Slope of the HNLF	0.023 $ps.nm^{-2}.km^{-1}$
Bandwidth of the Ouput Optical Filter	75 GHz
Center Frequency/Wavelength of the Output Optical Filter	194.4 THz/1542 nm

In order to elaborate further on the operating principle of the regenerator, the broadened spectra after the HNLF recorded for different values of the input signal power are shown in Figure 4.4 along with the spectra at the ouput of the filter centered at an offset frequency. It should be noted that the attenuation of the output filter is considered negligible for the plots shown in Figure 4.4. It can be observed from the plots that upon increasing the input signal power, the broadening of the spectrum after the HNLF increases. For low spectral broadening, which corresponds to a low-power input signal, the filtered output spectrum has a low peak value, as shown in Figure 4.4. This in turn results in a low-power output signal in the time domain. However, as the spectral broadening increases, there is a steep rise in the number of spectral frequencies falling into the filter's bandwidth. This in turn causes a steep rise in the power of the time-domain output signal. Therefore, it may be deduced from the above arguments that the position of the output filter determines the power of the time-domain output signal, which in turn determines the power transfer function of the regenerator.

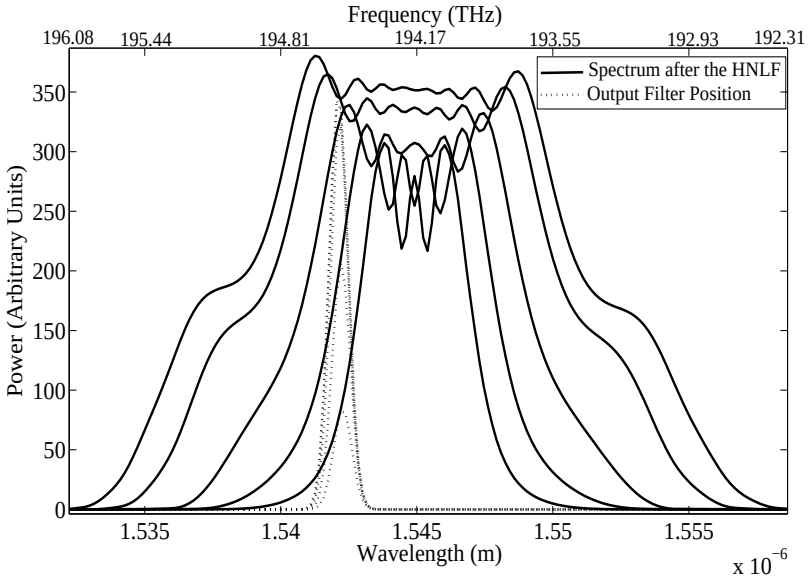

Figure 4.4: Plots of the broadened spectra after the HNLF as well as the corresponding output spectra.

4.2.3 Self Phase Modulation Based Regenerator Transfer Functions

In order to elaborate on the effect of the HNLF impulse-response duration on the regenerator's output signal, the temporal and spectral plots of the signal at the output of the HNLF of Figure 4.3 are obtained for three different fiber lengths, namely for 0.6 km, 1 km and 1.4 km. For illustration, the average input power used for generating the plots seen in Figure 4.5a and Figure 4.5b is equal to 0.18 W. The shape of the spectral plots shown in Figure 4.5b determines the shape of the regenerator's Transfer Function (TF) [112], [113], as shown in Figure 4.6.

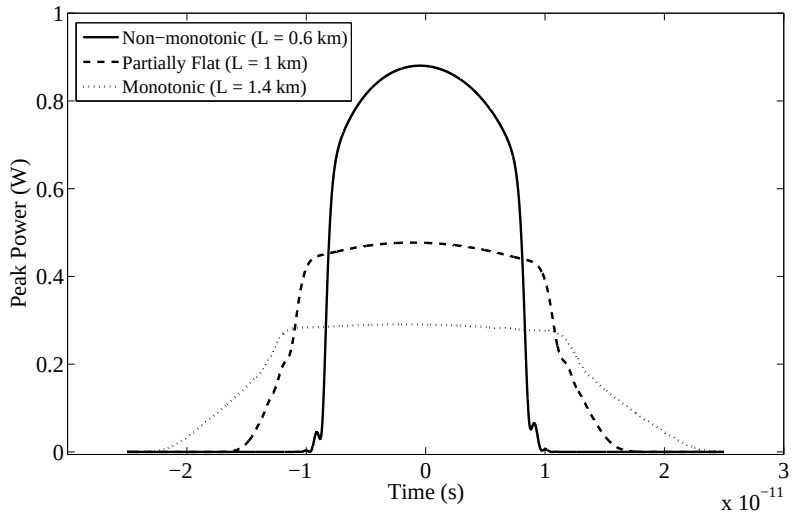

(a) Temporal-domain plot

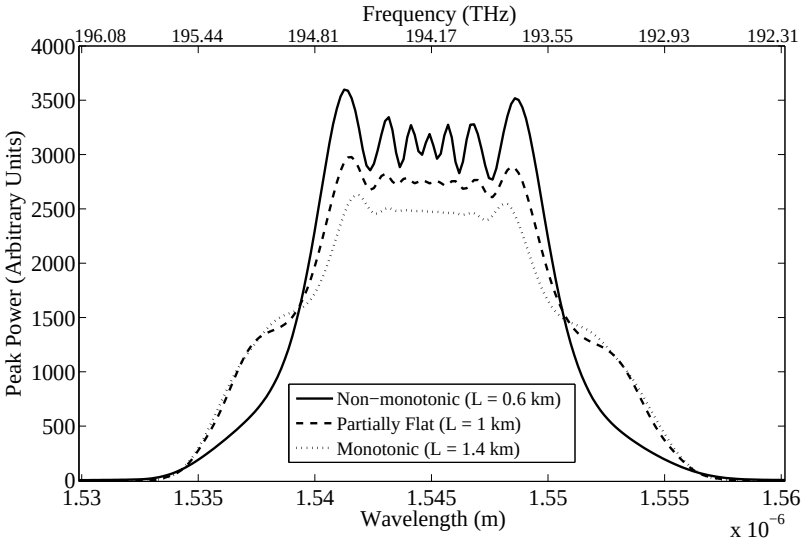

(b) Spectral-domain plot

Figure 4.5: Signal at the output of the HNLF for three different fiber lengths.

It can be observed from Figure 4.6 that the TFs of the SPM based regenerator are obtained for the three different fiber lengths of 0.6 km, 1 km and 1.4 km. It may be inferred from Figure 4.4, that the output signal power and therefore the TF of the regenerator depends upon the shape of the broadened spectrum at the output of the HNLF as well as upon the center frequency of the output

filter. This dependence of the TFs may also be observed in Figure 4.6, where the shape of the TFs for the three different fiber lengths of 0.6 km, 1 km and 1.4 km depends upon the shape of the respective broadened spectra shown in Figure 4.5b. The TFs of Figure 4.6 are nonlinear functions, where the steep rise in the output power corresponds to a steep rise in the number of spectral frequencies falling into the filter's output bandwidth, hence imposing an increased in broadening, as shown in Figure 4.4. The TFs shown in Figure 4.6 become relatively flat, once the input signal power exceeds about 100 mW. This flat region of the TF corresponds to the flat plateau of the broadened spectra shown in Figure 4.4. The operating point of the regenerator is generally chosen to be in the middle of the TF's flat region to reduce the amplitude jitter of the output signal [112].

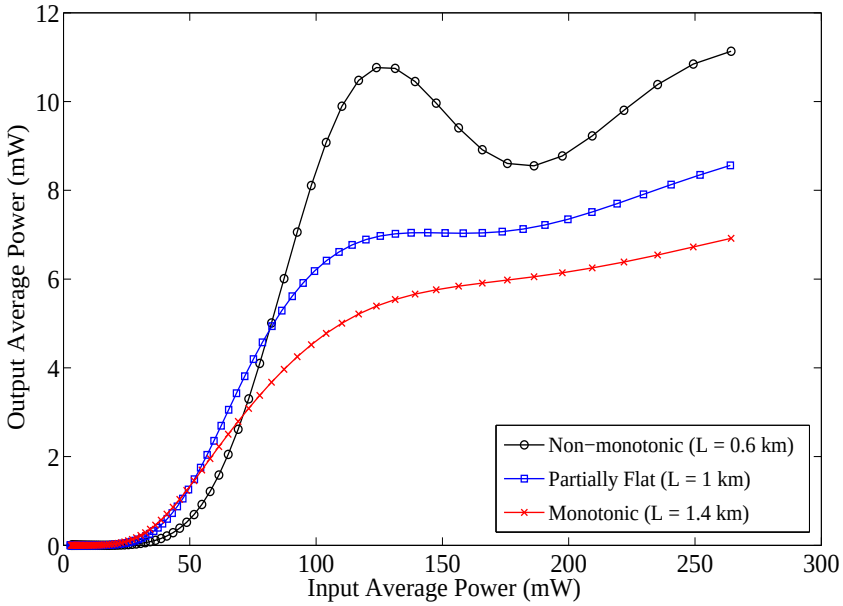

Figure 4.6: The three types of TFs obtained by varying the length of HNLF.

4.3 Characterization of the SPM Based Regenerator

Let us commence by portraying the state-of-the-art. Table 4.3 summarizes the major contributions that relate to the selection of physical design parameters of the SPM based regenerator for its efficient operation.

Table 4.3: Summary of major contributions on characterizing the SPM based regenerator.

Author(s)	Contribution
[114] T.H. Her *et al.* 2004	The effect of the regenerator's physical parameters, such as the HNLF length, input signal power and output filter offset are studied. It has been reported that the best performance may be

Continued on Next Page...

Table 4.3 – Continued

Author(s)	Contribution
	achieved by keeping the duty cycle of the input data signal below 33 %.
[105] P. Johannisson *et al.* 2005	Theoretical investigations of the trade-offs between noise reduction and amplitude jitter suppression were provided. Furthermore, the effects of the HNLF length and output filter center frequency are described.
[115] A. G. Striegler *et al.* 2006	Optimization of input power, output filter center frequency and bandwidth are discussed, complemented by the regenerator design rules based on the input pulse duration and fiber type.
[112] L. Provost *et al.* 2007	The authors related the physical parameters of the regenerator to its performance. This design procedure may be used to identify the optimum parameters for operating the regenerator.
[116] P. P. Baveja *et al.* 2009	Numerical investigation of the linear distortion-related and the nonlinear distortion effects are discussed for optimizing the performance of the regenerator. A scaling parameter is introduced which can be used for enhancing the regenerator's performance.

As discussed in Table 4.3, much of the research on the physical structure of the regenerator has been focussed on the properties of the HNLF for the sake of optimizing the regenerator's performance. However, all theoretical and numerical studies in the open literature have considered so far a negligible dispersion slope for the HNLF used in the regenerator, where the dispersion slope is a measure of the dispersion versus the signal's wavelength/frequency, as discussed in Section 2.2.2. In this section we numerically investigate the effect of the nonlinear fiber's dispersion slope on the SPM based optical regenerator's performance. Our numerical study will demonstrate that the dispersion slope has a significant impact on the regenerator's transfer function. The dispersion slope may therefore be used together with the dispersion parameter and the filter offset as an additional parameter of controlling the regenerator's performance.

4.3.1 Spectral and Temporal Effects of Dispersion Slope

Let us now observe how the spectral-domain and temporal-domain plots vary with the dispersion slope of the HNLF. The dispersion slope is varied, while keeping the dispersion parameter defined in Section 2.2.2 constant at the signal wavelength considered and commensurately adjusting the dispersion slope with the wavelength. Figure 4.7a and Figure 4.7b shows the temporal-domain and spectral-domain profiles of the HNLF's output pulses upon varying its dispersion slope between 0 and $0.3ps \cdot nm^{-2} \cdot km^{-1}$. It should be noted that these values of the dispersion slope are rather high, when considering step-index fibers, but become more typical in the case of silica holey fibers, where it has been shown that appropriate control of the hole size and pitch may result in high dispersion slope values, while maintaining a relatively high nonlinearity coefficient [117], as

defined in Section 2.2.3.

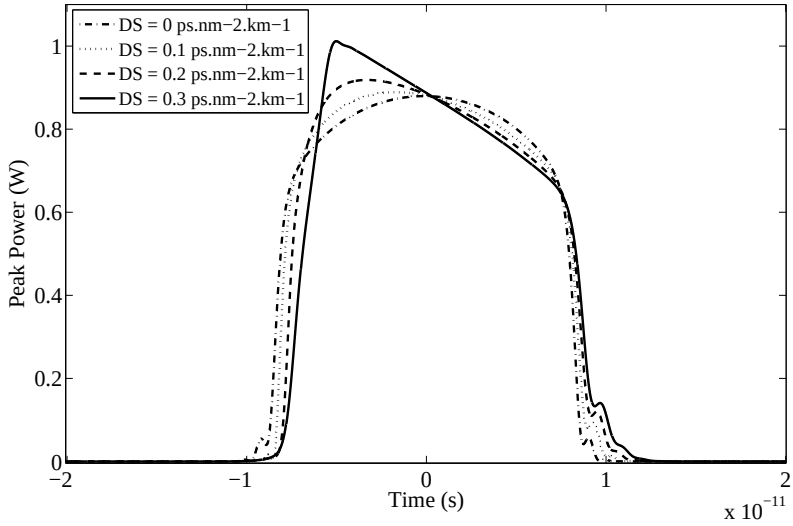

(a) Temporal-domain plot.

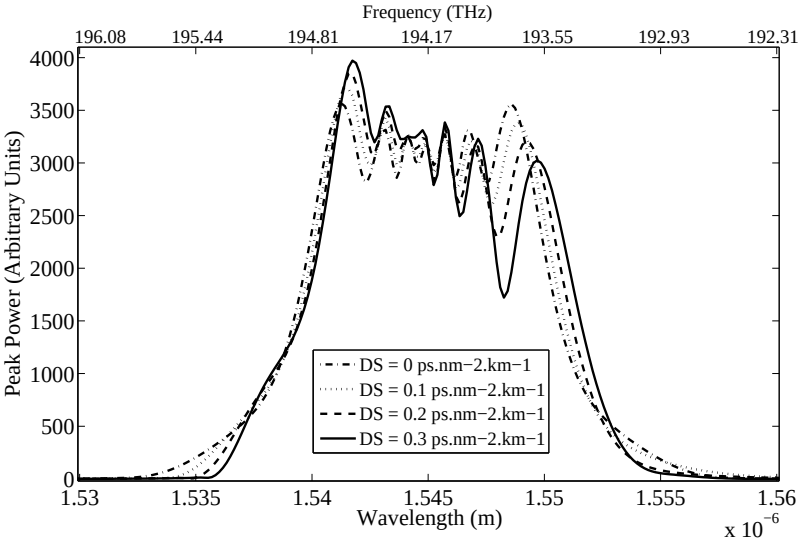

(b) Spectral-domain plot.

Figure 4.7: Ouput signal of the HNLF of Figure 4.3 having a length of 0.6 km and different dispersion slope values. The corresponding curves for a dispersion slope of $0.023 ps \cdot nm^{-2} \cdot km^{-1}$ are shown in Figure 4.5a and 4.5b

The input signal parameters used for the plots in Figure 4.7a and Figure 4.7b are the same as those used in Figure 4.5a and Figure 4.5b and mentioned in Table 4.2. However, the length of the HNLF is maintained at L = 0.6 km in these cases. As expected, an increase in the dispersion slope gives rise to an asymmetry in the power distribution of the broadened spectrum [115], [118]. Additionally, as the dispersion slope increases, the side of the spectrum that corresponds to lower power components (longer wavelengths in Figure 4.7b) has more pronounced lobes, whereas the spectral lobes on the opposite side (shorter wavelengths in Figure 4.7b) become less pronounced. This behaviour is reminiscent of the effect of varying the HNLF length, as shown in Figure 4.5b, where the spectral lobes of the broadened spectrum become flatter as the HNLF length is increased.

The two effects are in fact related and result from the larger value of the dispersion at the wavelengths of observation. Therefore by keeping the rest of the regenerator parameters constant, while controlling the dispersion slope of the HNLF should allow us to change the shape of the TF. It is worth mentioning here that similar conclusions may also be drawn for dispersion slope values having a sign opposite to those used in Figure 4.7a and Figure 4.7b. The only difference in that case would be the asymmetry of the spectrum, which will now be opposite to that shown in Figure 4.7b.

4.3.2 Effect of Dispersion Slope on the Transfer Functions

As shown in Figure 4.6, we obtain a non-monotonic TF when the HNLF has a length of 0.6 km, a dispersion of -1.7$ps \cdot nm^{-1} \cdot km^{-1}$ at the signal wavelength and a dispersion slope of 0.023 $ps \cdot nm^{-2} \cdot km^{-1}$. Figure 4.8 shows the shape of the non-monotonic TF versus the dispersion slope.

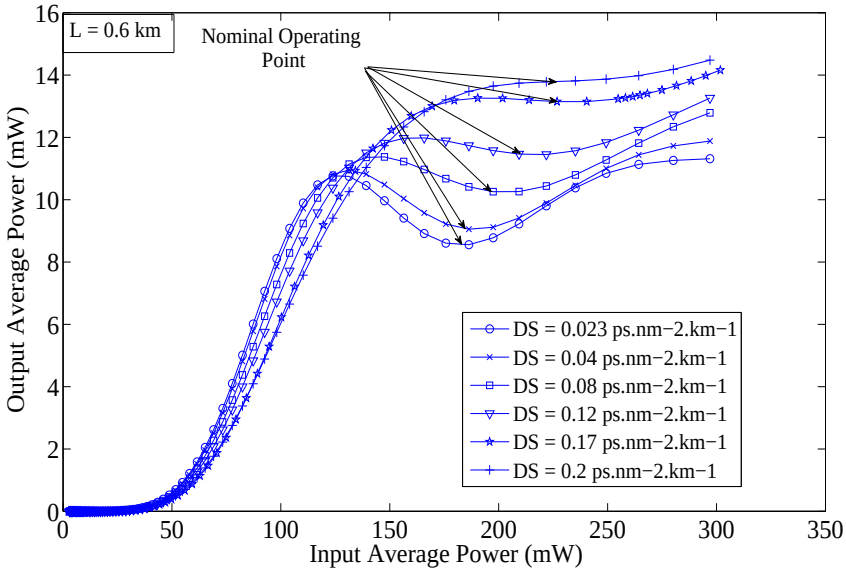

Figure 4.8: Effect of varying the dispersion slope on the Non-Monotonic TF at L = 0.6 km. The corresponding curve with DS = 0.023 $ps \cdot nm^{-2} \cdot km^{-1}$ was shown in Figure 4.6.

In the plots shown in Figure 4.8, we increase the dispersion slope towards negative values. Therefore, as discussed previously in Section 4.3.1, this increase in the magnitude of the dispersion slope will restrict the effect of spectral broadening on the long-wavelength side of the spectrum, thus making the spectral lobes flatter on that side. This in effect, tends to flatten the power TF in Figure 4.8 when the filter offset remains constant. Note that we focus on the high-output section of the transfer curve above an input power of about 150 mW that is concerned with the average input power of logical ones, since a change in dispersion slope is not expected to have a significant effect on the average input power of logical zeros. It can be seen in Figure 4.8 that the average power equalization of logical ones improves upon increasing the magnitude of dispersion slope, until the

value of 0.17 $ps \cdot nm^{-2}. \cdot km^{-1}$, for which the TF exhibits a partially flat region. With a further increase in the magnitude of the dispersion slope, the TF becomes reminiscent of a monotonic type and therefore the average power equalization of logical ones becomes worse. In Figure 4.8 the operating point on the TFs, which results in minimum variation of the output signal power for a variation in the input signal power is also indicated. The input average power at these operating points is termed as the nominal average input power in the remainder of the text.

Next we consider the power TF of L = 1 km having a partially flat section, as shown in Figure 4.6. Again, for the HNLF considered in our study, the locally flat region occurs for a length of L = 1 km. Figure 4.9 shows the effect of different dispersion slope values on the shape of this type of TF. It may be observed from the figure that as we increase the magnitude of the dispersion slope, the TF may become either monotonic or non-monotonic, depending upon the sign of the dispersion slope. The reason for this variation in the power TF is due to the variation in the shape of the broadened spectrum, as mentioned earlier in Section 4.3.1. Since the output offset filter of Figure 4.3 is placed at the shorter wavelength side of the broadened spectrum, an increase in the magnitude of the dispersion slope flattens the spectral lobes on the shorter wavelength side. This effect is similar to increasing the length of the HNLF as observed in Figure 4.5b. Therefore the power TF shape becomes reminiscent of the monotonic type. The opposite happens when the dispersion slope is increased towards negative values.

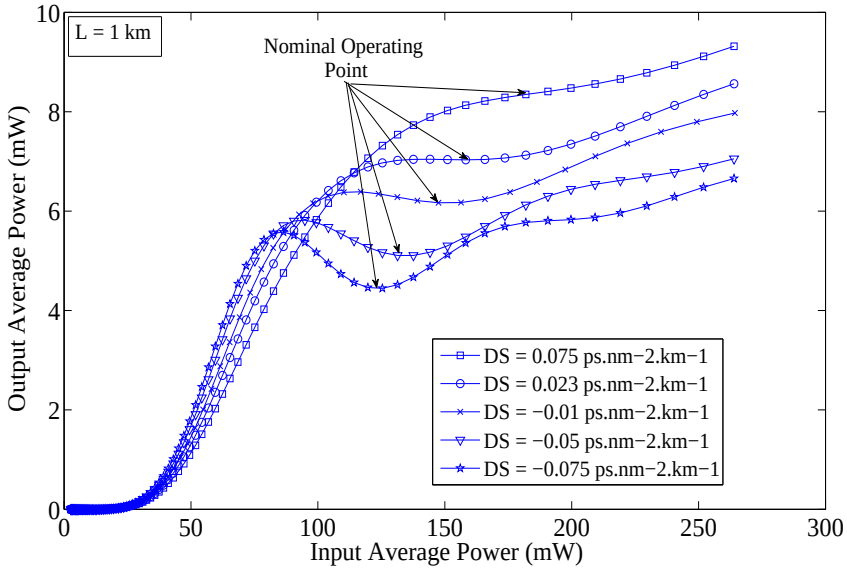

Figure 4.9: Effect of varying the dispersion slope on the power TF having a Locally Flat region for L = 1 km. The corresponding curve with DS = 0.023 $ps \cdot nm^{-2} \cdot km^{-1}$ was shown in Figure 4.6.

We obtain a monotonic power TF when the HNLF considered in the simulations of Figure 4.3 has a length of L = 1.4 km. The effect of varying the magnitude of the dispersion slope in this power TF is shown in Figure 4.9. It can be observed from the figure that the monotonic power TF tends towards the one with a partially flat region as the value of dispersion slope increases, whereas a further increase in the magnitude of the dispersion slope gives rise to a non-monotonic

TF. For this to happen of course, the sign of dispersion slope has to be the opposite of that applied previously for the non-monotonic power TF as seen in Figure 4.8).

The results shown in Figures 4.8, 4.9 and 4.10 demonstrate that it is important to consider the effects of the dispersion slope on the system's behaviour when HNLFs with a dispersion slope of a considerable magnitude are considered, as may be the case for certain small-core holey fibre designs.

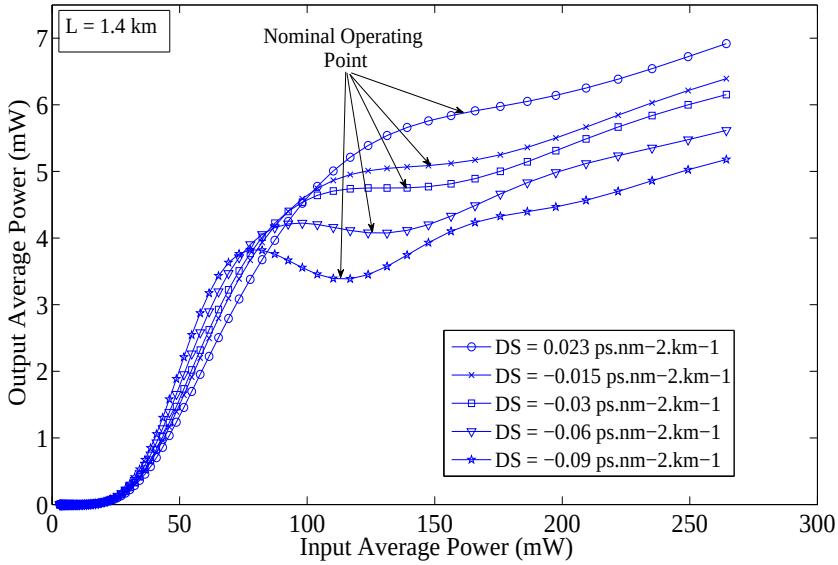

Figure 4.10: Effect of varying the dispersion slope on the Monotonic power TF for L = 1.4 km. The corresponding curve with DS = 0.023 $ps \cdot nm^{-2} \cdot km^{-1}$ was shown in Figure 4.6.

4.3.3 Effect on Power Gain of the Regenerator

As discussed in Section 4.3.1, when the dispersion slope is high, the spectral density of the nonlinearly generated frequency components on the two sides of the spectrum about the central frequency is not equal, as seen in Figure 4.7b. This effect is beneficial in the case of a relatively short HNLF which exhibits a partially flat power TF by virtue of a high dispersion slope, as shown in Figure 4.8. This regenerator will exhibit an increased power gain, since the filter is placed on the high-power side of the spectrum, where the power gain is defined as the ratio of the power at the output of the filter to the power at the input of the HNLF [112]. By contrast, a relatively long HNLF having a high dispersion slope may exhibit a partially flat power TF if the filter is centered on the low-power part of the spectrum accompanied by a further power-loss imposed by the regenerator. Figure 4.11 summarizes these findings by showing the power gain at the nominal average input power versus the dispersion slope for the power TFs shown in Figures 4.8, 4.9 and 4.10. The range of values used in Figure 4.10 are chosen in order to observe the effect of varying the magnitude as well as sign of the dispersion slope on the power-loss.

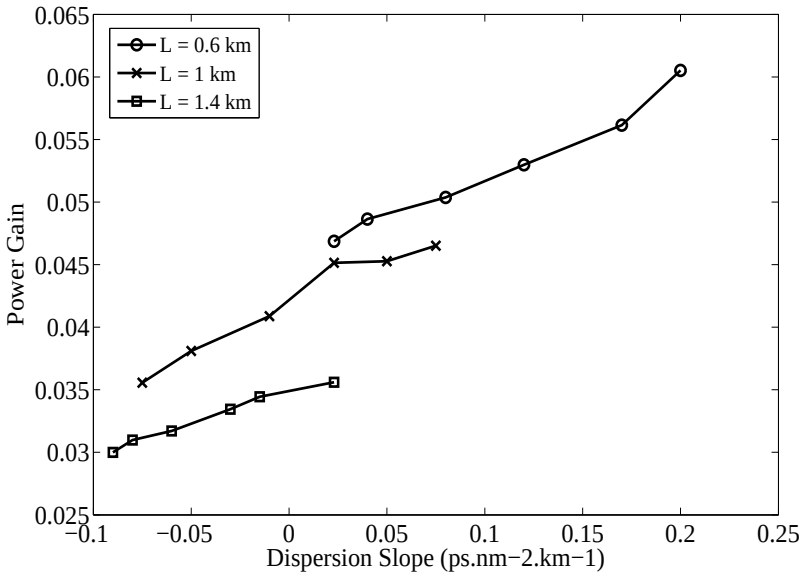

Figure 4.11: Power gain at nominal input average power as a function of the dispersion slope.

4.3.4 Reduction in Pulse-to-Pulse Overlapping

As discussed in [112] and [107], the chromatic dispersion induced pulse broadening within the HNLF results in broadend pulses to an extent that they might overlaps with the adjacent pulses travelling through the fiber. We refer to this overlap of adjacent pulses within the regenerator as pulse-to-pulse overlapping, which results in amplitude jitter at the output of the regenerator. The amplitude jitter increases upon increasing the bit rate of the system, since the pulses become shorter, i.e. more dense in time. It will be shown in this section that the effect of pulse-to-pulse overlapping may be reduced by suitably choosing the HNLF length and dispersion slope. Let us consider the two power TFs having a locally flat region associated with L = 0.6 km and L = 1 km in Figure 4.8 and 4.9, respectively. More explicitly, the two power TFs of Figures 4.8 and 4.9 are obtained by using HNLFs of length L = 0.6 km and L = 1 km as well as dispersion slopes of 0.17 $ps \cdot nm^{-2} \cdot km^{-1}$ and 0.023 $ps \cdot nm^{-2} \cdot km^{-1}$, respectively. We chose these power TFs, since they result in minimum fluctuation of the output power versus the input power, when operated at the nominal input power level. It can be observed from Figures 4.8 and 4.9 that the power TF obtained for a high dispersion slope requires more power to operate at the locally flat region between 150 mW to 250 mW and 100 mW to 200 mW, respectively, as compared to the TF obtained for a low dispersion slope. On the other hand, the power gain of the regenerator based on the HNLF associated with a high dispersion slope is higher than that obtained for a low dispersion slope HNLF. Since pulse-to-pulse overlapping occurs within the HNLF, we consider the pulse widths at the output of the HNLFs used for generating the power TFs shown in Figures 4.8 and 4.9. Figure 4.12 shows the variation in the pulse widths at the output of the two HNLFs, plotted against a 20 $\%$ deviation from the nominal input peak power. It should be noted that for the purpose of illustration, we are considering the brodening of a single optical pulse, therefore, we use the peak power of the pulse to obtain the results shown in Figure 4.12

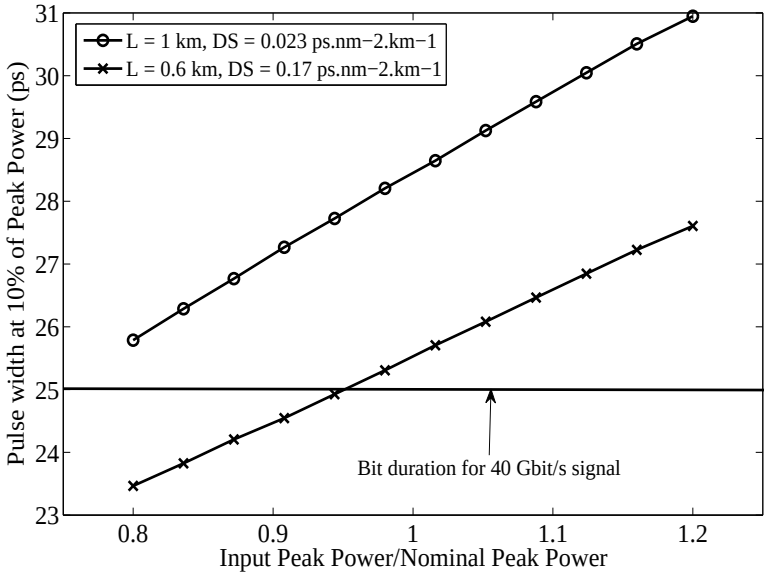

Figure 4.12: Pulse width variation at the output of the HNLFs versus input peak power variations for the two different HNLFs of length L = 1 km and L = 0.6 km.

In pulse-to-pulse overlapping, it is the wings of the pulses that play a predominant role. Therefore, the extent of their broadening is of interest in this study. Hence, we have ploted the pulse widths at 10 $\%$ of the maximum amplitude in Figure 4.12, instead of the widths at half of the maximum. For the temporal-domain plots shown in Figure 4.5a, the 10 $\%$ of the maximum amplitude will be nearly 0.09 W, where it can be observed that the broadening is higher compared to the upper part of the pulse. The peak powers are normalised with respect to the nominal input peak power (which is different for the two cases examined). For reference, Figure 4.12 also shows the 25 ps bit duration for a 40 $Gbit/s$ signal in order to observe wheather pulse-to-pulse overlapping would or would not affect the signal at this repetition rate, where the 6 ps pulses considered in this work are highly suitable for 40 $Gbit/s$ RZ systems [96]. It can be observed from the figure that the pulse at the output of the HNLF exhibiting a high dispersion slope are significantly shorter than those at a low dispersion slope. Therefore, it may be concluded that the effect of pulse-to-pulse overlapping for a regenerator using a short fiber length along with a high dispersion slope HNLF will be less severe compared to a longer length fiber exhibiting a low dispersion slope.

4.4 Baseband ROF Aided 60 GHz Wireless Systems

The previous sections of this chapter discussed signal regeneration for pulsed optical systems. The remaining sections of this chapter will focus on BROF systems relying on optical pulses for the transmission of RF baseband data, as described in Section 3.5. Our study makes use of optical signal processing techniques for transmitting baseband data at mm-wave frequencies to multiple RAUs. Table 4.4 summarizes some of the major contributions towards the transmission

of baseband data in ROF communications.

Table 4.4: Summary of major contributions towards BROF

Author(s)	Contribution
[25] G. H. Smith *et al.* 1998	A hybrid of a star-tree architecture is conceived for amalgamating their benefits using a combination of WDM and SCM transmission, where local oscillators are used at the RAU for mm-wave signal generation. The multiplexing schemes used allow sharing of the equipment at the CU, which enables the implementation of a simple and cost-effective radio distribution architecture.
[119] C. Lim *et al.* 2000	A dual-electrode modulator located at the CU is used for transmitting baseband data as well as a local oscillator for frequency up- and down-conversion at the RAU. The high frequency local oscillator was constructed for reducing the effects of the fiber's chromatic dispersion. The scheme supports a single RAU.
[73] A. Wiberg *et al.* 2005	A dual-frequency optical source is conceived using optical double-sideband modulation and carrier suppression. The carrier is suppressed using a narrow-band optical filter. This scheme enables the transmission of baseband data in the DL direction to a single RAU at a high data rate of 2.5 $Gbits/s$ over a fiber of length 44 km.
[120] L. Chen *et al.* 2007	A pair of coherent optical carriers generated using Optical Carrier Suppression (OCS) at the CU. One of the optical carriers is modulated by baseband data at 2.5 $Gbits/s$, while the other is transmitted along with the baseband data without modulation. The unmodulated carrier is used for transmitting UL data from the RAU to CU. This scheme enables the employment of a single laser source for duplex transmission of high data rate to a single RAU.
[121] J. Yu *et al.* 2007	A phase modulator is used for generating multiple coherent sidebands with carrier, while suppressing the odd-indexed sidebands. Duplex baseband data is transmitted to a single RAU at a mm-wavelength frequency of 40 GHz. The ROF architecture is simplified by using a single optical source located at the CU. All the optical power is efficiently utilized in the CU with some power margin available even without the use of an optical amplifier in the whole system.
[122] Y-T. Hsueh *et al.* 2009	Two high frequency (20 GHz and 40 GHz) local oscillators are employed in conjuction with intensity modulation to generate multiple coherent sidebands at the CU. The baseband data is transmitted at a mm-wavelength frequency of 60 GHz using narrow-band optical filters and interleavers at the at the RAUs.
[123] C-H. Chang *et al.* 2010	A low-cost ROF experimental transport system is demonstrated using direct modulation of a laser source with a local oscillator to generate multiple coherent sidebands. A combination of optical circulators and FBGs is used for narrow-band filtering of the multiple sidebands. This scheme reduces the required number of optical sources, local oscillators and mixers in the ROF system.
[28] X. Xu *et al.* 2011	A system-level design of a cooperative DAS architecture using baseband optical communications is presented. The suitability of ROF communication

Continued on Next Page...

Table 4.4 – Continued

Author(s)	Contribution
	for increasing the cell throughput and coverage is discussed using a single optical pulse model for proof of concept.

4.4.1 The Proposed Baseband Distributed Antenna System Architecture

In this section ROF architectures are designed in the form of a Distributed Antenna System (DAS), where the number of RAUs is increased, for the sake of providing a seamless, uniform coverage of the cell area, where all the signal processing is performed at the CU such as the Mobile Switching Center (MSC). Given this motivation, we propose a novel DAS architecture constituted by six RAUs that are fed using BROF data in a star-like network topology. Figure 4.13 shows the star architecture in detail. It may be observed from the figure that the data is forwarded from the CU to a single BS that is surrounded by 6 RAUs. The CU-to-BS and BS-RAU link is constituted by optical fiber that transmits baseband data using optical pulses. At the CU, the baseband electronic signal is multiplexed in the electronic domain. The resultant multiplexed data is used for modulating a pulsed optical carrier, which is then transmitted to the BS, where it is distributed to each of the six RAUs using low-complexity optical splitters discussed in Section 2.6.1. At each RAU, the baseband data is transmitted over different RF carriers towards the MSs. It will be shown that the proposed DAS architecture is cost-effective, since it relies on efficient all-optical signal processing. As shown in Figure 4.13, the proposed star topology may be beneficially implemented in a cellular architecture for enhancing the cellular coverage quality, especially near the cell-edge.

It may be observed from Table 4.4 that all of the studies in the open literature use CW optical transmission of the BROF data. However, using CW transmission is not feasible for performing cost-effective all-optical signal processing [102], [103]. The only publically available study that uses a baseband optical link is reported in [28]. However, in [28] a system-level design of the optical link is presented without taking into account the design of the optical physical layer. We embark on closing this open problem and present a novel physical layer design for BROF communication systems that has the following major qualities:

1- The proposed system uses TDM baseband over fiber communication in a DAS architecture to transmit data simultaneously to six different RAUs.

2- The baseband data dedicated to each RAU may be transmitted over a range of frequencies around 60 GHz that are generated using only two pulsed signal sources and without any change of hardware components. By contrast, hardware changes would be required for the solutions found in the open literature mentioned in Table 4.4.

3- The photodetector used at each RAU carries out the tasks of demultiplexing as well as heterodyning for generating the 60 GHz RF signal.

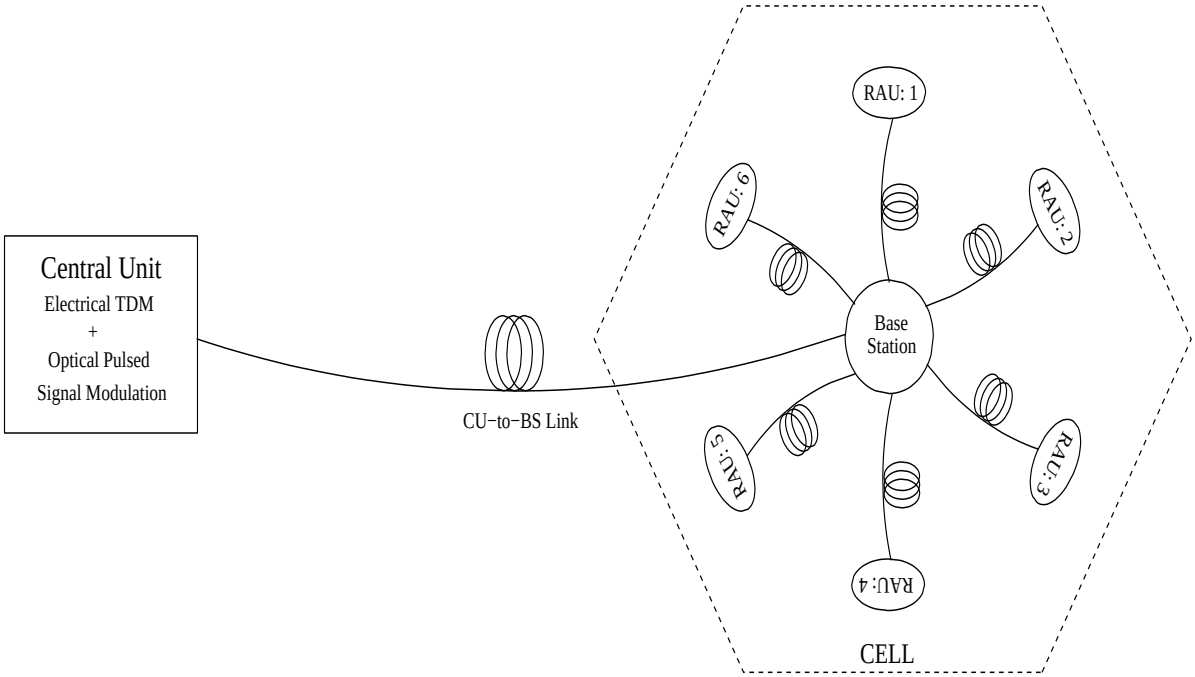

Figure 4.13: Architecture of the proposed Distributed Antenna System.

The details of the physical layer design of the proposed architecture are discussed in the next section.

4.4.2 Physical Layer Design of the Baseband DAS Architecture

Figure 4.14 shows the physical layer architecture of the proposed baseband fiber link. At the MSC, the baseband data scheduled for transmission to six RAUs are multiplexed by using electronic delay lines. The data transmitted to each RAU has a rate of 128 $Mbps$, hence the total data rate of the multiplexed signal is 6 x 128 = 768 $Mbps$. Since the bit duration of the multiplexed signal is about 1.3 ns, the electronic pulse duration is chosen to be 0.2 ns, in order to avoid the overlap of the six pulses multiplexed in time. The multiplexed electronic signal is amplified and fed to the input of the Electroabsorption Modulator (EAM) of Figure 4.14, as discussed in Section 2.1.4. The optical input of the EAM is constituted by an optical time-domain Gaussian pulse-shaped source having a repetition rate of 768 MHz i.e. a period of 1.3 ns. The pulse width of the time-domain Gaussian pulses is 40 ps, while the center frequency is f_1 = 193.1 THz. The modulated optical signal at the output of the EAM is coupled with a second optical pulsed source, which is phase-coherent with the first optical source. The second optical pulsed source has a repetition rate of 128 $Mbps$ and a center frequency of f_2 = 193.16 THz, which is 60 GHz higher than the first optical source. The second optical pulsed source will be used to optically demultiplex the baseband data for each RAU as well as to generate the data at 60 GHz frequencies at each RAU. The optically coupled signal at the output of the MSC shown by the stylized spectral plot in Figure 4.13, is transmitted over a 20 km SMF towards the BS, as shown in Figure 4.13. The parameters of the design are summarized in Table 4.5.

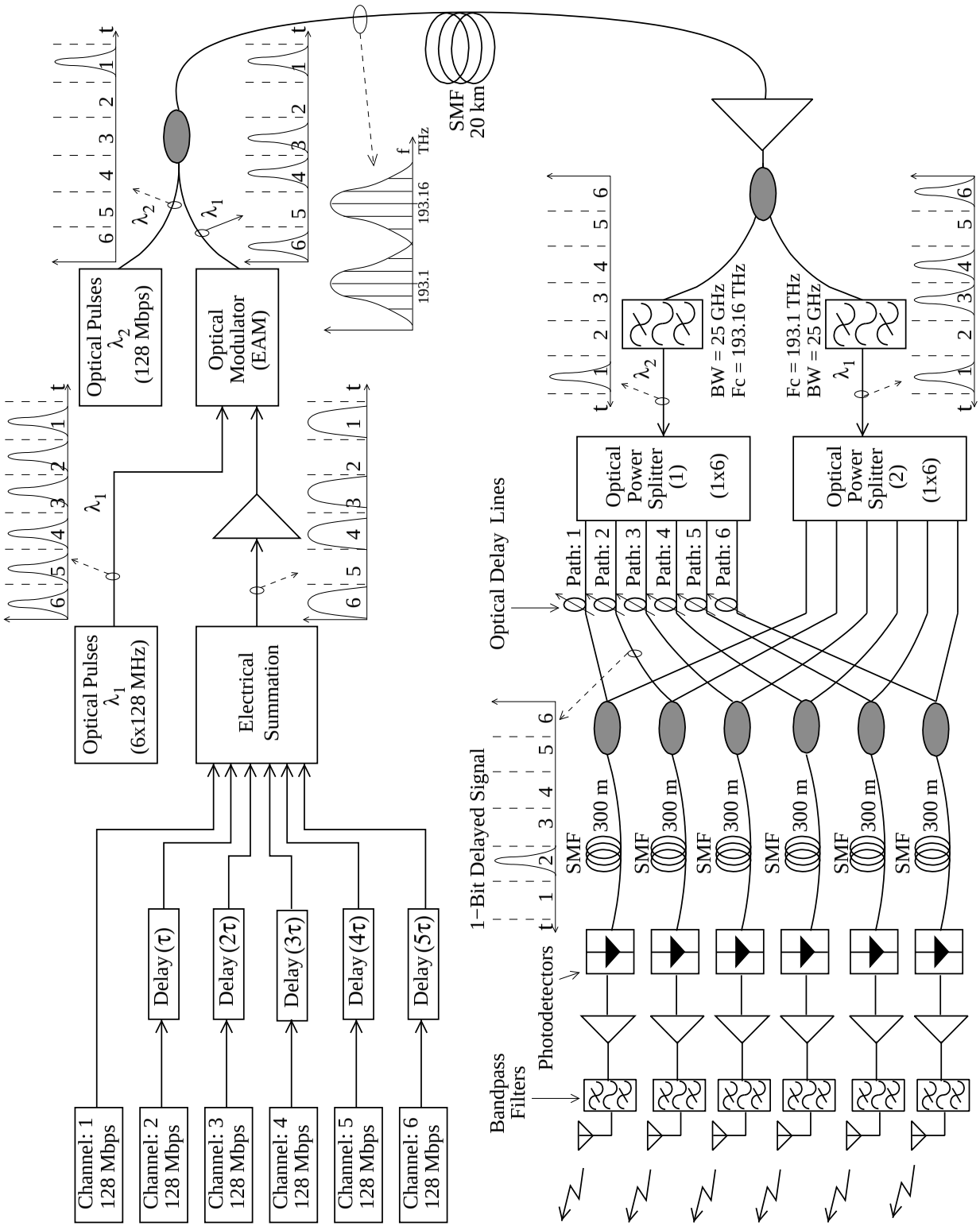

Figure 4.14: Physical layer architecture of the baseband DAS.

Table 4.5: Paramters of the baseband architecture.

Parameter	Value
Number of RAUs	6
Data transmitted to each RAU	128 $MBits/s$
Electrical bit duration	1.3 ns
Electrical pulse duration	0.2 ns
Optical pulse repetition rate	768 MHz
Optical pulse width	40 ps
Optical signal center frequency	193.1 THz
Fiber length between the MSC and BS	20 km
Fiber length between the BS and RAU	0.3 km

Observe in Figure 4.14 that at the BS, the incoming optical signal is amplified using an EDFA and split into two paths using an optical coupler. Optical filters having center frequencies of f_1 = 193.1 THz and f_2 = 193.16 THz are used in each path to separate the two optical pulsed sources, as shown by the stylized plots in Figure 4.14. The output of each optical filter is fed to an optical power splitter which demultiplexes the input signal into six paths, as shown in Figure 4.14. The six optical signals each at the frequency of f_2 193.16 THz are then coupled with an optical signal at the output of Splitter 2 in Figure 4.14 and transmitted to each RAU over 0.3 km fibers. It can be observed from the stylized plots in Figure 4.14 that the signal at each output of Splitter 1 is delayed in time by different amounts using optical delay lines. The amount of time delay imposed by each delay line is adjusted to ensure that at the end of the 0.3 km SMF, the optical pulses at f_2 in each path overlap in time with one of the channels in the multiplexed optical signal for each of the RAU. The time domain overlap of the pulses in the two signals at frequencies f_1 and f_2 can be seen in Figure 4.15, indicating that the pulse in path 1 of Splitter 1, namely the one transmitted to RAU 1, overlaps in time with the binary data in channel 1 of the TDM signal at frequency f_1 = 193.1 THz. The plot shown in Figure 4.15 is a magnified version of the stylized plots shown in Figure 4.14. Therefore, the first delay line, which is in path 1 of the splitter applies a small time delay to the signal in order to compensate for the difference in transmission speeds between the signals at f_1 and f_2 [56], as discussed in Section 2.2.2. Similarly, it can be observed from Figure 4.15 that the pulse in path 2 at f_2 = 193.16 THz overlaps in time with the binary data of channel 2 of the TDM signal at f_1. The same overlap of pulses is achieved for the rest of the channels. The overlap of pulses will be used to optically demultiplex the data of each channel at the RAU as well as to transmit the data at 60 GHz frequency by involving heterodyning, as detailed in Section 3.1.

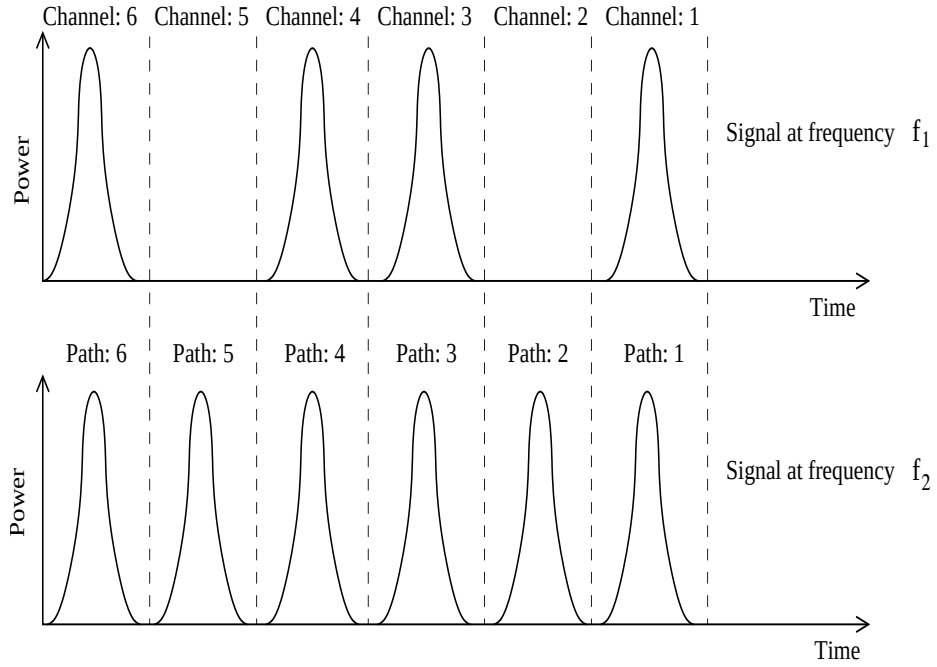

Figure 4.15: Time domain representation of signals at frequencies f_1 and f_2.

4.4.2.1 Demultiplexing and Multiple 60 GHz Signal Generation

The optical signals at frequencies f_1 and f_2 that are coupled together at the BS are received at each of the RAUs, as shown in Figure 4.14. The combined optical signal is photodetected at the RAU to generate a frequency of 60 GHz through heterodyne detection [124], as detailed in Section 3.1. The 60 GHz signal will be generated at the output of the PD only if both the pulses of the signals f_1 and f_2 are input to the PD at the same instant in time. An electronic filter is used at the output of the PD to retain the 60 GHz signal. Therefore, the signal at frequency f_2 is used to optically demodulate the data at the center frequency f_1 at each of the RAUs. Apart from performing demultiplexing, the signal f_2 also helps in generating the baseband data at 60 GHz frequency. Figure 4.16 shows the time domain overlap of the two pulses at the input of the PD in order to demultiplex and transmit the data at 60 GHz frequency. Since the difference in frequency between the coherent signals at f_1 and f_2 is 60 GHz, the RF signal generated at the output of the PD has a frequency of 60 GHz.

In order to avoid interference among the 60 GHz signals transmitted by different RAUs, it is desirable to generate the 60 GHz signal for each RAU at a different center frequency. The proposed scheme allows us to achieve this desirable feature by simply varying the overlap-duration between the signals at frequency f_1 and f_2 that are input to the PD of Figure 4.14. As shown in Figure 4.16, the optical signals at the input of the PD are chirped[1] owing to the fiber-induced dispersion [56]. As mentioned in [56], an optical pulse consists of a carrier wave with an envelope that is Gaussian in time. It has been mentioned in Section 2.2.2, that fiber dispersion varies the phase of the optical pulse. Since the instantaneous frequency is defined as the rate of change of

[1]Chirp is defined as the linear variation in the instantaneous frequency of the optical pulse with time. [56]

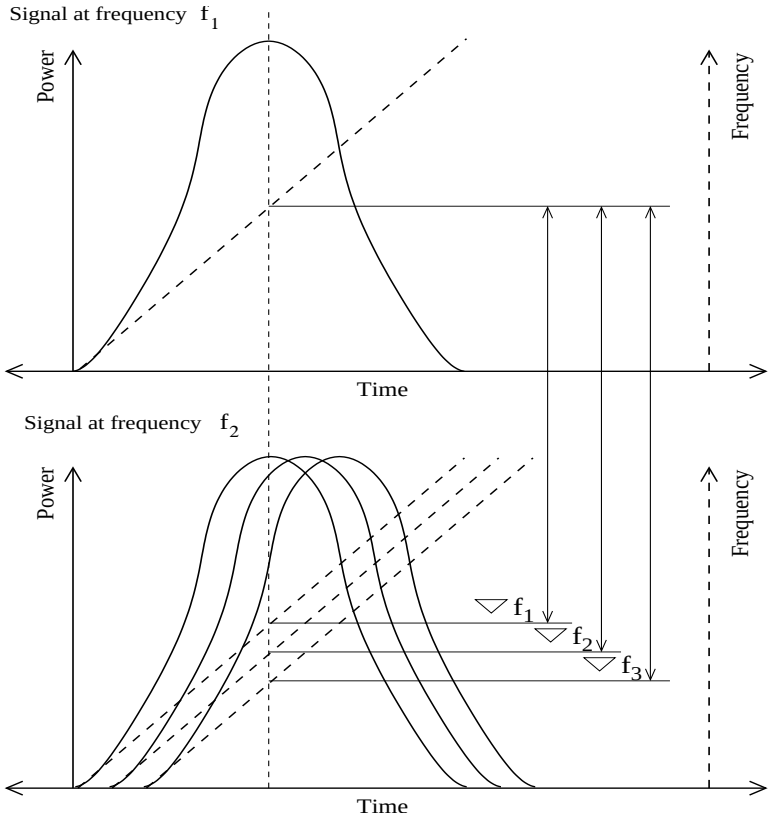

Figure 4.16: Time domain overlap of signals at frequencies f_1 and f_2.

phase, therefore, a change in phase due to dispersion results in a linear variation in the instantaneous frequency versus time with in the pulse. Therefore, by controlling the time delay between the two overlapping pulses at f_1 and f_2, the instantaneous difference in frequency between the two pulses that are input to the PD can be varied by simply tuning the optical delay lines located at the BS. The delay line generally consists of a short length of fiber or a free space region whose length can be mechanically controlled. It will be shown in the next section that the 60 GHz baseband data generated at each RAU having a different center frequency gives BER result, which is within 1 dB of the idealized non-dispersive back-to-back (BB) channels.

4.4.3 Performance Results

In this section, we discuss the BER results obtained for the six baseband channels transmitted from the CU to RAUs through the BS. The components used at the MS's receiver in order to retrieve the baseband data transmitted at a carrier frequency of 60 GHz by the RAUs are shown in Figure 4.17. The wireless signal received at the MS is filtered by an Electronic Filter (EF) at the 60 GHz frequency and it is then passed through an Electronic Amplifier (EA). The signal at the output of the amplifier is divided into two paths by a splitter, as shown in Figure 4.17. The signal is down-converted to baseband signal with the aid of self-mixing, as described in [73]. Self-mixing is a technique for down-converting a high-frequency signal without using a separate oscillator, by mixing together two copies of the signal [73]. The down-converted signal is filtered using a Low-

Pass Filter (LPF) and finally, BER measurements are performed in order to assess the performance of the proposed link.

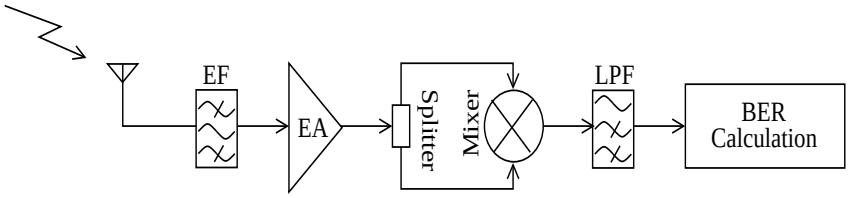

Figure 4.17: Components of the MS receiver.

As mentioned in Section 4.4.2.1, the center frequency of the 60 GHz signal transmitted by each RAU may be varied by appropriately adjusting the delay lines used at the BS. We have set the time delay for each of the delay lines to values that generate frequencies ranging from 56 GHz to 61 GHz for channels 1 to 6, respectively, where the frequency spacing between the 128 MHz wide adjacent channels is 1 GHz. Therefore, the baseband channels have different center frequencies, which results in avoiding the interference among them. Figure 4.18 shows the BER results for all the six baseband channels. The BER is calculated using statistical methods, where the received signal is compared to the transmitted signal. For sake of comparison, the figure also shows the back-to-back BER results for all the channels. The back-to-back results are obtained by removing the fibers used in the network. The optical pulsed sources used in our simulations are assumed to be chirp-free, therefore, the chirp imposed on the pulses received at the PD is due to the dispersion of the optical fiber used in the network, as discussed in Section 2.2.2. Chirp is defined in Section 4.4.2.1 as the linear variation in the instantaneous frequency of the optical pulse with time. Since the back-to-back case does not use any optical fiber, there will be no chirp imposed on the pulses received at the PD. Hence, we generate all the channels at the same frequency of 60 GHz for the back-to-back BER measurements.

It can be observed from Figure 4.18 that the proposed baseband architecture results in BER values which are within a dB of the back-to-back results. The sensitivity of the receiver is defined as the optical power required for achieving a BER of 10^{-9}. Figure 4.18 shows that the difference in sensitivity among the six channels is about 0.8 dB. The major reason for this difference is the selection of different center frequencies for the channels. Ideally, each channel should generate the transmitted signal at a frequency of 60 GHz, which is the actual frequency difference between the two coherent pulsed sources used at the MSC. However, in order to avoid interference among the signals of different RAUs, the center frequencies chosen are different. This frequency difference is achieved by varying the delay between the optical signals at f_1 and f_2, which in turn causes a sensitivity difference amongst the received signals. It can be observed from Figure 4.18 that channel 1 has the worst sensitivity among the six channels. This is due to the maximum frequency shift between the center frequency of channel 1 (56 GHz) and the nominal frequency of 60 GHz. Figure 4.18 also shows that the BER results of the back-to-back scenario are also different. The main reason for this variation is the use of rounded values for the time delays applied at the BS, given the total bit rate of 128 x 6 = 768 $Mbits/s$, the time delay per channel is not an integer

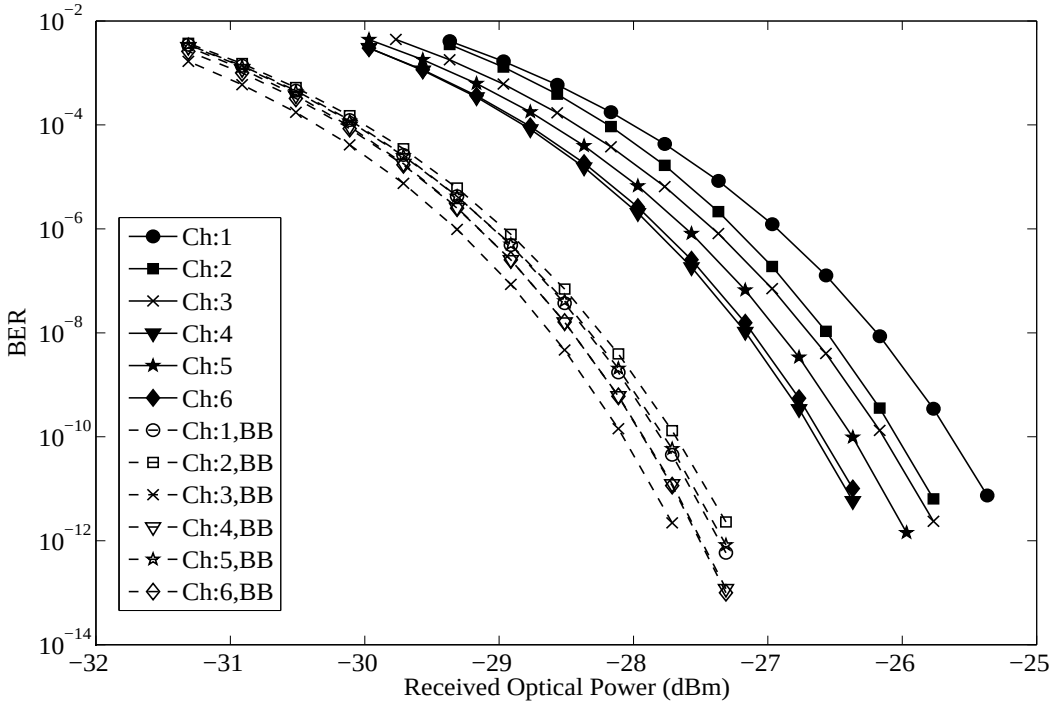

Figure 4.18: BER results for the six baseband channels. The BER is calculated using statistical methods, where the received signal is compared to the transmitted signal.

number and it is therefore rounded to the nearest decimal value. This rounding of the time delay results in some variation in the BER results for both the back-to-back as well as for the fiber transmission scenario.

In order to observe the received baseband signal quality, the eye diagrams for channel 1 and channel 6 are plotted in Figure 4.19. The eye diagrams for the two channels are obtained after photodetection and down-conversion for a sensitivity value required for achieving a BER of 10^{-9}. It can be observed from Figure 4.19 that the received baseband signals exhibit an open eye, which implies that the distance of the ROF link may be further increased.

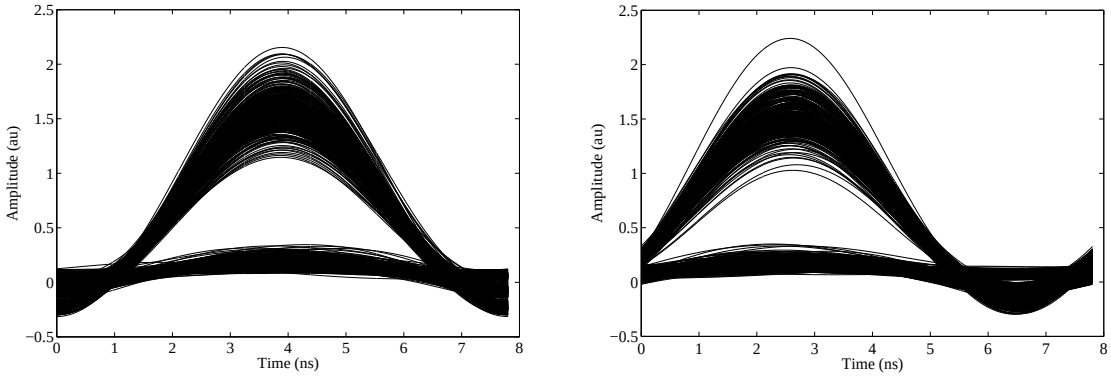

(a) Channel: 1 (b) Channel: 6

Figure 4.19: Eye diagrams of Channel 1 and Channel 6.

4.4.4 Effect of Time Delay Mismatch

It has been shown in Section 4.4.3 that the BER results obtained for all the six baseband channels are close to those of their back-to-back counterparts. However, the BER results of Section 4.4.3 were obtained using the optimum time delay between the signals at frequencies f_1 and f_2. However, due to the presence of a large number of components in the optical link as well as due to the usual temperature effects, the time delay imposed on the optical signal by the optical link and the delay lines may vary. This variation in the time delay may result in a performance degradation for our proposed BROF architecture. Hence we also generated the BER results for different values of time delay mismatch between the signals at frequencies f_1 and f_2. Observe from the results of Figure 4.20 that the received powers of each of the six baseband channels were set to a value, which gives a BER of 10^{-9} for the optimum time delay. At this point, time delay variations are imposed at the BS to observe the variation in the BER of each of the channels. Figure 4.20 shows the BER results against the time delay between the signals at frequencies f_1 and f_2. The variation in time delay is plotted as a percentage of the pulse width which was chosen to be 40 ps, as mentioned in Section 4.4.2. It can be observed from Figure 4.20 that the performance of our proposed architecture remains largely unaffected by the time delay variations. The worst-case BER is 10^{-6} for a time delay as high as 50% of the pulse width. Therefore, the proposed BROF architecture may be deemed to be resistant to changes in the parameters of the passive elements used in the network.

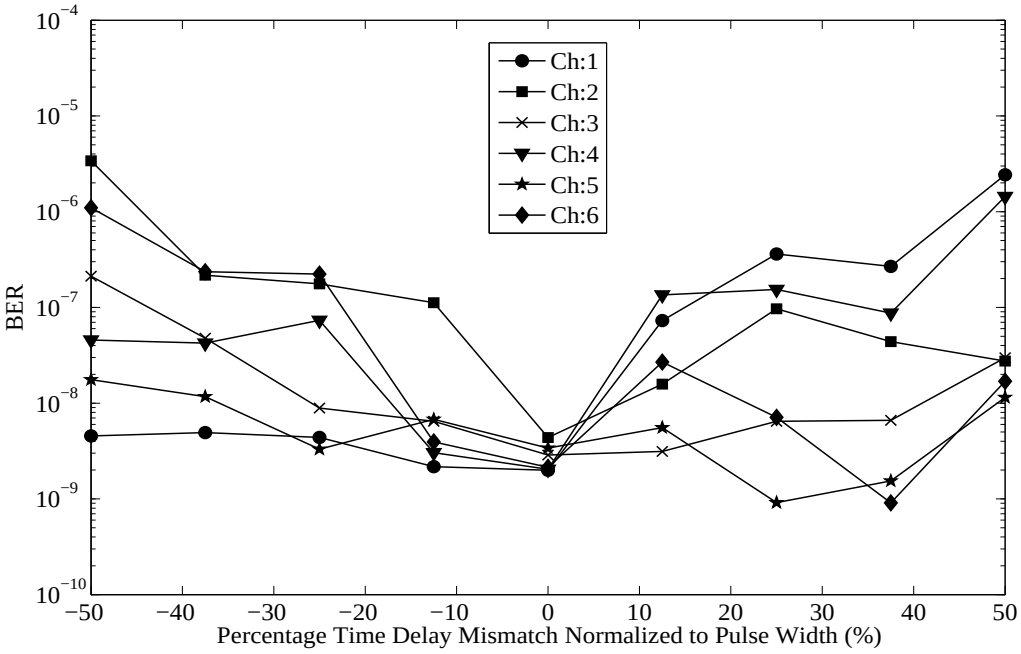

Figure 4.20: BER versus time delay mismatch.

4.5 Conclusions

We have discussed the SPM based regenerator of Figure 4.3 in detail, which is one of the simplest, yet effective all-optical regenerator that has been proposed. Our numerical study characterizes the performance of the regenerator by taking into account the dispersion slope parameter of the HNLF used in the regenerator setup. The main conclusions from our study are as follows:

- Both the dispersion slope and the dispersion parameter may be used as an additional parameter of controlling the regenerator's performance.
- The power gain of the regenerator may be increased by using a HNLF having a high dispersion slope along with a suitable value of the output filter's center frequency.
- The effect of pulse-to-pulse overlapping imposed in the regenerator may be reduced by choosing a short HNLF section having a high dispersion slope.

We have also presented a ROF architecture that uses TDM baseband over fiber communications to simultaneously transmit data to six different RAUs. The data is transmitted to each RAU at a different frequency in the 60 GHz band. The perfromance results of the proposed architecture are close to those of to the back-to-back benchmarker. We have also considered the effect of timing jitter on the system performance. It has been shown that the worst-case BER of the six channels is 10^{-6} for a time delay as high as 50% of the optical pulse width.

Table 4.6 summarizes the performance of the BROF architecture in terms of the optical receiver sensitivity of each RAU. The sensitivity of an optical receiver is defined as the received power required to achieve a BER of 1x10^{-9}.

Table 4.6: Performance summary of the baseband architecture of Figure 4.14. The receiver sensitivity results were extracted from Figure 4.18.

RAU	Receiver Sensitivity with Fiber	Back-to-Back Receiver Sensitivity
RAU 1	-25.8 dBm	-28.1 dBm
RAU 2	-26.3 dBm	-27.9 dBm
RAU 3	-26.4 dBm	-28.4 dBm
RAU 4	-26.9 dBm	-28.2 dBm
RAU 5	-26.6 dBm	-28.1 dBm
RAU 6	-26.8 dBm	-28.2 dBm

Chapter 5

Analogue ROF Communication

In this chapter, we will present our contributions to the second major family of ROF communication systems, namely to the class of AROF arrangements portrayed in Figure 5.1. We will present a cost-effective physical layer design conceived for centralized DAS architectures relying on AROF communication. Section 5.5 presents a low-complexity, hence cost effective solution designed for the duplex transmission of SCM RF signals using QAM between the CU and MSs in a ring architecture. The second study provided in Section 5.8 discusses the feasibility of ROF transmission of SCM mm-wavelength signals to a pair of RAUs, which form part of a virtual MIMO architecture under the control of a CU. The ROF signal is transmitted over intermediate frequency carriers in order to avoid the effects of dispersion in the fiber. Heterodyne detection is used at the RAUs to generate mm-wavelength signals. The multiple optical carriers used for both data transmission as well as for heterodyning at the RAUs are generated using a single laser source in both Section 5.5 and 5.8.

5.1 Analogue ROF Architecture

Figure 5.1 shows the typical architecture of an AROF communication system. The baseband data is upconverted to a RF signal in the upconversion block. The RF signal is converted to an optical signal in the E-O block and the resultant optical signal is transmitted over the optical medium. At the receiver, O-E conversion is performed for retrieving the RF signal, as shown in Figure 5.1. The resultant RF signal is transmitted through the antenna after performing filtering and amplification, as shown in Figure 5.1. Observe in Figure 5.1 that in contrast to the baseband architecture of Figure 4.1, the upconversion is performed at the transmitter. Furthermore, it will be shown in Section 6.1 that in case of DROF transmission, the upconverted signal is digitized before performing E-O conversion.

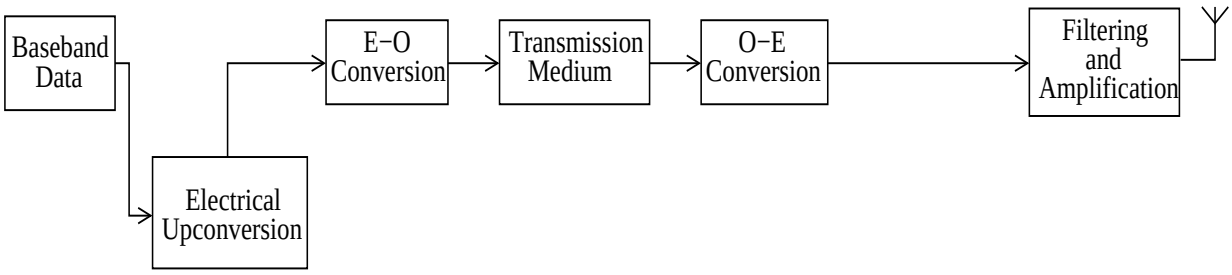

Figure 5.1: General architecture of an AROF system. In contrast to BROF system of Figure 4.1, the upconversion is performed at the transmitter rather than the receiver.

5.2 Background - Centralized Distributed Antenna Systems

ROF systems constitute a cost effective solution for the interconnection of BSs or for feeding the so-called distributed antennas [125]. The Distributed Antenna Systems (DASs) seen in Figure 4.13 are capable of supporting high data rate services with the aid of ROF links. In a DAS architecture, the RAUs transmit to the MSs in the DL. These RAUs are in turn connected to the CU seen in Figure 4.13, where joint processing of all the data arriving from the RAUs is performed [13], [9]. A centralized ROF link design provides a cost effective solution for connecting all these RAUs to the CU. A significant amount of work has been carried out on centralizing the DAS architecture for ensuring that the minimum number of optical components is required. Table 5.1 summarizes the major contributions in the area of centralized DAS architectures over the past decade. In all the contributions mentioned in Table 5.1, the aim was to conceive an architecture, where most of the system components are located at the CU. Against this background, we will discuss our novel contributions in the area of centralized DAS architectures in the following sections.

Table 5.1: Summary of major contributions towards centralized DASs.

Author(s)	Contribution
[124] T. Kuri *et al.* 2003	DQPSK-modulated RF signal is transmitted to a single RAU at a mm-wavelength carrier frequency, which is generated by heterodyning the received ROF signal with a dual-mode laser located at the RAU.
[126] X. Zhang *et al.* 2006	DPSK RF signals are transmitted at a mm-wavelength frequency using two separate optical carriers that are transmitted from the CU to the RAU.
[120] L. Chen *et al.* 2007	A dual-mode light generated using Optical Carrier Suppression (OCS) at the CU is used for transmitting duplex baseband data to a single RAU.
[121] J. Yu *et al.* 2007	A phase modulator is used for generating multiple coherent sidebands while retaining the carrier, but suppressing the odd-indexed sidebands. Duplex baseband data is transmitted to a single RAU.

Continued on Next Page...

Table 5.1 – Continued

Author(s)	Contribution
[127] Y. Kim *et al.* 2008	A phase modulator along with two Fiber Bragg Gratings (FBGs) is used for transmitting a unidirectional 64-QAM signal to a single RAU. The FBGs are used for retaining the optical sidebands that have a separation of 12.5 GHz.
[128] M. F. Huang *et al.* 2008	The technique mentioned in this study is similar to the one proposed in [127], except that in [128], an intensity modulator (IM) is used for generating multiple coherent side-bands.
[122] Y-T. Hsueh *et al.* 2009	Two high-frequency (20 GHz and 40 GHz) local oscillators are used in conjuction with intensity modulation for generating multiple coherent sidebands at the CU. The baseband data is transmitted using narrow-band optical filters and interleavers at the RAUs.
[129] H-C. Ji *et al.* 2009	A single 16-QAM signal is transmitted to a single RAU by phase modulating an optical carrier in the DL, while intensity modulating the same optical carrier for UL data transmission.
[130] J. Yu *et al.* 2010	Different methods are conceived for transmitting RF signals at different mm-wavelength frequencies using high-frequency cascaded modulators at the CU.
[131] J. James *et al.* 2010	A local oscillator having a frequency of 23.152 GHz is used for generating coherent optical sidebands for mm-wavelength signal generation. A unidirectional single RF signal is transmitted to a single RAU.
[123] C-H. Chang *et al.* 2010	Direct modulation of a laser source is used for generating multiple sidebands used for transmitting a single RF baseband signal in the DL direction. A combination of optical circulators and FBGs is used for narrow-band filtering of the multiple sidebands.

5.3 Single Laser Based DAS Ring Architecture

In this section we will design an AROF system that is used for facilitating duplex communication among three BSs located at different positions in the ring architecture of Figure 5.2. An early ring architecture conceived for the distribution of ROF signals using multiple optical sources has been proposed in [77]. However, as a further advance, the architecture discussed in this section uses a single laser source at the MSC for generating multiple coherent sidebands used for duplex data transmission. As discussed in Section 3.3, an AROF system only requires a PD for detecting the optical signal received and an electronic amplifier for amplifying the resultant RF signal. The amplified RF signal is then transmitted in the DL to the MSs using BS antennas, as seen in Figure 5.2. Again, in our proposed scheme, we use the ring architecture of Figure 5.2, where a MSC transmits data for example to three BSs using an optical link. Observe in Figure 5.2 that a PSTN delivers

the tele-traffic to the MSC using an optical fiber. The MSC then routes the tele-traffic from the PSTN to the appropriate BSs in the particular ring that is associated with the MSC. Finally, the BSs forward the corresponding RF signal to the MSs and also return the UL RF signals received from the MSs to the MSC through the same ring. At the MSC, the OCS technique [132]- [133] of Section 5.4 is used for generating six side-bands for the bi-directional data of each of the BSs, as seen in Figure 5.2. The wavelength of each side-band is also shown in Figure 5.2. Again our goal is to design a single-diode aided OCS transmitter-receiver pair (transceiver) for employment either at the MSCs or BSs. Against this background, we will discuss the following contributions towards

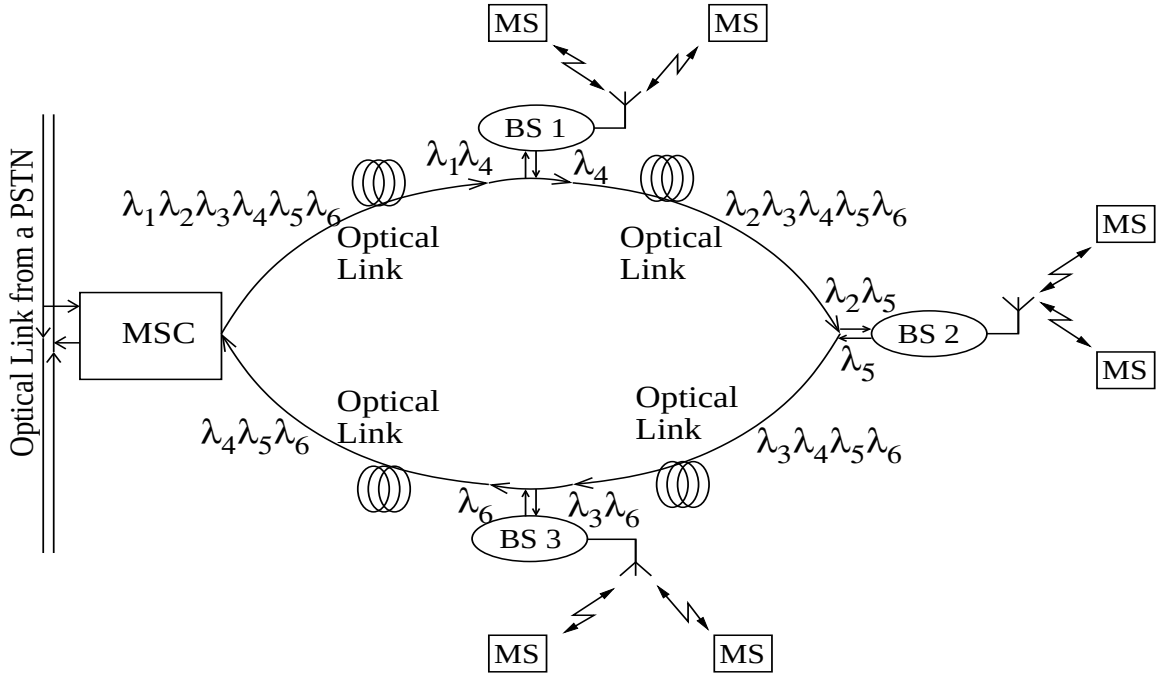

Figure 5.2: The duplex UL/DL AROF based ring architecture. In contrast to BROF based star architecture of Figure 4.13, the upconversion is performed at the transmitter rather than the receiver.

ROF communications:

1- We generate multiple optical side-bands using a single laser source at the MSC of Figure 5.2. The feasibility of transmitting four 16-QAM SCM channels at 10 $MSymbols/s$ in the DL and at 5 $MSymbols/s$ in the UL on each side-band of the carrier is assessed on the basis of the ROF link's EVM performance.

2- The duplex UL/DL transmissions are supported simultaneously for the three different BSs of Figure 5.2 without requiring a separate laser source at the BSs. Hence all the high-complexity signal processing tasks are performed at the MSC, which facilitates a low-complexity BS design.

3- We also show that the quality of the RF signals transmitted to any particular BS of Figure 5.2 can be dynamically controlled by simply varying the parameters of the remote RF local oscillator located at the MSC.

The distance between the BSs is limited to 10 km to achieve satisfactory performance in both the DL and UL directions. Furthermore, the number of SCM channels and the symbol rate of each channel is optimized to obtain the best performance. Upon increasing the distance between the BSs, the number of SCM channels or the symbol rate, the performance of the system is degraded due to the impairments induced by the ROF link. The simulation tool used for our numerical study is the VPITransmissionMaker 8.6 (www.vpiphotonics.com) commercial software.

5.4 Generating Multiple Side-bands Using OCS

To elaborate further in the context of Figure 5.3, we use the OCS technique for generating six optical side-bands from a single laser source using a DD-MZM similar to Figure 2.8, whose operating principle was discussed in Section 2.1.4.2. We observe from Figure 5.3 that the MZM is biased to a non-zero DC value. At this point a sinusoidal RF signal is superimposed on the DC bias in order to generate an optical signal, whose carrier is suppressed. The optical carrier of $E_c(t) = A_c exp(jw_c t)$ generated by the LD of Figure 2.3 having an amplitude of A_c and a frequency of w_c is applied to the input of the DD-MZM detailed in Figure 2.8. The two arms of the MZM are driven by sinusoidal RF signals having equal amplitudes and a 180^o phase shift between them. The two drive voltages applied to the MZM's electrodes may be written as $V_{r1}(t) = V_{dc1} + V_r cos(w_r t + \phi_1)$ and $V_{r2}(t) = V_{dc2} + V_r cos(w_r t + \phi_2)$, where V_{dc}, V_r, w_r and ϕ are the DC bias voltages, RF signal amplitude, RF signal frequency and phase, respectively. As seen in Figure 5.3, the MZM's transmittance versus bias characteristic is a nonlinear function, therefore it will generate higher-order optical side-bands, when a RF signal is applied to its terminals. The number of higher-order side-bands generated depends on the RF signal's amplitude V_r. As seen in Figure 5.3, a high value of

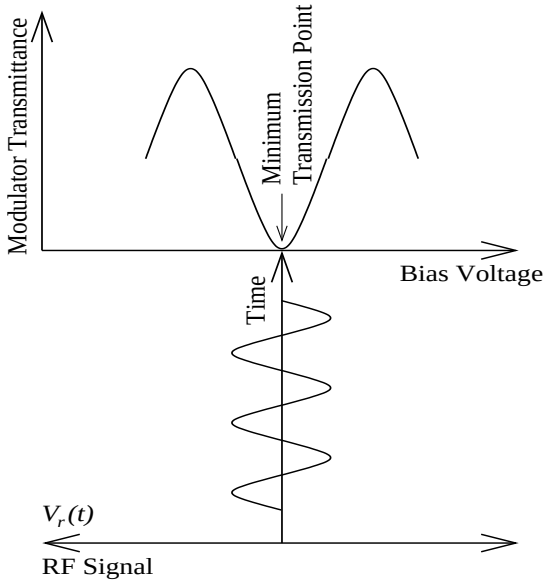

Figure 5.3: Time-domain operation of the OCS.

V_r increases the non-linearity of the MZM's transfer characteristic, which results in an increased

number of higher-order side-bands generated at the output. The optical signal at the output of the DD-MZM may be written as the sum of the optical signal in each arm of the MZM as follows:

$$E_M(t) = \frac{A_c}{2}\left(e^{j\frac{\pi V_{r1}(t)}{V_\pi}} + \psi e^{j\frac{\pi V_{r2}(t)}{V_\pi}}\right)e^{jw_c t}, \tag{5.1}$$

where V_π is the voltage required for inducing a phase-shift of π for each of the MZM arms and ψ accounts for the non-ideal extinction ratio ε of the MZM. The value of ψ lies between 0 and 1, which is related to ε as $\psi = (\sqrt{\varepsilon}-1)/(\sqrt{\varepsilon}+1)$ [134], [133]. The output of the DD-MZM may be further expressed in terms of Bessel functions as [135]:

$$E_M(t) = \frac{A_c}{2}\left[\sum_{n=-\infty}^{\infty} J_n(m_r)\left(e^{j(\phi_v+n\phi_d)} + \psi e^{-j(\phi_v+n\phi_d)}\right)e^{jn(w_r t+\phi_m)}\right]\cdot e^{jw_c t}, \tag{5.2}$$

where J_n is the Bessel function of first kind and order n, while

$$m_r = \frac{\pi V_r}{V_\pi}, \tag{5.3a}$$

$$\phi_v = \frac{\pi(V_{dc1}-V_{dc2})}{2V_\pi}, \tag{5.3b}$$

$$\phi_d = \frac{(\phi_1-\phi_2)}{2}, \tag{5.3c}$$

$$\phi_m = \frac{(\phi_1+\phi_2)}{2}. \tag{5.3d}$$

The value of V_r chosen in our simulations is $V_r = 0.9 \cdot V_\pi$, therefore the argument of the Bessel function m_r becomes 2.82. Furthermore, in order to operate the DD-MZM in a double side-band suppressed carrier (DSB-SC) configuration, we choose $\phi_1 - \phi_2 = \pi$ and $V_{dc1} - V_{dc2} = V_\pi$. Substituting these values into Equation 5.2 and further simplifying it gives the following relation for the optical signal at the output of the DD-MZM:

$$E_M(t) = \frac{A_c}{2}\left[\sum_{n=-\infty}^{\infty} J_n(2.82)\left(j(e^{jn\pi} - \psi) \times e^{jn(w_r t+\phi_1)}\right)\right]\cdot e^{jw_c t}. \tag{5.4}$$

It can be observed from the Bessel function expansion of Equation 5.4 that for an argument of 2.82, we arrive at six side-bands having a sufficiently unattenuated magnitude on each side of the input optical carrier. The power of each side-band depends upon the value of the extinction ratio ε of the MZM and can be calculated using Equation 5.4. Equation 5.4 suggests that a high value of ε will result in a higher suppression of both the carrier and of the even-indexed side-bands. It is useful to suppress both the carrier and the even-indexed side-bands in order to avoid power saturation of the PD. The DD-MZM used in our study has an extinction ratio of 35 dB.

The spectrum of the OCS signal generated in our simulations is shown in Figure 5.4. This spectrum was obtained by applying a RF signal having a frequency of 12.5 GHz. It can be observed from Figure 5.4 that the output spectrum of the MZM contains a carrier attenuated by 40

dB, while the even-indexed side-bands are attenuated by 32 dB compared to the first-order odd-indexed side-bands. The frequency spacing between consecutive odd-indexed side-bands is twice that of the RF frequency applied. The OCS technique allows us to obtain six sufficiently high-power different-wavelength optical carriers from a single laser source. Therefore this technique is useful in terms of reducing both the cost and complexity of a MSC or BS, which would require six different-wavelength laser sources in the absence of the proposed OCS technique. Furthermore, the OCS technique allows us to accurately control the spacing between the side-bands by simply varying the frequency of the RF signal applied.

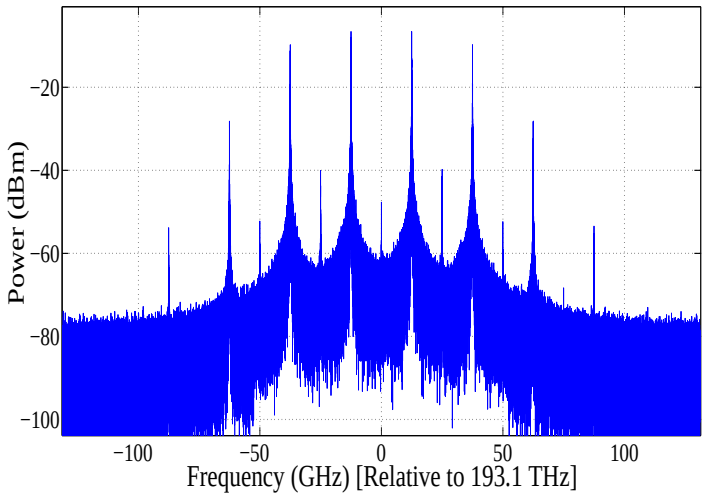

Figure 5.4: Optical spectrum at the output of DD-MZM.

5.5 The Proposed Bi-directional Ring Architechture

The schematic of our system is shown in Figure 5.5. The signal generated by the LD having the parameters shown in Figure 5.5, is passed through a DD-MZM biased using a DC source. Again, a sinusoidal signal having a frequency of 12.5 GHz is applied to the upper and lower branches of the MZM with the aim of generating multiple side-bands at the desired frequencies, as seen in Figure 5.4. The signal at the output of the DD-MZM having multiple side-bands is amplified using the EDFA of Figure 2.18 and having a noise figure of 6 dB as well as a constant output power of 1 W. As observed in Figure 5.4, the side-bands at the output of the DD-MZM that are located farthest from the center frequency of the LD exhibit the lowest powers. Therefore, these side-bands will have lower SNR owing to the higher ASE noise imposed on them due to the EDFA. The output of the EDFA is fed to the 1x8 AWG of Figure 2.20 having a channel spacing of 25 GHz. Each of the AWG's channel performs Gaussian filtering having a 3-dB bandwidth of 25 GHz centered at the odd-indexed optical side-bands. The optical signals having different central frequencies at the output of the AWG are labelled by λ_1, λ_2, λ_3, λ_4, λ_5 and λ_6, as shown in Figure 5.5. The signals λ_1, λ_2 and λ_3, used for the MSC-BSs DL transmission are intensity-modulated by RF signals at the MSC using a MZM. The RF signals transmitted over the carriers λ_1, λ_2 and λ_3 are composed of

four SCM signals having central frequencies of $f_1 = 1GHz$, $f_2 = 1.16GHz$ and $f_3 = 1.32GHz$, respectively. Each SCM channel carries 16-QAM data at a symbol rate of 10 $MSymbols/s$. Therefore the data rate transmitted over each optical side-band is 160 $MBit/s$ and hence the total data rate in the DL direction over the three optical side-bands is 480 $MBit/s$. After intensity modulation, the resultant ROF signals having optical carriers of λ_1, λ_2 and λ_3 are multiplexed with the remaining three unmodulated signals, namely with λ_4, λ_5 and λ_6. The average optical power of each optical side-band throughout the link is maintained at about 8 dBm so as to avoid the effects of XPM between the channels. The XPM imposes phase noise on the signal, which is converted to amplitude noise due to fiber dispersion [18], [136], as detailed in Section 2.2.3. The phase noise increases upon increasing the average power of the signal, therefore the average power per optical side-band should be kept low. The spectral plot of the resultant multiplexed signal is shown in Figure 5.6.

It can be observed from the spectral plot of Figure 5.6 that the extinction ratio of the signal is limited by the noise at the base of the signal. This noise is imposed by the EDFA at the transmitter, which again becomes more pronounced for the side-bands that are farthest from the center of the spectrum. Since the AWG filters are not ideal, some noise contaminates the signal. After optical multiplexing, the signals are transmitted to three different BSs that are separated by spans of 10 km of SMF. Observe in Figure 5.5 that at each BS, an Optical Add-Drop Multiplexer (OADM) similar to that of Section 2.6.1 is used for dropping a modulated DL MSC-BS signal and an unmodulated carrier signal, which is used for transmitting the UL RF data from the BS to the MSC. The optical side-bands used for each BS as shown in Figure 5.5, are chosen on the basis of their Optical Signal to Noise Ratio (OSNR) and the distance covered by them. Accordingly, the side-bands λ_1 and λ_6, which have the lowest OSNR are used for transmitting data over a short span of SMF. The UL 16-QAM data transmitted by each BS has a symbol rate of 5 $MSymbols/s$. Since four SCM channels are used, the total UL data rate transmitted by each BS is $4 \cdot 4 \cdot 5 = 80MBit/s$. In the absence of the unmodulated signals λ_4-λ_6, the BSs would require separate LDs to transmit the UL signal back to the MSC's receiver. After propagating through the ring, the ROF signals λ_4-λ_6 are received at the MSC.

The architecture of the MSC's receiver has elements reminiscent of the BS's receiver, but it is nevertheless different in the sense that the BS receiver multiplexes the UL ROF signal with the signals intended for the rest of the BSs or for the MSC. The structure of the BS transceiver including the OADM is shown in Figure 5.7.

A 25 GHz AWG separates the different optical frequencies contained in the input signal. One of the received unmodulated optical signal is modulated by the BS's UL RF data and multiplexed with the remaining signals. The optical signal carrying the DL RF data for the BS is photodetected in order to extract the RF signal. The parameters of the PD are shown in Figure 5.7. The output of the PD is amplified using an electronic amplifier having a noise spectral density of $10 \times 10^{-12} A/Hz^{1/2}$. The signal at the output of the electronic amplifier is then demodulated by the 16-QAM demodulator, as shown in Figure 5.7 [137]. The demodulator is also used for quantifying the EVM of the received signals. Table 5.2 summarizes the parameters of the proposed ring

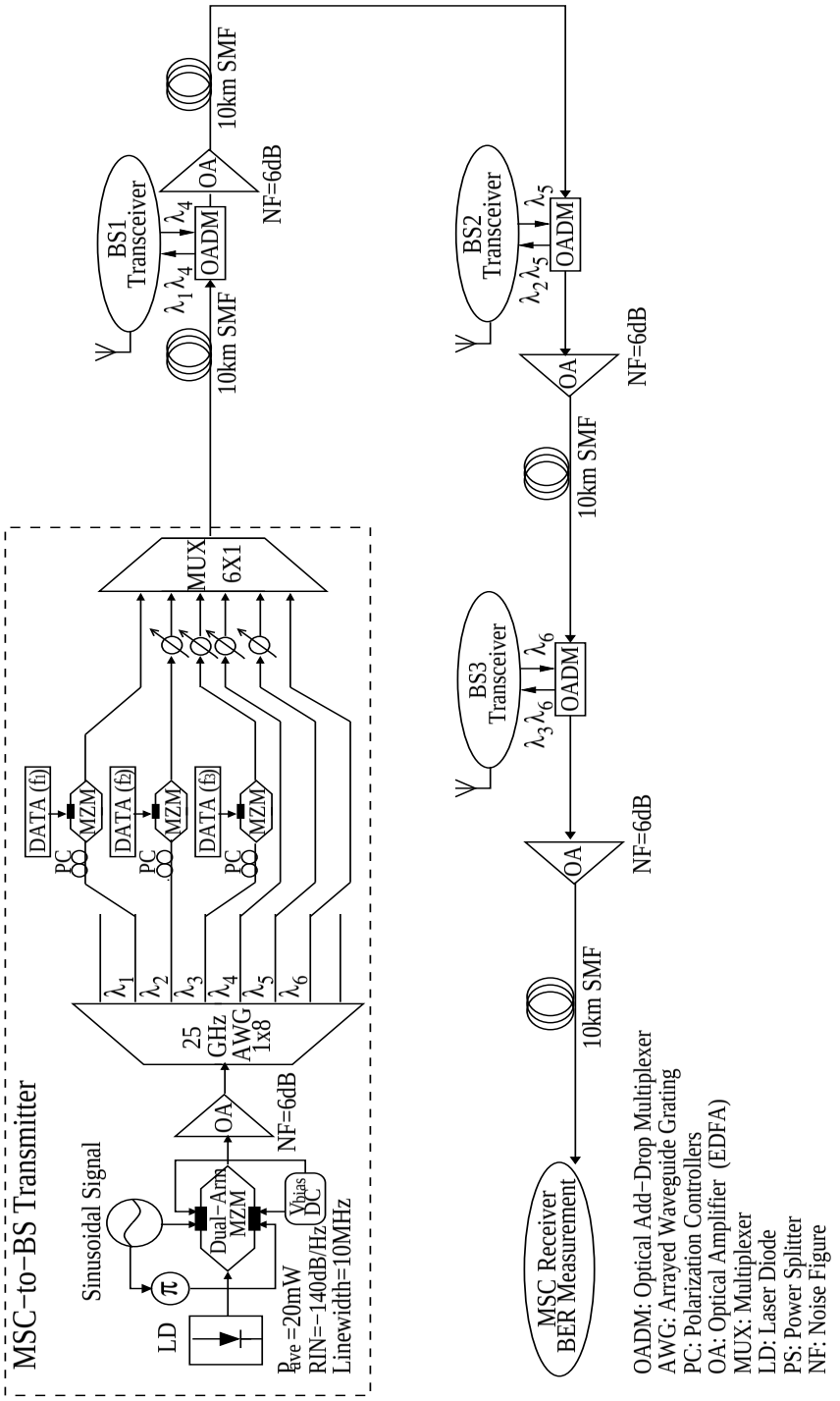

Figure 5.5: Schematic of the bi-directional ring architecture showing the physical layer design of the ring architecture of Figure 5.2.

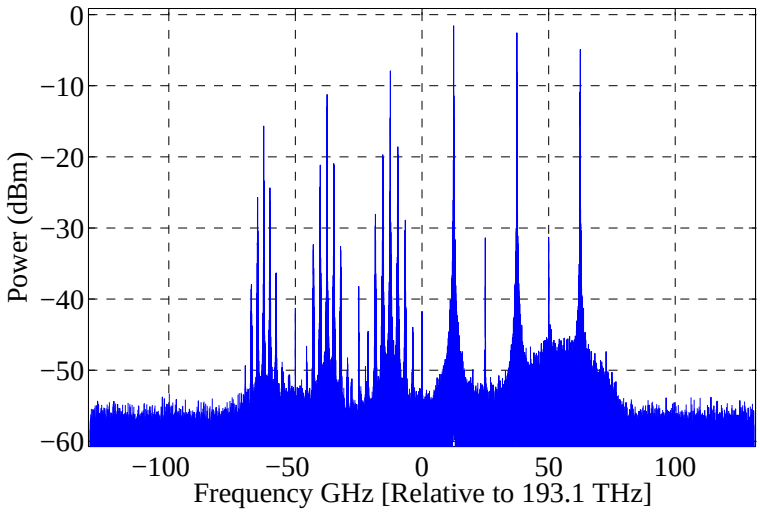

Figure 5.6: Optical spectrum of the multiplexed downstream signal at the output of the MSC. In contrast to the spectrum at the output of the DD-MZM shown in Figure 5.4, the three sidebands on the left are modulated with the DL ROF signals.

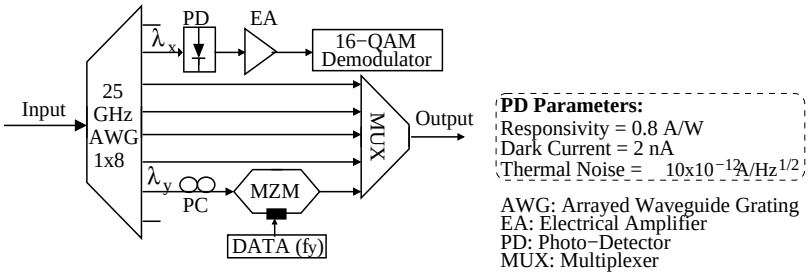

Figure 5.7: BS receiver schematic designed for the transmitter of Figure 5.5.

architecure of Figure 5.4.

Table 5.2: Parameters of the ring architecture of Figure 5.5.

Parameter	**Value**
SCM Channels per Optical Sideband	4
Number of DL and UL Optical Sidebands	3 DL and 3 UL
DL SCM Signal	16-QAM, 10 $MSymbols/s$
UL SCM Signal	16-QAM, 5 $MSymbols/s$
Optical Carrier Centre Frequency	193.1 THz
AWG Channel Spacing	25 GHz
AWG Channel Bandwidth	25 GHz
Fiber Dispersion	16 $ps/nm/km$
Fibre Span Between Successive BSs	10 km

Continued on Next Page...

Table 5.2 – Continued

Parameter	Value
Number of BSs	3
Noise Figure of Optical Amplifiers	6 dB
Photodetector Responsivity	0.8 A/W

5.6 Performance of the AROF Ring Network

Let us now characterize the proposed architecture of Figure 5.4 in terms of its EVM performance. The EVM is a measure of the difference between the expected complex-valued voltage of a demodulated symbol and the actual received symbol [138], which is formulated as [139], [140]:

$$EVM = \sqrt{\frac{\sum_{n=1}^{T}\left[\left(I_{Rx_n} - I_{Tx_n}\right)^2 + \left(Q_{Rx_n} - Q_{Tx_n}\right)^2\right]}{\sum_{n=1}^{T}\left(I_{Tx_n}^2 + Q_{Tx_n}^2\right)}}, \tag{5.5}$$

where T is the number of symbols transmitted, I_{Tx} and I_{Rx} represent the positions of the transmitted and received I-components, while Q_{Tx} and Q_{Rx} those of the transmitted and received Q-components, respectively. It may be observed from Equation 5.5 that the EVM is a measure of the relative root-mean-square error between the transmitted and received constellation points. In Figure 5.8, the EVM of the received RF signals is plotted against the Signal-to-Noise Ratio (SNR) of the RF signals. The SNR is measured after photo-detection at the receiver and it is varied by imposing ASE noise on the optical side-band carrying the RF signal. Figure 5.8 shows the EVM versus SNR results of the DL and UL RF signals of BS 1 in the schematic of Figure 5.5. The DL RF signal for BS 1 is transmitted using the side-band λ_1, while the UL RF signal is transmitted using the side-band λ_4, which has a considerably better OSNR than λ_1, as seen in the spectrum of Figure 5.6. Therefore the UL performance is higher than that for the DL RF signals. The higher achievable SNR and lower symbol rate of the UL signals results in EVM values as low as 2.2%, as observed in Figure 5.8. The worst EVM values obtained for the DL RF signals are close to 4 $\%$ and hence are still within the acceptable limit of 6 $\%$ for a 16-QAM 802.16a WiMax signal operating without channel equalization [37].

Figure 5.9 shows the corresponding EVM measurements for the DL and UL signals of BS 2 seen in Figure 5.4. The side-bands used for transmitting the DL and UL signals are λ_2 and λ_5. As seen from the spectrum of Figure 5.6, they have similar OSNR values. Therefore the maximum achievable SNRs for both the DL and UL RF signals of BS 2 are close to 35 dB. The lowest EVM values for UL transmission are seen in Figure 5.8 to be in the range of 2 $\%$, while for the

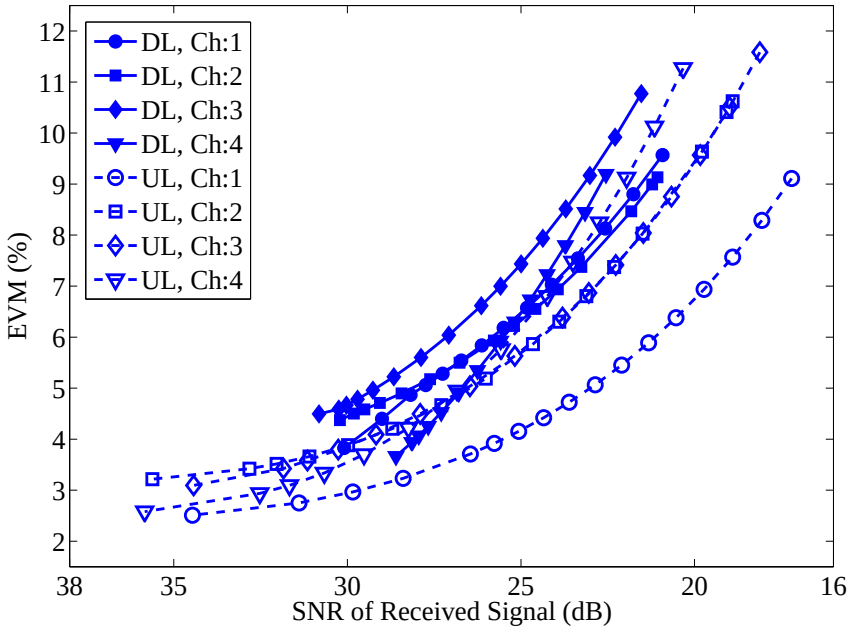

Figure 5.8: EVM of the received DL and UL RF signals of BS 1 seen in Figure 5.4. The system parameters are summarized in Table 5.2.

DL transmission they are in the range of 3 %. The difference in the EVM is a result of the higher symbol rate of the DL RF signals.

Finally, the EVM values of the DL and UL RF signals for BS 3 of the ring network seen in Figure 5.4 are shown in Figure 5.10. Here the DL signal is transmitted over the side-band λ_3, while the UL signal is transmitted over $\lambda_{6.}$. Again, since the OSNR of λ_3 is better than that of λ_6, therefore the maximum achievable SNR of the RF signals is higher for the DL signals than for the UL. It can be observed from Figure 5.10 that all the EVM values may fall below 4.5 %, which implies that our proposed architecture is suitable for transmitting higher-order modulation formats over long fibers.

5.6.1 EVM to BER Performance Relationship

In this section, we discuss the relationship between the EVM mentioned in Equation 5.5 as well as the BER of a QAM signal and observe the performance of the ring architecture in terms of the BER. In order to obtain the relationship between EVM and BER, it is assumed that the noise in the system is Gaussian and both the carrier as well as the phase of the received ROF signal is perfectly recovered. For M-ary modulation and Gaussian noise sources the BER may be written as [141],

$$BER = \frac{2(1-\frac{1}{L})}{\log_2 L} \cdot Q\left[\sqrt{\left(\frac{3\log_2 L}{L^2-1}\right)\frac{2E_b}{N_\circ}}\right], \tag{5.6}$$

where L is the number of levels in each dimension of the M-ary modulation system, E_b is the energy per bit and $N_\circ/2$ is the noise power spectral density. Furthermore, Q is the Gaussian Q-

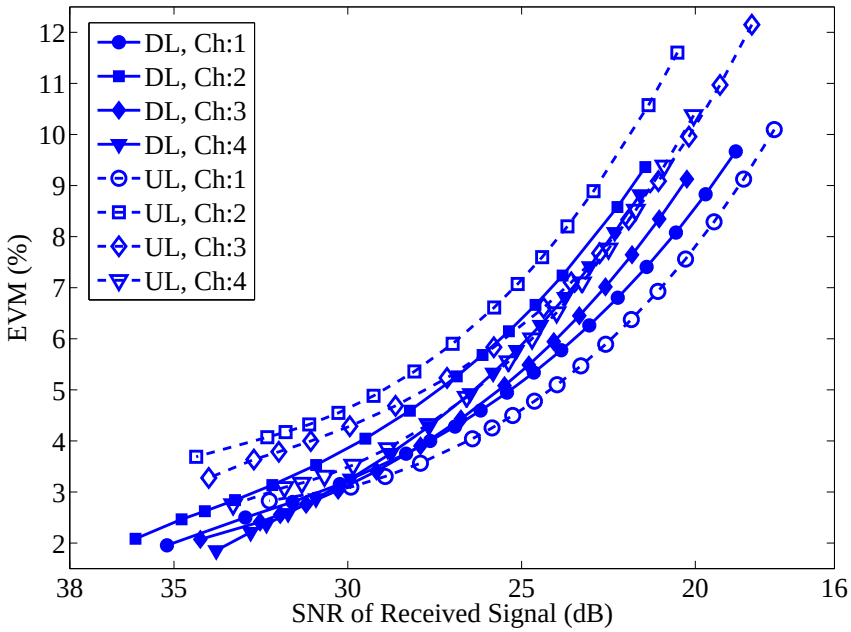

Figure 5.9: EVM of the received DL and UL RF signals of BS 2 seen in Figure 5.4. The system parameters are summarized in Table 5.2.

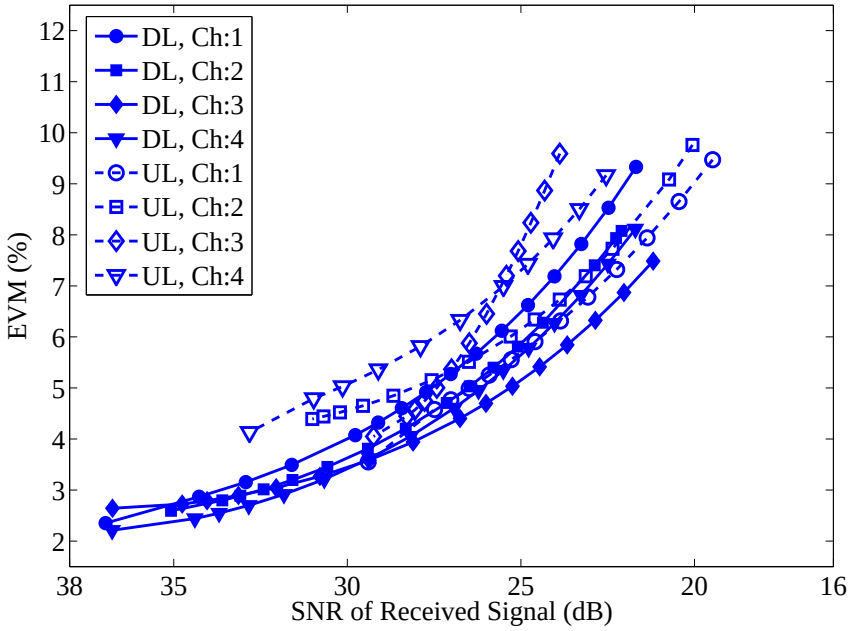

Figure 5.10: EVM of the received DL and UL RF signals of BS 3 seen in Figure 5.4. The system parameters are summarized in Table 5.2.

function given by [140],

$$Q(x) = \int_{x}^{\infty} \frac{1}{\sqrt{2\pi}} e^{\frac{-y^2}{2}} dy \tag{5.7}$$

For an M-ary system, the bit-energy and symbol-energy are related by:

$$E_b = \frac{E_s}{\log_2 M}, \tag{5.8}$$

where E_s is the energy per symbol. Substituting Equation 5.8 into 5.6 yields:

$$BER = \frac{2(1-\frac{1}{L})}{\log_2 L} \cdot Q\left[\sqrt{\left(\frac{3\log_2 L}{L^2-1}\right)\frac{2E_s}{N_\circ \log_2 M}}\right] \tag{5.9}$$

From Equation 5.5, the transmitted signal S_{Tx_n} and received signal S_{Rx_n} may be written as,

$$S_{Tx_n} = I_{Tx_n} + jQ_{Tx_n} \tag{5.10}$$

and

$$S_{Rx_n} = I_{Rx_n} + jQ_{Rx_n}. \tag{5.11}$$

Furthermore, the signal power may be written in terms of the transmitted signal as,

$$P_s = \frac{1}{T}\sum_{n=1}^{T}\left[(I_{Tx_n})^2 + (Q_{Tx_n})^2\right]. \tag{5.12}$$

Assuming an additive noise, the received signal may be written in terms of the transmitted signal S_{Tx_n} and complex noise n_n as,

$$S_{Rx_n} = S_{Tx_n} + n_n. \tag{5.13}$$

The complex noise n_n may be written as,

$$n_n = n_{I,n} + jn_{Q,n}, \tag{5.14}$$

where $n_{I,n}$ and $n_{Q,n}$ represent the I- and Q-component of the complex noise. From Equations 5.10, 5.11 and 5.14, the complex noise may be written as the difference between the received and transmitted signals as follows,

$$n_{I,n} + jn_{Q,n} = (I_{Rx_n} - I_{Tx_n}) + j(Q_{Rx_n} - jQ_{Tx_n}). \tag{5.15}$$

Substituting Equations 5.12, 5.14 and 5.15 into the EVM of Equation 5.5 gives the following result,

$$EVM = \sqrt{\frac{\frac{1}{T}\sum_{n=1}^{T} \mid n_n \mid^2}{P_s}}. \tag{5.16}$$

It can be observed that the numerator of Equation 5.16 represents the power of the noise imposed by the ROF link, while the denomenator represents the signal power, as mentioned in the context

of Equation 5.12. Therefore, Equation 5.16 characterizes the relation between the EVM and SNR as follows,

$$SNR = \frac{1}{EVM^2}. \tag{5.17}$$

Substituting Equation 5.17 into Equation 5.9 and using the relation of $SNR = E_s/N_\circ$ gives the following result for the BER of the signal in terms of EVM,

$$BER \simeq \frac{2(1-\frac{1}{L})}{\log_2 L} \cdot Q\left[\sqrt{\left(\frac{3\log_2 L}{L^2-1}\right)\frac{2}{EVM^2 \log_2 M}}\right]. \tag{5.18}$$

Equation 5.18 is used for generating the correspoding BER values of the ROF signals transmitted through the ring architecture. Figure 5.11 shows the BER values for the DL and UL signals of BS 1. It may be observed from Figure 5.11 that the BER results follow the trends observed in Figure 5.8 for the EVM values of BS 1. The BER of the UL signals is better in comparison to the DL signals, since the 16-QAM signals transmitted in the UL direction have half the symbol rate compared to the signals transmitted in the DL direction. The performance of the UL signals with the symbol rate equal to that of DL signals is not satisfactory. Therefore, the symbol rate in the UL direction is chosen half of the symbol rate in the DL direction.

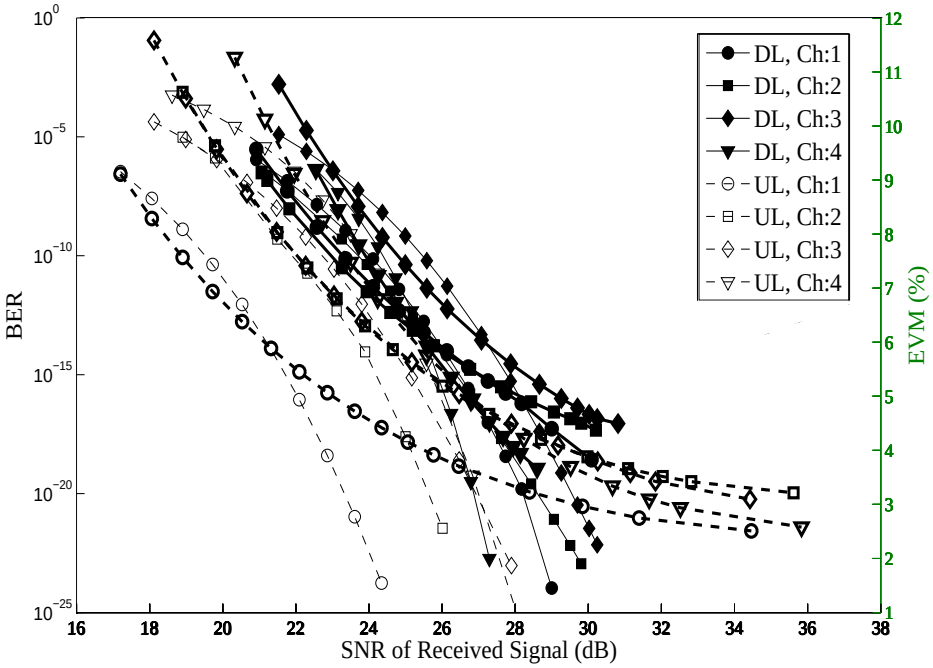

Figure 5.11: BER and EVM of the received DL and UL RF signals of BS 1 seen in Figure 5.4. The system parameters are summarized in Table 5.2. The BER results are obtained by using the EVM to BER performance relationship described in Section 5.6.1.

5.7 Effect of Parameter Variations on the Proposed Ring Architecture

The parameters of the components considered in our proposed ring architecture are similar to the parameters of commercially available devices. As noted in Sections 5.6 and 5.6.1, even with these imperfect components, the performance of the ROF link is of high integrity, as detailed further in this section by varying certain device parameters. This will enable us to assess the suitability of our proposed technique for employment in practical ROF links. The key feature of the link is the OCS technique of Section 5.4 relying on a high-amplitude sinusoidal signal for generating multiple side-bands. The two main components of the OCS technique that are prone to parameter variations are the DC bias source and the RF sinusoidal signal applied to the DD-MZM of Section 2.1.4.2. We consider their effects separately in the following sections.

5.7.1 Effect of DC Bias Variations

The DC sources used in electronic circuits are prone to variations in the output voltage due to temperature or aging effects. A variation in the DC bias applied to the DD-MZM of Section 2.1.4.2 changes the bias point and hence results in a reduced suppression of both the carrier and of the even-indexed side-bands. To quantify the extent to which bias point variations affect the performance of the architecture of Figure 5.4, we vary the bias point of the DD-MZM and observe the resultant variations in the EVM of the received RF signals. For this study, the SNR is chosen to ensure that the EVM of the RF signals is 4.5%, while operating the DD-MZM at the optimum bias point. Figure 5.12 shows a plot of the EVM versus the percentage of DC variations on either side of the bias point for both the DL and UL signals of BS 1 seen in Figure 5.4. Again, the DL RF signal is carried by the side-band λ_1 to BS 1, while the UL RF signal is carried by the side-band λ_4. Figure 5.12 shows that the EVMs of the DL RF signals do not unduly vary with a variation in the DC bias of the DD-MZM. On the other hand, the EVM value of the UL RF signals increases upon increasing the offset of the DC bias from the optimum value. When the DC bias is increased to the extreme value of 24 $\%$, the EVM of the RF signals reach a maximum of 7 $\%$. It can be observed from Figure 5.12 that for a DC bias variation as high as 15 $\%$, the EVM of the RF signals remains below 6 $\%$, which corresponds to a low BER value of nearly 10^{-12} for 16-QAM systems, as seen in Figure 5.11.

We now investigate the reason for the increased EVM of the UL RF signals of BS 1 upon increasing the offset of the DC bias from its optimum value. In order to understand this behaviour, the corresponding spectral plots of the amplified optical signal recovered at the output of the DD-MZM are shown in Figure 5.13. More explicitly, Figure 5.11a portrays the spectrum of the signal, when the DD-MZM is biased at the optimum point, while Figure 5.11b displays its counterpart for a DC bias offset of +24 $\%$. It can be observed from Figure 5.11b that due to inaccurate biasing, the suppression of both the carrier and of the even-indexed side-bands is degraded. Therefore at the

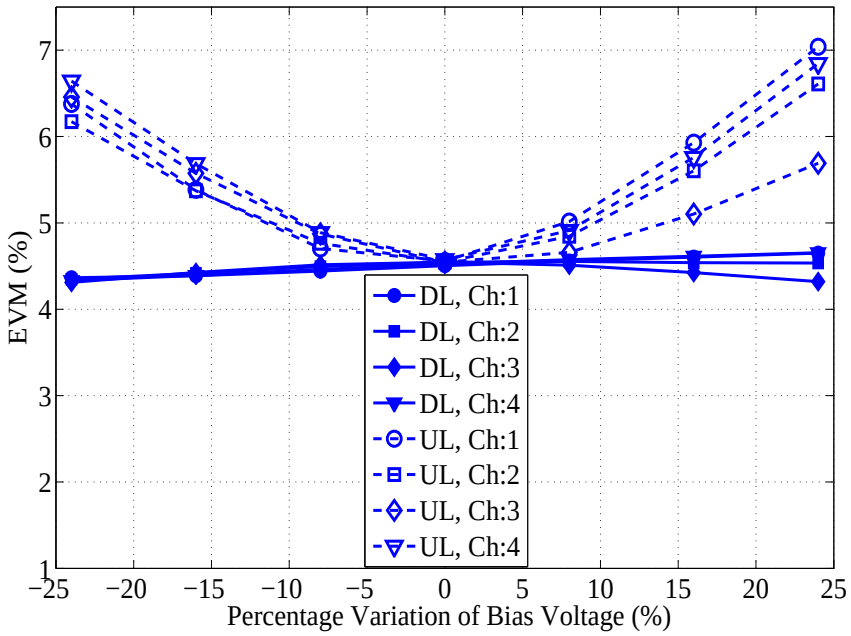

Figure 5.12: EVM versus DC bias variation of the DD-MZM for BS 1 seen in Figure 5.4. The system parameters are summarized in Table 5.2.

output of the DD-MZM, we generate undesired optical signals in the form of the carrier and of the even-indexed side-bands, which are not used for carrying any ROF data. These unwanted optical signals, which cannot be completely removed by the AWG used in our link seen in Figure 5.4, affect the ROF signals in two ways. Firstly, the presence of these optical signals imposes phase variations on the data-carrying odd-indexed side-bands by the XPM phenomenon discussed in Section 2.2.3. These phase variations are converted into amplitude variations by the effect of fiber dispersion [18], [136], as discussed in Section 2.2.2, which degrades the link quality. Secondly, the unwanted optical signals increase the nonlinearity of the PD and hence result in a further distortion of the RF signals. As observed in Figure 5.13, the power of the unwanted side-bands is higher close to the carrier frequency. This explains why the EVM degradation is seen to be higher for the UL RF signal of Figure 5.13, which is transmitted by the optical side-band λ_4, located close to the carrier frequency. Similar trends are shown by the EVM versus DC bias variation plot for the DL and UL RF signals of BS 2 and BS 3 seen in Figure 5.4.

5.7.2 Effect of DD-MZM RF Drive Signal Frequency Variations

Let us now consider the effects of varying the signal frequency of the RF drive signal applied to the DD-MZM of Section 2.1.4.2 for the generation of multiple optical side-bands, as discussed in Section 5.4. Similar to Section 5.6.1, we choose a noise power that gives an EVM of 4.5 $\%$ for all the RF signals received at the three BSs, where the BER is about 10^{-23} in Figure 5.11. The EVM is then plotted against the offset of the RF drive frequency on both sides of the optimum frequency. The maximum frequency offset considered in our study is ± 7 $\%$, which is equivalent to a frequency

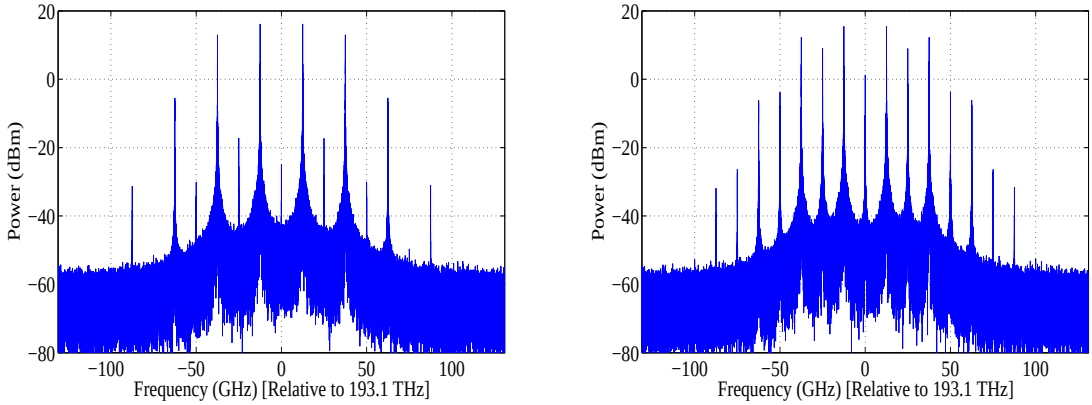

(a) Optimum DC bias.

(b) DC bias offset of 24 %.

Figure 5.13: Optical spectrum at the output of the high-power EDFA with optimum DC bias and a DC bias offset of 24 %. With a DC bias offset of 24 %, undesired optical signals in the form of the carrier and of the even-indexed side-bands are generated.

variation of $\pm 0.9375\ GHz$. In practice the frequency offset is lower than our chosen value, but we will use this as a worst-case value for the purpose of illustration. Figure 5.14 shows the plot of EVM versus the frequency offset. It can be observed from the figure that the EVM values for the DL signals are not affected significantly by a variation in the drive signal's frequency. On the other hand, the EVM values recorded for the UL signals have increased to a maximum of 6.8 % upon increasing the frequency offset. This behaviour of the received RF signal's EVM can be understood from the fact that a variation in the drive signal's frequency will affect the center frequency of each of the optical side-bands used for transmitting the RF signals. These side-bands are reduced in power by the AWG filters of Section 2.5 and by the OADMs of Section 2.6.1 that are used in the link. This reduction in optical power has a lesser effect on the DL RF signals of BS 1 of Figure 5.4, since they are transmitted by the optical side-band λ_1 over 10 km of SMF only. Furthermore, the signal carried at λ_1 passes through less filter-stages as compared to other side-bands in the link, as seen in Figure 5.4. On the other hand, the UL RF signals of BS 1 are transmitted by the wavelength λ_4, which undergoes multiple filtering operations in Figure 5.4 and also passes through the entire 40 km fiber used in the ring architecture of Figure 5.4. The combined effect of filtering and noise contamination imposed by the amplifiers of Figure 5.4 reduces the OSNR of λ_4, which results in a higher EVM for the UL RF signals of BS 1. Similar trends were also observed for BS 2 and BS 3.

It is worth mentioning here that since the side-bands are amplified and filtered before being transmitted over a span of optical fiber between each BS, it is difficult to find the most suitable value of optical power for each of them. This would require multiple attenuators at each BS, which results in an increase in the component count of the ROF link. In our simulations, we amplify the optical side-bands at each BS as a whole in order to avoid using separate attenuators for each side-band. Therefore, for certain values of RF drive signal frequencies, the attenuation of the optical side-band is such that it results in a slightly better EVM, as observed in Figure 5.14.

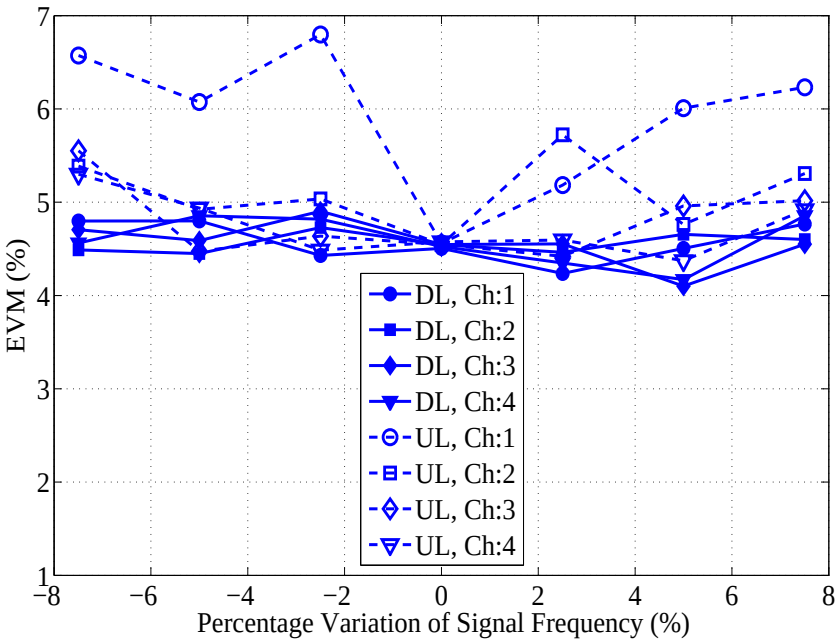

Figure 5.14: EVM versus RF drive frequency variation of the DD-MZM for BS 1 seen in Figure 5.4. The system parameters are summarized in Table 5.2.

5.7.3 Effect of DD-MZM RF Drive Signal Amplitude Variations

Having considered the effects of the DD-MZM drive signal's frequency, let us now vary the amplitude of the RF signal applied to the electrodes of the DD-MZM. The amplitude of the RF signal applied to a MZM is generally limited by the voltage tolerance of lithium niobate used in the design of the MZM, as discussed in Section 2.1.4. We assume in our study that the RF signal amplitude applied remains within the tolerance limit of the material used in the MZM design. Figure 5.15 shows the variations in the EVM of each of the four SCM signals for BS 1 in the DL and UL directions versus the RF signal amplitude. The percentage variation in the RF signal amplitude is obtained by increasing and decreasing the normalized amplitude from the operating value of $0.9{\cdot}V_{\pi}$. It can be observed from Figure 5.15 that the EVM of the DL signals increases upon reducing the RF signal amplitude, while it decreases upon increasing the RF signal amplitude. The opposite is true for the signal transmitted in the UL direction. The trends observed in Figure 5.15 can be explained with the aid of the spectral plot shown in Figure 5.16, which is recorded for a 15 $\%$ increased value of the RF amplitude. Figure 5.16 may be contrasted to Figure 5.4 relying on the nominal RF amplitude of $0.9{\cdot}V_{\pi}$. As mentioned in Section 5.3, the DL and UL signals of BS 1 are transmitted over sidebands λ_1 and λ_4, respectively, as shown in Figure 5.4. It can be observed by contrasting the spectral plot of Figure 5.16 to Figure 5.4 that upon increasing the RF signal amplitude, the power of the sideband λ_1 is increased, while the power of sideband λ_4 is reduced. This trend explains the results obtained in Figure 5.15 for BS 1. Although the extinction ratio of the sideband at λ_4 at the input stage of the link remains adequate, nonetheless, due to the specific setting of the attenuation and amplification in the link, the SNR of the received UL signal is degraded. Similar trends were observed for the EVM plots of BS 2 and BS 3.

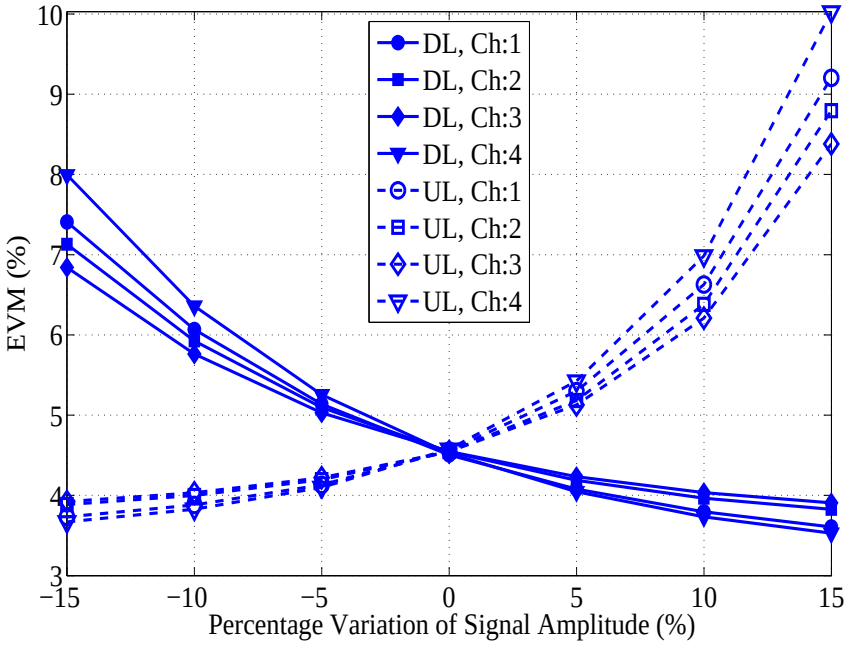

Figure 5.15: EVM versus RF drive amplitude variation of the DD-MZM for BS 1 seen in Figure 5.4. The system parameters are summarized in Table 5.2.

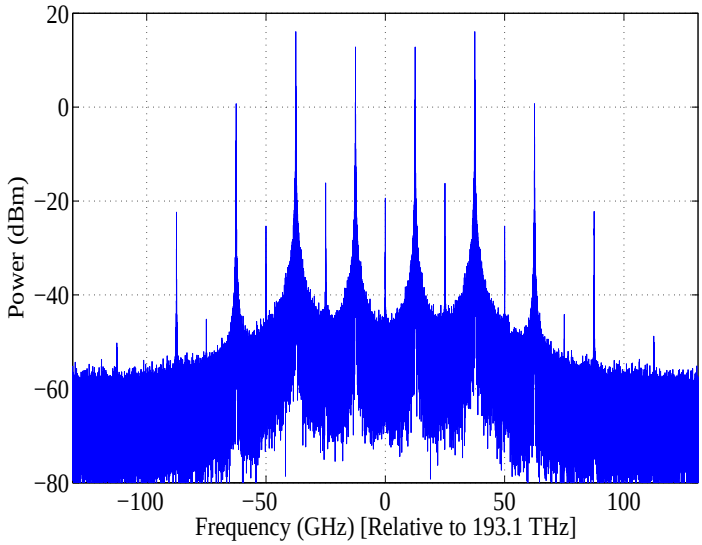

Figure 5.16: Optical spectrum at the output of the high-power EDFA for a RF signal amplitude variation of 15 %, which may be contrasted to the spectrum shown in Figure 5.4.

5.8 Millimeter-Wave DAS Architecture

In this section we discuss our second contribution towards the optical physical layer design of a mm-wavelength DAS architecture. In a DAS, the throughput per subscriber can be increased by using higher frequency bands at high carrier frequencies, such as mm-waves relying on higher-order modulation formats. High-frequency radio signals, which have a reduced propagation range due to their higher pathloss require small cells [142]. The reduction in cell size is naturally accompanied by an increase in the number of cells and consequently the number of BSs. In order to have a cost-effective architecture, the BSs have to be of low complexity and cost [8]. In this scenario, the optical fiber backbone linking the BSs plays an important role as a benefit of its high bandwidth, transparency to RF signals and low attenuation. Hence, as seen in Figure 5.17 the BSs are connected to a CU by their optical fiber backbone and all the signal processing tasks can be performed at the CU, where the BS antennas effectively form a virtual MIMO architecture [10], [142], [143] and [144].

Figure 5.17 shows the architecture of a virtual MIMO system, where the RAUs may be considered to be the distributed antenna elements. Consider Link 1, which consists of two RAUs connected through two spans of optical fiber with a CU. Each RAU is surrounded by MSs, which are connected wirelessly to a particular RAU depending upon their received signal quality. The architecture may consist of an arbitrary number of links, but they have not been shown in Figure 5.17 to avoid obfuscating details. The aim of future wireless systems is to increase the capacity per MS by exploring the capabilities of DAS architectures. In order to achieve this, the fiber-dispersion induced impairments associated with high-data-rate systems using mm-wavelength frequencies have to be quantified.

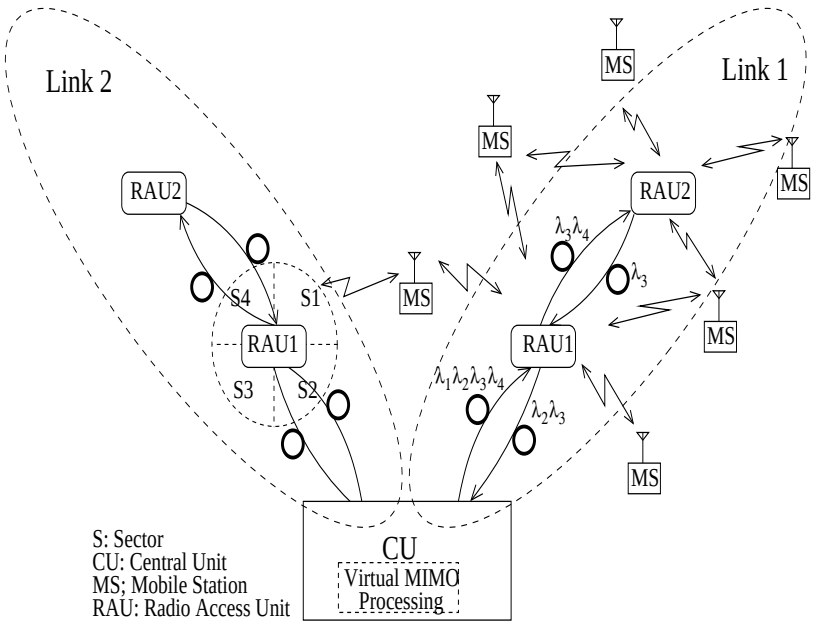

Figure 5.17: A virtual MIMO architecture similar to a star architecture as opposed to the ring architecture of Figure 5.2.

5.8.1 Generation of Millimeter-Waves by Low-Frequency Local Oscillators

As summarized in Table 5.1, a considerable amount of research has been carried out in recent years to generate multiple lightwave carriers as well as mm-wavelength RF signals with the aid of low frequency oscillators at a central unit [121], [128], [145], [130]. The technique generally used for generating mm-wavelength frequencies at the RAU utilizes the RHD of Figure 3.3, where two separate laser sources are mixed in a PD to obtain RF signals at the output [146], [147], [85], [148]. The transmission of mm-waves utilizing RHD at the RAU, while relying on separate lasers has been proposed in [124], [126]. However, the separate laser sources used in [124] and [126] require complex signal processing for achieving coherence amongst them. The RHD technique of Section 3.1 relies on generating multiple phase-coherent sidebands from a single laser using a phase modulator in [121] and intensity modulator in [128], which were involved for transmitting baseband data at a mm-wave frequency from a single RAU. The technique used in [121] and [128] transmits a high-power optical carrier along with the coherent sidebands through the fiber. The presence of a high-power optical carrier along with the sidebands may however distort the more vulnerable higher-order modulation formats, such as for example 64-QAM, due to the effects of XPM, which is less of a problem for conventional 1 bit/symbol OOK [18]. The XPM of Section 2.2.3 also imposes phase noise on the ROF signal, which is converted to amplitude fluctuations by the fiber-induced dispersion [18]. In [130], two different methods of generating multiple coherent sidebands using cascaded optical modulators and/or high frequency local oscillators were conceived for generating multiple mm-wavelength frequencies. However, since cascaded modulators are used, the number of components in the system was increased and both methods of [130] transmitted only uni-directional, rather than duplex DL/UL data. Finally, all the methods mentioned above transmitted a 1 bit/symbol modulation format and only to a single RAU.

Against this background, our aim is to design an efficient physical layer architecture for broadband mm-wavelength frequencies, while using higher-order modulation formats. We conceive and characterize high-throughput dispersion-tolerant transmission of multiple mm-wavelength signals over fiber in the virtual MIMO architecture of Figure 5.17, that uses a single laser source for transmitting bi-directional data to two spatially separate RAUs. Furthermore, our proposed technique allows the mm-wavelength signals generated at the RAUs to be transmitted at two different center frequencies, namely either at 25 GHz or at 50 GHz. This makes the system flexible to the choice of RF components and frequencies. Hence the novel contributions of our work described in the forthcoming sections are:

1- We demonstrate the feasibility of transmitting 4 SCM 6 bit/symbol 64-QAM mm-wavelength signals in a DAS by incorporating coherent optical carriers in the transmitted signal for heterodyne detection at the RAUs.

2- Our scheme simultaneously transmits ROF signals to two different RAUs in a duplex DL/UL architecture and at two different 50 GHz bands while requiring only a single laser source located at the CU.

3- We will also demonstrate the effect of varying the parameters of our proposed method of generating centralized multiple carriers as well as mm-wave signals.

The basic philosophy of a DAS is to move the antenna elements of a MIMO system closer to the edge of a traffic cell in the interest of providing a high-quality, uniform radio coverage. The antenna elements in the DAS are then linked to the CU with the aid of optical fiber. We designed and characterized a cost-efficient, yet cutting-edge 6 bit/symbol 64 QAM solution for this application, which is the first one of its kind and hence imposes substantial design-challenges.

5.9 The Proposed Millimeter-Wave Architecture

Figure 5.18 shows the design of one of the links, for example Link 1, as seen in Figure 5.17. Four CW optical signals are generated from a single LD using the OCS technique, as mentioned in Section 5.2. The sinusoidal signal applied to the DD-MZM of Figure 2.8 for the generation of multiple sidebands has a frequency of 12.5 GHz and an amplitude of 0.7$\times V_\pi$, where V_π is the voltage required to induce a phase shift of π for each of the DD-MZM arms. The output of the DD-MZM is amplified using an EDFA having a NF of 6 dB. The amplified signal is fed to a 1x4 AWG having a channel spacing of 25 GHz. Each channel of the AWG performs Gaussian filtering with a 3-dB bandwidth of 25 GHz centered at the odd-indexed optical side-bands generated during OCS. The first-order odd-indexed side-bands are λ_2 and λ_3, while the second-order odd-indexed side-bands are labelled λ_1 and λ_4, as shown in Figure 5.18. The first-order side-bands λ_2 and λ_3 have a higher OSNR compared to the second order side-bands λ_1 and λ_4, as seen in Figure 5.4. Therefore, λ_1 and λ_4 are used for transmitting DL RF data, which usually requires lower OSNR compared to the UL RF data, since we can afford the employment of more sophisticated receivers at the CU. The single-drive MZM of Figure 2.7 is used for intensity-modulating the optical carriers λ_1 and λ_4 with four 64-QAM RF signals that are sub-carrier multiplexed according to Section 3.2.1 [29], as portrayed in Figure 5.18. Each RF signal has a symbol rate of 20 $MSymbols/s$ and the resultant SCM signals have center frequencies in the range spanning from 1 GHz to 1.12 GHz for RAU1 and 1.16 GHz to 1.28 GHz for RAU2. Hence the total transmission rate conveyed to each RAU is 480 $Mbit/s$ (4 channels x 20 $MSymbols/s$ x 6 bits per symbol).

Our proposed scheme also supports potential BS sectorization at the RAU by forwarding each of the four SCM channels to four separate antennas of the sectors S1, S2, S3 and S4, as shown in Figure 5.17, albeit four-way 90 $^\circ$-sectorization would typically require beam-formers at the RAUs, rather than using single omni-directionally radiating elements. The unmodulated optical carriers λ_2 and λ_3 are coupled together using an optical coupler similar to that of Figure 2.6 and attenuated using an optical attenuator, before being coupled with the modulated optical carriers λ_1 and λ_4, as seen at the output optical coupler of the CU in Figure 5.18. The unmodulated carriers λ_2 and λ_3 are attenuated in order to reduce the effect of XPM on the modulated carriers. As detailed in Section 2.2.3, the XPM imposes phase noise on the signal, which is converted to amplitude noise by the fiber-induced dispersion mechanism detailed in Section 2.2.2 [18], [136]. The phase noise

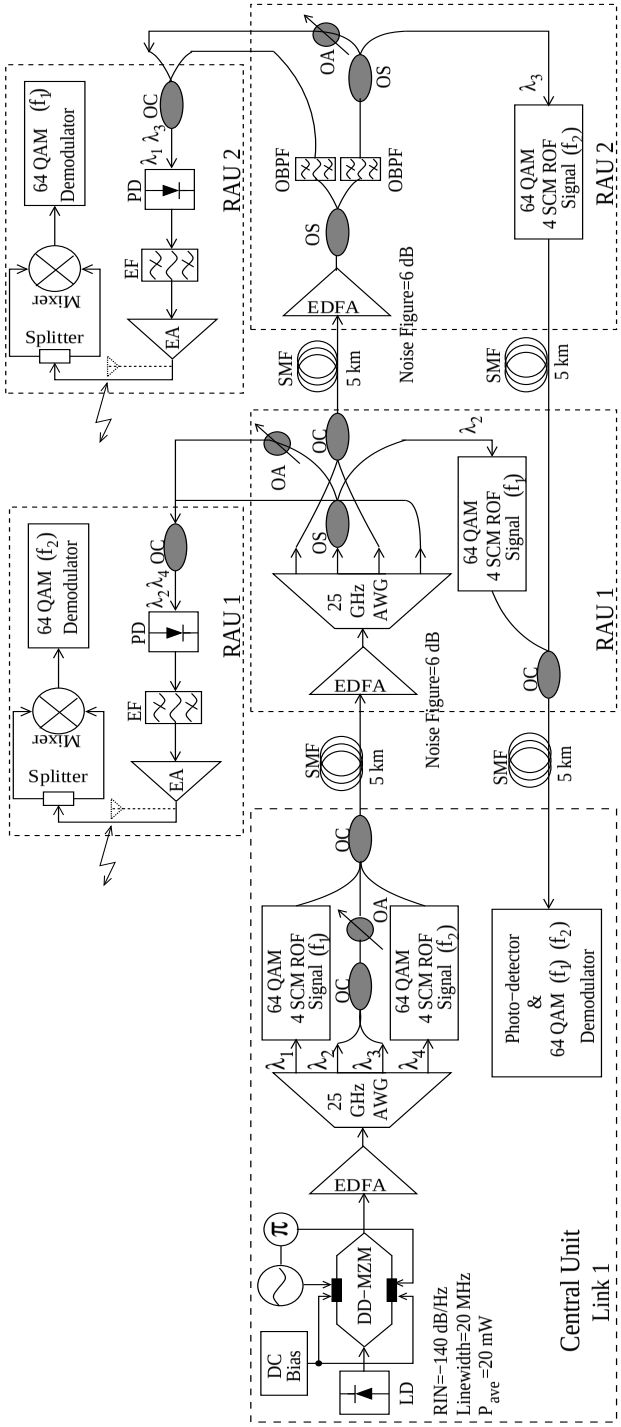

Figure 5.18: Schematic of the proposed optical link based virtual MIMO architecture, where the boxes printed using the dashed lines expand the less detailed architecture of Figure 5.17. The architecture is similar to a star architecture as opposed to the ring architecture of Figure 5.5.

increases upon increasing the average power of the signal, therefore the average power per optical side-band should be kept low.

The spectral plot of the resultant optical signal at the output of the optical coupler is shown in Figure 5.19. It may be observed from this spectral plot that due to the imperfection of the OCS of Section 5.4 and owing to the finite extinction ratio of the AWG based Gaussian filtering, the even-indexed side-bands are still partially present along with the odd-indexed side-bands. The composite optical signal is then transmitted from the CU through 5 km of SMF towards the first RAU, namely RAU 1 of Figure 5.17. At RAU 1, the received signal is amplified using an EDFA and Gaussian filtered using the 1x4 AWG, which has the same parameters as the AWG employed at the transmitter. The EDFA is placed before the AWG so that the ASE noise generated by the EDFA is filtered by the AWG. At RAU 1, the modulated optical channel λ_4 is dropped. The signal λ_2 is split into two parts using a 3 dB optical splitter, as seen in Figure 5.18. The lower branch is modulated by the data of the UL RAU1 for transmission to the CU, while the upper branch is coupled with λ_4 and detected by a high-speed PD. The PD has a responsivity of 0.8 A/W, a dark current value of 2 nA and thermal noise of $10\times10^{-12}A/W^{1/2}$. At the output of the PD, a 50 GHz mm-wavelength RF carrier modulated by the RF data is obtained through the process of heterodyning, as detailed in Section 3.1 [85], [146], [147], [148]. After the PD, a Gaussian band-pass electronic filter having a 3-dB bandwidth of 4 GHz and a center frequency of 50 GHz is used for removing the unwanted frequencies from the mm-wave RF signal, which are generated during photo-detection. At this stage, the amplified output of the electronic filter can be directly transmitted to the MSs from the RAU's antenna, as shown in Figure 5.18. However, in order to characterize the quality of the received mm-wavelength signal, it is down-converted to its initial radio frequency using self-mixing, as discussed in [73].

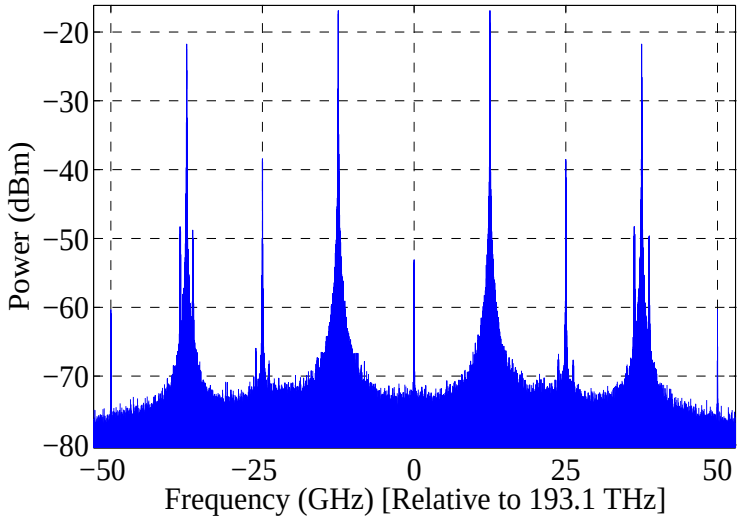

Figure 5.19: Spectral plot of the signal at the output of the CU, where four optical sidebands are generated as opposed to six optical sidebands seen in Figure 5.4.

After down-conversion, the resultant RF signal having four SCM channels enters the 64-QAM

demodulator block seen at the top of Figure 5.18, where each of the SCM channels is processed separately to evaluate the EVM. It is worth noting here that instead of using λ_2 for heterodyning and for the UL RAU1 to CU data transmission, we can also use the unmodulated signal λ_3. This would generate the mm-wavelength RF signal having a center frequency of 25 GHz. Hence our method provides two options for the center frequency of the mm-wavelength RF signal. The RAU to CU UL data signal is also composed of four SCM channels at RAU1 having center frequencies spanning from 1 GHz to 1.06 GHz. Each SCM channel is a 64-QAM signal having a symbol rate of 10 $MSymbol/s$. Hence the total data rate transmitted in the UL direction by a single RAU is 240 $Mbits/s$. As seen in Figure 5.18, the ROF signals λ_1 and λ_3 are coupled together at RAU1 and transmitted over 5 km SMF towards RAU2. The signal received at RAU2 is amplified and optically bandpass filtered to separate λ_1 and λ_3. The ROF signal λ_3 is then optically split into two paths in Figure 5.18, one of which is used for heterodyning to generate the mm-wave RF signal, while the other is used for transmitting the UL data received at the RAU2. The mm-wave RF signal is then generated and processed in the same way as at RAU1. The UL SCM RF signal transmitted by RAU2 has center frequencies in the range of 1.16 GHz to 1.22 GHz and has the same data rate as well as modulation format as that of RAU1. After propagating through 5 km SMF, the ROF signal λ_3 of RAU2 is combined with the UL ROF signal λ_2 of RAU1. The combined signals are received at the CU after they propagate through another span of 5 km of SMF. At the CU, the optical signals are filtered and photo-detected to obtain the RF signals, as seen in Figure 5.18. A 64-QAM demodulator is used for evaluating the EVM results of all the RF signals received from each of the RAUs. Table 5.3 summarizes the parameters of the proposed architecture of Figure 5.18.

Table 5.3: Paramters of the proposed optical link based virtual MIMO architecture.

Parameter	**Value**
SCM Channels per Optical Sideband	4
Number of DL and UL Optical Sidebands	2 DL and 2 UL
DL SCM Signal	64-QAM, 20 $MSymbols/s$
UL SCM Signal	64-QAM, 10 $MSymbols/s$
Optical Carrier Centre Frequency	193.1 THz
AWG Channel Spacing	25 GHz
AWG Channel Bandwidth	25 GHz
Fiber Dispersion	16 $ps/nm/km$
Fibre Span Between Successive RAUs	5 km
Number of RAUs	2
Noise Figure of Optical Amplifiers	6 dB
Photodetector Responsivity	0.8 A/W

5.10 Performance of the Proposed Virtual MIMO Architecture

Let us now discuss the EVM results for the DL and UL signals of RAU 1 and RAU 2 in Figure 5.20 and Figure 5.22, respectively. Similar to Section 5.4, the EVM values are plotted against the SNR of the received RF signals. The SNR of the RF signals was varied by imposing ASE noise on the optical side-band carrying the ROF data. Using Equation 5.18 derived in Section 5.6.1, the corresponding BER values for RAU 1 are plotted in Figure 5.21. Figure 5.20 shows that EVM values below 6 $\%$ are obtained for both the DL and UL RF signals for SNRs in excess of 25 dB. Observe from Figure 5.21 that this corresponds to a BER of 10^{-4}. The DL signals of RAU 1 are transmitted over the side-band λ_4, which has a lower SNR compared to side-band λ_2 used for transmitting the UL signals. Therefore the maximum achievable SNR for the DL signals is about 34 dB, while for the UL signals, it is 38 dB. Again, Figure 5.22 shows the EVM versus SNR

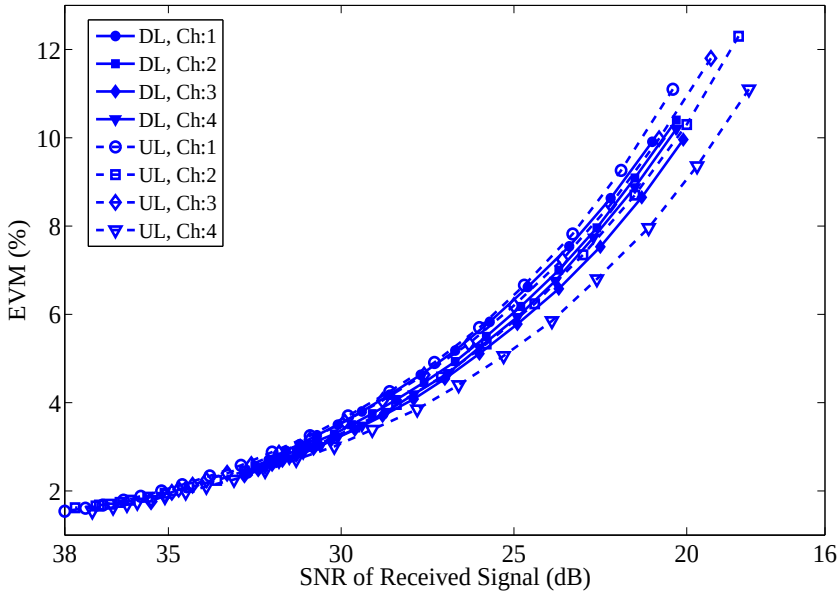

Figure 5.20: EVM versus received signal SNR for DL and UL RF signals of RAU 1 seen in Figure 5.18. The system parameters are summarized in Table 5.3.

plots for the DL and UL RF signals of RAU 2. These results are quite close to those obtained for the signals of RAU 1. The maximum SNR values achieved for the DL and UL signals match quite closely those of the corresponding signals of the two RAUs. It can be deduced from the performance results of our proposed virtual MIMO architecture that this setup provides us with an efficient method of transmitting mm-wavelength signals over optical fiber, using a reduced number of low-cost off-the-shelf components.

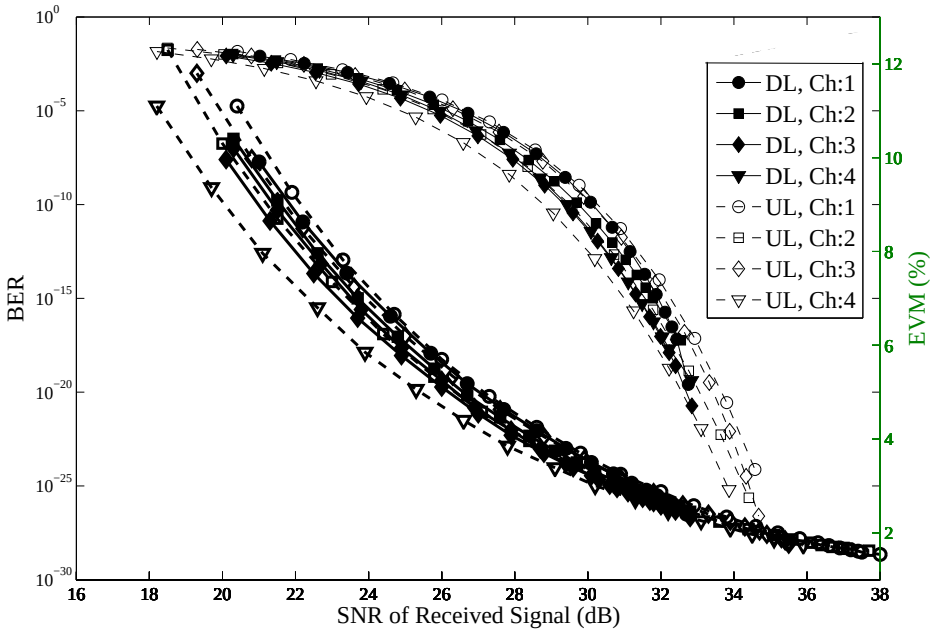

Figure 5.21: BER and EVM versus received signal SNR for DL and UL RF signals of RAU 1 seen in Figure 5.18. The system parameters are summarized in Table 5.3. The BER results are obtained by using the EVM to BER performance relationship described in Section 5.6.1.

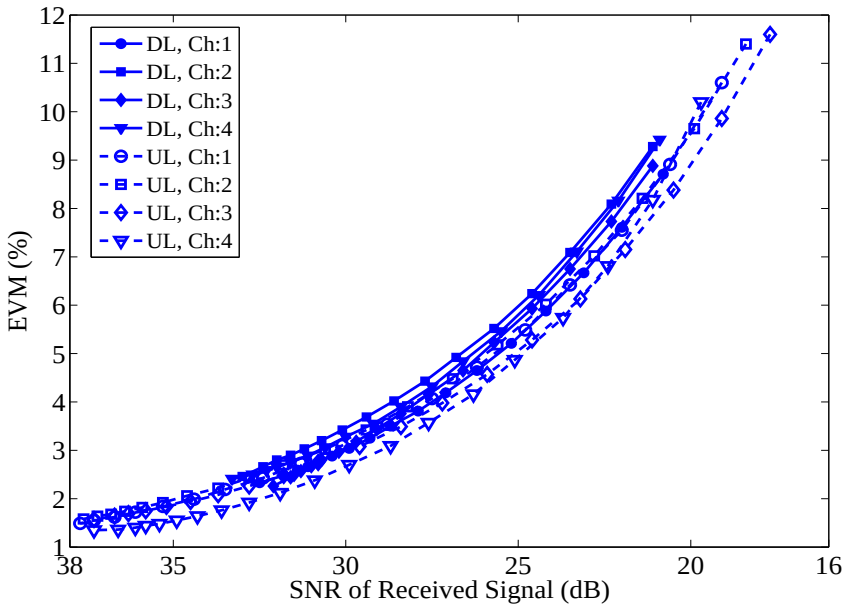

Figure 5.22: EVM versus received signal SNR for DL and UL RF signals of RAU 2 seen in Figure 5.18. The system parameters are summarized in Table 5.3.

5.11 Effect of Parameter Variations on the Proposed Virtual MIMO Architecture

Let us now observe the robustness of our proposed architecture to changes in the parameters of the devices used. As mentioned earlier, the proposed architecture uses the OCS technique of Section 5.4 for generating multiple side-bands, which are used for transmitting ROF data. Therefore we observe the effects of imperfections on the OCS to quantify the robustness of our link. The two main parameters that are involved in the generation of multiple side-bands, which are prone to variations include the DC bias source of the DD-MZM and the RF drive signal frequency applied to the arms of the DD-MZM. Evaluating the impact of the drive signal frequency is also helpful in understanding the effect of small drifts in the center frequencies of optical filters used in the network. Optical filters, specially the AWG filters of Section 2.5, may have small variations in their center frequency due to enviromental effects, such as for example temperature changes.

5.11.1 Effect of DC Bias Variations

As discussed in Section 5.5.1 and shown in Figure 5.11b, DC bias drift of the DD-MZM of Section 2.1.4.2 from its optimum value degrades the suppression achieved both for the carrier and for the even-indexed side-bands. Therefore the un-modulated carrier and even-indexed side-bands, which are not completely removed by the optical filters of the link, travel along with the odd-indexed side-bands that are used for ROF signal transmission. This will inflict strong XPM on the ROF signals as well as will reduce their OSNR. Figure 5.23 shows a plot of EVM versus the off-set in the bias voltage of the DD-MZM for both the DL and UL signals of RAU 1 seen in Figure 5.18. It can be observed from Figure 5.23 that even in the presence of the above-mentioned impairments, the variation in the EVM with the off-set is not significant. The maximum increase in the EVM is just above 1 $\%$ for as high a value of DC off-set as 24 $\%$. This implies that the effect of XPM-induced distortions on the proposed virtual MIMO architecture is less substantial compared to the ring architecture of Figure 5.5. The plausable explanation for this is the shorter length of the SMF used among the two RAUs and the CU as well as having a reduced number of optical side-bands travelling through the fiber. The shorter length of fiber spans reduces the interaction time between the optical side-bands travelling through the fiber and therefore results in a reduction of the effects of XPM.

Figure 5.24 shows the results for the variation in the EVM of both the DL and UL RF signals of RAU 2. The variation in the EVM observed for the RF signals of RAU 2 is even lower than for RAU 1. The maximum increase in the value of EVM remains below 0.5 $\%$ even for a large DC off-set of 24 $\%$. The reduced variation in EVM for RAU 2 compared to RAU 1 is a benefit of having multiple optical filtering stages for removing the unwanted signals in the form of the un-suppressed carrier and the even-indexed side-bands. The ROF signals destined for RAU 2 are filtered at RAU 1 and upon reaching RAU 2 they are passed through another optical filter in Figure 5.18. This ensures

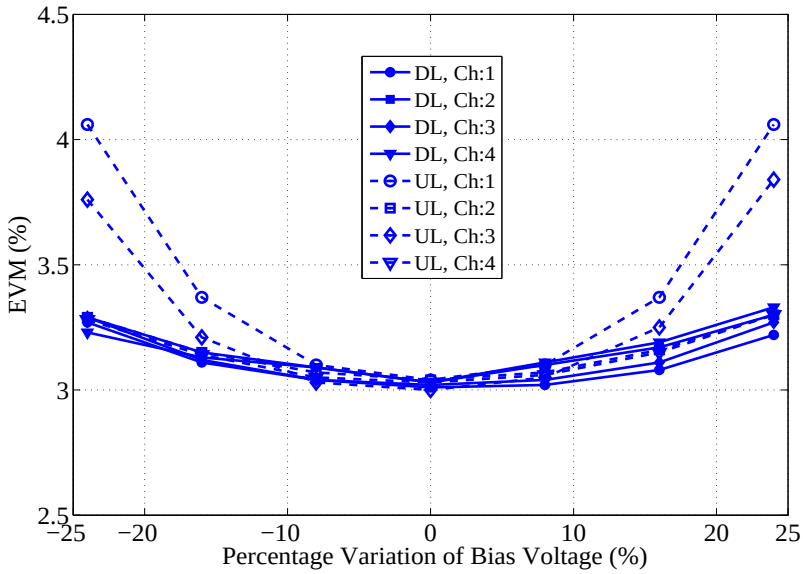

Figure 5.23: EVM versus DC bias variation of the DD-MZM for RAU 1 seen in Figure 5.18. The system parameters are summarized in Table 5.3.

having a higher rejection of the unwanted side-bands and therefore reduced nonlinear distortion effects are imposed by photo-detection in Figure 5.18 [67].

5.11.2 Effect of DD-MZM RF Signal Frequency Variations

We now observe the effect of frequency variations in the drive signal of the DD-MZM on the performance of the virtual MIMO architecture of Figure 5.18. Figure 5.25 shows the EVM versus frequency off-set of the drive signal for the RF signals of RAU 1. As mentioned in Section 5.5.2, a variation in the frequency of the drive signal will vary the center frequency of each of the optical side-bands. This variation in the center frequency will cause attenuation of the side-bands, while passing through the optical filters of the link. It can be observed from Figure 5.25 that the attenuation in the optical side-bands does not have any major impact on the EVM of the UL RF signals carried by the optical side-band λ_2. This is expected, since as observed in Figure 5.19, it has a good OSNR. Since the side-band λ_2 is amplified at RAU 1 of Figure 5.18 before being used for UL signal transmission, therefore its optical power is sufficiently high to carry the UL RF signals without any distortion. On the other hand, the EVM recorded in Figure 5.25 for the DL RF signals of RAU 1 becomes significant for a drive signal frequency off-set higher than 5 $\%$. By contrast, the DL ROF signals are more sensitive to the drive signal's frequency variations compared to the UL due to the heterodyning technique used in the schematic of Figure 5.18. For an increase in the off-set beyond 5 $\%$, the maximum EVM reaches 12 $\%$, as shown in Figure 5.25.

Figure 5.26 shows the EVM variation of the RF signals of RAU 2 plotted against the off-set in the drive signal's frequency. The trends shown in Figure 5.26 are similar to Figure 5.25, except that the maximum EVM of the DL RF signals is as high as 15.5 $\%$ at a 7$\%$ drive-signal frequency

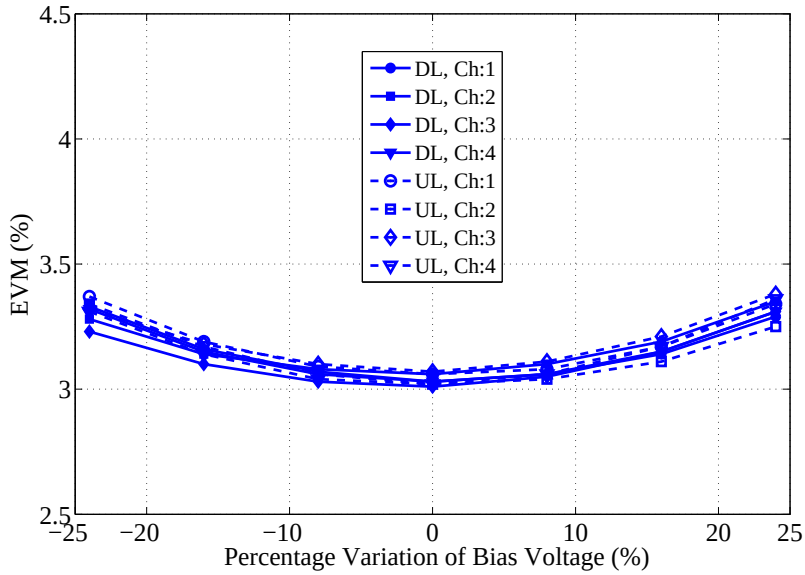

Figure 5.24: EVM versus DC bias variation of the DD-MZM for RAU 2 seen in Figure 5.18. The system parameters are summarized in Table 5.3.

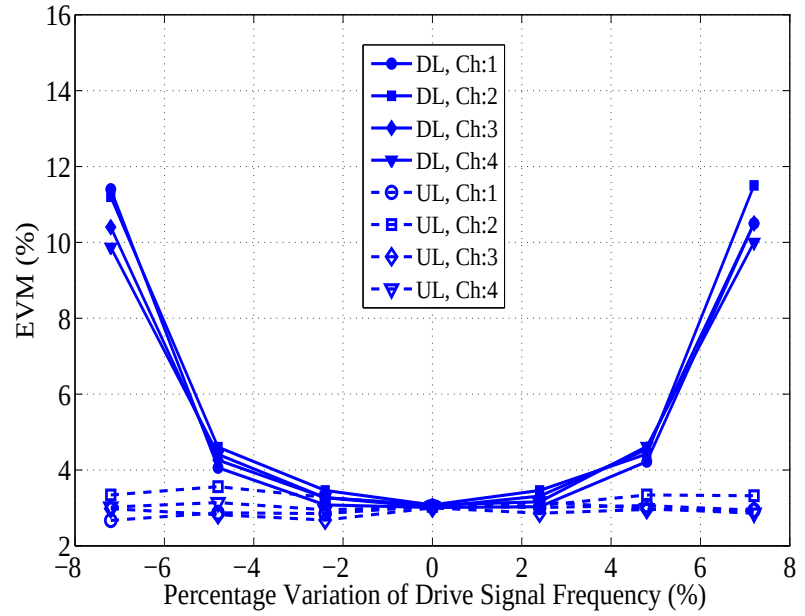

Figure 5.25: EVM versus RF signal frequency variation of the DD-MZM for RAU 1 seen in Figure 5.18. The system parameters are summarized in Table 5.3.

deviation. It can be deduced from the above discussions that the performance of our proposed architecture remains acceptable, as long as the drive signal frequency variations are within 5 % of the optimum value. An off-set of 5 % in our case is equivalent to a frequency variation of 0.625 GHz, which is hardly reached for most practical sinusoidal sources. As mentioned earlier, the effects imposed on the link due to drive signal frequency variations is analogous to the effects of optical filter center frequency variations. Therefore the above results demonstrate the robustness of the link against different types of parameter variations.

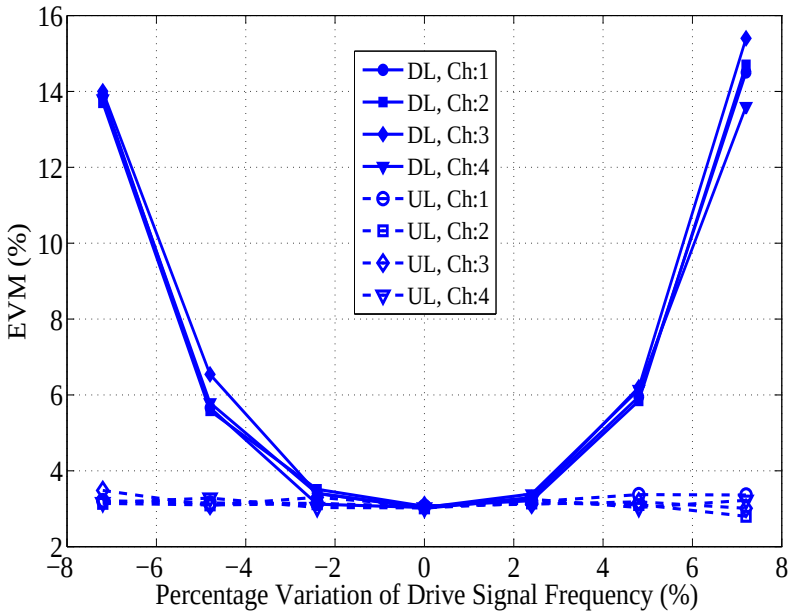

Figure 5.26: EVM versus RF drive frequency variation of the DD-MZM for RAU 2 seen in Figure 5.18. The system parameters are summarized in Table 5.3.

5.11.3 Effect of DD-MZM RF Signal Amplitude Variations

In this section, we observe the effects of varying the amplitude of the RF signal that is applied to the electrodes of the DD-MZM. It has been shown in Section 5.5.3 that an increase in the amplitude of the RF signal increases the number of sidebands generated, therefore resulting in an increase in both the optical power and extinction ratio of the higher-order sidebands. Figure 5.27 shows the variation in the EVM of the DL and UL signals for RAU 1, with a variation in the RF signal amplitude. The variation in the RF signal amplitude is plotted as a function of the normalized amplitude from the normalized operating value of $0.7 \cdot V_{\pi}$. Figure 5.27 shows that an increase in the RF signal amplitude decreases the EVM of the DL signals, while increasing the EVM of the UL signals. Naturally, the opposite happens, when the amplitude of the RF signal is decreased. The reason for the trends shown in Figure 5.27 can be understood by observing that the DL signals are transmitted over the second-order sideband λ_4 seen in the spectral plot of Figure 5.19, while the UL signal is transmitted over the first order sideband λ_2. With an increase in the amplitude of

the RF signal, the extinction ratio and power of the sideband λ_4 increases, which in turn increases its OSNR. Therefore, the EVM of the received DL signals is increased. The opposite is true for a decrease in the RF signal amplitude. For the UL signals, an increase in the power of the second-order sidebands increases the effect of XPM on the first-order sidebands. Furthermore, separating the sidebands at the RAU using non-ideal filters results in some residual power of the unwanted sideband being detected by the PD. This results in a decrease in the EVM of the UL signals received at the RAU. The DL and UL RF signals of RAU 2 are transmitted over sidebands

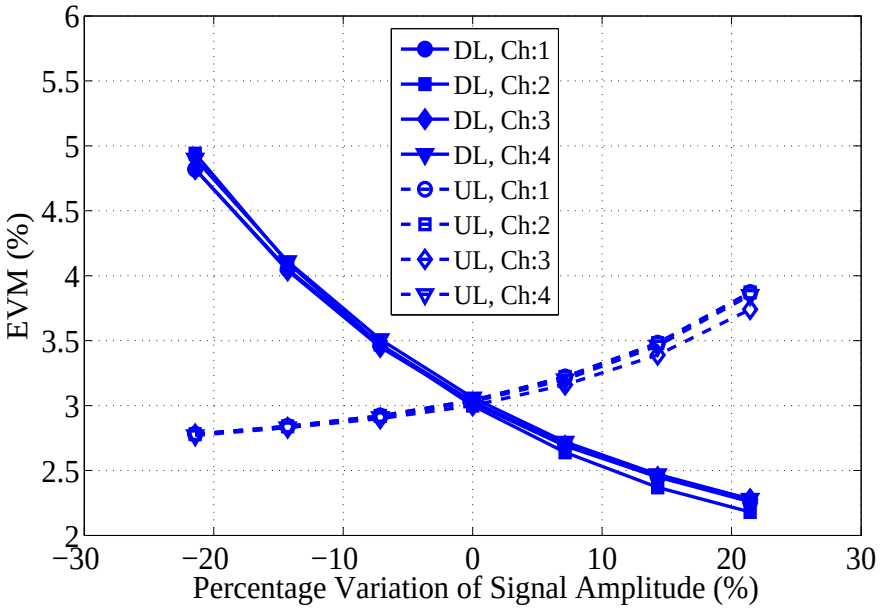

Figure 5.27: EVM versus RF signal amplitude variation of the DD-MZM for RAU 1 seen in Figure 5.18. The system parameters are summarized in Table 5.3.

λ_1 and λ_3 respectively, which are complementary to sidebands λ_4 and λ_2, respectively. Therefore, the trends observed for the DL and UL signals of RAU 2 are similar to those of RAU 1. The EVM versus RF signal amplitude variation results of RAU2 are shown in Figure 5.28. The studies that we have performed have demonstrated that our porposed technique of implementing a virtual MIMO architecture is robust and hence results in an efficient ROF link.

5.12 Conclusions

ROF communications provide a cost-efficient solution to the increasing demands of high bit-rate services. Much of the research carried out on ROF systems aims at reducing the cost of the optical infrastructure and at making the most of the already installed components. We have discussed the design of an optical ring network feeding multiple RAUs using a single LD. The ring network performs centralized processing at the MSC. The proposed network was characterized by observing the EVM performance in Figures 5.9 and 5.10. Despite communicating over 10 km spans of fiber in the ring, observe in Figure 5.11 that the system achieves good BER results. We have also shown

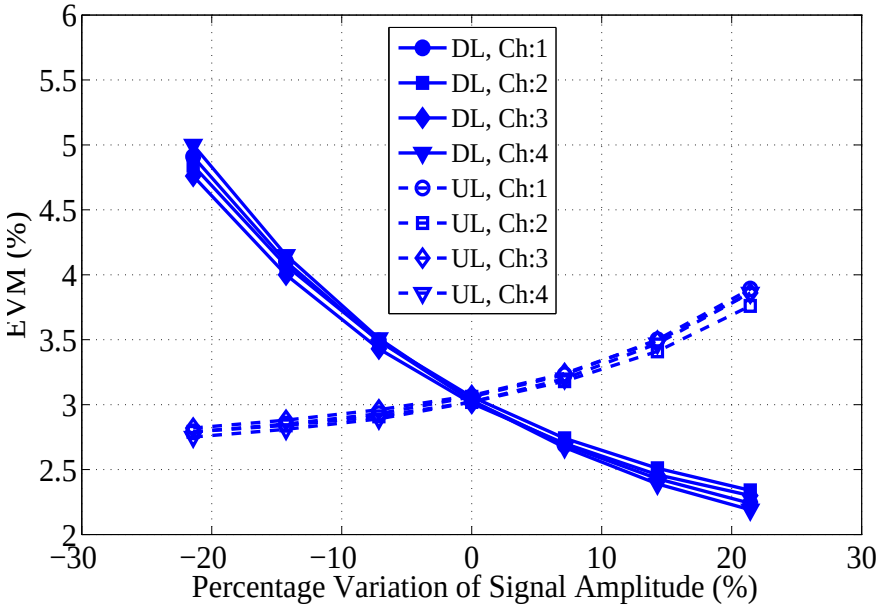

Figure 5.28: EVM versus RF signal amplitude variation of the DD-MZM for RAU 2 seen in Figure 5.18. The system parameters are summarized in Table 5.3.

in Section 5.7 that the ring architecture of Figure 5.5 is resilient against the parameter perturbations of the devices used. In Section 5.11 we have characterized the transmission of 64-QAM, 4-SCM duplex data to the two RAUs of Figure 5.17 that are located at 5 km and 10 km from the CU in a virtual MIMO architecture. Our technique uses a single laser source to transmit all the data. Millimeter wavelength carriers are generated at the RAUs for the transmission of the DL data. The technique of Section 5.9 allows two different center frequencies to be generated. EVM values below 6 % are obtained for both the DL and UL signals using components having parameter values close to commercially available components. This limits the BER degradation to 10^{-4}. Again, the architecture performs efficiently even in the presence of parameter variations of the different components. Tables 5.4 and 5.5 summarize the performance of the ring and the virtual MIMO architecture, respectively.

Table 5.4: Performance summary of the ring architecture of Figure 5.5. The EVM results were extracted from Figures 5.8, 5.9 and 5.10.

Ring Architecture, Downlink Transmission Performance

RAU	Distance	SCM Channel	Signal Type	SNR	EVM	BER
RAU 1	10 km	Channel 1	16-QAM, 10 $MSymbols/s$	27.5 dB	5.2 $\%$	10^{-18}
		Channel 2			5.2 $\%$	10^{-18}
		Channel 3			5.9 $\%$	10^{-14}
		Channel 4			4.3 $\%$	10^{-25}
RAU 2	20 km	Channel 1	16-QAM, 10 $MSymbols/s$	27.5 dB	4.0 $\%$	10^{-28}
		Channel 2			4.9 $\%$	10^{-20}
		Channel 3			4.0 $\%$	10^{-28}
		Channel 4			4.3 $\%$	10^{-25}
RAU 3	30 km	Channel 1	16-QAM, 10 $MSymbols/s$	27.5 dB	5.0 $\%$	10^{-19}
		Channel 2			4.5 $\%$	10^{-23}
		Channel 3			4.1 $\%$	10^{-27}
		Channel 4			4.3 $\%$	10^{-25}

Ring Architecture, Uplink Transmission Performance

RAU	Distance	SCM Channel	Signal Type	SNR	EVM	BER
RAU 1	10 km	Channel 1	16-QAM, 5 $MSymbols/s$	27.5 dB	3.2 $\%$	10^{-44}
		Channel 2			4.8 $\%$	10^{-21}
		Channel 3			4.8 $\%$	10^{-21}
		Channel 4			4.8 $\%$	10^{-21}
RAU 2	20 km	Channel 1	16-QAM, 5 $MSymbols/s$	27.5 dB	4.8 $\%$	10^{-21}
		Channel 2			5.8 $\%$	10^{-15}
		Channel 3			5.0 $\%$	10^{-19}
		Channel 4			4.2 $\%$	10^{-26}
RAU 3	30 km	Channel 1	16-QAM, 5 $MSymbols/s$	27.5 dB	4.5 $\%$	10^{-23}
		Channel 2			5.1 $\%$	10^{-18}
		Channel 3			5.0 $\%$	10^{-19}
		Channel 4			6.0 $\%$	10^{-14}

Table 5.5: Performance summary of virtual MIMO architecture of Figure 5.18. The EVM results were extracted from Figures 5.20 and 5.22.

Virtual MIMO Architecture, Downlink Transmission Performance

RAU	Distance	SCM Channel	Signal Type	SNR	EVM	BER
RAU 1	5 km	Channel 1	64-QAM, 20 $MSymbols/s$	27.5 dB	4.7 $\%$	10^{-7}
		Channel 2			4.6 $\%$	10^{-7}
		Channel 3			4.3 $\%$	10^{-8}
		Channel 4			4.5 $\%$	10^{-8}
RAU 2	10 km	Channel 1	64-QAM, 20 $MSymbols/s$	27.5 dB	4.0 $\%$	10^{-9}
		Channel 2			4.5 $\%$	10^{-8}
		Channel 3			4.2 $\%$	10^{-9}
		Channel 4			4.1 $\%$	10^{-9}

Virtual MIMO Architecture, Uplink Transmission Performance

RAU	Distance	SCM Channel	Signal Type	SNR	EVM	BER
RAU 1	5 km	Channel 1	64-QAM, 10 $MSymbols/s$	27.5 dB	4.8 $\%$	10^{-6}
		Channel 2			4.5 $\%$	10^{-8}
		Channel 3			4.5 $\%$	10^{-8}
		Channel 4			4.0 $\%$	10^{-9}
RAU 2	10 km	Channel 1	64-QAM, 10 $MSymbols/s$	27.5 dB	4.1 $\%$	10^{-9}
		Channel 2			4.2 $\%$	10^{-9}
		Channel 3			3.9 $\%$	10^{-9}
		Channel 4			3.7 $\%$	10^{-10}

Chapter 6

Digitized ROF Communication

This chapter discusses the digitized transmission of RF signals over optical fiber, a technique that is generally termed as DROF [37], [92], as mentioned in Section 3.4. In Section 6.4, we will present a novel physical layer design for the transmission of digitized data between the CU and BS using pulsed optical communication, which relies on a single pulsed laser source as well as on a single fiber link for the transmission of duplex RF data. In Section 6.3, the bandpass sampling technique used for the digitization of the analogue RF signal will be discussed in detail. Our simulation results characterizing the digitization and transmission of both a single and multiple 64-QAM RF signals over optical fiber are presented in Section 6.4.4.

6.1 Digitized ROF Architecture

Figure 6.1 shows the typical architecture of a DROF communication system. The baseband data is upconverted to a RF signal in the upconversion block. The analogue RF signal is converted to a digital signal in the analogue-to-digital conversion block shown in Figure 6.1. The electronic digital signal is converted to an optical signal and transmitted over the optical medium. The optical signal at the receiver is photodetected and the resultant digital signal is converted back to analogue signal, as shown in Figure 6.1. The analogue signal is transmitted through the antenna after filtering and amplification. It can be observed from Figure 6.1 that the DROF system performs analogue-to-digital conversion, in contrast to the AROF system of Figure 5.1. Furthermore, an additional block of DAC is required at the receiver in case of DROF to convert the digital signal back to analogue, as shown in Figure 6.1.

6.2 Background - Digitized ROF

DROF communications has been proposed in [93] where a microcellular design was conceived using a high-speed ADC for the transmission of RF signals over a digitally modulated optical

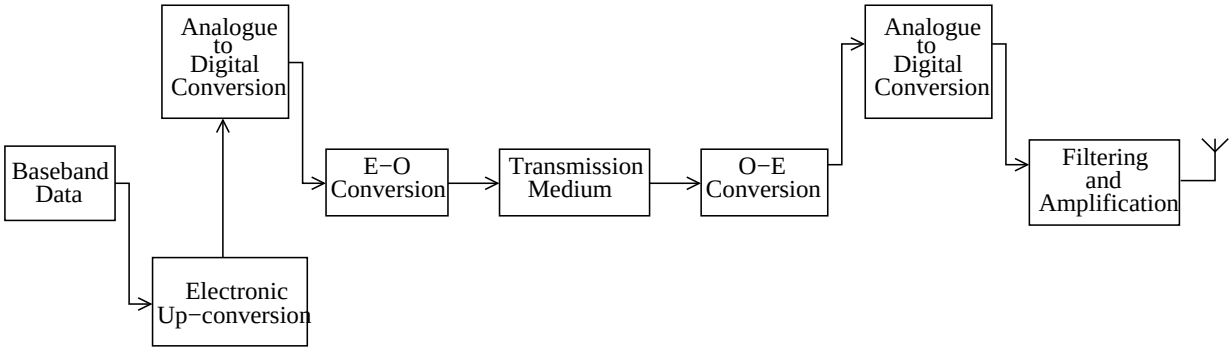

Figure 6.1: General architecture of a DROF system. A comparison with the AROF system of Figure 5.1 reveals that after the up-converter, the analogue signal is digitized in the analogue-to-digital conversion block and then passed on to the E-O converter.

fiber. It has been shown in [93] that the dynamic range of a DROF link remains fairly insensitive to the fiber length, as long as the received optical signal power remains within the sensitivity limits of the optical receiver. In recent years, DROF communication has attracted more attention as a benefit of high-speed analogue-to-digital (ADC) and digital-to-analogue converters (DAC). The most recent contributions in the area of DROF are summarized in Table 6.1, which shows that significant work on DROF started in the year 2009.

Table 6.1: Summary of major contributions towards DROF

Author(s)	Contribution
[93] P. M. Wala. 1993	A comparison between the digitized and analogue transport of RF signals in a microcell is characterized both by experimental and field tests. It has been shown that the BER of the DROF link remains insensitive to the fiber length, as long as the power of the received optical signal is higher than the sensitivity of the receiver.
[37] P. A. Gamage *et al.* 2009	An analytical model of digitized RF signals is used for analyzing the key design parameters, such as the ADC/DAC resolution, link bit rate, receiver sensitivity and link SNR. Based on this analytical model, a set of suitable design parameters is chosen for the transmission and performance analysis of a digitized 16-QAM RF signal.
[149] P. A. Gamage *et al.* 2009	Simultaneous transmission of digitized 16-QAM WiMAX and Gaussian Minimum Shift Keying (GMSK) GSM signals in a single direction using a CW optical carrier is presented. The experimental results using 8-bit resolution ADC showed satisfactory EVM values for the respective signals.
[150] Y. Yang *et al.* 2010	Experimental demonstration of digitized transmission of multiple RF channels in a single direction using a single ADC/DAC is presented. For the sake of comparison, the multiple RF signals are also transmitted as analogue signals. It has been shown that upon increasing the number of RF

Continued on Next Page...

Table 6.1 – Continued

Author(s)	Contribution
	channels, both the SNR and dynamic range degradation is less severe in case of digitized transmission compared to analogue transmissions.
[23] Y. Yang *et al.* 2011	Unidirectional transmission of a digitized SCM RF signal composed of three QPSK modulated signals over an optical link using CW carrier is presented. It has been shown that the DAC may be used for recovering the digitized signal at different frequencies without a mixer and without a local oscillator.
‘ [151] Y. Yang *et al.* 2011	Simultaneous transmission of digitized GSM, UMTS and WiMAX signals over a bidirectional optical link using CW optical carriers is presented. The bidirectional link uses separate fiber for each direction. It has been shown that the DL performance is dependent upon the amount of amplification required at the input of the DAC. By contrast, the UL performance is limited by the inter-channel interference among the spectral lobes of the regenerated RF signals at the input of the DAC.

6.3 Bandpass Sampling Technique

The operating principle of the ADC and DAC are discussed in the Appendix. In this section, we will highlight the principle of bandpass sampling. According to Nyquist's sampling theorem, in order to recover the analogue signal from the sampled data, the sampling rate should be equal to or higher than twice the highest frequency in the analogue signal. This would imply that for RF signals used in wireless communications having center frequencies in the GHz range, the sampling rates required would be excessive, thus making the design of the ADC/DAC complex and economically unfeasable. In order to avoid this difficulty in the design of ADC/DAC pairs, the bandpass sampling technique may be used [94], [95]. Since most of the wireless signals have a limited bandwidth that is lower than the center frequency, the bandpass sampling technique ensures that the sampling rate is dependent on the bandwidth of the analogue signal instead of its highest frequency. Sampling of an analogue signal generates a spectrum composed of spectral lobes at multiples of the sampling frequency [152]. If the sampling frequency is chosen by ensuring that the multiple copies of the original spectrum do not overlap in the frequency domain, then the original signal may be recovered by using a bandpass filter [94], [95].

Figure 6.2 shows the spectrum of an analogue signal and its sampled version. Again, it may be observed from Figure 6.2 that the sampled signal has a spectrum that contains the original signal's spectrum repeated periodically at the multiples of the sampling frequency. The frequency spectrum is divided into multiple Nyquist zones, each having a width equal to half the sampling frequency. It may be observed from Figure 6.2 that in order to avoid overlapping among the different spectral

lobes, the sampling frequency has to be sufficiently high. In case the sampling frequency used is insufficiently high, the different spectral replicas will overlap, which gives rise to aliasing. In the next section, we derive the values of the sampling frequencies, which will allow us to avoid aliasing.

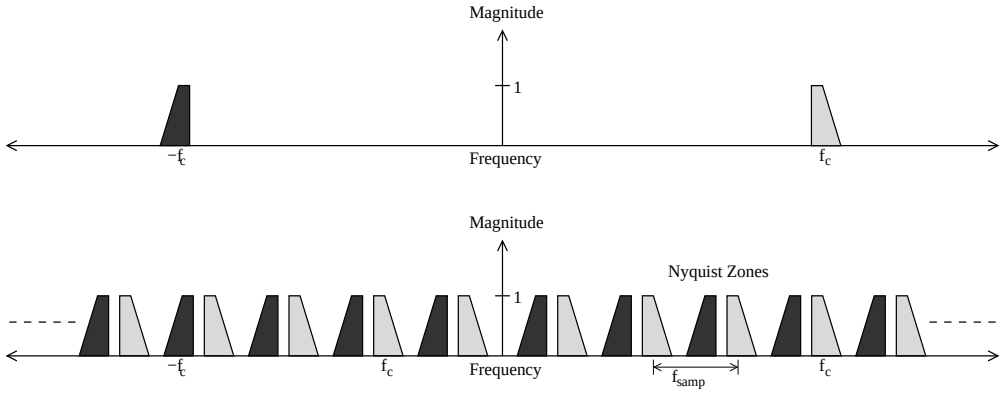

Figure 6.2: Spectrum of the analogue signal and its sampled version.

6.3.1 Sampling Frequencies Required for Bandpass Sampling

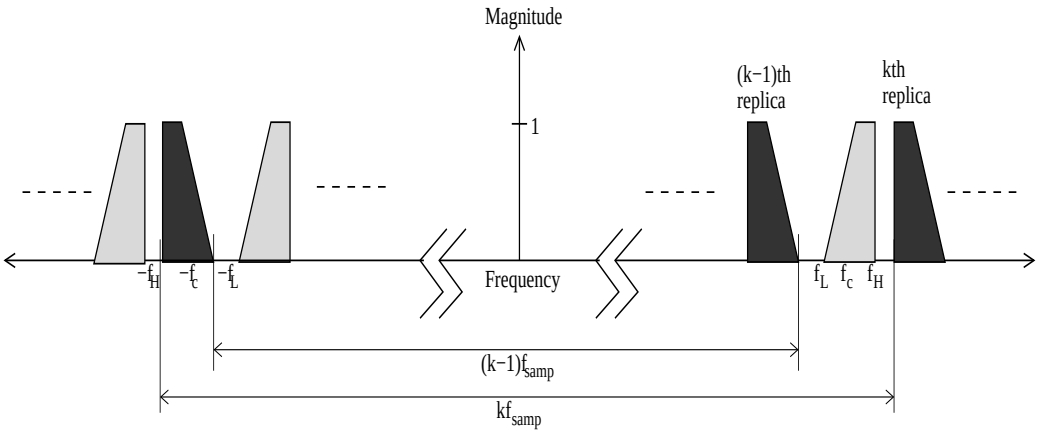

Figure 6.3: Spectrum of the sampled analogue signal.

Let the analogue signal shown in Figure 6.2 have a center frequency of f_c and lowest as well as highest frequencies of f_L and f_H, respectively. The bandwidth B of the signal is $B = f_H - f_L$. The sampling frequency chosen for bandpass sampling should ensure that the Nyquist zones shown in Figure 6.2 do not overlap and the Nyquist zone of the original signal spectrum should also remain free from aliasing [152]. Figure 6.3 shows an enlarged area extracted from the sampled spectrum shown in Figure 6.2 for the k^{th} replica of the original spectrum, where the variable k represents the position of the spectral replica. Considering the k^{th} and the $(k-1)$ other spectral replicas shown in Figure 6.3, the criterion for choosing a suitable sampling frequency f_{samp} may be written as [152]:

$$-f_L + (k-1)f_{samp} \leq f_L, \tag{6.1a}$$

$$-f_H + kf_{samp} \geq f_H. \tag{6.1b}$$

Solving Equation 6.1a and 6.1b for f_{samp} gives the following two relations:

$$f_{samp} \leq \frac{2f_L}{k-1}, \tag{6.2a}$$

$$f_{samp} \geq \frac{2f_H}{k}. \tag{6.2b}$$

In order to find the value of k, the expression for f_{samp} obtained in Equation 6.2b is substituted into Equation 6.1a to arrive at:

$$-f_L + (k-1)\frac{2f_H}{k} \leq f_L. \tag{6.3}$$

Equation 6.3 is then solved for the value of k as follows:

$$(k-1)\frac{2f_H}{k} \leq 2f_L, \tag{6.4a}$$

$$f_H - \frac{f_H}{k} \leq f_L, \tag{6.4b}$$

$$f_H - f_L \leq \frac{f_H}{k}, \tag{6.4c}$$

$$B \leq \frac{f_H}{k}, \tag{6.4d}$$

$$k \leq \frac{f_H}{B}. \tag{6.4e}$$

For the scenario, where there is no aliasing of the spectral replicas shown in Figure 6.4, the value of k should be a non-zero integer. Adding this constraint to the possible value of k will modify Equation 6.4e as follows:

$$1 \leq k \leq I_g\left[\frac{f_H}{B}\right], \tag{6.5}$$

where $I_g\left[x\right]$ is a function that returns the largest integer that is smaller than or equal to x. Considering the value of k mentioned in Equation 6.5, the bandpass sampling criterion may be written as follows:

$$\frac{2f_H}{k} \leq f_{samp} \leq \frac{2f_L}{(k-1)} \text{ for all } 1 \leq k \leq I_g\left[\frac{f_H}{B}\right]. \tag{6.6}$$

In order to graphically observe the bandpass sampling criterion described in Equation 6.6, normalized values are used for the quantities mentioned in Equation 6.6. The normalization is carried out with respect to the bandwidth B of the analogue signal. We first substitute $f_L = f_H - B$ into Equation 6.6 and divide the whole equation by B to arrive at:

$$\frac{2(f_H/B)}{k} \leq \frac{f_{samp}}{B} \leq \frac{2(f_H/B-1)}{(k-1)} \text{ for all } 1 \leq k \leq I_g\left[\frac{f_H}{B}\right]. \tag{6.7}$$

The relationship given in Equation 6.7 is plotted in Figure 6.4 by chosing different values of k and varying the normalized value of f_H for observing the corresponding normalized value of the sampling frequency f_{samp}. It may be observed from Figure 6.4 that for different values of k, the acceptable values of the sampling frequency are plotted in the form of shaded wedges. The tips of all the wedges are at a value of 2, when normalized by the sampling frequency of f_{samp}/B. Therefore, in order to avoid alisaing of the spectral replicas, the sampling frequency should be chosen within the shaded regions that are obtained for integer values of the parameter k.

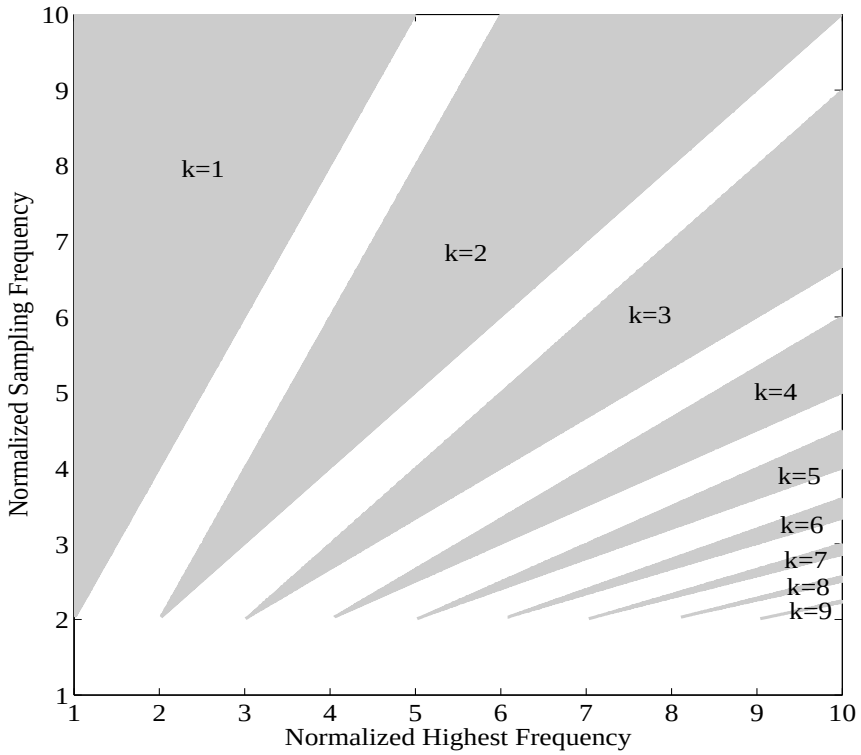

Figure 6.4: The aliasing-free and aliased bandpass sampling rates versus the band position are represented by the grey and white regions, respectively.

6.3.2 Effect of Guard Bands on Bandpass Sampling

It may be observed from Figure 6.4 that chosing a low sampling frequency will result in an operating point that is closer to the thinner edge of a specific wedge. Operating at these edges will make the ADC less tolerant to any changes in the sampling frequency. If the operating point is chosen to ensure that the ADC is operating at a sampling frequency close to the edge, then a small change in the sampling frequency due to hardware imperfections will push the operating point into the aliased region, where the spectral replicas overlap each other. This effect may be avoided by considering the bandwidth of the analogue signal to be somewhat larger than the actual bandwidth, a method that is generally described as the inclusion of guard bands [152]. Figure 6.5 shows the spectrum of the analogue signal along with the guard bands at each side.

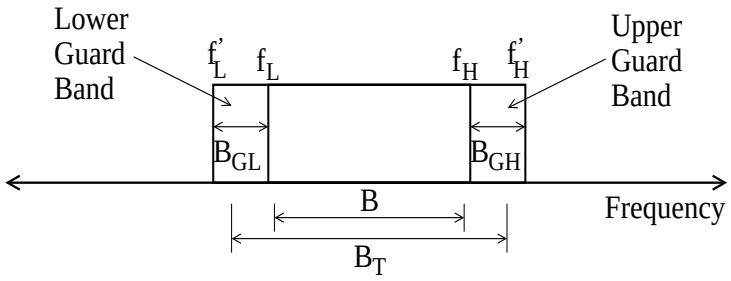

Figure 6.5: Analogue signal spectrum with the guard bands.

Let B_{GL} and B_{GH} be the guard bands attached both to the low- and high-frequency side of the analogue signal spectrum, respectively. Then the total bandwidth B_T may be written as:

$$B_T = B + B_{GL} + B_{GH}. \tag{6.8}$$

Therefore, the new low frequency $f_L^{'}$ and high frequency f_H' to be considered for bandpass sampling are given as:

$$f_L' = f_L - B_{GL}, \tag{6.9a}$$
$$f_H' = f_H + B_{GH}. \tag{6.9b}$$

The modified Equation 6.7, which now considers the guard bands may be written as follows:

$$\frac{2(f_H'/B_T)}{k'} \leq \frac{f_{samp}}{B_T} \leq \frac{2(f_H'/B_T - 1)}{(k'-1)} \text{ for all } 1 \leq k' \leq I_g\left[\frac{f_H'}{B_T}\right], \tag{6.10}$$

where k' represents the position of the replica for the scenario, where guard bands are considered to be part of the useful signal spectrum. Equation 6.10 gives the expression for the upper and lower boundary lines of any particular wedge. Figure 6.6 examplifies the operating point O for one of the wedges obtained for a certain value of k'.

The expression for the upper and lower boundary lines expressed from Equation 6.10 may be written as:

$$\text{Upper Boundary } : \frac{f_{samp}}{B_T} = \frac{2(f_H'/B_T - 1)}{(k'-1)}, \tag{6.11a}$$
$$\text{Lower Boundary } : \frac{f_{samp}}{B_T} = \frac{2(f_H'/B_T)}{k'}. \tag{6.11b}$$

It may be observed from Equations 6.11a amd 6.11b that the upper and lower boundary lines have slopes of $2/(k'-1)$ and $2/k'$, respectively. For the operating point O shown in Figure 6.6 the low and high frequency tolerance can be found using the triangles OBD and OAC, respectively. The low-frequency tolerance is represented by the vertical line OD, while the high frequency tolerance is represented by the vertical line OA. The expressions for the vertical lines OD and OA may be obtained using the right angled triangles OBD and OAC as follows:

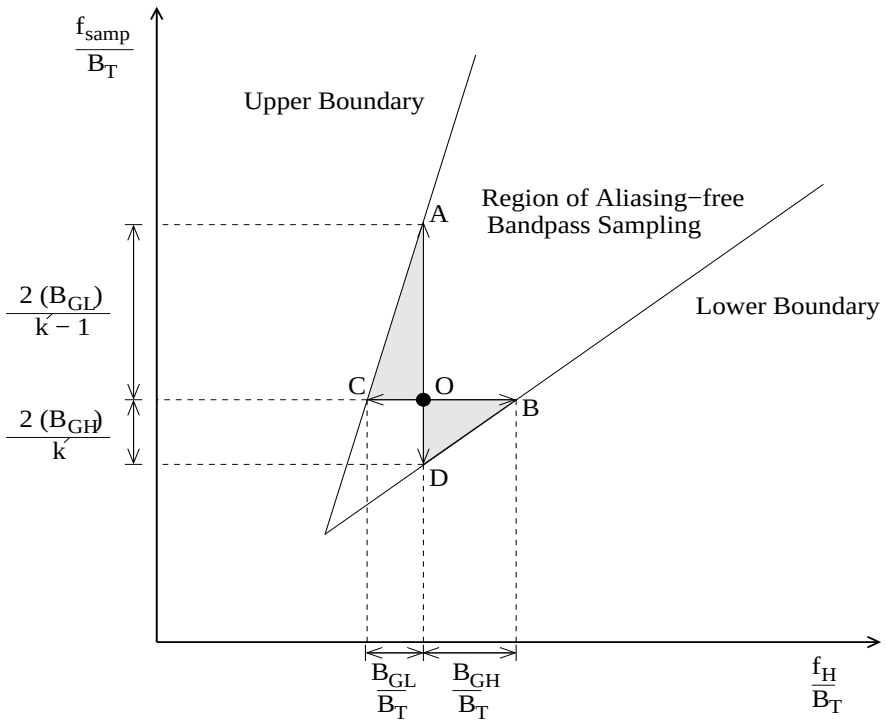

Figure 6.6: Operating point O on a wedge represented by spectral replica k'.

$$OD = \frac{2}{k'} B_{GH}, \tag{6.12a}$$

$$OA = \frac{2}{k'-1} B_{GL}. \tag{6.12b}$$

Equations 6.12a and 6.12b show that the low and high frequency tolerances are proportional to the higher and lower guard band values, repectively. The higher the values of the guard bands chosen, the higher is the tolerance of the ADC against frequency variations.

6.3.3 Effect of Spectral Replica on the Sampling Rate

It is clear from Equation 6.6 and Figure 6.6 that for each valid value of the integer k', there is a range of alising-free sampling frequencies. The width of this range can be found by subtracting the upper boundary of Equation 6.12a from the lower boundary of Equation 6.12b and substituting $f'_L = f'_H - B_T$. This results in the following equation for the width ∇f_{samp}:

$$\nabla f_{samp} = \frac{2}{k'(k'-1)}(f'_H - B_T k') \text{ for all } 1 \leq k' \leq I_g \left[\frac{f'_H}{B_T}\right]. \tag{6.13}$$

The relative precision is defined as the ratio of half the width of the sampling frequency's range and of the total bandwidth B_T [94], which may be written as:

$$\frac{\nabla f_{samp}}{2B_T} = \frac{1}{k'(k'-1)}\left(\frac{f'_H}{B_T} - k'\right). \tag{6.14}$$

For an operating point within the $(k')^{th}$ wedge and above the tip of the $(k'+1)^{th}$ wedge, the quantity $f'_H/B_T - k$ equals 1. Hence for such an operating point, Equation 6.14 may be reduced

to the following relation:

$$\frac{\nabla f_{samp}}{2B_T} \approx \frac{1}{k'^2}. \tag{6.15}$$

It may be deduced from Equation 6.15 that using lower values of k' or moving to lower order wedges relaxes the sampling frequency precision requirements of the oscillator as well as increases the guard bands. However, this relaxation and increase of the guard bands is coupled with an increase in the sampling frequency of the oscillator.

6.3.4 Nyquist Sampling

Substituting $k' = 1$ into Equation 6.10 gives the following relation for the sampling frequency:

$$2f_H \leq f_{samp} \leq \infty. \tag{6.16}$$

It may be observed that Equation 6.16 represents the Nyquist sampling criterion, which states that in order to recover an analogue signal correctly from its samples, the sampling frequency should be at least equal to or greater than the highest frequency present in the analogue signal. This implies that the Nyquist sampling criterion is a special case of the bandpass sampling criterion where the operating point is chosen to be with in the first wedge, as shown in Figure 6.4, which represents the baseband replica of the analogue signal's spectrum.

6.3.5 Retrieving the Analogue Signal from the Bandpass Sampled Signal

The analogue signal can be retreived from the bandpass sampled signal by retaining one of the Nyquist zones using an interpolation filter. In order to illustrate the function of the interpolation filter, we refer to Figure 6.3, which shows one of the spectral replicas having a center frequency equal to that of the analogue signal. In order to ensure that the recovered analogue signal is as similar to the original signal as possible, the filter has to have a sharp roll-off and a high attenuation outside the useful bandwidth. This specification may be relaxed for the spectral replicas that are located sufficiently far away from the desired spectral replica, as shown in Figure 6.3. For a certain set of parameters, the lowest possible sampling rate is referred to as the critical sampling rate, which may be deduced from Equation 6.2b as:

$$f_{critical} = \frac{2f_H}{k_{max}} = 2B, \tag{6.17}$$

where f_H is a multiple of B. As mentioned in Section 6.3.2, using guard bands will increase the distance between the spectral replicas. Therefore, having a large guard band will relax the interpolation filter's sharp roll-off and high out-of-band attenuation specifications, which in turn reduces the cost of the filter. Substituting B_T for B in Equation 6.17 shows that for large guard bands the critical sampling frequency will increase. It may be deduced from the above discussion that there is a trade-off between the cost of filtering and the sampling frequency chosen for the design of ADC and DAC.

6.4 Digitized Transmission of 64-QAM RF Signal

As mentioned in Table 6.1, digitized transmission of RF signals has attracted substantial attention in recent years, as facilitated by the development of fast ADC/DAC electronics and by the popularity of ROF communication conceived for high-bandwidth services [38]. The community aims for developing unified optical feeder networks that would allow seamless integration of both optical baseband as well as of wireless access networks. Against the background of the state-of-the-art summarized in Table 6.1, we propose a cost-efficient duplex UL/DL physical layer design for the DROF link. More explicitly, we conceive the digitized transmission of 64-QAM signals over a 25 km of SMF between a Mobile Switching Center (MSC) and a BS. The novel contributions of our work are summarized below:

1- We conceived the pulsed optical transmission of digitized RF 64-QAM signals using Optical Differential Phase Shift Keying (ODPSK) in the DL (MSC-BS), and On-Off Keying (OOK) in the UL (BS-MSC) directions.

2- The duplex digitized RF 64-QAM signal is transmitted between the MSC and BS using a single laser rather than a pair of-pulsed laser sources at the MSC's DL transmitter.

3- Moreover, the duplex UL/DL RF 64-QAM signal is transmitted over a single optical fiber, which is achieved by shifting the frequency of the DL optical signal at the BS by 50 GHz and then retransmitting it in the UL direction.

Our ultimate goal is to conceive a more cost-effective design than the previous DROF solutions discussed in Table 6.1. The cost-efficiency is achieved by using for the first time a single laser and a single fiber for duplex transmission. Furthermore, the proposed DROF link can be seamlessly integrated into the already operational long-haul Passive Optical Networks (PONs) [30], hence making DROF an attractive choice for future wireless services.

6.4.1 Simulation Model of the Digitized ROF Transmission

We use a combination of two commercial software libraries, namely VPI TransmissionMaker 8.6 and Matlab for designing our simulation model for DROF. Figure 6.7 shows the block diagram of our simulation model. The analogue 64-QAM RF signal is generated in VPI TransmissionMaker and passed to Matlab for analogue-to-digital conversion. Bandpass sampling is implemented in Matlab for digitizing the RF signal, as discussed in Section 6.3. The digital signal represented in the form of square-shaped pulses is returned to VPI TransmissionMaker, where the pulsed electronic signal is used for modulating a sequence of optical pulses. The optical pulses have the same repetition rate as the data rate of the electronic signal. The modulated optical pulsed signal is transmitted through the optical fiber and detected using a PD. The electronic signal at the output of the PD is passed to Matlab again, where the electronic bit sequence is used for recovering the

analogue RF 64-QAM signal using DAC. The analogue signal retreived in Matlab is returned to VPI again for performance evaluation.

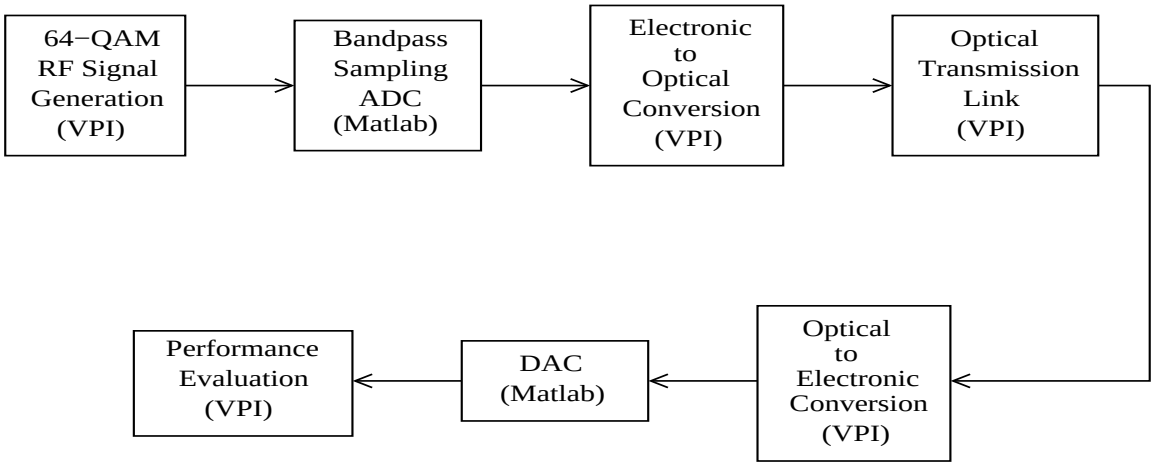

Figure 6.7: Block diagram of the simulation model.

6.4.2 Design of the Proposed Digitized Link

Figure 6.8 shows the architecture of our proposed digitized bidirectional link. A 64-QAM RF signal having a center frequency of 1.28 GHz and symbol rate of 16 MSymbols/s is passed on to the ADC block, as shown by the stylized plot in Figure 6.8. The 9-bit resolution is chosen based on the physical parameters of the link. As mentioned in [37], the ADC resolution should be chosen to ensure that the SNR of the link (SNR_{link}) is predominantly limited by the ADC jitter noise, rather than by the quantization noise. This implies that the SNR related to the quantization noise ($SNR_{quantization}$) should be higher than the SNR due to jitter noise (SNR_{jitter}), which can be written as [37]:

$$SNR_{quantization} \quad > \quad SNR_{jitter}. \tag{6.18}$$

or

$$6.02n + 10log(3) - 10log(PAPR) \quad > \quad -20log(2\pi f_{rf}\sigma_{jitter}), \tag{6.19}$$

where n is the number of bits/sample resolution of the ADC, $PAPR$ is the peak to average power ratio of the RF signal and σ_{jitter} is the standard deviation of the ADC's RMS jitter.

The first assumption in this model is that the ADC resolution is sufficiently high for ensuring that its quantization error is uniformly distributed, which results in doubling the SNR for each extra bit. This corresponds to 6.02 dB per bit, as seen in the first term of Equation 6.19. Secondly, the $PAPR$ for the 64-QAM RF signal used in our study is 9.36 dB. Hence the ADC has to have a 9.3 dB higher dynamic range than the average imput power. Furthermore, the value of σ_{jitter} is chosen to be 0.7 ps, which is similar to the value specific in [37]. Substituting these values in

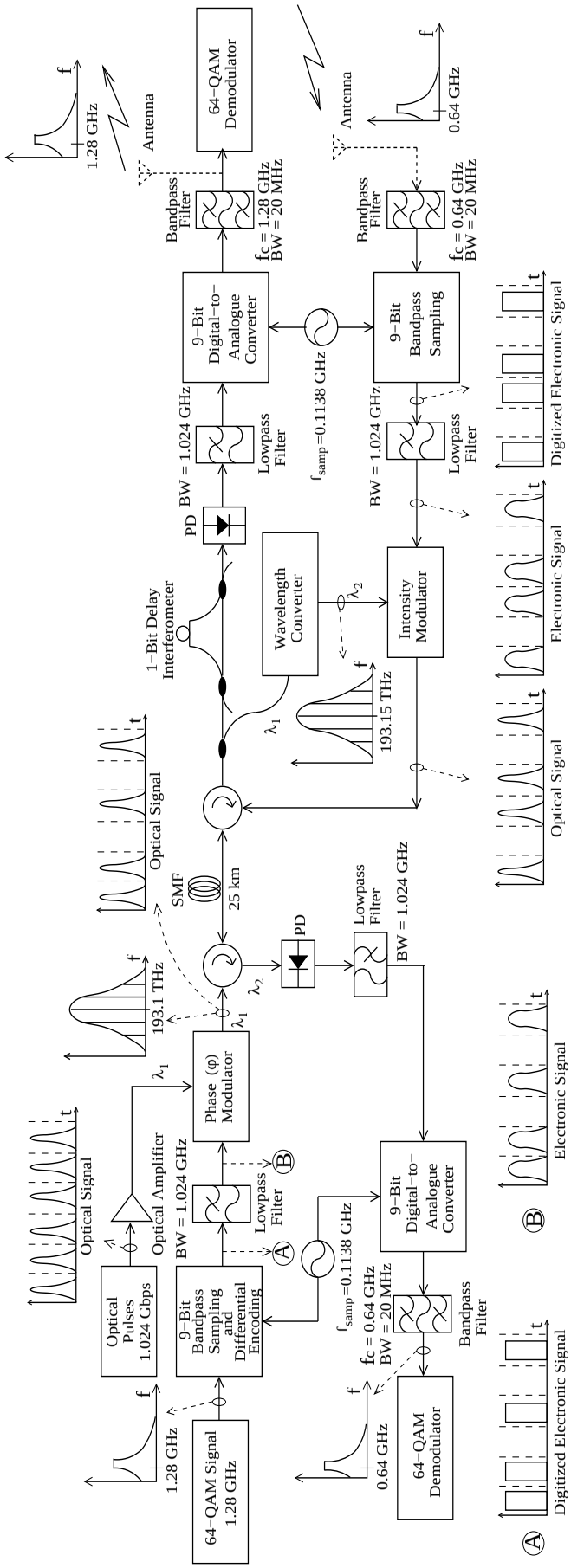

Figure 6.8: Architecture of the proposed DROF link. It can be observed that in contrast to the BROF architecture of Figure 4.14 and the AROF architectures of Figure 5.5 and 5.18, the DROF architecture uses up-conversion and digitization for transmitting the ROF signal.

Equation 6.19 results in $n > 8.23$. Hence the resolution was rounded to the next integer, i.e. to 9-bits.

In order to avoid spectral aliasing due to critical bandpass sampling [94], 16 MHz wide guard-bands are considered at both sides of the center frequency, which results in a total bandwidth of 48 MHz, where f_H and f_L become 1.304 GHz and 1.256 GHz, respectively. Given the total bandwidth of 48 MHz, the minimum sampling frequency, which is also referred to as the critical sampling frequency becomes 2x48 = 96 $MSamples/s$. Operating exactly at the minimum sampling frequency results in an ADC/DAC operating point that is less tolerant to variations in the sampling frequency due to hardware limitations [94]. Therefore we opted for a slightly higher sampling frequency of 113.8 MSamples/s for our system. For a 9-bit resolution ADC, f_s = 113.8 $MSamples/s$ generates a bitrate of 113.8 x 9 $\simeq$ 1.024 $Gbps$. The bits generated in the ADC after digitization are then differentially encoded with in the ADC block. The differential encoding is performed in order to phase modulate the optical carrier which will be reused for UL transmission. The Differential encoder performs Exclusive-OR (XOR) function between a current bit and a delayed bit. The output of the ADC is a Non-Return-to-Zero (NRZ) signal at a bit-rate of 1.024 Gbps, as shown by the stylized plot A in Figure 6.8. The resultant NRZ signal is then low-pass filtered using an electronic filter having a Gaussian spectral profile and a bandwidth equal to the bit-rate of the NRZ signal. The filtered output shown by the stylized plot B in Figure 6.8, is used for varying the phase of optical pulses that are input to the phase modulator (PM) of Figure 6.8. The optical pulse source generates $40ps$ duration Gaussian time-domain pulses at a rate of 1.024 GHz and a center frequency of 193.1 THz. The output of the phase modulator is transmitted through the circulator into the optical fiber. The circulator discussed in Section 2.6.2 is used for separating the DL signal from the UL signal.

After being transmitted through 25 km of SMF, the DL signal is passed through the circulator to the differential detector of Figure 6.8. Again, as discussed in Section 2.6.2, the circulator is used for separating the received DL signal from the transmitted UL signal, while the differential detector is used for recovering the differentially encoded optical signal and consists of an interferometer having a 1-bit delay and a PD. At the output of the differential detector, an OOK signal is obtained, which is passed on to the DAC for digital-to-analogue conversion, as described in Section 6.3.5. The analogue signal at the output of the DAC is bandpass filtered using a filter which has a Gaussian shaped spectral profile and a center frequency of 1.28 GHz. Finally, the filtered analogue signal is then input to the 64-QAM demodulator for evaluating our performance metrics.

It can be observed from Figure 6.8 that after the circulator of Section 2.6.2, which is located at the BS, the received optical signal is divided into two paths using a 3 dB coupler. One of the signal paths is input to the differential detector, while the other signal path is input to a wavelength/frequency converter. The wavelength/frequency converter is a simple SPM based device that uses a high-power amplifier, a HNLF and an optical filter to shift the frequency of the input signal by 50 GHz, as we will detail in Section 6.4.3. The operation of the wavelength convertor and its transfer function is reminiscent of the operation of the SPM based regenerator discussed in Section 4.2. The output of the wavelength converter is a sequence of optical pulses having the

same bit-rate and pulse-width as the signal used at the MSC, but mapped to a center frequency of 193.15 THz. The sequence of pulses generated by wavelength conversion is then intensity modulated using the electro-absorption modulator (EAM) of Section 2.1.4.3, which performs the E-O conversion.

The digitized UL data shown by the stylized plot in Figure 6.8 is generated from the UL 64-QAM RF signal and has a symbol rate of 16 MSymbols/s and a center frequency of 0.64 GHz. The ADC used for digitizing the UL signal has similar characteristics to those of the ADC used for digitizing the DL signal. The intensity modulated optical pulsed signal is then transmitted to the MSC using the same optical fiber as that used for DL signal transmission. The UL signal received at the MSC is separated from the DL signal using a circulator, as seen in Figure 6.8. The intensity modulated optical pulses are photodetected at the MSC and passed to the 9-bit DAC, as shown in Figure 6.8. The DAC used at the MSC has characteristics reminiscent of the DAC used at the BS. Again, the analogue output of the DAC is passed through a bandpass filter and detected using a 64-QAM demodulator. Finally, at the output of the demodulator block, we evaluate the link performance metrics. Table 6.2 summarizes the values of the main parameters used in our setup. The performance results of our proposed architecture are discussed in Section 6.4.4.

Table 6.2: Paramters of the digitized architecture.

Parameter	**Value**
64-QAM	6 Bits/Symbol
64-QAM Bit Rate	96 $MBits/s$
DL Signal Carrier Frequency	1.28 GHz
UL Signal Carrier Frequency	0.64 GHz
ADC Resolution	9 bits
ADC Sampling Frequency	113.8 $MSamples/s$
Standard Deviation of ADC RMS Jitter	0.7 ps
ADC Output Signal Bit Rate	1.024 $Gbps$
Standard Deviation of DAC RMS Jitter	0.7 ps
Optical Pulse Repetition Rate	1.024 GHz
Optical Pulse FWHM	40 ps
Optical Pulse Centre Frequency	193.1 THz
Fibre Dispersion	16 $ps/nm/km$
Fibre Transmission Distance	25 km
Noise Figure of Optical Amplifiers	6 dB
Photodetector Responsivity	0.8 A/W

The signals at different stages of the DROF link are shown by stylized plots in Figure 6.8. The 64-QAM RF signal at a center frequency of 1.28 GHZ is given as input to the 9-bit ADC as shown in Figure 6.8. The digital data stream at the output of the ADC is low-pass filtered in order to remove high-frequency components from the signal. The optical signal used to transmit the digitized electronic data over the fiber is shown as a sequence of pulses having a Gaussian shaped time-domain profile and a repetition rate of 1.024 GHz. The spectrum of the optical pulsed signal that is phase modulated by the digitized electronic signal, is also shown by the stylized plot in Figure 6.8. It may be observed from the stylized plot that the spectrum of the pulsed optical signal consists of discrete spectral lines that have a frequency spacing equal to the repetition rate of the optical source. The wavelength converted optical pulsed signal is shown by the stylized spectrum having a center frequency at 193.15 THz, as seen in Figure 6.8. Finally, the intensity modulated time-domain optical pulses transmitted in the UL direction are shown by the stylized plot at the output of the intensity modulator.

6.4.3 Design of the Wavelength Converter

The design of the wavelength converter is similar to that of the SPM based regenerator shown in Figure 4.3. The wavelength converter consists of a high-power amplifier, which amplifies the input signal pulses to a peak power of $1W$. The amplified signal is input to a HNLF similar to that of Figure 4.3 for broadening the spectrum of the pulses. The HNLF has a length of $1km$, an attenuation of $2.1dB.km^{-1}$, dispersion of $-1.7ps.nm^{-1}.km^{-1}$, nonlinearity of $18W^{-1}.km^{-1}$ and a dispersion slope of $0.023ps.nm^{-2}.km^{-1}$. At the output of the HNLF, a Gaussian optical filter is placed at a frequency offset of $50GHz$. The offset of 50 GHz is chosen in order to shift the UL optical signal frequency with respect to the DL optical signal frequency. The bandwidth of the output filter is chosen to ensure that it generates optical pulses having a pulse width of $40ps$, which is the same as that of the DL transmitted signal. At the output of the filter, the frequency shifted pulsed signal of Figure 6.8 is obtained for transmitting the UL digital data. The output versus input power transfer function of the wavelength converter along with its operating point chosen is shown in Figure 6.9. The operating point is chosen for ensuring that small amplitude variations in the input signal are compressed by the wavelength converter [109], [111]. The compression of amplitude variations results in the reduction of amplitude jitter in the UL pulsed optical signal.

6.4.4 Performance Results of the Digitized ROF Link

In this section, we observe the EVM performance of the received 64-QAM signal. Figure 6.10 shows the EVM versus SNR results obtained for both the DL and UL signals. For the sake of comparison, the EVM of the analogue signal detected without digitization and transmission over the fiber is also plotted for both the DL and UL cases. The SNR of the signal is varied by imposing bandlimited Gaussian noise on the pure analogue signal having a bandwidth equal to the 64-QAM signal's bandwidth. As it will be discussed in Section 6.5.1, the out-of-band noise has a detrimental

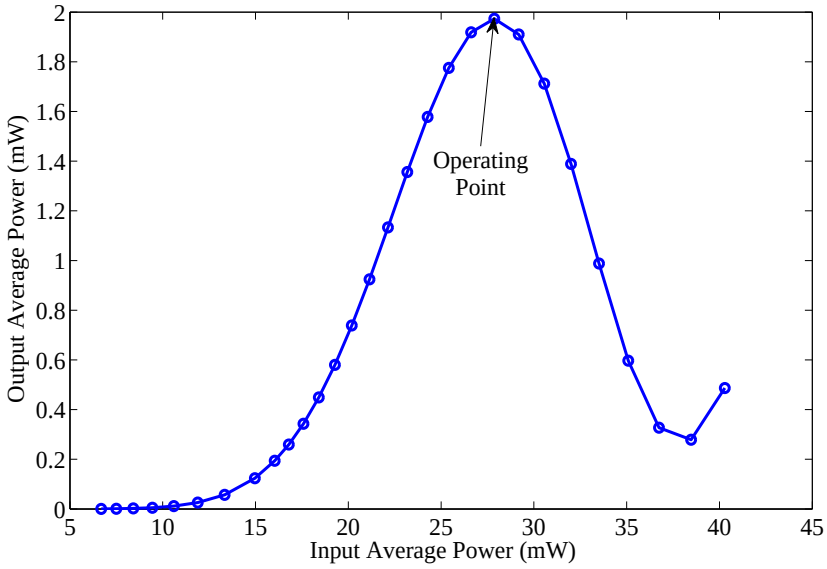

Figure 6.9: Transfer function of the wavelength converter.

effect on the digitized signal due to the sampling of the out-of-band noise along with the useful signal. Therefore, the out-of-band attenuation of the filter was designed to be as high as 50 dB for generating the results shown in Figure 6.10. It may be observed from the plots seen in Figure 6.10 that the EVM values recorded for both the DL and UL directions remain below 6% for a SNR of $25dB$. Furthermore, for low values of SNR, the EVM curves plotted for the analogue signal closely match the digitized RF signal. Since the resolution of the ADC/DAC is kept high (9-bit) and the out-of-band noise is almost totally eliminated, the noise due to quantization and out-of-band aliasing remained low. Therefore, there are essentially two types of noise contributions imposed on the digitized link. The first is the jitter noise inflicted by the ADC/DAC clocks, as defined in Section 6.4.2, while the second source of noise is the in-band ASE noise. At low values of SNR, the dominant source of noise is the in-band noise, which has a similar impact on both the analogue and digitized signal. Therefore, the EVM plots of the digitized and analogue signals overlap each other. By contrast, at high SNR the in-band noise is low, hence the jitter noise due to digitization becomes dominant. Therefore the EVM plot of the digitized signal deviates from that of the analogue signal, with the digitized signal having a higher EVM than the analogue.

In order to observe the quality of the optical pulses transmitted and received in both the DL as well as in the UL directions, the corresponding eye diagrams are shown in Figure 6.11. Since the eye diagrams represent the pulsed optical signals modulated by the digital data at the output of the ADC, they are independent of the SNR of the analogue signal. Furthermore, since the optical signal in the DL direction is phase modulated as opposed to amplitude modulated, the DL signal eye diagrams consist of only ones. By contrast, in the UL direction, the digital data is transmitted as an OOK signal, therefore the UL signal's eye diagrams consist of both ones as well as zeros. The eye diagrams of Figure 6.11 show that even after bidirectional transmission over 25 km of SMF, the optical signal quality is good and the impairments imposed by fiber are not significant. One of the major impairments caused in bidirectional transmission through a single

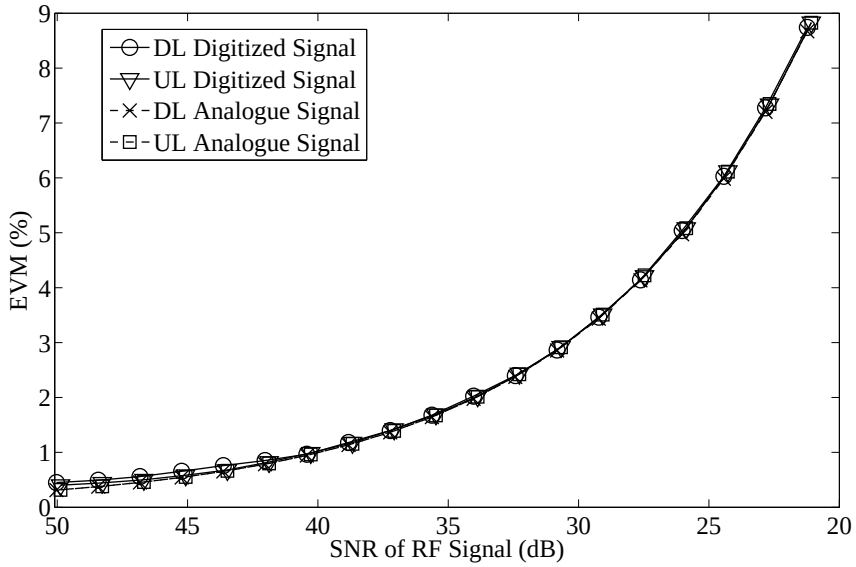

Figure 6.10: EVM versus SNR plots for the DL and UL digitized and for the analogue RF signals. The EVM versus SNR plots for the digitized RF signals are close to the plots for the corresponding analogue RF signals.

fiber is the Rayleigh scattering effect, as described in [153], [154]. Figure 6.11 shows that the effect of Rayleigh scattering is not strong enough to distort the signal after transmission over the single SMF. The eye diagrams plotted for the UL transmission shown in Figure 6.13c and 6.13d, show modest amplitude variations at the peak of the signals. This variation at the peak of the UL signal is due to the noise of the high power amplifier which has a noise figure of 6 dB at the BS.

Finally, to quantify the quality of the pulsed optical signals received after transmission through 25 km of fiber in the DL and UL directions, the corresponding BER results were shown in Figure 6.12. For comparison, the BER results of the back-to-back scenarios are also plotted. It can be observed from Figure 6.12 that even after transmission through 25 km of fiber, the BER results recorded both back-to-back and with the fiber are similar. The 0.5 dB difference observed between the back-to-back results of the DL and UL signals is due to the optical noise induced by the high-power amplifier, which has a noise figure of 6 dB. The results of Figure 6.12 show that with the aid of optical pulsed communication, digitized transmission of RF signals can be achieved over long fibers. It is worth mentioning here that baseband transmission over fiber was not preferred due to its higher installation costs imposed by the signal processing and frequency translation components at the RAU [155].

6.5 Effect of ADC/DAC Parameters on the Performance

The results of Section 6.4.4 were obtained by using fixed values of the ADC/DAC parameters that are mentioned in Table 6.2. Let us now consider the effect of varying the different paramters of the ADC/DAC on the performance of our proposed architecture. Our study will consider the effect of

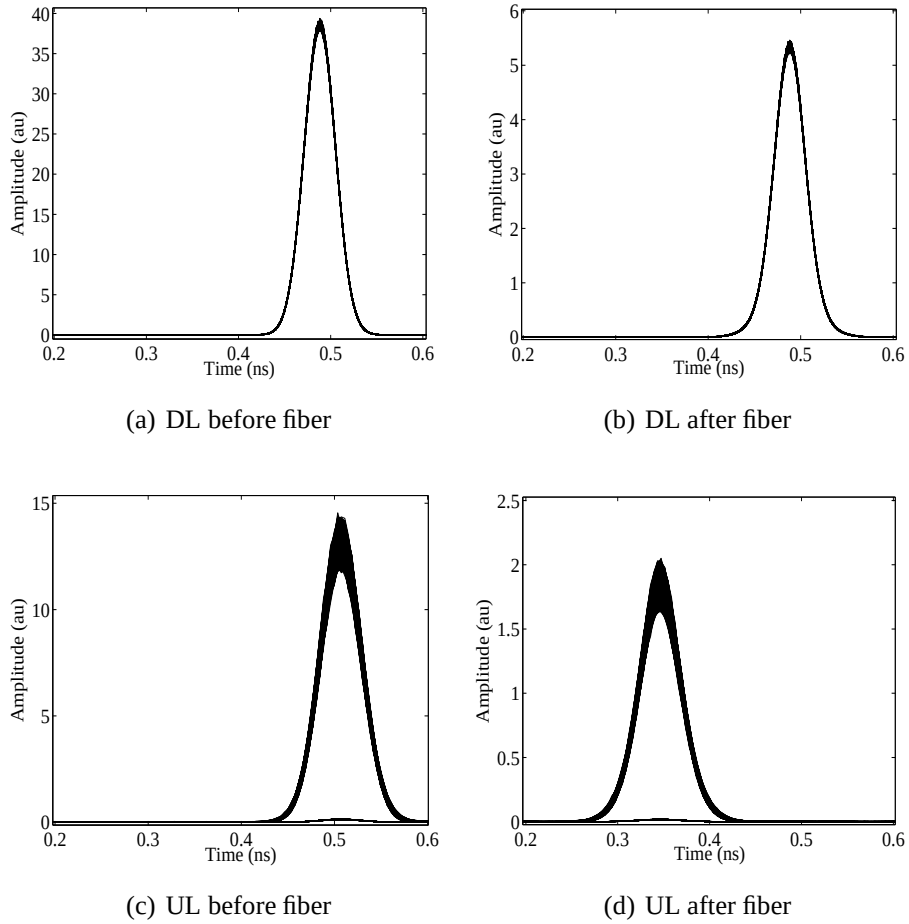

(a) DL before fiber (b) DL after fiber

(c) UL before fiber (d) UL after fiber

Figure 6.11: Eye diagrams for the DL and UL signals before and after transmission through the fiber. The eye diagrams are independent of the SNR of the analogue signal being digitized.

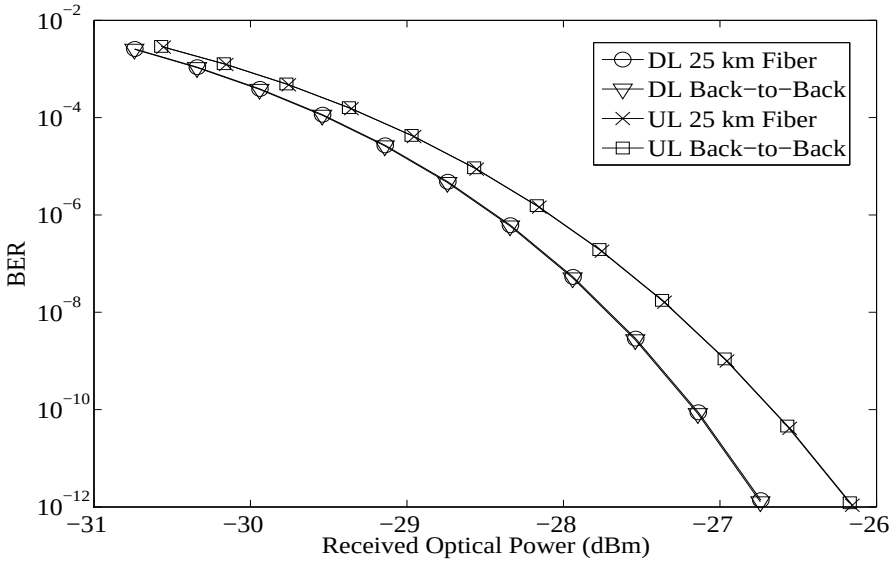

Figure 6.12: BER plots for the digitized DL and UL optical pulsed signals using the schematic of Figure 6.8 and the parameters of Table 6.2.

varying the amount of out-of-band noise imposed on the analogue signal, the effect of ADC/DAC jitter noise and the clipping effect induced by the ADC, while digitizing the input signal.

6.5.1 Noise in Bandpass Sampled Signal

Typically, the analogue signal input to the ADC is passed through a bandpass filter in order to reduce the out-of-band noise as exemplified in Figure 6.8. The bandpass filter used before bandpass sampling an analogue signal is used as the anti-aliasing filter [94]. Critical Bandpass sampling dispensing with a guard-band aliases any out-of-band noise present in the analogue signal being sampled [94], [156]. In this section, we calculate the SNR degradation caused by the bandpass sampling of an analogue signal having a bandwidth of B. Let S, N and N_{out} be the power spectral densities of the signal, of the in-band noise and of the out-of-band noise, respectively. Therefore, the SNR of the analogue signal denoted as SNR_A, before bandpass sampling is given as:

$$SNR_A = \frac{S}{N}. \tag{6.20}$$

The maximum analogue signal frequency that the sampling device can handle is termed as its effective bandwidth of B_{eff}. The total noise spectral density, which is the sum of the in-band and out-of-band spectral densities N and N_{out} respectively, is distributed along the total effective bandwidth of the sampling device spaning from $-B_{eff}$ to B_{eff}. We divide the total effective bandwidth into m segments, each having a width equal to the sampling frequency f_{samp} as:

$$m = \frac{2B_{eff}}{f_{samp}}. \tag{6.21}$$

One of these m segments contains the in-band noise N, while the rest of the $m-1$ segments contain the out-of-band noise N_{out}. Therefore, the SNR after bandpass sampling denoted as SNR_{bps} may be written as:

$$SNR_{bps} = \frac{S}{N + (m-1)N_{out}}. \tag{6.22}$$

It may be observed from Equation 6.22 that the SNR for the bandpass sampled signal is reduced as compared to the SNR of the analogue signal. The minimum effective bandwidth that the sampling device should have equals the highest frequency component f_H present in the analogue signal. Therefore the number of segments for this case equals the parameter k, which represents the position of spectral replicas in the sampled signal, as shown in Figure 6.2. Hence Equation 6.22 may be modified to arrive at the following relation for the SNR of a bandpass sampled signal:

$$SNR_{bps} = \frac{S}{N + (k-1)N_{out}}. \tag{6.23}$$

If the analogue signal is not bandpass filtered before being sampled, then we have $N_{out} \approx N$ and Equation 6.23 reduces to the following:

$$SNR_{bps} = \frac{S}{kN}. \tag{6.24}$$

The minimum SNR degradation is calculated in dBs and is defined as the ratio of the analogue signal's SNR to the maximum SNR of the bandpass sampled signal. The minimum SNR degradation D_{min} without using an anti-aliasing filter is given by:

$$D_{min} = 10log_{10}(k). \tag{6.25}$$

For the scenario, when the analogue signal is bandpass filtered prior to sampling, the SNR degradation D is given by the following equation:

$$D = 10log_{10}\left(1 + (k-1)\frac{N_{out}}{N}\right). \tag{6.26}$$

If the out-of-band noise attenuation of the anti-aliasing filter is denoted by the parameter $\varphi = N/N_{out}$, then Equation 6.26 may be written as:

$$D = 10log_{10}\left(1 + (k-1)/\varphi\right). \tag{6.27}$$

It may be observed from Equation 6.27 that a high value of the parameter φ will reduce the SNR degradation caused by out-of-band noise aliasing. Therefore, using an anti-aliasing filter having a high value of out-of-band attenuation helps in increasing the SNR of the bandpass sampled signal. Equation 6.27 also implies that operating at reduced sampling rates i.e. at higher k, increases the SNR degradation D [156].

6.5.1.1 Effect of Varying the Out-of-Band Noise

Let us now consider the effect of varying the out-of-band attenuation of the anti-aliasing filter on the 64-QAM signal transmitted in the DL direction. The attenuation used for generating the results discussed in Section 6.4.4 was $40dB$. As shown in Figure 6.13, the out-of-band attenuation is varied from 10 dB to 35 dB to obtain the EVM versus SNR plots. The noise is imposed on the analogue signal before the anti-aliasing filter. Figure 6.13 also shows the EVM versus SNR variation for the analogue signal without digitization and transmission over the optical link. It can be observed from Figure 6.13 that the lowest achievable EVM increases upon decreasing the out-of-band (OOB) attenuation of the anti-aliasing filter. Upon decreasing the OOB attenuation with a step-size of 5 dB, the EVM difference between any two curves plotted for digitized transmission increases due to a higher alised noise. By contrast, upon icreasing the out-of-band attenaution, the EVM plots recorded for the digitized signals shift closer to the analogue signal plot. Observe from Figure 6.13 that the anti-aliasing filter has no effect on the EVM of the analogue signal. Hence the analogue signal related curves obtained for different values of out-of-band attenuation of the anti-aliasing filter overlap each other.

6.5.2 Effect of ADC Sampling Clock Jitter

One of the main factors that limits the accuracy and speed of sampling devices is the clock jitter [157]. Clock jitter is the small variation in the instantaneous time period of the clock and

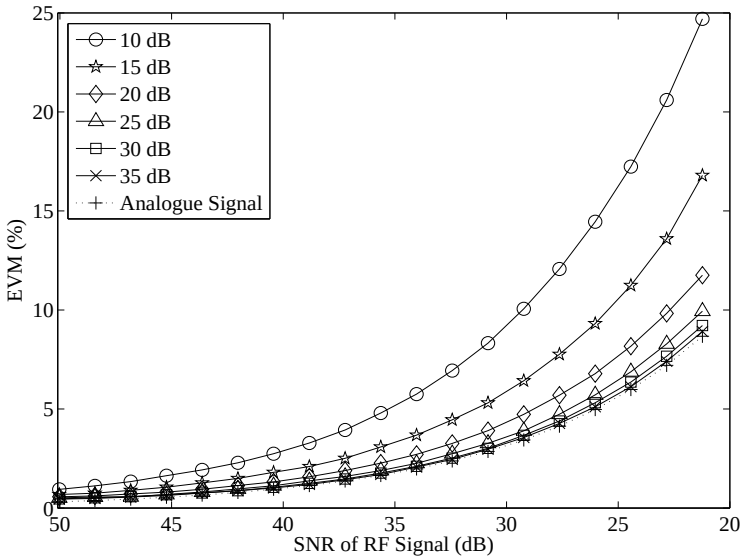

Figure 6.13: EVM versus SNR plots for different values of out-of-band attenuation using the schematic of Figure 6.8 and the parameters of Table 6.2.

results in sampling with a slight timing offset. Therefore, the clock jitter may be viewed as a source of noise that modifies the amplitude of the samples. If V_s is the correct sample obtained at the correct instant t_s and V_o is the wrong sample obtained at the wrong instant t_o, then the sampling error in time Δt and the amplitude error ΔV can be written as:

$$\Delta t = t_o - t_s, \tag{6.28a}$$

$$\Delta V = V_o - V_s. \tag{6.28b}$$

Since the timing jitter has a small value, the ΔV versus Δt relationship may be written as:

$$\Delta V = \left(\frac{dV}{dt}\right)_{t=t_o} \cdot \Delta t, \tag{6.29}$$

where the derivative represents the slope of the sampling signal at time instant $t = t_o$. Since the jitter in the sampling instant is independent of the analogue signal being sampled, the slope of the analogue signal and the timing error Δt may be treated as independent variables. Therefore, the RMS value of the sample amplitude error ΔV_{rms} can be obtained from the mean of the squared amplitude error denoted as $E\{(\Delta V)^2\}$, yielding:

$$\Delta V_{rms} = \sqrt{E\{(\Delta V)^2\}}, \tag{6.30a}$$

$$\Delta V_{rms} = \sqrt{E\{\left(\frac{dV}{dt}\right)^2\}}.\sqrt{E\{(\Delta t)^2\}}, \tag{6.30b}$$

$$\Delta V_{rms} = \sqrt{\frac{1}{T}\int_0^T \left(\frac{dV}{dt}\right)^2 dt}\Delta t_{rms}, \tag{6.30c}$$

$$\Delta V_{rms} = \sqrt{2}A\pi f_c \Delta t_{rms}. \tag{6.30d}$$

Equation 6.30d gives the RMS amplitude error in the sampled signal. Since the square of the RMS amplitude error is equal to the noise power added to the signal, the SNR quantifying the effect of the jitter noise can be expressed as:

$$SNR = \frac{SignalPower}{NoisePower}, \tag{6.31a}$$

$$SNR = \frac{E\{(\Delta V(t))^2\}}{(\Delta V_{rms})^2}, \tag{6.31b}$$

$$SNR = \frac{1}{4\pi^2 f_c^2 \Delta t_{rms}}, \tag{6.31c}$$

$$SNR(dB) = -20log(2\pi f_c \Delta t_{rms}). \tag{6.31d}$$

Equation 6.31d quantifies the SNR degradation imposed by the timing jitter of the ADC clock. Let us now use Equation 6.31d to vary the SNR of the 64-QAM signal used in our simulations. Figure 6.14 shows the EVM variation of the received DL signal upon varying the standard deviation of the ADC sampling clock's timing jitter. The sampling rate of the ADC used is 113.8 $MSamples/s$ and the SNR of the RF signal is kept at 50 dB. The typical value of the ADC clock jitter's standard deviation is in the range of $0.7ps$ [37]. It can be observed from Figure 6.14 that for a standard deviation as high as $4ps$, the EVM remains close to 2%. Therefore, it can be deduced from these results that the noise induced by the timing jitter of the ADC in our simulations is insignificant, because we the use a relatively low sampling rate of 113.8 $MSamples/s$, which is made possible by the use of the bandpass sampling technique.

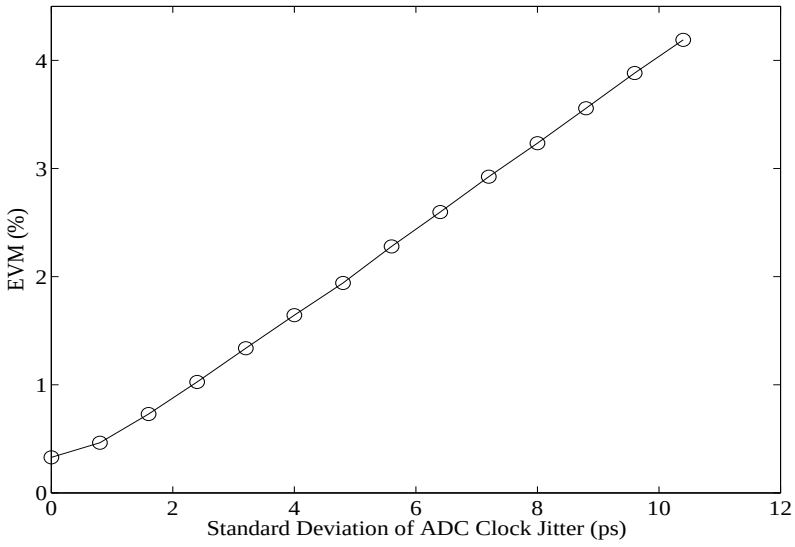

Figure 6.14: EVM versus ADC timing jitter plot using the schematic of Figure 6.8 and the parameters of Table 6.2.

6.6 Digitized Transmission of Multiple 64-QAM RF Signals

In Section 6.4, the digitized transmission of a single 64-QAM analogue signal was discussed in detail. Optical pulses generated at a repetition rate of 1.024 GHz were used for transmitting the electronic pulses at the output of the ADC. In this section, we propose the optical pulsed transmission of multiple digitized RF 64-QAM signals using a single optical pulsed source having the same repetition rate of $1.024GHz$. The transmission of multiple digitized RF signals is achieved using optical signalling. In order to use low complexity optical signalling, digitized data of two RF channels is transmitted, where the DL data is transmitted using Optical Differential Quadrature Phase Shift Keying (ODQPSK) modulation, mapping the two signals to the I and Q component, respectively. By contrast, the two channel's bits of the UL data are transmitted using 4-level Amplitude Shift Keying (4-ASK). A pair of bits composed of one bit from each digitized channel, is assigned a unique amplitude to form the 4-ASK signal. A single fiber is used for duplex transmission of the optical signal, where the wavelength converter discussed in Section 6.4.3 is used at the BS to shift the center frequency of the received ODQPSK signal pulses. The wavelength conversion aids in avoiding the deleterous effects of Rayleigh Scattering, as discussed in Section 6.4.3. The frequency-shifted optical pulses are amplitude shifted to four different levels in order to carry the data of the two RF digitized UL signals over the same optical fiber used for transmitting the DL data, as detailed in Section 6.6.2.

6.6.1 Transmitter Setup for Downlink Signals

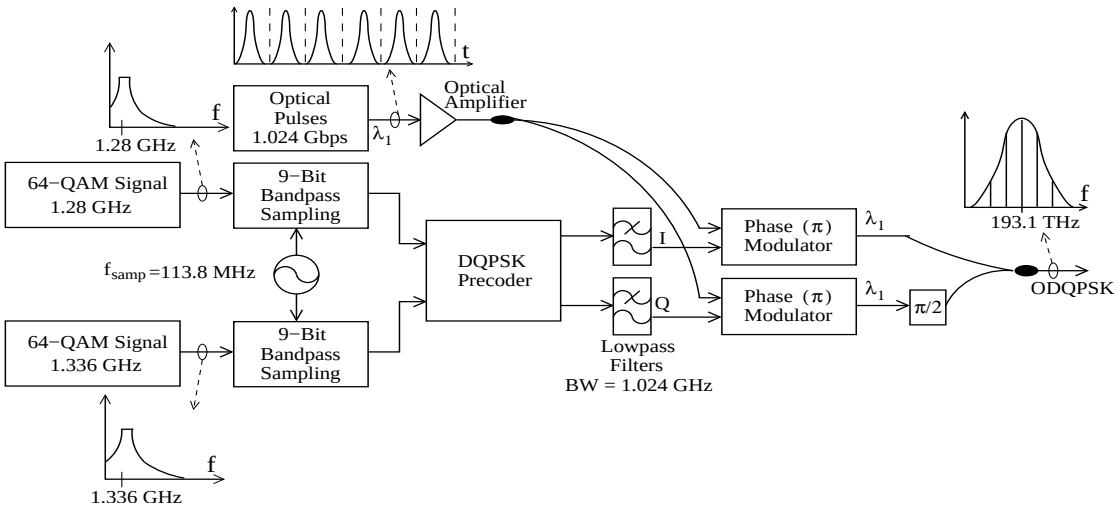

Figure 6.15: Transmitter schematic of the two-channel Link. A DQPSK precoder is used as opposed to a DPSK precoder of Figure 6.8. Furthermore, two phase modulators are used for the I and Q components of the digitized data, as opposed to a single phase modulator of Figure 6.8.

The transmitter architecture of the 2-channel case is shown in Figure 6.15, where two 64-QAM signals having center frequencies of 1.28 GHz and 1.336 GHz are bandpass sampled using separate ADCs. The frequencies of 1.28 GHz and 1.336 GHz are chosen in order to satisfy

Equation 6.7 as well as to generate samples that are a multiple of 2, which results in reduced simulation time. The outputs of the two ADCs are forwarded to a DQPSK modulator, which outputs the In-phase (I) and Quadrature-phase (Q) components of the DQPSK signal, each at a repetition rate of 1.024 GHz. Since the parameters of the 64-QAM RF signals used in this section are similar to that of Section 6.4.2, the parameters of the digitized signals generated in this section are the same as in Section 6.4.2. The electronic I and Q components are used for phase modulating two separate streams of optical pulses having a pulse width of 40 ps and a repetition rate of 1.024 GHz. As shown in Figure 6.15, after phase modulation, one of the optical signals is phase shifted by 90 degrees in order to keep it in quadrature with the other optical signal. The resultant I and Q components are coupled together using the optical coupler of Section 2.6.1, as shown in Figure 6.15. The output of the coupler is a pulsed ODQPSK signal at a repetition rate of 1.024 GHz.

6.6.2 Receiver Setup for Downlink Signals

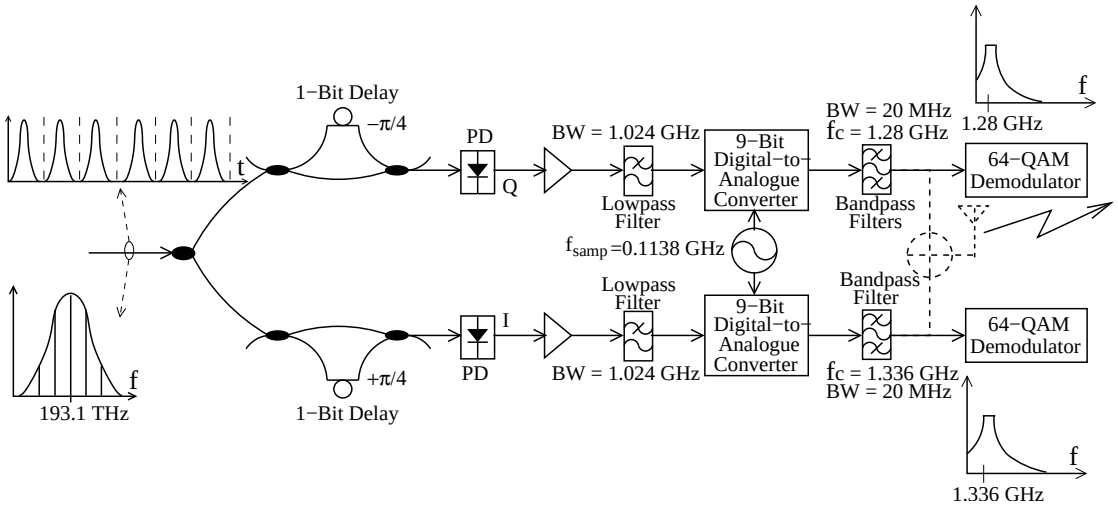

Figure 6.16: Receiver schematic of two-channel link. Two receiver setups shown in Figure 6.8 are used to recover the analogue signal from the digitized data.

The DL ODQPSK signal is detected using differential detection, as shown in Figure 6.16. The received optical signal is decoded using an optical delay-and-add structure [158]. The decoder consists of a pair of MZIs, where a differential optical delay of $+\pi/4$ and $-\pi/4$ is maintained between the arms of each MZI, respectively. At the output of each MZI, I and Q components of the ODQPSK signal are recovered, respectively and photo-detected to obtain the electronic I and Q signals, as shown in Figure 6.16. The electronic I and Q signals are amplified and passed through low pass filters having bandwidth, which equal to the bit rate, namely 1.024 GHz. The I and Q bit sequences represent the digital data for each of the two analogue 64-QAM signals transmitted by the MSC. Therefore, the I and Q bit sequences are input to the 9-bit DACs, as shown in Figure 6.16. The output of each of the DAC is composed of the analogue RF signal having spectral replicas at multiples of the sampling frequency. A bandpass filter centered at the original analogue signal

frequency is used at the output of each of the DACs in order to receover the required spectral replica. The outputs of the two bandpass filters are then combined and transmitted using the antenna, as shown in Figure 6.16.

6.6.3 Transmitter/Receiver for the Uplink Signals

Since optical 4-ASK modulation is used in the UL direction, the design of the optical transmitter and receiver is simple. The two data signals generated after digitizing the 64-QAM RF signals are encoded into a single sequence having four amplitude levels, where each level represents a pair of bits having one bit from each data signal. The 64-QAM signals used in the UL direction have frequencies of 0.64 GHz and 0.696 GHz and a symbol rate of 16 $MSymbols/s$ each. Again, the frequencies of of 0.64 GHz and 0.696 GHz are chosen in order to satisfy Equation 6.7 as well as to generate samples that are a multiple of 2, which results in reduced simulation time. The digitized output for each of the analogue signal has a bit rate of 1.024 $Gbps$, therefore, the symbol rate of the 4-ASK signal is 1.024 $GSymbols/s$. The electronic 4-ASK signal is used for amplitude modulating an optical pulse sequence having a repetition rate of 1.024 GHz and a center frequency of 193.15 THz. As discussed in Section 6.4, the optical pulsed signal generated for the UL direction is obtained by wavelength shifting the DL optical pulsed signal. At the output of the amplitude modulator, a 4-ASK modulated optical signal is obtained, which is transmitted through the same optical fiber as that used for DL signal transmission. At the receiver, the optical signals are photo-detected and the electronic output of the PD is decoded in order to obatin two separate electronic bit sequences representing the digital data of the two UL analogue RF signals. The digital signal is converted back to its analogue form by the DACs, as discussed in Section 6.3.5

6.6.4 Performance Results of the Two-Channel Transmission Link

This section discusses the performance results of the proposed digitized multiple RF 64-QAM channel transmission system. The performance results are obtained by plotting the EVM values of both the RF channels in the DL and UL directions, as shown in Figure 6.17. The EVM values of the corresponding back-to-back analogue RF signals that are not transmitted over the optical link are also plotted for comparison. It can be observed from Figure 6.17 that the relation between the EVM values of the digitized and analogue RF signals is the same, as observed in Figure 6.10 for the case of a single RF channel. However, there is a significant difference between the EVM values of the DL and UL signals, with the UL signal having higher values of EVM for the same value of SNR, as shown in Figure 6.17. Since the UL signals are received through a single antenna, bandpass filters are used for separating the two received RF signals before being digitized. Due to the use of realistic bandpass filter parameters, some of the frequency-shifted out-of-band signal contaminates the desired signal that is being digitized. This out-of-band signal of the other channel becomes a source of out-of-band noise while digitizing the RF signals, as discussed in Section 6.5.1. It is due to this out-of-band noise power that the EVM values of the UL signals are higher compared

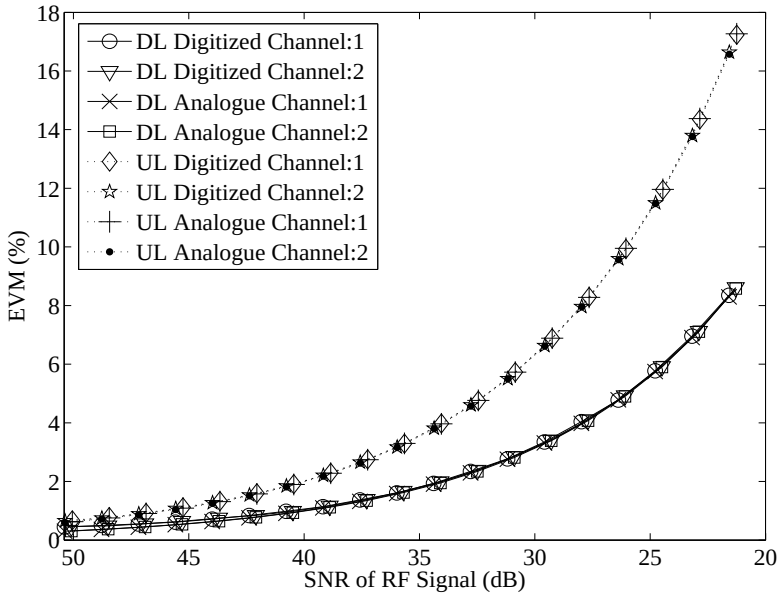

Figure 6.17: EVM versus SNR plots for DL and UL digitized and analogue signals.

to the DL signals. Therefore, the results shown in Figure 6.17 suggest that in order to achieve an acceptable performance in the UL direction, the bandpass filters used after the antenna should have a high out-of-band attenuation value. The out-of-band attenaution chosen in our simulations is 45 dB.

Figure 6.18 shows the eye diagrams of the DL and UL optical pulsed signals both before and after transmission through the 25 km optical fiber. It can be observed from Figure 6.18 that the eye diagrams are quite open. Since the UL digitized signal is transmitted using optical ASK modulation, the eye diagrams recorded for the UL signals have four amplitude levels, as shown in Figures 6.20c and 6.20d.

6.7 Conclusions

We have presented a detailed study of the digitized transmission of RF signals over fiber. The bandpass sampling technique, which is widely used for digitizing analogue RF signals was detailed. Based on this technique, novel studies have been presented for the duplex transmission of one and two 64-QAM RF signals over fibre. The main conclusions of the chapter are summarized below,

- The Bandpass sampling technique digitizes RF signals using sampling frequencies, which are much lower than the center frequency of the RF signals being digitized, namely on the order of the signal's bandwidth.
- In order to faithfully retreive the analogue RF signal from the digitized signal, suitable guard

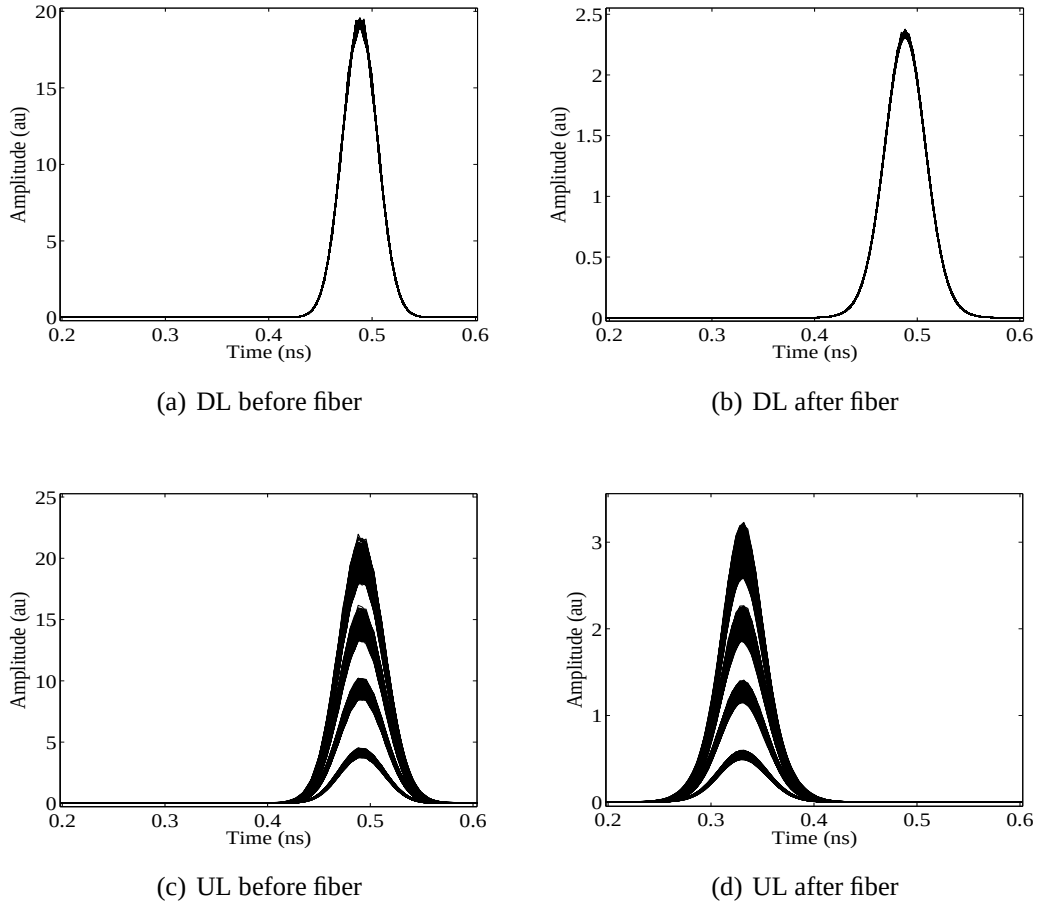

(a) DL before fiber

(b) DL after fiber

(c) UL before fiber

(d) UL after fiber

Figure 6.18: Eye diagrams for the DL and UL optical signals before and after transmission through the fiber. The eye diagrams are independent of the SNR of the analogue signal being digitized.

bands should be chosen, while the out-of-band noise of the RF signal was strongly attenuated.

- Finally, the digitized transmission of RF signals over fiber allows them to be transmitted over long fiber lengths.

Table 6.3 summarizes the performance of both the single and two RF channel DROF architecture, respectively.

Table 6.3: Performance summary of both the single and two RF channel DROF architecture. The EVM results for single channel digitized transmission were extracted from Figure 6.10. The EVM results for two channel digitized transmission were extracted from Figure 6.17

Single digitized channel transmission performance

Channel Number	Direction	Signal Type	SNR	EVM	BER
Channel 1	Downlink	64-QAM, 16 $MSymbols/s$	27.5 dB	4.2 $\%$	10^{-7}
Channel 1	Uplink	64-QAM, 16 $MSymbols/s$	27.5 dB	4.2 $\%$	10^{-7}

Two digitized channel transmission performance

Channel Number	Direction	Signal Type	SNR	EVM	BER
Channel 1	Downlink	64-QAM, 16 $MSymbols/s$	27.5 dB	4.1 $\%$	10^{-8}
Channel 2	Uplink	64-QAM, 16 $MSymbols/s$	27.5 dB	8.1 $\%$	10^{-3}
Channel 1	Downlink	64-QAM, 16 $MSymbols/s$	27.5 dB	4.1 $\%$	10^{-8}
Channel 2	Uplink	64-QAM, 16 $MSymbols/s$	27.5 dB	8.1 $\%$	10^{-3}

Chapter 7

Conclusions and Future Work

This report discusses the three main types of ROF communication systems that may form a vital part of future high-bandwidth wireless communication. Chapter 1 of the report highlights the challenges faced by service providers and network designers while coping with the ever-increasing bandwidth demand of wireless subscribers. Chapter 2 aids the reader in understanding the operating principles of the most commonly used optical components in fiber optic communication systems. Chapter 3 introduces the three fundamental types of ROF communication systems by discussing their similarities and differences, as well as the limitations of each type of system. Chapter 4 of the report discusses the family of the BROF communication systems, along with our novel contributions in the area. Finally, Chapter 5 and Chapter 6 investigate AROF and DROF communications, repectively, along with our novel contribtions in these two areas. This chapter summarizes the key contributions of each chapter and present a range of ideas for our future work.

7.1 Chapter Summaries

This section presents the summary of each chapter in the report.

7.1.1 Chapter 1 - Introduction

Chapter 1 highlights the growth in the number of wireless subscribers and their increased bandwidth requirement with the aid of statistics. Due to development of bandwidth-thirsty portable devices such as smartphones and tablet PCs, bandwidth demands have increased considerably over the past decade. The current technologies used for providing wireless services may be divided into cellular, WiFi and WiMax type systems.

Finally, we discussed some of the solutions proposed in literature for coping with the increase in bandwidth demand, such as bandwidth-efficient modulation schemes as well as polarization multiplexing. The transmission bands of fiber optic communication systems may be extended as

well as multicore fibers may be used. The use of network coding to increase the throughput of PONs was also discussed. Finally, architectural changes in the optical networks which enable them to perform dynamic routing and bandwidth allocation were highlighted.

7.1.2 Chapter 2 - Components of Optical Communication Systems

Chapter 2 reviewed the operating principle of the main components in optical communication systems. Firstly, the generation of both continuous wave and pulsed optical signals was detailed. The optical carrier is typically generated by the DFB semiconductor laser of Section 2.1.1.1. The optical carrier may be either directly or externally modulated with the data as discussed in Section 2.1.2 and 2.1.4, respectively. The simplest form of optical carrier modulation is direct modulation, where the electronic signal is superimposed on the bias signal of the laser source. External modulation is used for high-frequency RF signals ($\geq 10GHz$) and requires external optical modulators, as described in Section 2.1.4.

The optical fiber transmission medium is discussed in Section 2.2, which imposes certain impairments on the signal transmitted. As discussed in Section 2.2.1, the simplest of these impairments is the attenuation of the fiber, which occurs due to the absorption by the silicon fiber and Rayleigh scattering of the light travelling through it. The second major type of impairment is dispersion of the optical fiber, as discussed in Section 2.2.2. Fiber-induced dispersion is a phenomenon, where light of different wavelength/frequency travels at different speeds within the fiber. This gives rise to broadening of the optical pulses at the output of the fiber. Finally, the third type of impairment is the nonlinearity of the fiber discussed in Section 2.2.3 which becomes dominant upon increasing the intensity of light travelling through it.

The optical receiver is discussed in Section 2.3, which performs the OE conversion of its input signal with the aid of a photo-detector. The operating principle of a commonly used semiconductor photo-detector termed as the PIN photodiode is highlighted in Section 2.3.

Finally we discuss the auxillary components used in the optical link, such as optical amplifiers, optical filters and passive optical components. Optical amplifiers make use of external pumping and stimulated emission for amplifying the input signal, as discussed in Section 2.4. The most common optical amplifier used in optical communication systems is the EDFA, whose operating principle is discussed in Section 2.4. Section 2.5 details the operating principle of optical filters, which may be used for separating a single or multiple optical signals from a WDM signal or to reject out-of-band ASE noise imposed on the desired signals. Three main types of optical filters namely Grating, Arrayed Waveguide and Fabry-Perot filters are discussed in detail in Section 2.5. Finally, Section 2.6 touches upon passive components, such as optical couplers/splitters, optical multiplexers/demultiplexers, optical isolators and optical circulators.

7.1.3 Chapter 3 - Radio Over Fiber Communication

Chapter 3 introduces the three main types of ROF communication systems that are detailed later in Chapters 4 to 6. Firstly, the two main methods of transporting RF signals in the three types of ROF systems are presented in Section 3.1. The first method is the simple intensity modulation relying on the classic direct detection technique, as discussed in Section 3.1.1. The second method is remote heterodyne detection, which relies on the coherent mixing of two optical carriers in a PD, resulting in a high-frequency current at the output of the PD, as described in Section 3.1.2. Section 3.2 discusses the two commonly used multiplexing techniques of ROF communication systems, namely Sub-Carrier Multiplexing (SCM) and Wavelength Division Multiplexing (WDM). In the SCM technique, the signals of multiple channels having different center frequencies are simply superimposed electronically and the resultant electronic signal is used for intensity modulating an optical carrier, as described in Section 3.2.1. In the WDM technique described in Section 3.2.2, multiple channels are transmitted upon modulating different optical carriers by the RF channels and then multiplexing them optically.

In Section 3.3 we then briefly introduced the AROF communication system philosphy where the RF carrier modulated by the baseband data is transmitted over the fiber using an optical carrier, while up-conversion and carrier modulation are peformed at the CU. The practical impairments imposed on the AROF signal by the optical link are discussed in Section 3.3.1. Furthermore, some of the optical linearization techniques suggested in the literature are summarized in Section 3.3.3.

Finally, we introduced the DROF and BROF communication systems in Section 3.4 and 3.5, respectively. DROF involves the digitization of the RF signal before tramsission over the fiber. The RF signal is converted to a series of binary electronic pulses in an ADC and following EO conversion, the resultant optical signal is transmitted over the fiber. By contrast, in BROF communication, the baseband data is directly transmitted over the fiber using an optical carrier without up-conversion to a high-frequency RF carrier. Since digitized and baseband ROF communication may use pulsed optical signals, a pulse propagation model is presented in Section 3.6 in order to characterize the behaviour of optical pulses travelling through the fiber.

7.1.4 Chapter 4 - Baseband ROF and Optical Pulse Regeneration

Chapter 4 of the thesis discusses BROF communications in detail. In order to elaborate on the similarities and differences among the three types of ROF communication system, the top-level architecture of a BROF system is presented in Figure 4.1. Figure 4.2 elaborates on the principle of TDM and WDM that are commonly used in baseband communication systems. Section 4.2 discusses the appropriate optical pulsed signal regeneration techniques required in scenarios, where the optical signal is degraded beyond a certain limit, while travelling through the optical link. An SPM based regenerator is presented in Section 4.3. Among the various fiber-based regenerators that have been proposed for all-optical signal regeneration, the SPM based regenerator proposed by Mamyshev [106] is the most popular one owing to its implementational simplicity and efficiency.

It may be concluded that both the dispersion slope and the dispersion parameter may be used as an additional parameter of controlling the regenerator's performance.

A BROF aided 60 GHz DAS relying on optical signal processing techniques for transmitting baseband data at mm-wave frequencies to multiple RAUs is described in Section 4.4. The DAS architecture is constituted by six RAUs that are fed using baseband ROF data in a star-like network topology, as shown in Figure 4.13. The baseband data destined for each RAU may be transmitted over a range of frequencies around 60 GHz that are generated using only two pulsed signal sources. The performance results presented in Section 4.4.3 show that the proposed baseband architecture results in BER values which are within a dB of the idealized back-to-back results. Furthermore, the eye-diagrams of the received optical signals shown in Figure 4.19 reveal that the distance of the ROF link may be further increased beyond the distances considered.

7.1.5 Chapter 5 - Analogue ROF Communication

Chapter 5 of the thesis discusses AROF communications in detail by presenting our contributions in the area. AROF is contrasted to both BROF and DROF in the a top-level diagram of Figure 5.1. Our study of an AROF system that is used for facilitating duplex communication among three RAUs located at different positions in a ring architecture is presented in Section 5.3. The duplex transmission of 16-QAM signals to the three RAUs is achieved by using a single laser source located at the MSC. The performance of the architecture is assessed on the basis of both the EVM as well as of the corresponding BER results. The results show that the worst-case EVM values that are obtained for the DL RF signals are close to 4 $\%$. These values are still within the acceptable limit of 6 $\%$ for a 16-QAM 802.16a WiMax signal even when operating without channel equalization [37]. Furthermore, the performance of the proposed ring architecture in the presence of parameter variations is presented in Section 5.7, where it was shown that the ROF link is of high integrity.

The optical physical layer design of a mm-wavelength DAS architecture is proposed in Section 5.8. The proposed mm-wavelength design uses a single laser source for transmitting bi-directional data to two spatially separate RAUs in a virtual MIMO architecture shown in Figure 5.17. The proposed technique allows the mm-wavelength 64-QAM signals generated at the RAUs to be transmitted at two different center frequencies, namely either at 25 GHz or at 50 GHz, therefore, making the system flexible. The performance results discussed in Section 5.10 show that EVM values below 6 $\%$ are obtained for both the DL and UL RF signals for SNRs in excess of 25 dB. Furthermore, the performance of the proposed virtual MIMO architecture in the presence of parameter variations is presented in Section 5.11, where it was shown that the ROF link has a BER of $< 10^{-9}$ for OSNR of 28 dB.

7.1.6 Chapter 6 - Digitized ROF Communication

Chapter 6 discusses DROF communications in detail. The digitization of the analogue signal is performed using bandpass sampling, which ensures that the sampling rate of the ADC/DAC is dependent on the bandwidth of the analogue signal instead of its highest frequency. In Section 6.4, a novel cost-efficient physical layer is designed for a DROF link, where a single pulsed laser source and a single fiber is used for duplex transmission of digitized 64-QAM signals. In order to avoid the impairments caused by Rayleigh scattering in bidirectional transmission through a single fiber, wavelength conversion is employed at the BS, as described in Section 6.4.3. The performance results of the proposed link are presented in Section 6.4.4, where the EVM values recorded for both the DL and UL directions remain below 6% for a SNR of $25dB$. To quantify the quality of the pulsed optical signals received after transmission through 25 km of fiber in the DL and UL directions, the corresponding BER results were also presented in Section 6.4.4. It was observed from Figure 6.12 that even after transmission through 25 km of fiber, the BER results recorded for both back-to-back and for fiber-based transmissions were similar. Hence it may be concluded that the dynamic range of the DROF system is dependent upon the sensitivity of the optical receiver used at the BS.

The optical pulsed transmission of multiple digitized RF 64-QAM signals using a single optical pulsed source over a single fiber is discussed in Section 6.6. The transmission of multiple digitized RF signals was achieved using optical signalling, where the DL data was transmitted using Optical Differential Quadrature Phase Shift Keying (ODQPSK) modulation, mapping the two digitized signals to the I and Q components, respectively. By contrast, the two channel's bits of the UL data were transmitted using 4-level Amplitude Shift Keying (4-ASK). The performance results were obtained by plotting the EVM values of both the RF channels in the DL and UL directions, as discussed in Section 6.6.4. It was shown in Section 6.6.4 that due to the out-of-band noise power in the UL analogue signals, the EVM values of the UL signals are higher compared to the DL signals. Therefore, in order to achieve an acceptable performance in the UL direction, the bandpass filters used after the antenna should have a high out-of-band attenuation.

7.2 Design Guidelines

In this section, we will summarize our design guidelines conceived for ROF communication systems based on the studies performed throughout Chapter 4 to Chapter 6. These guidelines are aimed at aiding the system designer of a ROF communication system in choosing the most suitable type of ROF system based on the parameters of the link and the type of service provided.

1. The length of the ROF link plays an important role in choosing the type of ROF communication system. The performance results discussed in Section 4.4.3 for the BROF and in Section 6.4.4 for the DROF system show that these systems have a good performance over long fibers. Therefore, in a ROF system where the RAUs are located far from the CU, both

BROF and DROF systems provide a suitable solution.

2. As discussed in Section 3.3.1, the ROF link imposes different types of impairments on the signal travelling through it. The BROF and DROF systems are generally more immune to such impairments due to the digital nature of the optical signal travelling through the ROF link. Hence, for ROF links that have a high link noise, the BROF and DROF systems provide a better choice in contrast to the analogue ROF system.

3. A major factor to be considered in designing the ROF link is the simplicity of the RAUs. This is specially true in situations where a large number of RAUs are supported by the CU. As discussed in Chapter 5, the design of the RAU for an AROF system is the simplest compared to BROF and DROF systems. The simplest RAU for an AROF system requires a PD, an electronic bandpass filter and a RF amplifier, as seen in Figure 3.6. The BROF system of Figure 3.10 may require bit-to-symbol mapping at the RAU in case of RF signals using complex modulation schemes, while the DROF system of Figure 3.9 requires digital signal processing at the RAU.

4. The choice of the ROF system is also dependent upon the complexity of the RF signal. The AROF system is transparent to the type of RF signal being transmitted. Therefore, complex-valued modulation schemes such as for example 64-QAM RF signals may be readily transmitted by the AROF system. The same is true for the DROF system, where the RF signal would require digitization before transmission over the fiber. In case of BROF system, the transmission of a RF signal having a complex modulation scheme would require bit-to-symbol mapping at the RAU, which is not a desirable feature in scenarios, where simplicity of the RAU is also a concern.

5. It was shown in Section 4.4.2 that with the aid of a combination of OTDM and WDM, the BROF system simultaneously supported six different RAUs. The number of RAUs may be further increased depending upon the type of system. Therefore, in situations where a large number of RAUs are supported, BROF systems provide a feasible solution. Similarly, DROF systems may take advantage of the combination of OTDM and WDM in order to support a large number of RAUs, but the requirement of DACs at the RAUs make it a less attractive option compared to the BROF system. By contrast, AROF systems can only use WDM due to the use CW optical carriers. Therefore, the number of RAUs supported by AROF communication is lower compared to BROF systems.

6. The bandwidth of the ROF signal in case of AROF and BROF systems depends mainly upon the bandwidth of the RF signal transmitted. In AROF systems, the bandwidth of the AROF signal may be reduced by using complex-modulated RF signals. Whereas, in BROF systems, baseband data is used to modulate the optical carrier, as shown in Figure 3.10. Therefore, the bandwidth of the BROF signals for the same data rate will be higher compared to the bandwidth of the AROF signals. By contrast, the bandwidth of the DROF signal depends both on the bandwidth of the RF signal as well as on the resolution of the ADC/DAC pair, as

discussed in Section 6.3. Therefore, the bandwidth expansion imposed by the DROF systems is commensurate with the number of bits/sample used by the ADC. Hence it is invariably higher than that of both the AROF and BROF systems.

7. BROF systems are capable of supporting RF signals having bit-rates in the range of 1 $Gbit/s$ to 2.5 $Gbit/s$ to a single or multiple RAUs [73], [120]. By contrast, AROF systems suffer from severe impairments imposed by the fiber-induced dispersion, when high-symbol-rate RF signals are transmitted, as discussed in Section 3.3.1.3. Furthermore, in case of DROF systems, the sampling frequency of the ADC required for high-symbol-rate RF signal will increase, resulting in increase in the cost and complexity of the ADC/DAC pair. Therefore, BROF systems provide the most feasible solution for transmitting high-bit-rate RF signals to the RAUs.

8. Due to the digital nature of the optical signals, the both BROF and DROF systems may make use of the already deployed optical fiber infrastructure. In a pulsed optical fiber network, optical signal processing techniques such as wavelength conversion and logical operations are performed in order to control and direct the flow of data [102], [103]. Such operations may also be performed on BROF and DROF signals, hence enabling them to be seamlessly integrated into the already deployed optical fiber networks. By contrast, due to the analogue nature of the optical carrier used in AROF communication, the optical signal prosessing techniques are not feasible and hence integration with the already deployed systems is difficult.

9. In scenarios where optical fiber has to be deployed in order to reach different RAUs, both the BROFand DROF communications may use a single optical fiber for duplex transmission with the aid of wavelength conversion, as dicussed in Section 6.4.2. The use of a single fiber is made possible due the pulsed nature of the BROF and DROF communication, which makes them less prone to noise due to Rayleigh scattering [153], [154]. Therefore, the cost of employing two fibers for the DL and UL direction may be eliminated with the use of BROF or DROF communication. On the other hand, CW optical signals used in AROF systems are strongly affected by Rayleigh scattering, where a single fiber is used for duplex transmission.

10. As mentioned under 4 above, the AROF system is transparent to the type of modulation used by the RF signal. Therefore, AROF communication may be used for simultaneously providing multiple services to the MSs. By contrast, the bit-rate of the baseband ROF system depends upon the type of RF signal transmitted. Hence a change in the bit-rate would require the use of a different pulsed laser source. Similarly, a change in the type of RF signal transmitted through DROF systems may require changes in both the ADC/DAC pair as well as in the pulsed laser source.

11. Finally, the transparency of the AROF system to the type of RF signal transmitted makes it attractive for use in future RF communication systems. On the other hand, the BROF and

DROF systems would require changes in the hardware, when different future RF communication systems are introduced.

7.3 Future Work

7.3.1 Radio Over Plastic Optical Fiber

Research interest in the employment of Plastic Optical Fiber (POF) for fiber-to-the-home infrastructure have increased recently [159], [160] and [161]. The reason for the increase in popularity of POF lies in its attractive physical properties, which include a higher flexibility, resilience to both bending as well as shock, vibration and handling [159]. These characteristics of the POF make it an inexpensive choice for fiber-to-the-home networks, compared to the classic silicon fiber [160]. Since ROF systems typically used for short-range wireless communication such as in-home or in-building communication, POF is a suitable choice for ROF communications. However, its bandwidth limitation and high transmission loss has to be mitigated. An extention of our work presented in this thesis would be to investigate the use of POF in our proposed architectures for the three types of ROF communication systems. The use of a single laser source along with single POF increases the cost-efficiency of the overall link. The high transmission loss of POF may be addressed by using pulsed optical communication systems, as suggested in Chapter 4 and Chapter 6 of the thesis. Therefore, our future work is to extend the work reported in this thesis by using POFs.

7.3.2 Radio Over Wireless Optical Links

The use of wireless optical transmission for indoor communication is also the subject of extensive study due to the availability of a broad unregulated bandwidth [162], [163], [164] and [165]. The employment of visible light for indoor optical wireless communication provides high-rate communication as well as illumination inside a room [162]. Both the visible and infrared spectrum can penetrate through glass but not through walls, which confines the communication within a room and hence enhances privacy and security [163]. The use of optical spectrum in the C-band (1550 nm/ 193.1 THz) for indoor optical wireless communication has been demonstrated experimentally in [164], where the optical signal received after transmission through the fiber is re-transmitted directly in the air using lens and mirror arrangements. Similar arrangements may be used along with our proposed schemes reported in this thesis to make the whole link cost-effective. Additionally, the ability to directly transmit the optical signal at the output of the fiber without OE conversion would enhance the power efficiency of our proposed links.

Chapter 8

Appendix

8.1 Pulse Propagation Equation - Split Step Fourier Method

In this section, a numerical solution to the NLSE for the propagation of optical pulse is presented using the Split-Step Fourier Method (SSFM) [56]. The general equation for the propagation of an optical pulse in a fiber having attenuation α, second and third order dipsersion β_2 and β_3 and nonlinearity γ is given below:

$$\frac{\partial A(z,t)}{\partial z} + \beta_1 \frac{\partial A(z,t)}{\partial t} + \frac{i\beta_2}{2}\frac{\partial^2 A(z,t)}{\partial t^2} - \frac{\beta_3}{6}\frac{\partial^3 A(z,t)}{t^3} + \frac{\alpha}{2}A(z,t) = i\gamma \mid A(z,t) \mid^2 A(z,t). \tag{8.1}$$

The term β_1 represents the group velocity of the pulse, $A(z,t)$ represents the slowly varying pulse envelope and γ the nonlinearity parameter formulated as:

$$\gamma = \frac{n_2 \omega_0}{c A_{eff}}, \tag{8.2}$$

where the parameter A_{eff} is the effective area of the core, n_2 is the nonlinear refractive index of the fiber material and ω_0 is the center frequency of the optical signal, as described in Section 2.2. The nonlinear refractive index n_2 has a non-neglibile value when the input signal power is high. A_{eff} is related to the modal distribution of the fundamental mode of SMF $F(x,y)$ by the following relation:

$$A_{eff} = \frac{\left(\int \int_{-\infty}^{\infty} \mid F(x,y) \mid^2 \, dx\, dy. \right)}{\int \int_{-\infty}^{\infty} \mid F(x,y) \mid^4 \, dx\, dy}, \tag{8.3}$$

where x and y represent the two spatial axes. For a Gaussian modal distribution, $A_{eff} = \pi\omega^2$, where ω is the mode width parameter [56]. In the simulation of a propagating pulse, we consider a frame of reference moving with the pulse at a group velocity of $1/\beta_1$, hence the term β_1 in Equation 3.6 which represents the group velocity of the pulse can be removed. In order to simplify Equation 3.6, it is written in the following form:

$$\frac{\partial A(z,t)}{\partial z} = (\hat{D} + \hat{N})A(z,t), \tag{8.4}$$

where $\hat{D}$ is a differential operator that accounts for dispersion and attenuation in a linear medium and $\hat{N}$ is a nonlinear operator that takes into account fiber nonlinearity. These operators are expressed as below:

$$\hat{D} = -\frac{i\beta_2}{2}\frac{\partial^2}{\partial t^2} + \frac{\beta_3}{6}\frac{\partial^3}{\partial t^3} - \frac{\alpha}{2}, \tag{8.5}$$

and

$$\hat{N} = i\gamma \mid A(z,t) \mid^2 . \tag{8.6}$$

In a fiber, dispersion and nonlinearity act together but the SSFM obtains an approximate solution by applying these effects separately. SSFM assumes that for a small segment of fiber the dispersion and nonlinearity can act independently; thus it first applies nonlinearity and then dispersion to the small segment of fiber. In this way the whole length of fiber is covered by splitting it into segments that are small enough, so that the dispersive and nonlinear effects remain almost constant over them. For a segment h, the exact formal solution of Equation 3.6 is:

$$A(z+h,t) = exp[h(\hat{D} + \hat{N})A(z,t)]. \tag{8.7}$$

The approximate solution according to SSFM is:

$$A(z+h,t) \approx exp[h(\hat{D})exp(\hat{N})A(z,t)]. \tag{8.8}$$

Let $B(z,t)$ denote the result obtained after applying the nonlinear operator in time domain over step size h. The operator $exp(h\hat{N})$ can be evaluated as:

$$B(z,t) \approx exp(h\hat{N})A(z,t). \tag{8.9}$$

In the second step dispersion is applied in the Fourier domain using the operator $exp(h\hat{D})$ as below:

$$\hat{B}(z+h,\omega) \approx exp(h\hat{\hat{D}}(i\omega)\tilde{B}(z,\omega), \tag{8.10}$$

where $\tilde{B}(z,\omega)$ is the Fourier transform of $B(z,\omega)$ and $\hat{\hat{D}}(i\omega)$ is the Fourier transform of the linear operator $\hat{D}$. $\hat{\hat{D}}(i\omega)$ is obtained by replacing the operator $\partial/\partial t$ by $i\omega$ in the frequency domain. Finally we go back to the time domain by taking the inverse Fourier transform as below:

$$exp(h\hat{D})B(z,t) = F^{-1}(exp(h\hat{\tilde{D}}(i\omega)\tilde{B}(z,\omega)). \tag{8.11}$$

A variation of the above procedure in order to improve the accuracy for a segment h is to apply the dispersion on half segments that is $h/2$ while nonlinearity is applied in the middle. Hence Equation 3.13 can be replaced by following relation:

$$A(z+h,t) \approx exp(\frac{h}{2}\hat{D})exp(\int_{z}^{z+h}\hat{N}(z')dz').exp(\frac{h}{2}\hat{D}A(z,t)). \tag{8.12}$$

The integral in the middle exponential is useful to include the z dependence of the nonlinear operator N but it can be replaced by $exp(h\hat{N})$ if step size h is chosen to be very small.

8.2 Analogue-to-Digital and Digital-to-Analogue Conversions

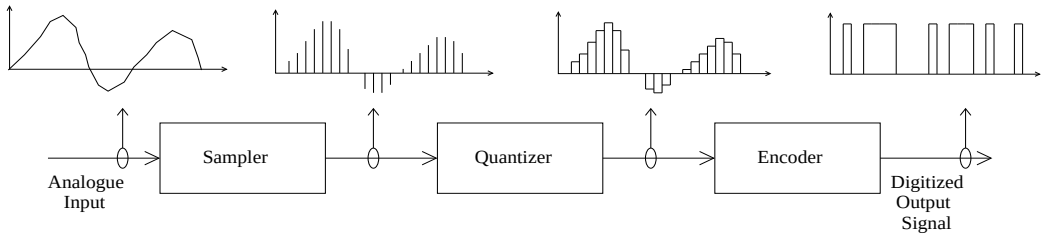

(a) Analogue-to-Digital Conversion

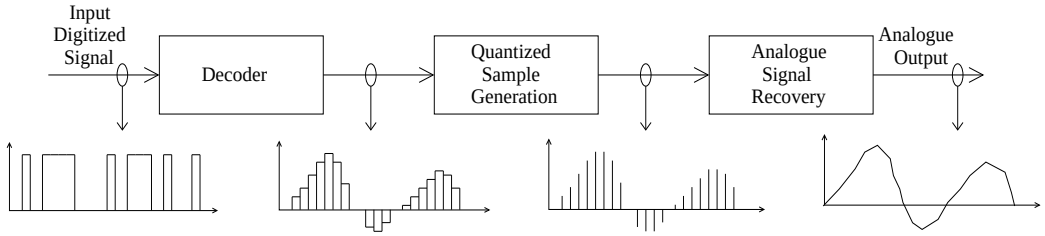

(b) Digital-to-Analogue Conversion

Figure 8.1: Block Diagrams of the ADC and DAC.

The ADC first samples the analogue signal of Figure 8.1 at a certain sampling rate in order to generate discrete-time samples repeated at regular intervals of time. The block diagram of a typical ADC is shown in Figure 6.2a, where the analogue input signal and its discrete-time samples are shown by the stylized plots. The discrete-time samples are then passed on to the quantization block, where each sampled value is assigned to a discretized amplitude. Each of the quantized signals is given a binary code in the encoder block, hence the output of the encoder is a sequence of bits, as shown by the stylized plot of Figure 6.2a. The DAC carries out the inverse operations of the ADC, as shown by the block diagram of Figure 6.2b. The input of the DAC is a sequence of

bits that was generated by the ADC. In the decoder block, the bit sequence is then converted back to discretized amplitudes, as shown by the stylized output signal. In the following low-pass filter, the discrete-time discrete-amplitude signal is converted back into an analogue signal. Finally the analogue signal is recovered from the discrete samples, as shown in Figure 6.2b.

Bibliography

[1] T. Jasny, "New Approaches in the New Chapter of Telecommunications," *IEEE Communications Magazine*, vol. 49, no. 10, pp. 20–22, October 2011.

[2] "International Telecommunication Union, www.itu.int."

[3] "Cisco Visual Networking Index: Global Mobile Data Traffic Forecast Update," February 2011.

[4] S. Sarkar, S. Dixit and B. Mukherjee, "Hybrid Wireless-Optical Broadband-Access Network (WOBAN): A Review of Relevant Challenges," *IEEE Journal of Lightwave Technology*, vol. 25, no. 11, pp. 3329–3340, November 2007.

[5] L. Hanzo, J. S. Blogh and S. Ni, "3G, HSDPA, HSUPA and FDD Versus TDD Networking: Smart Antennas and Adaptive Modulation," *John Wiley and Sons, Second Edition, 2008*.

[6] L. G. Kazovsky, W-T Shaw, D. Gutierrez, N. Cheng and S-W. Wong, "Next-Generation Optical Access Networks," *IEEE Journal of Lightwave Technology*, vol. 25, no. 11, pp. 3428–3442, November 2007.

[7] Hamed Al-Raweshidy and Shozo Komaki, "Radio Over Fiber Technologies for Mobile Communications Networks," *Artech House; 1st Edition*, March 2002.

[8] P. Monteiro, S. Pato, E. Lopez, D. Wake, N. J. Gomes and A. Gameiro, "Fiber Optic Networks for Distributed Radio Architectures: FUTON Concept and Operation," Sydney, April 2010, pp. 1–5.

[9] A. Hekkala, M. Lasanen, I. Harjula, L. C. Vieira, N. J. Gomes, A. Nkansah, S. Bittner, F. Diehm, and V. Kotzsch, "Analysis Of And Compensation For Non-Ideal ROF Links In DAS," *IEEE Wireless Communications*, vol. 17, no. 3, pp. 52–59, June 2010.

[10] D. Wake, A. Nkansah, N. J. Gomes, G. de Valicourt, R. Brenot, M. Violas, Z. Liu, F. Ferreira and S. Pato, "A Comparison of Radio Over Fiber Link Types for the Support of Wideband Radio Channels," *IEEE Journal of Lightwave Technology*, vol. 28, no. 16, pp. 2416–2422, August 2010.

[11] K. Fukuchi, T. Kasamatsu, M. Morie, R. Ohhira, T. Ito, K. Sekiya, D. Ogasahara and T. Ono, "10.92-Tb/s (273 40-Gb/s) Triple-Band/Ultra-Dense WDM Optical-Repeatered Transmission Experiment," March 2001, pp. PD24:1–3.

[12] J. Yu, Z. Dong, X. Xiao, Y. Xia, S. Shi, C. Ge, W. Zhou, N. Chi and Y. Shao, "Generation, Transmission and Coherent Detection of 11.2 Tb/s (112x100Gb/s) Single Source Optical OFDM Superchannel," March 2011, pp. 1–3.

[13] D. Wake and A. Nkansah and N. J. Gomes, "Radio over Fiber Link Design for Next Generation Wireless Systems," *IEEE Journal of Lightwave Technology*, vol. 28, no. 16, pp. 2456–2464, August 2010.

[14] N. Ghazisaidi and M. Maier, "Fiber-Wireless (FiWi) Access Networks: Challenges and Opportunities," *IEEE Network*, vol. 25, no. 1, pp. 36–42, January 2011.

[15] J. J. V. Olmos, T. Kuri, and K-I. Kitayama, "Dynamic Recongurable WDM 60-GHz Millimeter-Waveband Radio-Over-Fiber Access Network: Architectural Considerations and Experiment," *IEEE Journal of Lightwave Technology*, vol. 25, no. 11, pp. 3374–3380, November 2007.

[16] D. Wake, A. Nkansah, P. Assimakopolous, N. Gomes, M. Violas, L. Zhansheng, S. Pato, F. Ferreira, G. De Valicourt, R. Brenot, F. Van Dijk, "Design and Performance of Radio Over Fibre Links for Next Generation Wireless Systems Using Distributed Antennas," in *IEEE Future Network and Mobile Summit*, Italy, June 2010, pp. 1–9.

[17] S-H. Lee, J. G. Kim, M-H. Kang, "Performance Enhancement in Future PON and Mobile Convergence Networks," in *IEEE International Conference on Advanced Communication Technology (ICACT)*, Korea, February 2009, pp. 233–236.

[18] W. H. Chen and W. I. Way, "Multichannel Single-Sideband SCM/DWDM Transmission Systems," *IEEE Journal of Lightwave Technology*, vol. 22, no. 7, pp. 1679–1693, July 2004.

[19] A. H. Gnauck and P. J. Winzer, "Optical Phase-Shift-Keyed Transmission," *IEEE Journal of Lightwave Technology*, vol. 23, no. 1, pp. 115 – 130, January 2005.

[20] O. Shumao, Y. Kun, C. Hsiao-Hwa, "Integrated Dynamic Bandwidth Allocation in Converged Passive Optical Networks and IEEE 802.16 Networks," *IEEE Systems Journal*, vol. 4, no. 4, pp. 467–476, November 2010.

[21] D. Shifang, Z. Zeyu, W. Jianping and Z. Xinming, "Wavelength Assignment Scheme of ONUs in Hybrid TDM/WDM Fiber-Wireless Networks," in *IEEE International Conference on Communications (ICC)*, South Africa, May 2010, pp. 1–5.

[22] M. Maier, "WDM Passive Optical Networks and Beyond: the Road Ahead," *IEEE/OSA Journal of Optical Communications and Networking*, vol. 1, no. 4, pp. C1–C16, September 2009.

[23] Y. Yang, C. Lim, P. Gamage and A. Nirmalathas, "Demonstration of SCM Signal Transmission based on Digitized Radio-Over-Fiber Technique," in *IEEE International Topical Meeting on Microwave Photonics*, Valencia, Spain, October 2009, pp. 1–4.

[24] S. Betti, E. Bravi, and M. Giaconi, "Analysis of Distortion Effects in Subcarrier Multiplexed (SCM) Externally Modulated Lightwave Systems: A Generalized Approach," *IEEE Photonics Technology Letters*, vol. 9, no. 1, pp. 118–120, January 1997.

[25] G. H. Smith, D. Novak and C. Lim, "A Millimeter-Wave Full-Duplex Fiber-Radio Star-Tree Architecture Incorporating WDM and SCM," *IEEE Photonics Technology Letters*, vol. 10, no. 11, pp. 1650–1652, November 1998.

[26] P. C. Becker, N. A. Olsson, Jay R. Simpson, "Erbium-Doped Fiber Amplifiers: Fundamentals and Technology," *Academic Press, 1999*.

[27] E. Desurvire, "Erbium-Doped Fiber Amplifiers: Principles and Applications," *New York: Wiley, 1994*.

[28] X. Xu, R. Zhang, S. Ghafoor and L. Hanzo, "Imperfect Digital-Fiber-Optic-Link-Based Cooperative Distributed Antennas With Fractional Frequency Reuse in Multicell Multiuser Networks," *IEEE Transactions on Vehicular Technology*, vol. 60, no. 9, pp. 4439–4449, December 2011.

[29] S. Pato1, F. Ferreira1, P. Monteiro1, and H. Silva, "On Supporting Multiple Radio Channels over a SCM-Based Distributed Antenna System: A Feasibility Assessment," *International Conference on Transparent Optical Networks*, p. We.A3.5, June 2010.

[30] K. Fouli, M. Maier and M. Medard, "Network Coding in Next-Generation Passive Optical Networks," *IEEE Communications Magazine*, vol. 49, no. 9, pp. 38–46, September 2011.

[31] A.A.M. Saleh and J.M. Simmons, "Technology and Architecture to Enable the Explosive Growth of the Internet," *IEEE Communications Magazine*, vol. 49, no. 1, pp. 126–132, January 2011.

[32] R-J. Essiambre, G. Kramer, P. J. Winzer, G. J. Foschini and B. Goebel, "Capacity Limits of Optical Fiber Networks," *IEEE Journal of Lightwave Technology*, vol. 28, no. 4, pp. 662–701, February 2010.

[33] K. Imamura, K. Mukasa, Y. Mimura and T. Yagi, "Multi-Core Holey Fibers for the Long-Distance (¿100 km) Ultra Large Capacity Transmission," in *Optical Fiber Communications Conference (OFC)*, San Diego, USA, March 2009, pp. 1–3.

[34] T. Ho and D. Lun, "Network Coding: An Introduction," *Cambridge University Press, April 2008*.

[35] M. Belzner and H. Haunstein, "Network Coding in Passive Optical Networks," in *European Conference on Optical Communications (ECOC)*, Viena, Austria, September 2009, pp. 1–2.

[36] D. Novak, "Hybrid Fiber Radio - The Application of Photonic Links in Wireless Communication Systems," *OFC 2009 Short Course 217*, 2009.

[37] P. A. Gamage, A. Nirmalathas, C. Lim, D. Novak and R. Waterhouse, "Design and Analysis of Digitized RF-Over-Fiber Links," *IEEE Journal of Lightwave Technology*, vol. 27, no. 12, p. 2052 2061, June 2009.

[38] A. Nirmalathas, P. A. Gamage, C. Lim, D. Novak and R. Waterhouse, "Digitized Radio-Over-Fiber Technologies for Converged Optical Wireless Access Network," *IEEE Journal of Lightwave Technology*, vol. 28, no. 16, pp. 2366–2375, August 2010.

[39] S. Ghafoor and P. Petropoulos, "Effect of Dispersion Slope of Highly Nonlinear Fibre on the Performance of Self Phase Modulation Based 2R-Optical Regenerator," in *IEEE International Conference on Computer Technology and Development (ICCTD)*, Cairo, Egypt, November 2010, pp. 144–148.

[40] S. Ghafoor and L. Hanzo, "Baseband Fiber Aided 60 GHz Star-Like Distributed Antenna System Architecture," *IEEE Submitted to Communications Letters*, 2012.

[41] Salman Ghafoor and Lajos Hanzo, "Single-Laser-Based Radio-Over-Fiber Ring Network Using Multiple Side-bands," *IEEE Submitted to Transactions on Vehicular Technology*.

[42] S. Ghafoor and L. Hanzo, "Sub-Carrier-Multiplexed Duplex 64-QAM Radio-over-Fiber Transmission for Distributed Antennas," *IEEE Communications Letters*, vol. 15, no. 12, pp. 1368–1371, December 2011.

[43] S. Ghafoor, V. A. Thomas and L. Hanzo, "Duplex Digitized Transmission of 64-QAM Signals Over a Single Fiber Using a Single Pulsed Laser Source," *IEEE Communications Letters*, vol. PP, no. 99, pp. 1–4, June 2012.

[44] G. P. Agrawal, "Fiber-Optic Communication Systems," *John Wiley and Sons, Third Edition, 2002*.

[45] A. E. Siegman, "Lasers," *University Science Books*, 1986.

[46] H. Ghafouri-Shiraz, "Distributed Feedback Laser Diodes and Optical Tunable Filters," *John Wiley ans Sons, New York, 2003*.

[47] X. Qian, P. Hartmann, J. D. Ingham, R. V. Penty and I. H. White, "Directly-Modulated Photonic Devices for Microwave Applications," in *IEEE International Microwave Symposium Digest*, California, June 2005, pp. 1–4.

[48] H. Ito, H. Yokoyama, S. Murata and H. Inaba, "Picosecond optical pulse generation from an R.F. modulated AlGaAs D.H. diode laser," *Electronics Letters*, vol. 15, pp. 738 – 740, November 1979.

[49] H. Ito, H. Yokoyama, S. Murata, and H. Inaba, "Generation of picosecond optical pulses with highly RF modulated AlGaAs DH laser," *IEEE Journal of Quantum Electronics*, vol. 17, pp. 663–670, May 1981.

[50] D. S. Seo, H. F. Liu, D. Kim and D. Sampson, "Injection Power and Wavelength Dependence of an External-Seeded Gain-Switched Fabry-Perot Laser," *Applied Physics Letters*, vol. 67, no. , pp. 1503–1505, 1995.

[51] M. A. F. Roelens, "Precise intensity and phase characterisation of optical telecommunication signals," *PhD Thesis*, July 2006.

[52] G. L. Li and P. K. Yu, "Optical Intensity Modulators for Digital and Analog Applications," *IEEE Journal of Lightwave Technology*, vol. 21, no. 9, pp. 2010–2030, September 2003.

[53] W. K. Marshall, B. Crosignani and A. Yariv, "Laser Phase Noise to Intensity Noise Conversion by Lowest-Order Group-Velocity Dispersion in Optical Fiber: Exact Theory," *IEEE Optics Letters*, vol. 25, no. 3, pp. 165–167, February 2000.

[54] "Photonic Modules Reference Manual: VPI Systems."

[55] K. Noguchi, O. Mitomi, and H. Miyazawa, "Millimeter-Wave Ti:LiNbO3 Optical Modulators," *IEEE Journal of Lightwave Technology*, vol. 16, no. 4, pp. 615–619, April 1998.

[56] G. P. Agrawal, "Nonlinear Fiber Optics," *Elsevier, Third Edition, January 2001*.

[57] G. H. Smith, D. Novak and Z. Ahmed, "Overcoming Chromatic-Dispersion Effects in Fiber-Wireless Systems Incorporating External Modulators," *IEEE Transactions on Microwave Theory and Techniques*, vol. 45, no. 8, pp. 1410–1415, August 1997.

[58] F. Koyama and K. Iga, "Frequency Chirping in External Modulator," *IEEE Journal of Lightwave Technology*, vol. 6, no. 1, pp. 87–93, January 1988.

[59] R. Ramaswami and K. N. Savarajan, "Optical Networks: A practical Perspective," *Academic Press, 2nd Eidtion, 2002*.

[60] H. Schmuck, "Comparison of optical millimeter-wave concepts with regard to chromatic dispersion," *Electronics Letters*, vol. 31, no. 21, pp. 1848 – 1849, October 1995.

[61] E. Sackinger, "Broadband Circuits for Optical Fiber Communication," *John Wiley and Sons, First Edition, 2005*.

[62] C. Palmer and E. Loewen, "Diffraction Grating Handbook," *Newport Corporation, Sixth Edition, 2005*.

[63] C. R. Doerr and K. Okamoto, "Advances in Silica Planar Lightwave Circuits," *IEEE Journal of Lightwave Technology*, vol. 24, no. 12, pp. 4763–4789, December 2006.

[64] H. Uetsuka, "AWG Technologies for Dense WDM Applications," *IEEE Journal of Selected Topics in Quantum Electronics*, vol. 10, no. 2, pp. 393–402, March/April 2004.

[65] M. K. Smit and C. V. Dam, "PHASAR-Based WDM-Devices: Principles, Design and Applications," *IEEE Journal of Selected Topics in Quantum Electronics*, vol. 2, no. 2, pp. 236–250, June 1996.

[66] U. Gliese, S. Ngrskov, and T. N. Nielsen, "Chromatic Dispersion in Fiber-0ptic Microwave and Millimeter-Wave Links," vol. 44, no. 10, October 1996, pp. 1716–1724.

[67] C. Cox, E. Ackerman, R. Helkey and G. E. Betts, "Techniques and Performance of Intensity-Modulation Direct-Detection Analog Optical Links," vol. 45, no. 8, August 1997, pp. 1375–1383.

[68] J. J. OReilly, P. M. Lane and M. H. Capstick, "Optical Generation and Delivery of Modulated mm-waves for Mobile Communications," *Analogue Optical Fibre Communications (Institute of Electrical Engineers, London, UK)*, pp. 229–249, 1995.

[69] D. Wake, C. R. Lima, and P. A. Davies, "Optical Generation of Millimeter-Wave Signals for Fiber-Radio Systems Using a Dual Mode DFB Semiconductor Laser," *IEEE Transactions on Microwave Theory and Technique*, vol. 43, no. 9, pp. 2270–2276, September 1995.

[70] M. Tamburrini, M. Parent, L. Goldberg, and D. Stillwell, "Optical Feed for a Phased Array Microwave Antenna," *IET Electronics Letters*, vol. 23, no. 13, pp. 680–681, June 1987.

[71] M. Izutsu, S. Shikama, and T. Sueta, "Integrated Optical SSB Modulator/Frequency Shifter," *IEEE Journal of Quantum Electronics*, vol. QE-17, no. 11, pp. 2225–2227, June 1987.

[72] H. Schmuck, R. Heidemann, and R. Hofstetter, "Distribution of 60 GHz Signals to More Than 1000 Base Stations," *IET Electronics Letters*, vol. 30, no. 1, pp. 59–60, January 1994.

[73] A. Wiberg, P. Prez-Milln, M. V. Andrs, P. A. Andrekson and P. O. Hedekvist, "Fiber-Optic 40-GHz mm-Wave Link With 2.5-Gb/s Data Transmission," *IEEE Photonics Technology Letters*, vol. 17, no. 9, pp. 1938–1940, September 2005.

[74] X. Yu, X. Zheng, and H. Zhang, "Polarization State Rotation Filter For Optical Generation Of Continuously Tunable Millimeter-Wave Signal Employing An External Intensity Modulator," *Elsevier Optical Fiber Technology*, vol. 13, no. 1, pp. 56–61, 2007.

[75] M-K. Hong, Y-Y. Won and S-K. Han, "Gigabit Optical Access Link for Simulatneous Wired and Wireless Signal Transmission Based on Dual Parallel Injection-Locking Fabry-Perot Laser Diodes," *IEEE Journal of Lightwave Technology*, vol. 26, no. 15, p. 27252731, August 2008.

[76] A. Kaszubowska, P. Anandarajah, and L. P. Barry, "Multifunctional Operation of a Fiber Bragg Grating in a WDM/SCM Radio Over Fiber Distribution System," *IEEE Photonics Technology Letters*, vol. 16, no. 2, pp. 605–607, January 2004.

[77] C. Lim and A. Mirmalathas and M. Attygalle, D. Novak and R. Waterhouse, "On the Merging of Millimeter-Wave Fiber-Radio Backbone With 25-GHz WDM Ring Networks," *IEEE Journal of Lightwave Technology*, vol. 21, no. 10, pp. 2203–2210, October 2003.

[78] J. Yu, Z. Jia, L. Yi, Y. Su, G-K. Chang, and T. Wang, "Optical Millimeter-Wave Generation or Up-Conversion Using External Modulators," *IEEE Photonics Technology Letters*, vol. 18, no. 1, pp. 265–267, January 2006.

[79] J. Yu, Z. Jia, L. Xu, L. Chen, T. Wang, and G-K. Chang, "DWDM Optical Millimeter-Wave Generation for Radio-Over-Fiber Using an Optical Phase Modulator and an Optical Interleaver," *IEEE Photonics Technology Letters*, vol. 18, no. 13, pp. 1418–1420, July 2006.

[80] H-H Lu, H-C Peng, W-S Tsai, C-C Lin, S-J. Tzeng and Y-Z Lin, "Bidirectional hybrid CATV/radio-over-fiber WDM transport system," *OSA Optics Letters*, vol. 35, no. 3, p. 279 281, February 2010.

[81] T-S. Cho and K. Kim, "Optimization of Radio-On-Fiber Systems Employing ODSB Signals by Utilizing a Dual-Electrode Mach-Zhender Modulator Against IM3," *IEEE Photonics Technology Letters*, vol. 18, no. 9, pp. 1076–1078, May 2006.

[82] C. Lim, A. Nirmalathas, K-L. Lee, D. Novak, and R. Waterhouse, "Intermodulation Distortion Improvement for FiberRadio Applications Incorporating OSSB+C Modulation in an Optical Integrated-Access Environment," *IEEE Journal of Lightwave Technology*, vol. 25, no. 6, pp. 1602–1612, June 2007.

[83] M . R. Phillips, T. E. Darcie, D . Marcuse, G. E. Bodeep, and N. J. Frigo, "Nonlinear Distortion Generated by Dispersive Transmission of Chirped Intensity-Modulated Signals," *IEEE Photonics Technology Letters*, vol. 3, no. 5, pp. 481–482, May 1991.

[84] S. Betti, E. Bravi, and M. Giaconi, "Nonlinear Distortions due to the Dispersive Transmission of SCM Optical Signals in the Presence of Chirping Effect: An Accurate Analysis," *IEEE Photonics Technology Letters*, vol. 9, no. 12, pp. 1640–1642, December 1997.

[85] T. Chikama, S. Watanabe, T. Naito, H. Onaka, T Kiyonaga, Y. Onoda, H. Miyata, M. Suyama, M. Seino and H.Kuwahara, "Modulation and Demodulation Techniques in Optical Heterodyne PSK Transmission Systems," *IEEE Journal of Lightwave Technology*, vol. 8, no. 3, pp. 309–322, March 1990.

[86] K. I. Kallimani and M. j. O'Mahony, "Relative Intensity Noise for Laser Diodes with Arbitrary Amounts of Optical Feedback," *IEEE Journal of Quantum Electronics*, vol. 34, no. 8, pp. 1438–1446, August 1998.

[87] A. M. J. Koonen, M. G. Larrod, A. Ngoma, K. Wang, H. Yang, Y. Zheng, E. Tangdiongga, "Perspectives of Radio over Fiber Technologies," San Diego, February 2008, pp. 1–3.

[88] D. Wake, M. Webster, G. Wimpenny, K. Beacham and L. Crawford, "Radio Over Fiber for Mobile Communications," October 2004, pp. 157–160.

[89] C. Cox, E. Ackerman, G. E. Betts and J. L. Prince, "Limits on the Performance of RF-Over-Fiber Links and Their Impact on Device Design," *IEEE Transactions on Microwave Theory and Techniques*, vol. 54, no. 2, pp. 906–920, February 2006.

[90] Q. Jiang and M. Kavehrad, "A Subcarrier-Multiplexed Coherent FSK System Using a Mach-Zehnder Modulator with Automatic Bias Control," *IEEE Photonics Technology Letters*, vol. 5, no. 8, pp. 941–943, August 1993.

[91] A. Ferreira, T. Silveira, D. Fonseca, R. Ribeiro and P. Monteiro, "Highly Linear Integrated Optical Transmitter for Subcarrier Multiplexed Systems," *IEEE Photonics Technology Letters*, vol. 21, no. 7, pp. 438–440, April 2009.

[92] A. Nirmalathas, P. A. Gamage, C. Lim, D. Novak, R. Waterhouse, Y. Yang, "Digitized RF Transmission Over Fiber," *IEEE Microwave Magazine*, vol. 10, no. 4, pp. 75–81, June 2009.

[93] P. M. Wala, "A New Microcell Architecture Using Digital Optical Transport," vol. , no. , May 1993, pp. 585–588.

[94] R. G. Vaughan, N. L. Scott and R. White, "The Theory of Bandpass Sampling," *IEEE Transactions on Signal Processing*, vol. 39, no. 9, pp. 1973–1984, September 1991.

[95] D. M. Akos, M. Stockmaster, J. B. Y. Tsui and J. Cashera, "Direct Bandpass Sampling of Multiple Distinct RF Signals," *IEEE Transactions on Communications*, vol. 47, no. 7, pp. 983–988, July 1999.

[96] O. Leclerc, B. Lavigne, E. Balmefrezol, P. Brindel, L. Pierre, D. Rouvillain, and F. Seguineau, "Optical Regeneration at 40 Gb/s and beyond," *IEEE Journal of Lightwave Technology*, vol. 21, pp. 2779 – 2790, November 2003.

[97] L. Provost, F. Parmigiani, P. Petropoulos and D. J. Richardson, "Investigation of Simultaneous 2R Regeneration of Two 40-Gb/s Channels in a Single Optical Fiber," *IEEE Photonics Technology Letters*, vol. 20, no. 4, pp. 270–272, February 2008.

[98] M. Matsumoto, Y. Shimada and H. Sakaguchi, "Two-Staged SPM-Based All-Optical 2R Regeneration by Bidirectional Use of a Highly Nonlinear Fiber," *IEEE Journal of Quantum Electronics*, vol. 45, no. 1, pp. 51–58, January 2009.

[99] B-E Olsson and D. J. Blumenthal, "Pulse Restoration by Filtering of Self-Phase Modulation Broadened Optical Spectrum," *IEEE Journal of Lightwave Technology*, vol. 20, no. 7, pp. 1113–1117, July 2002.

[100] R. J. Essiambre, B. Mikkelsen and G. Raybon, "Intra-Channel Cross-Phase Modulation and Four-Wave Mixing in High-Speed TDM Systems," *Electronics Letters*, vol. 35, no. 18, pp. 1576–1577, September 1999.

[101] J. A. Harrison, K. J. Blow and A. J. Poustie, "All-Optical Bit-Level Retiming and Jitter Suppression," *Optics Communications*, vol. 240, pp. 221–226, June 2004.

[102] A. Bogris, P. Velanas and D. Syvridis, "Numerical Investigation of a 160-Gb/s Reconfigurable Photonic Logic Gate Based on Cross-Phase Modulation in Fibers," *IEEE Photonics Technology Letters*, vol. 19, no. 6, pp. 402–404, March 2007.

[103] A. Bogoni, L. Poti, R. Proietti, G. Meloni, F. Ponzini and P. Ghelfi, "Regenerative and Reconfigurable All-Optical Logic Gates For Ultra-Fast Applications," *Electronics Letters*, vol. 41, no. 7, pp. 435–436, March 2005.

[104] J. H. Lee, T. Nagashima, T. Hasegawa, S. Ohara, N. Sugimoto and K. Kikuchi, "40 Gbit/s XOR and AND Gates Using Polarisation Switching Within 1 m-Long Bismuth Oxide-Based Nonlinear Fibre," *Electronics Letters*, vol. 41, no. 19, pp. 1074–1075, March 2005.

[105] P. Johannisson and M. Karlsson, "Characterization of a Self Phase Modulation based all-optical Regeneration system," *IEEE Photonics Technology Letters*, vol. 17, no. 12, pp. 2667–2669, Dec 2005.

[106] P. V. Mamyshev, "All-Optical Data Regeneration Based on Self-Phase Modulation Effect," *ECOC1998*, pp. 20–24, Sep 1998.

[107] C. Finot, T. N. Nguyen, J. Fatome, T. Chartier, L. Bramerie, M. Gay, S. Pitois and J. C. Simon, "Numerical study of an optical regenerator exploiting self-phase modulation and spectral offset filtering at 40 Gbit/s," *Optics Communications*, vol. 281, pp. 2252–2264, Dec 2008.

[108] N. Yoshikane, I. Morita, T. Tsuritani, A. Agata, N. Edagawa and S. Akiba, "Benefit of SPM-Based All-Optical Reshaper in Receiver For Long-Haul DWDM Tranmission Systems," *IEEE Journal of Selected Topics in Quantum Electronics*, vol. 10, no. 2, pp. 412–420, March 2005.

[109] T. N. Nguyen, M. Gay, L. Bramerie, T. Chartier, J. C. Simon and M. Joindot, "Noise Reduction in 2R-Regeneration Technique Utilizing Self-Phase Modulation and Filtering," *Optics Express*, vol. 14, no. 5, pp. 1737–1739, March 2006.

[110] M. Aoudeh and J. C. Cartledge , "Impact of Residual dispersion and ASE Noise on the Performance Optimization of All-Optical Regenerators Utilizing Self-Phase Modulation in Highly Nonlinear Fiber," *IEEE Journal of Lightwave Technology*, vol. 12, no. 4, pp. 717–725, August 2006.

[111] M. Rochette, L. Fu, V. Ta'eed, D. J. Moss and B. J. Eggleton, "2R Optical Regeneration: An All-Optical Solution For BER Improvement," *IEEE Journal of Selected Topics in Quantum Electronics*, vol. 12, no. 4, pp. 736–744, July 2006.

[112] L. Provost, C. Finot, P. Petropoulos, K. Mukasa and D. J. Richardson, "Design scaling rules for 2R-optical self-phase modulation-based regenerators," *IEEE Optics Express*, vol. 15, no. 8, pp. 5100–5113, 2007.

[113] L. Provost, C. Finot, K. Mukasa, P. Petropoulos and D. J. Richardson, "Generalisation and experimental validation of design rules for self-phase modulation based 2R-regenerator," in *Optical Fiber Communications Conference (OFC)*, California, March 2007, pp. 1–3.

[114] T.-H. Her, G. Raybon and C. Headley, "Optimization of Pulse Regeneration at 40 Gb/s Based on Spectral Filtering of Self-Phase Modulation in Fibre," *IEEE Photonics Technology Letters* , vol. 16, pp. 200–202, 2004.

[115] A. G. Striegler and B. Schmauss, "Analysis and Optimization of SPM-Based 2R Signal Regeneration at 40 Gb/s," *IEEE Journal of Lightwave Technology*, vol. 24, pp. 2835–2843, Mar 2006.

[116] P. P. Baveja, D. N. Maywar and G. P. Agrawal, "Optimization of All-Optical 2R Regenerators operating at 40 Gb/s: Role of dispersion," *IEEE Journal of Lightwave Technology*, vol. 27, no. 17, pp. 3831–3836, Sep 2009.

[117] F. Poletti, K. Furusawa, Z. Yusoff, N. G. R. Broderick and David J. Richardson, "Nonlinear tapered holey fibers with high stimulated Brillouin scattering threshold and controlled dispersion," *IEEE Journal of Optical Society of America B*, vol. 24, no. 9, Sep 2007.

[118] T. Yamamoto, H. Kubota and S. Kawanishi, "Supercontinuum generation at 1.55 um in a dispersion-flattened polarization-maintaining photonic crystal fibre," *IEEE Optics Express*, vol. 11, no. 13, pp. 1537–1540, 2003.

[119] C. Lim, A. Nirmalathas, D. Novak, R. Waterhouse, and G. Yoffe, "Millimeter-Wave Broad-Band Fiber-Wireless System Incorporating Baseband Data Transmission Over Fiber and Remote LO Delivery," *IEEE Journal of Lightwave Technology*, vol. 18, no. 10, pp. 1355–1363, October 2000.

[120] L. Chen, Y. Shao, X. Lei, H. Wen and S. Wen, "A Novel Radio-Over-Fiber System With Wavelength Reuse for Upstream Data Connection," *IEEE Photonics Technology Letters*, vol. 19, no. 6, pp. 387 – 389, March 2007.

[121] J. Yu, Z. Jia, T. Wang and G. K. Chang, "A Novel Radio-Over-Fiber Conguration Using Optical Phase Modulator to Generate an Optical mm-Wave and Centralized Lightwave for Uplink Connection," *IEEE Photonics Technology Letters*, vol. 19, no. 3, pp. 140–142, February 2007.

[122] Y-T. Hsueh, Z. Jia, H-C. Chien, J. Yu and G-K. Chang, "A Novel Bidirectional 60-GHz Radio-Over-Fiber Scheme With Multiband Signal Generation Using a Single Intensity Modulator," *IEEE Photonics Technology Letters*, vol. 21, no. 18, pp. 1338–1340, September 2009.

[123] C-H. Chang, P-C. Peng, H-H. Lu, C-L. Shih and H-W. Chen, "Simplified Radio-Over-Fiber Transport Systems With a Low-Cost Multiband Light Source," *OSA Optics Letters* , vol. 35, no. 23, pp. 4021–4023, December 2010.

[124] T. Kuri and K. Kitayama, "Optical Heterodyne Detection Technique for Densely Multiplexed Millimter-Wave-Band Radio-on-Fiber Systems," *IEEE Journal of Lightwave Technology*, vol. 21, no. 12, pp. 3167–3179, December 2003.

[125] M. G. Larrode, A. M. J. Koonen, J. J. V. Olmos and A. Ng, "Bidirectional Radio-Over-Fiber Link Employing Optical Frequency Multiplication," *IEEE Photonics Technology Letters*, vol. 18, no. 1, pp. 241–243, January 2006.

[126] X. Zhang, B. Liu, J. Yao, K. Wu and R. Kashyap, "A Novel Millimeter-Wave-Band Radio-Over-Fiber System With Dense Wavelength-Division Multiplexing Bus Architecture," *IEEE Journal of Lightwave Technology*, vol. 54, no. 2, pp. 929–937, February 2006.

[127] Y. Kim, S. Doucet, M. E. M. Pasandi and S. LaRochelle, "Optical Multicarrier Generator for Radio-Over-Fiber Systems," *OSA Optics Express* , vol. 16, no. 2, pp. 1068–1076, January 2008.

[128] M. F. Huang, J. Yu, Z. Jia and G. K. Chang, "Simultaneous Generation of Centralized Lightwaves and Double/Single Sideband Optical Millimeter-Wave Requiring Only Low-Frequency Local Oscillator Signals for Radio-Over-Fiber Systems," *IEEE Journal of Lightwave Technology*, vol. 26, no. 15, pp. 2653–2662, August 2008.

[129] H-C. Ji and H. Kim and Y. C. Chung, "Cost-Effective Radio-Over-Fiber Systems Employing Phase-Modulated Downlink and Intensity-Modulated Uplink," in *Optical Fiber Communication Conference (OFC)*, San Diego, March 2009, p. OTuJ8.

[130] J. Yu, G-K. Chang, Z. Jia, A. Chowdhury, M-F. Huang, H-C. Chien, Y-T. Hsueh, W. Jian, C. Liu and Z. Dong, "Cost-Effective Optical Millimeter Technologies and Field Demonstrations for Very High Throughput Wireless-Over-Fiber Access Systems," *IEEE Journal of Lightwave Technology*, vol. 28, no. 16, pp. 2376–2397, August 2010.

[131] J. James, P. Shen, A. Nkansah, X. Liang and N. J. Gomes, "Nonlinearity and Noise Effects in Multi-Level Signal Millimeter-Wave Over Fiber Transmission Using Single and Dual Wavelength Modulation," *IEEE Transactions on Microwave Theory and Techniques*, vol. 58, no. 11, pp. 3189–3198, November 2010.

[132] J. Yu and G-K. Chang, "A Novel Technique for Optical Label and Payload Generation and Multiplexing using Optical Carrier Suppression and Separation," *IEEE Photonics Technology Letters*, vol. 16, no. 1, pp. 320 – 322, January 2004.

[133] S. Ghafoor and L. Hanzo, "Reduced Dispersion Duplex DQPSK Radio-Over-Fiber Communications Using Single-Laser-Based Multiple Side-Bands," in *IEEE International Conference on Communications (ICC)*, Kyoto, Japan, June 2011, pp. 1–5.

[134] N. Chi, J. Zhang and P. Jeppensen, "All-Optical Subcarrier Labeling Based on the Carrier Suppression of the Payload," *IEEE Photonics Technology Letters*, vol. 15, no. 5, pp. 781–783, May 2003.

[135] J. L. Corral and J. Marti and J. M. Fuster, "General Expressions for IM/DD Dispersive Analog Optical Links With External Modulation or Optical Up-Conversion in a MachZehnder Electro-Optical Modulator," *IEEE Transaction on Microwave Theory and Techniques*, vol. 49, no. 10, pp. 1968–1976, October 2001.

[136] O. Vassilieva, T. Hoshida, X. Wang, J. Rasmussen, H. Miyata and T. Naito, "Impact of Polarization Dependent Loss and Cross-Phase Modulation Multiplexed DQPSK Signals," *Optical Fiber communication Conference*, February 2008.

[137] J. G. Proakis, "Digital Communications," *McGraw-Hill International; 4th Edition*, August 2000.

[138] R. A. Shafik, M. S. Rahman, R. Islam and N. S. Ashraf, "On the Error Vector Magnitude as a Performance Metric and Comparative Analysis," in *IEEE-ICET International Conference on Emerging Technologies*, Peshawar, Pakistan, November 2006, pp. 27–31.

[139] "IEEE 802.11.a Standardization (ISO/IEC 8802-11:1999/Amd 1:2000(E)."

[140] R. A. Shafik, M. S. Rahman and A. R. Islam, "On the External Relationships Among EVM, BER and SNR as Performance Metrics," in *Imternational Conference on Electrical and Computer Engineering (ICECE)*, , December 2006, pp. 408–411.

[141] L. Hanzo, S. X. Ng, T. Keller and W. Webb, "Quadrature Amplitude Modulation: From Basics to Adaptive Trellis-Coded, Turbo-Equalised and Space-Time Coded OFDM, CDMA and MC-CDMA Systems," *John Wiley and Sons, Second Edition, 2004*.

[142] N. Pleros, K. Tsagkaris and N. Tselikas, "A Moving Extended Cell Concept For Seamless Communication in 60 GHz Radio-Over-Fiber Networks," *IEEE Commun Lett*, vol. 12, no. 11, pp. 852–854, November 2008.

[143] L. Hanzo, O. Alamri, M. El-Hajjar and N. Wu, "Near-Capacity Multi-Functional MIMO Systems: Sphere-Packing, Iterative Detection and Cooperation," *John Wiley and Sons, First Edition, 2009*.

[144] C-P Liu and A. J. Seeds, "Transmission of Wireless MIMO-Type Signals Over a Single Optical Fiber Without WDM," *IEEE Transactions on Microwave Theory and Techniques*, vol. 58, no. 11, pp. 3094–3102, November 2010.

[145] C-T. Lin, P-T. Shih, J. Chen, W-Q Xue, P-C Peng and S. Chi, "Optical Millimeter-Wave Signal Generation Using Frequency Quadrupling Technique and No Optical Filtering," *IEEE Photonics Technology Letters*, vol. 20, no. 12, pp. 1027–1029, June 2008.

[146] U. Gliese, S. Ngrskov and T. N. Nielsen, "Chromatic Dispersion in Fiber-Optic Microwave and Millimeter-Wave Links," *IEEE Transactions on Microwave Theory and Techniques*, vol. 44, no. 10, pp. 1716–1724, October 1996.

[147] R. Sambaraju, D. Zibar, A. Caballero, I. T. Monroy, R. Alemany and J. Herrera, "100-GHz Wireless-Over-Fiber Links With Up to 16-Gb/s QPSK Modulation Using Optical Heterodyne Generation and Digital Coherent Detection," *IEEE Photonics Technology Letters*, vol. 22, no. 20, pp. 1650–1652, November 2010.

[148] C- K. Wang, Y- M. Lin and W. I. Way, "Radio-Over-Fiber 16-QAM, 100-km Transmission at 5 Gb/s Using DSB-SC Transmitter and Remote Heterodyne Detection," *IEEE Journal of Lightwave Technology*, vol. 26, no. 6, pp. 643–653, March 2008.

[149] P. A. Gamage, A. Nirmalathas, C. Lim, D. Novak and R. Waterhouse, "Experimental Demonstration of the Transport of Digitized Multiple Wireless Systems Over Fiber," *IEEE Photonics Technology Letters*, vol. 21, no. 11, pp. 691–693, June 2009.

[150] Y. Yang, C. Lim and A. Nirmalathas, "Multichannel Digitized RF-Over-Fiber Transmission Based on Bandpass Sampling and FPGA," *IEEE Transactions on Microwave Theory and Techniques*, vol. 58, no. 11, pp. 3181–3188, November 2010.

[151] Y. Yang and C. Lim and A. Nirmalathas, "Experimental Demonstration of Multi-Service Hybrid Fiber-Radio System Using Digitized RF-Over-Fiber Technique," *IEEE Journal of Lightwave Technology*, vol. 29, no. 14, pp. 2131–2137, July 2011.

[152] J. G. Proakis and D. G. Manolakis, "Digital Signal Processing," *Pearson Education, Fourth Edition, 2007*.

[153] P. Gysel and R. K. Staubli, "Statistical Properties of Rayleigh Backscattering in Single-Mode Fibres," *IEEE Journal of Lightwave Technology*, vol. 8, no. 4, pp. 561–567, April 1990.

[154] J. Ko, S. Kim, J. Lee, S. Won, Y. S. Kim and J. Jeong, "Estimation of Performance Degradation of Bidirectional WDM Transmission Systems due to Rayleigh Backscattering and ASE Noises using Numerical and Analytical Models," *IEEE Journal of Lightwave Technology*, vol. 21, no. 4, pp. 938–946, April 2003.

[155] C. Lim, A. Nirmalathas, Y. Yang, D. Novak and R. Waterhouse, "Radio-Over-Fiber Systems," in *IEEE Communications and Photonics Conference and Exhibition*, Shanghai, China, November 2009, pp. 1–10.

[156] Y. Sun and S. Signell, "Effect of Noise and Jitter in Bandpass Sampling," vol. 1, no. 1, May 2004, pp. 761–764.

[157] M. Shinagawa, Y. Akazawa and T. Wakimoto, "Jitter Analysis of High-Speed Sampling Systems," *IEEE Journal of Solid-State Circuits*, vol. 25, no. 1, pp. 220–224, February 1990.

[158] R. A. Griffin and A. C. Carter, "Optical Differential Quadrature Phase-Shift Key (oDQPSK) for High Capacity Optical Transmission," in *Optical Fiber Communications Conference (OFC)*, California, March 2002, pp. 367–368.

[159] M. Atef, R. Swoboda and H. Zimmermann, "1.25 Gbit/s Over 50 m Step-Index Plastic Optical Fiber Using a Fully Integrated Optical Receiver With an Integrated Equalizer," *IEEE Journal of Lightwave Technology*, vol. 30, no. 1, pp. 118–122, January 2012.

[160] Y. Shi, M. Morant, C. Okonkwo, R. Llorente, E. Tangdiongga and A. M. J. Koonen, "Multi-standard Wireless Transmission Over SSMF and Large-Core POF for Access and In-Home Networks," *IEEE Photonics Technology Letters*, vol. 24, no. 9, pp. 736–738, May 2012.

[161] S. Karabetsos, E. Pikasis, T. Nikas, A. Nassiopoulos and D. Syvridis, "DFT-Spread DMT Modulation for 1-Gb/s Transmission Rate Over 100 m of 1-mm SI-POF," *IEEE Photonics Technology Letters*, vol. 24, no. 10, pp. 836–838, May 2012.

[162] H. Chen, H. P. A van den Boom, E. Tangdiongga and T. Koonen, "30-Gb/s Bidirectional Transparent Optical Transmission With an MMF Access and an Indoor Optical Wireless Link," *IEEE Photonics Technology Letters*, vol. 24, no. 7, pp. 572–574, April 2012.

[163] D. J. F. Barros, S. K. Wilson and J. M. Kahn, "Comparison of Orthogonal Frequency-Division Multiplexing and Pulse-Amplitude Modulation in Indoor Optical Wireless Links," *IEEE Transactions on Communications*, vol. 60, no. 1, pp. 153–163, January 2012.

[164] K. Wang, A. Nirmalathas, C. Lim, and E. Skafidas, "Experimental Demonstration of a Full-Duplex Indoor Optical Wireless Communication System," *IEEE Photonics Technology Letters*, vol. 24, no. 3, pp. 188–190, February 2012.

[165] S. Dimitrov, S. Sinanovic and H. Haas, "Signal Shaping and Modulation for Optical Wireless Communication," *IEEE Journal of Lightwave Technology*, vol. 30, no. 9, pp. 1319–1328, May 2012.